Universidad Autónoma de Madrid
Facultad de Ciencias
Departamento de Física Teórica

Exocomets: a study of the gaseous environment of A type main sequence stars.

A thesis submitted by

Isabel Rebollido Vázquez

in partial fulfillment of the requirements for the degree of Doctor of Astrophysics

Supervised by

Eva Gloria Villaver Sobrino
Departamento de Física Teórica - UAM

Benjamín Montesinos Comino
Centro de Astrobiología - CAB, CSIC-INTA

Madrid, November 2019

A Samuel,
que sexa esta tamén a túa tese.

E a meu irmán,
e a meus primos, que son meus imáns.
Sempre Xuntos.

Abstract

In main sequence stars, infrared excesses attributed to the presence of circumstellar dust in debris discs has been the empirical indirect probe of the existence of minor bodies for more than 40 years, as they were needed to explain the dust emission. But it was not until 1987 that the first evidence of the presence of exocomets was found. It was around the β Pictoris star and it came with the detection of non-photospheric variable absorptions superimposed to the photospheric Ca II lines. Since then, the number of known stars with exocomet-like absorptions has grown slowly, through sporadic works, up to $\sim$20 stars, all of them A-type. The growth of the exoplanetary field, and the possible relevance of minor bodies in the configuration, building-up and architecture of planetary systems, have turned the attention of the scientific community again to the study of small bodies around stars other than the Sun. Encouraging are the first detections of exocometary bodies in photometric light curves from data taken by exoplanet search missions such as *Kepler* and *TESS*. Photometric detection using the exquisite light curves from these space observatories, in addition of providing a new methodology, has demonstrated that exocomets, as was expected from the early detection of infrared excesses, are present around stars of different spectral types in the main sequence.

This thesis carries out a systematic spectroscopic survey in the time domain with the aim of detecting exocometary activity around main-sequence stars. The main objectives are, first, to enlarge the sample of known exocomet-host stars, and second, determine the possible environmental characteristics of the exocomet-host systems that could help to understand and detect them.

A large survey to search for exocometary signals was conducted, where around 1500 high-resolution optical spectra of 117 stars with spectral types G to B were inspected. Although it was performed on a biased sample, this is, to our knowledge, the largest exocometary survey that allows for the first time to evaluate the possible dependence of the presence of exocomets with the characteristics of the circumstellar environment. In this thesis, exocomet-like variability has been found in six new stars, increasing from 20 to 26 –a 30%– the number of exocomet host stars known prior to this work. We have also detected non-photospheric variations in the Ca II, and in some cases in the Na I lines, in another 12 stars that were already known in the literature to present spectroscopic variability. Moreover, we do not find any strong evidence that relates the presence of a debris disc with exocometary activity.

The presence of narrow non-photospheric stable absorptions in those systems where cold gas had been previously detected in far-infrared or (sub-)mm wavelengths was analysed. A dependency with the inclination angle of the system is found, proving that hot and cold gas are most likely co-existing, both having a common origin in sublimating or colliding small bodies.

Finally, we have performed a deeper analysis of three objects, namely ϕ Leo, HR 10 and HD 37306, that we single out from the original sample because they showed non-photospherical variable absorptions that could originate from different mechanisms.

For ϕ Leo we find that is the most variable star in our sample, with changes in the line profiles occurring in time scales of hours, a frequency comparable to that of the well-studied star β Pic. We have found that the origin of its variability is more likely the presence of exocometary bodies. In the case of HR 10, that was known as a classical exocomet-host star, a strict periodicity in its variations was observed, consistent with the star being actually a binary and not an exocomet active star. Finally, we find that HD 37306 shows variability of longer duration and larger equivalent widths and line depths than the typical exocometary signatures, and with a shape similar to those observed in shell stars. The origin of this variation remains unclear, although it seems to originate in a close-in circumstellar disc, as is the case for most shell stars.

Resumen

En las estrellas de secuencia principal, los excesos fotométricos en el infrarrojo atribuidos a la presencia de polvo circunestelar en los discos conocidos como *debris* o escombro, ha sido la única prueba empírica indirecta de la existencia de cuerpos menores durante más de 40 años. No fue hasta 1987 cuando se encontró la primera evidencia de la presencia de exocometas en el entorno de la estrella β Pictoris, al detectarse absorciones variables no fotosféricas superpuestas a las líneas estelares de Ca II. Desde entonces, el número de estrellas conocidas con absorciones tipo exocometario ha crecido lentamente, hasta llegar a 20 estrellas con detecciones, todas ellas de tipo A. El crecimiento del campo exoplanetario, y la posible relevancia de los cuerpos menores en la configuración, composición y arquitectura de los sistemas planetarios, han vuelto a llamar la atención de la comunidad científica hacia el estudio de cuerpos pequeños alrededor de estrellas distintas al Sol. Además, recientemente se han publicado las primeras detecciones de cuerpos exocometarios en curvas de luz fotométrica a partir de datos tomados por misiones de búsqueda de exoplanetas como Kepler y TESS. Las detecciones en fotometría utilizando las curvas de luz de estos observatorios espaciales, además de proporcionar una nueva metodología, han demostrado que los exocometas están presentes alrededor de estrellas de diferentes tipos espectrales en la secuencia principal.

En esta tesis se lleva a cabo el primer estudio espectroscópico sistemático cuyo objetivo es el de detectar actividad exocometaria alrededor de estrellas de secuencia principal. Los objetivos principales son, primero, agrandar la muestra de estrellas conocidas con exocometas; y segundo, determinar las posibles características ambientales de los sistemas exocometarios que podrían ayudar a comprenderlos y detectarlos.

Para ello, se seleccionó una gran muestra de estrellas para buscar señales exocometarias, donde se inspeccionaron alrededor de 1500 espectros ópticos de alta resolución de 117 estrellas con tipos espectrales de G hasta B. Aunque la muestra estaba sesgada hacia estrellas con evidencias de material circunestelar, este es, a nuestro entender, el estudio exocometario más grande realizado hasta la fecha, que permite por primera vez evaluar la posible dependencia de la presencia de exocometas con las características del entorno circunestelar. Como resultado de este estudio, se ha encontrado variabilidad de tipo exocometario en seis nuevas estrellas, aumentando de 20 a 26 – un 30%–, la cantidad de estrellas con evidencias de presencia de exocometas conocidas antes de este trabajo. También hemos detectado variaciones

no fotosféricas en Ca II y en algunos casos en las líneas de Na I, en otras 12 estrellas en las que ya se habían detectado variaciones espectroscópicas con anterioridad. Sin embargo, no encontramos ninguna evidencia sólida que relacione la presencia de un disco de *debris* con la actividad exocometaria.

Por otra parte, se analizó la presencia de absorciones estrechas no fotosféricas estables en aquellos sistemas donde se había detectado previamente gas frío en longitudes de onda de infrarrojo lejano o (sub-) mm, y se encontró una dependencia con el ángulo de inclinación del sistema, probando que ambos tipos de gas coexisten, y probablemente tienen un origen común como la sublimación (o colisiones) de cuerpos pequeños.

Finalmente, hemos realizado un análisis más profundo de tres objetos –ϕ Leo, HR 10 y HD 37306– que seleccionamos de la muestra original debido a que las absorciones variables no fotosféricas detectadas se originan a partir de diferentes mecanismos.

ϕ Leo es la estrella más variable en nuestra muestra, con cambios en las líneas en escalas de tiempo de horas. Una frecuencia comparable a la de la estrella β Pic, y muy probablemente originada en cuerpos exocometarios. En el caso de HR 10, una de las estrellas con exocometas más estudiadas hasta la fecha, se observó periodicidad en sus variaciones, consistente con el hecho de que la estrella sea realmente una binaria. HD 37306 muestra una variabilidad de mayor duración y cuyas anchuras equivalentes y profundidades de las líneas son mayores que las observadas en exocometas y presentan características similares a las observadas en las estrellas de tipo *shell*. El origen de este tipo de variaciones sigue sin estar claro, aunque podrían deberse a la presencia de un disco circunestelar cercano.

Resumo

Nas estrelas de secuencia principal, os excesos fotométricos no infravermello atribuídos á presenza de polvo circunestelar nos discos coñecidos como *debris* ou escombro, ten sido a única proba empírica indirecta da existencia de corpos menores durante máis de 40 anos. Non foi ata 1987 cando se encontrou a primeira evidencia da presenza de exocometas na contorna da estrela β Pictoris, ao detectarse absorcións variables non fotosféricas superpostas ás liñas estelares de Ca II. Dende entón, o número de estrelas coñecidas con absorcións tipo exocometario medrou lentamente, ata chegar a 20 estrelas con detección, todas elas de tipo A. O crecemento do campo exoplanetario, e a posible relevancia dos corpos menores na configuración, composición e arquitectura dos sistemas planetarios, volveu chamar a atención da comunidade científica cara ao estudo de corpos pequenos arredor de estrelas distintas ao Sol. Ademais, recentemente foron publicadas as primeiras detección de corpos exocometarios en curvas de luz fotométrica a partir de datos tomados por misións de busca de exoplanetas como Kepler e TESS. As detección en fotometría empregando as curvas de luz destes observatorios espaciais, ademais de proporcionar unha nova metodoloxía, teñen demostrado que os exocometas, están presentes ao redor de estrelas de diferentes tipos espectrais na secuencia principal.

Na presente tese de doutoramento, lévase a cabo o primeiro grande estudo espectroscópico cuxa finalidade é detectar actividade exocometaria arredor de estrelas de secuencia principal. Os obxectivos principais son, primeiro, agrandar a mostra de estrelas coñecidas con exocometas; e segundo, determinar as posibles características ambientais dos sistemas exocometarios que poderían axudar a comprendelos e detectalos.

Seleccionouse unha gran mostra de estrelas para buscar sinais exocometarias, onde foron inspeccionados arredor de 2000 espectros ópticos de alta resolución de 117 estrelas con tipos espectrais de G ata B. Aínda que a mostra privilexiaba estrelas con evidencias de material circunestelar, este é, ao noso entender, o estudo exocometario máis grande realizado ata a data, que permite por primeira vez avaliar a posible dependencia da presenza de exocometas respecto das características da contorna circunestelar. Como resultado deste estudo, atopouse variabilidade de tipo exocometario en seis novas estrelas, aumentando de 20 a 26 – un 30%-, a cantidade de estrelas con evidencias de presenza de exocometas coñecidas antes deste traballo. Tamén temos detectado variacións non fotosféricas en Ca II, e nalgúns casos nas liñas de Na I, e noutras 12 estrelas nas que xa foran detectadas variacións espectroscópicas.

Porén, non encontramos ningunha evidencia sólida que relacione a presenza dun disco de *debris* coa actividade exocometaria.

Por outra banda, analizouse a presenza de absorcións estreitas non fotosféricas estables naqueles sistemas onde se tiña detectado previamente gas frío en lonxitudes de onda de infravermello afastado ou (sub-) mm, e atopouse unha dependencia co ángulo de inclinación do sistema, probando que ambos tipos de gas coexisten, e probablemente teñen unha orixe común como a sublimación (ou colisións) de corpos pequenos.

Finalmente, realizamos unha análise máis profunda de tres obxectos –ϕ Leo, HR 10 e HD 37306,– que seleccionamos da mostra orixinal debido a que as absorcións variables non fotosféricas detectadas orixínanse a partir de diferentes mecanismos.

ϕ Leo é a estrela máis variable na nosa mostra, con cambios nas liñas en escalas de tempo de horas. Unha frecuencia comparable á da estrela β Pic, e moi probablemente orixinada en corpos exocometarios. No caso de HR 10, unha das estrelas con exocometas máis estudadas ata a data, observouse periodicidade nas súas variacións, consistente co feito de que a estrela sexa realmente unha binaria. HD 37306 amosa unha variabilidade de maior duración e cuxas anchuras equivalentes e profundidades das liñas son maiores que as observadas en exocometas e presentan características similares ás observadas nas estrelas de tipo *shell*. A orixe deste tipo de variacións segue sen estar claro, aínda que poderían deberse á presenza dun disco circunestelar próximo.

Contents

Chapter 1

Introduction

1.1 Extrasolar planetary systems

For most of the human history, our solar system has been the only evidence of the presence of planets and minor bodies around a star. Some of the basic observables already known in the 18th century led to the postulation of the first planet formation theories (e.g. Swedenborg, Kant, and Laplace). The fact that solar system planets are in the same orbital plane and share the direction of revolution around the Sun led them to hypothesise that the solar system was formed from what was called a solar nebula, basically a giant cloud that collapsed. And this remains, with little modification but much more detailed, the current explanation for the formation of our planetary system 4.5 Gyr ago. In the current paradigm, most of the mass collapsed in the center, where lies the major body, the Sun. Conservation of angular momentum in the process led to the formation of a massive disc, composed of a large amount of gas and a small fraction of dust, i.e. a protoplanetary disc. As a consequence of star formation processes, most of the gas will be either accreted by the central star, or blown away by the stellar winds and radiation pressure. The material surviving those processes will aggregate into planetesimals, leading to the formation of the planets and minor bodies (for a review in planet formation, see Armitage, 2010, 2011). Through Gyrs of evolution, the actual configuration presents less than 0.2% of the total mass in planets, less than 0.002% in the form of smaller bodies, including moons, dwarf planets, asteroids and comets (Weidenschilling, 1977), and a negligible amount of dust. While planets and their moons have orbits mostly empty of other bodies, asteroids and comets are mainly located in two regions: the asteroid belt, in the inner solar system, and the Kuiper belt, beyond the planets; and at larger distances, the Oort cloud. All of them conform the circumstellar (hereafter CS) environment of the Sun.

The advances in modern astrophysics, lead to the evidence of complex CS environments around other stars, starting with the discovery of a dusty disc around Vega (Aumann et al., 1984). This was the first evidence of dust surrounding a main-sequence (hereafter MS)

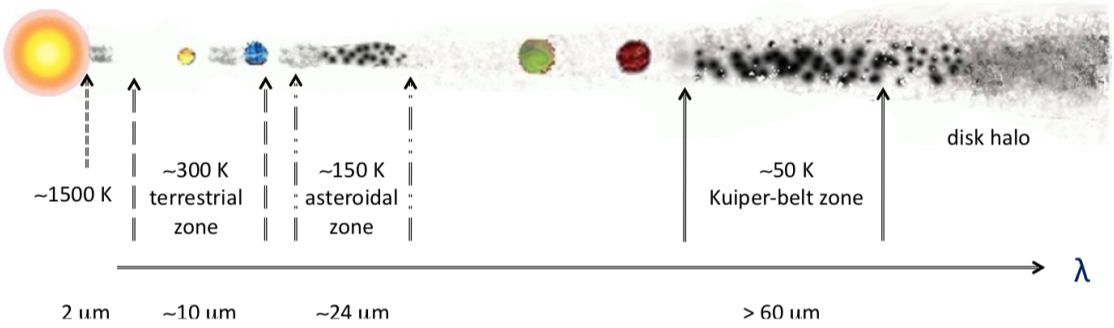

Figure 1.1: Sketch of a debris disc from Matthews et al. (2014). The locations of the dust and the wavelengths at which it is usually detected are shown. The presence of minor bodies is inferred from the dust detections.

star, supporting the molecular cloud collapse hypothesis and suggested that planets could be present as well. However, it was not until 1995 that the first exoplanet was detected around a MS solar-like star (Mayor & Queloz, 1995) using the radial velocity technique, showing that indeed planets are there orbiting other stars, and starting the exoplanetary field.

Instrumentation and analysis techniques have largely improved, and thanks to both ground and space-based missions (e.g., *Kepler,* Borucki et al., 2010) the number of known exoplanets has undergone an exponential growth, reaching $\sim$ 4000 discovered to date in our Galaxy[1]. From extrapolation of the current detection rates it seems that most planets belong to multiple planetary systems, and at least one planet is present around each solar-type star (F or cooler) (Batalha et al., 2013). Striking is the wide variety of the masses and sizes of the planets found orbiting other stars, ranging from several Jupiter masses, close to the brown dwarf mass, to the smallest known exoplanets, below 1 $M_\oplus$ (e.g. Ulmer-Moll et al., 2019), surpassing by far the diversity found in the Solar System. Furthermore, access to the diversity regarding the age and mass of the star allow to probe the dependency of the planetary formation process with different parameters. Discoveries of planets around young, pre-MS stars, are shedding light into the early stages of the planet formation process (Müller et al., 2018), and the presence of planetesimal material around white dwarfs (Kraus & Ireland, 2012) show that some of the components of planetary systems might survive to some extent the evolution out of the main sequence of the star (Villaver & Livio, 2007).

1.2 The circumstellar environment of MS stars

The main indirect evidence of the presence of planets around a star has been for many years the presence of mid- and far-infrared (IR) and (sub-)mm excesses, corresponding to the thermal emission from small mm- or μm-sized dust. As the planetary systems evolve and

[1]https://exoplanet.eu

while still in the MS, a large amount of dust should be removed in the first Myrs, mainly by Poynting-Robertson drag, while the gas in the disc is blown away by the radiation of the star in the first stages of evolution (Backman & Paresce, 1993; Wyatt et al., 2015). Therefore, planetary systems are expected to be almost free of gas and with moderately low quantities of dust. Despite of this, there is evidence for a large number of MS systems containing large amounts of dust (and to a lesser extent, gas), that can only be explained as the outcome of violent dynamical scenarios where minor bodies have a main role (e.g. Wyatt, 2008). Thus, planetary systems containing dust are also expected to host a plethora of minor bodies, including moons, asteroids and comets.

The minor bodies are therefore fundamental not only to understand the process by which major bodies grow via coalescence, but as the origin of the detectable dusty material in the form of the so-called *debris discs* around MS stars, that gives insights on the formation and evolution of the system. However, the study of these minor bodies in extrasolar planetary systems has not attracted much attention within the exoplanet science community, most likely due to the inherent difficulty associated to their detection.

On the other hand, debris discs have been widely studied, as they are present in MS stars with ages ranging from 10 Myr to several Gyr (Matthews et al., 2014,, and see Fig. 1.1), and can last for hundreds of Myr, in a steady-state with sporadic stirring and collisional breakups. Large photometric studies carried out with *Spitzer Space Telescope* (Werner et al., 2004) or *Herschel Space Observatory* (Pilbratt et al., 2010), allowed for the detection of far-IR excesses correspondent to small dust grains, and have shown that around 22% of FKG stars in the solar vicinity have these structures, analogous to the solar system Kuiper belt (e.g. Eiroa et al., 2013; Montesinos et al., 2016). The dust particles in debris discs are most likely the result of collisions and dynamical processes within the disc, and have therefore a secondary origin, rather than being part of the primordial dust generated in the protoplanetary phase (e.g. Hughes et al., 2018). Observations in optical and sub-mm wavelengths, and in scattered light (e.g. Kalas et al., 2013), have allowed to resolve some of the brighter and closer debris discs, e.g. β Pic (Smith & Terrile, 1984) or Fomalhaut (Holland et al., 1998) (see Fig. 1.2). Both photometric and imaging data suggest the presence of at least two *rings* in a fraction of debris discs, one warmer at $\sim 200 - 300$ K and relatively close to the star, and an outer one much colder, at $\lesssim 100$ K (Chen et al., 2014; Pawellek et al., 2014; Kennedy & Wyatt, 2014); they are reminiscent of the structures present in the solar system, as asteroid and Kuiper belts respectively. This two-belt structure could be formed as a result of resonances with a chain of planets, similar to the Kirkwood gaps in the solar sytem's asteroid belt (Moons & Morbidelli, 1995), but at larger scales, or even as the outcome of clearing processes in the system (Tabeshian & Wiegert, 2016). Nothing precludes these dynamical mechanisms from being the main drivers of comets in those systems by scattering inwards bodies in the outskirts of the disc, acting possibly on the colder belt.

While most detections of debris discs are around MS stars, there is also evidence for dust –and sometimes gas– structures around white dwarfs, formed as the disruption of asteroid-like bodies when they reach the Roche lobe limit of the star (see e.g. Manser et al., 2019).

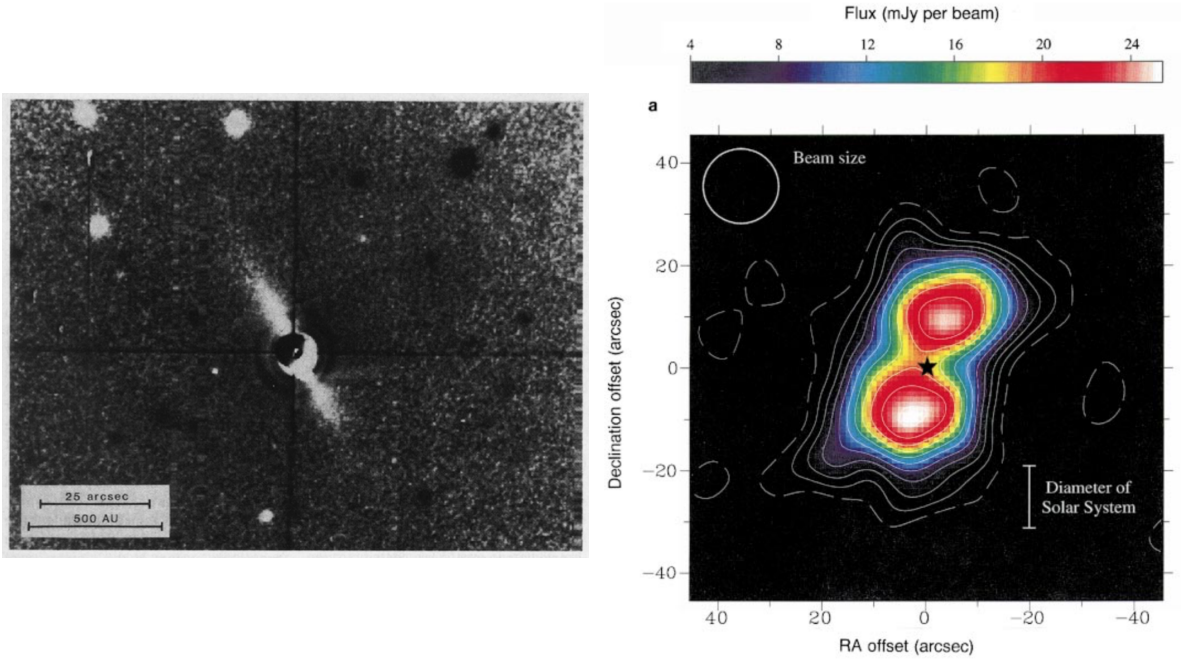

Figure 1.2: First images of the detection of a debris disc around β Pic (left) (Smith & Terrile, 1984, in the optical) and Fomalhaut (right) (Holland et al., 1998, at submillimetric wavelengths).

The origin of the small bodies in these evolved systems is not clear, but are most likely scattered remnants of the MS planetary system (Mustill et al., 2018).

There are also near-IR studies targeting MS stars (e.g. Absil et al., 2013; Ertel et al., 2014; Nuñez et al., 2017) showing some of them present excess emission, attributed in many cases to the presence of dust in the inner regions of the system, likely due to the combination of thermal and scattered emission of sub μm sized grains. This material is expected to be at high temperatures, close to ~ 1500 K, and very close to the sublimation zone which lies at distances of < 1 au from the star. Due to the radiation pressure from the star, and dynamical mechanisms like collisions, these small dust particles are expected to have short lifetimes, and therefore require a replenishment mechanism, like the classical debris discs observed in mid- and far-IR. Magnetic field trapping (Rieke et al., 2016) or Poynting-Robertson drag have been proposed as explanations for the presence of hot dust so close to the central star, but still the most accepted hypothesis is the evaporation of rocky bodies, such as exocomets, thrown inwards as a result of dynamical instabilities (Faramaz et al., 2017; Marino et al., 2018; Sezestre et al., 2019). This mechanism has also been proposed to explain the presence of dust in the zodiacal cloud (Nesvorný et al., 2010) in the solar system.

While secondary dust can be explained in the environment of MS stars, the presence of large amounts of gas is not well understood since, as explained above, the radiation and winds from the star should lead to the depletion of most of it in the first Myrs. Even so, non negligible amounts of gas, mostly molecular CO, have been detected in (sub-)mm or far-

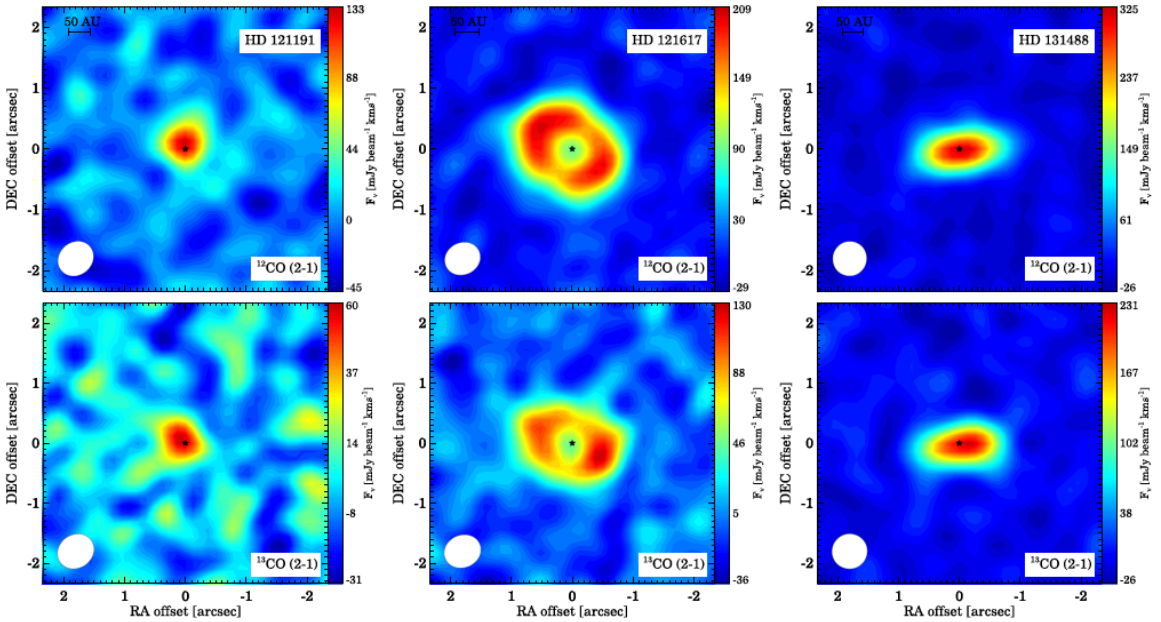

Figure 1.3: ALMA line images with ^{12}CO and ^{13}CO detections from Moór et al. (2017).

IR wavelengths in $\sim$ 20 debris discs around MS stars, most of them A-type (see e.g. Moór et al., 2015a, 2017; Riviere-Marichalar et al., 2012, 2014; Marino et al., 2016; Matrà et al., 2019,and Fig. 1.3). This gas has been suggested to be a remnant from the protoplanetary disc (Kóspál et al., 2013; Moór et al., 2015a; Kral et al., 2017), but for most cases, the origin is likely secondary (Marino et al., 2016; Matrà et al., 2017; Kral et al., 2018) as a result of collisions of (proto-) planetary bodies or dust, photoevaporation or sublimation of rocky material.

Gas around MS stars, has also been detected through ultraviolet (UV) and optical spectroscopy, in the form of narrow non-photospheric stable absorptions at (or close to) the radial velocity of the star, superimposed on photospheric lines of e.g. C, O, Ca, Na, Fe or Mg (e.g. Lagrange et al., 1998; Brandeker et al., 2004; Roberge et al., 2006; Iglesias et al., 2018). This gas is hot, with temperatures between 1000 and 2000 K, and most likely located at distances $<$ 1 au (Hobbs et al., 1988; Beust et al., 1998; Vidal-Madjar et al., 2017). The presence of Ca II K and Fe I in the β Pictoris disc has been reported in emission, up to large distances ($\sim$ 80 au) and at a large scale height from the plane of the disc (Nilsson et al., 2012), but possibly sharing the origin with the gas detected in absorption.

Broad non-photospheric stable absorptions are also observed in the metallic lines (and sometimes in the Balmer lines) of rapid rotating A-type MS stars. These objects, called in the literature *shell stars* (e.g. Slettebak, 1982; Jaschek et al., 1988) show a strong, somehow triangular-like absorption profile, superimposed on the photospheric lines. The origin of these hot, gaseous features denoting the presence of a spherical shell or a CS disc is not

clear, and possibly is not unique. In some stars, the features reported show variability similar to that attributed to exocometary activity (e.g. Abt et al., 1997).

Along with the narrow stable features, there are also variable gas detections, as transient absorptions in the metallic lines at optical and ultraviolet (UV) ranges.Variations at the bottom of the Ca II K photospheric line, observed in high-resolution spectroscopy, appear mostly redshifted, and less frequently blueshifted, with respect to the radial velocity of the star. These events have durations that can vary from hours to days, both in radial velocity and equivalent width (EW). They are interpreted as the passing of gaseous clumps, originated as icy bodies come at close distances from the star, which evaporate or sublimate, generating an atmosphere linked to the body, much like comets and their comae in our own solar system (e.g. Vidal-Madjar et al., 1994; Roberge et al., 2006; Kiefer et al., 2014a).

1.3 The state-of the-art on exocomets knowledge

The first detection of exocomets around a star was reported by Ferlet et al. (1987) (Fig. 1.4) in the β Pictoris system. β Pic has been the focus of many studies before and after this discovery, as it is one of the most complex CS environments found outside the solar system. This A6V star located at 19 pc, with a reported age of 23 Myr (Vidal-Madjar et al., 1998), hosts a massive debris disc first resolved by Smith & Terrile (1984).

The right panel of Fig. 1.4 illustrates how the absorption is generated superimposed on the photospheric lines as the gaseous tail of a sublimating body transits in front of the star. These bodies, or exocomets, were formed in the outskirts of the system, beyond the snow line, and are transported inwards as their orbits are perturbed by a large mass in the system, i.e. a planet (Beust et al., 1991, 1998; Beust & Morbidelli, 2000). Independently of the models for the perturbing body for β Pic, but in agreement with them, a 9 Jupiter-mass planet, β Pic b, was found in the system located at 8-15 au (Lagrange et al., 2010). Recently, a second planet of similar mass has been found orbiting much close to the star ($\sim$ 3.5 au), with no clear relation between its presence and the exocometary activity in the system (Lagrange et al., 2019).

Besides those observed at optical wavelengths, variations were also found in Fe II and Mg II lines (Lagrange et al., 1987) in the UV. Further reports of gas detected in β Pic, include the presence of a large number of metallic lines, and the overabundance of carbon (Roberge et al., 2006), that could explain the prevalence of Ca in the system, as it acts as a braking mechanism (Fernández et al., 2006). Atacama Large Millimiter/submillimiter Array (*ALMA*, Wootten & Thompson (2009)) observations also revealed the presence of large amounts of CO, axi-symmetrically distributed in the disc (Dent et al., 2014), that is possibly originated as the icy bodies evaporate (Kral et al., 2016).

β Pic remains the best studied exocometary system as the subject of numerous observational campaigns. After an intensive spectroscopic survey including over 1000 spectra

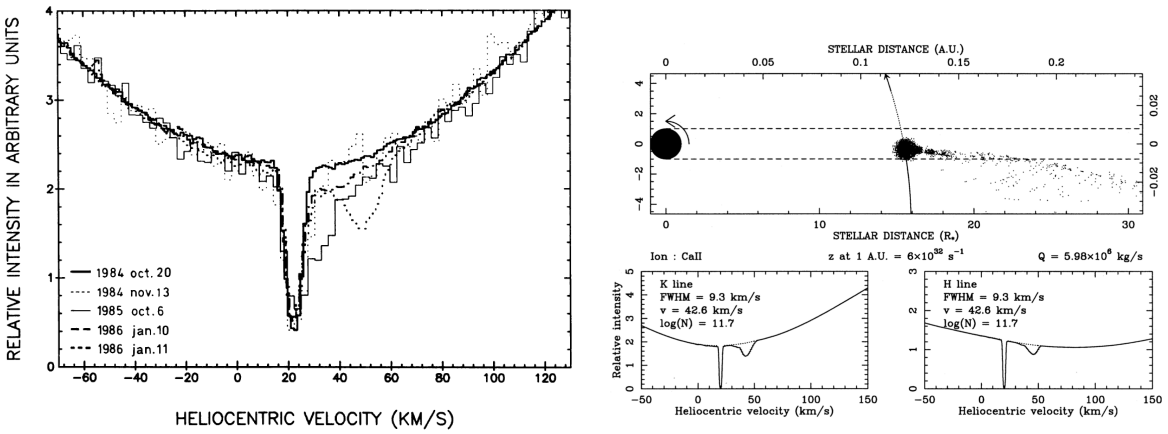

Figure 1.4: Left: First detection of falling evaporating bodies (FEBs) in the Ca II K line, from Ferlet et al. (1987). Each linestyle represents a different date, showing the characteristic variability of the absorptions. A narrow stable non-photospheric absorption is also present. Right: sketch of how the transit of the gaseous tail causes an absorption superimposed on the photospheric spectrum (Beust et al., 1998).

obtained through eight years of observations, Kiefer et al. (2014b) found two families of exocomets, with two different sets of orbits and compositions. Over 6000 different features arising from exocometary gaseous transits were reported in that study, allowing for their characterisation. Up to date, a similar study for any other exocomet-host star has not been reported possibly due to both the lack of an intensive monitoring, and the lower frequency of exocomet-like variations.

Since 1987, around 20 stars, all of them with spectral type A, have been reported to host exocometary-like activity, and in most cases detected in the optical range, in Ca II and less frequently in Na I D lines (see e.g. Redfield et al., 2007; Kiefer et al., 2014a; Welsh & Montgomery, 2013, 2018). Table 1.1 lists the stars with exocomet-like detections, prior to the development of this work. The only exception to this trend, is the possible exocomet-like event in the F-type 1.4 Gyr-old star η Crv (Welsh & Montgomery, 2019). The lack of a massive debris disc in some of these systems is not inconsistent with the presence of small bodies, as an outer belt with luminosities compared to the solar system's Kuiper belt would be enough to reproduce the signals (Faramaz et al., 2017), not being detectable with the current instrumentation.

Intensive planet-search photometric instruments and telescopes, like *Kepler*, and more recently the *Transiting Exoplanet Survey Satellite* (*TESS* (Ricker et al., 2015)), have allowed for the photometric detection of dusty tails of exocometary bodies in the lightcurves of stars. First reports of non periodic transits around a white dwarf, attributed to a disintegrating asteroid (Gänsicke et al., 2016), were followed by the detection of exocomet-like transits around MS stars (Rappaport et al., 2018, 2019; Ansdell et al., 2019), and the unusual activity reported by Boyajian et al. (2016) of a star with possible multiple transiting bodies. These

Table 1.1: List of known exocomet-host stars.

Name	Reference	Name	Reference
HD 256 (HR 10)	1,12,15	HD 108767 (δ Crv)	6
HD 9672 (49 Cet)	2	HD 109573 (HR 4796)	6,16
HD 21620	3	HD 110411	3
HD 32297	4	HD 138629 (HR 5774)	8
HD 42111	5,12	HD 145964	3
HD 50241	5,11	HD 148283 (HR 6123)	5,13
HD 56537 (λ Gem)	6	HD 172555	9
HD 64145 (ϕ Gem)	6	HD 182919 (5 Vul)	2
HD 80007 (HR 3685)	11,15	HD 183324	3,10,16
HD 85905	7,15	HD 217782	2,5,14

References: (1) Lagrange-Henri et al. (1990b); (2) Montgomery & Welsh (2012); (3) Welsh & Montgomery (2013); (4) Redfield (2007); (5) Roberge & Weinberger (2008); (6) Welsh & Montgomery (2015); (7) Welsh et al. (1998); (8) Lagrange-Henri et al. (1990c); (9) Kiefer et al. (2014a); (10) Montgomery & Welsh (2017); (11) Hempel & Schmitt (2003); (12) Lecavelier Des Etangs et al. (1997); (13) Grady et al. (1996b); (14) Cheng & Neff (2003); (15) Redfield et al. (2007); (16) Iglesias et al. (2018)

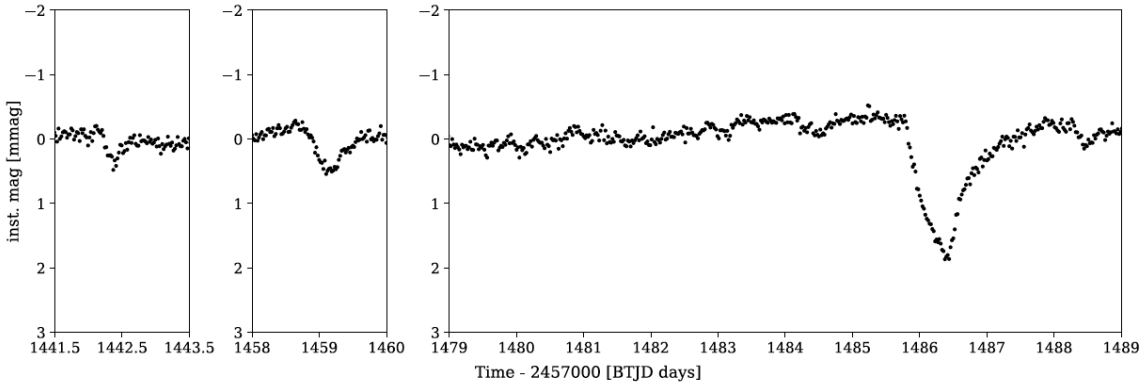

Figure 1.5: Photometric detection of exocomets in β Pic by Zieba et al. (2019). The shape of the transits corresponds to the ingress of a hard front edge of a solid body, whereas the egress results in an exponential growth in flux corresponding to the tail.

detections have proven the presence of exocomet-like evaporating bodies around stars with spectral types later than A.

More recently, the first detection of exocometary photometric transits on β Pic, a spectroscopic exocomet-host star, was reported by Zieba et al. (2019). The shape of the transit detected, shown in Fig. 1.5, is modelled as an ingress with the hard front edge of a solid body, and an egress where an exponential growth in flux occurs as the amount of gas diminishes; this is consistent with the shape predicted for photometric exocomet transits by Lecavelier Des Etangs et al. (1999).

The analysis of the detailed composition of exocomets is not possible yet, with one exception: the case of 2I/Borisov. (Fitzsimmons et al., 2019; de León et al., 2019). 2I/Borisov is a minor body recently discovered in the solar system to have a trajectory and velocity consistent with an extrasolar origin, showing cometary activity. Fitzsimmons et al. (2019) found that the CN content, and C_2 estimations, are compatible with the abundances of solar system comets (see also Opitom et al., 2019).

The only other interstellar visitor known to date, 1I/'Oumuamua did not show any evidence of outgassing, while its colours were compatible with icy bodies. Raymond et al. (2018a) suggested that this body could be an extinct comet, product of a disruption by a planet-size body, that also caused its ejection. Due to dynamical interactions, around 1 $M_\oplus$ of planetesimals are expected to be ejected per stellar mass in planetary systems (Raymond et al., 2018b).

While exocomets are directly detected as their gaseous tails transit in front of the star, other minor objects are also expected to be present in exoplanetary systems. In the past years there have been several attempts to find galilean-like exomoons (Teachey et al., 2018) or even exotrojan asteroids co-orbiting super-Earth sized exoplanets (Lillo-Box et al., 2018a,b), but there is still no clear evidence of their detection outside the solar system.

1.4 The broader scope of the importance of minor bodies

The presence of minor bodies in other solar systems, could also be related to the presence of life if we take into account their relevance in our own solar system.

The formation mechanisms for the Earth can not account for the large quantities of water present in our planet. The high temperatures at the distance from the Sun where the Earth was formed most likely evaporated most volatile ices, including water. This has led to the hypothesis that current levels of water could not have been here since our planet was formed and therefore water was more likely delivered later on (see e.g. O'Brien et al., 2018, and references therein).

At larger distances from the Sun, beyond the snowline, small bodies were probably able to hold most of their water ice, and could later deliver it to Earth in a catastrophic event,

such as the Late Heavy Bombardment (Morbidelli et al., 2000; Morbidelli, 2010). Comets have been hypothesised to be the source of most of the water on Earth, as they are part of the most primitive objects in our solar system, and have large amounts of water ice in their composition. This hypothesis has been ruled out for about two decades after the finding by Lécuyer et al. (1998) that the ratio of deuterium to hydrogen (D/H) in the water on Earth differed from that of solar system comets, and even from the estimated value for the protosolar cloud. However, this situation has changed recently, as we will see in the next paragraphs.

Most asteroids composed mainly of carbonaceous materials (C-type asteroids), and located in orbits inwards to Jupiter, host large amounts of water. They are considered the origin of carbonaceous chondrites meteorites. These bodies hold $\sim$ 20 % of water content (Kerridge, 1985) and have been proposed as the main candidates for the origin of water on Earth. As in the case of exocomets, the presence of a gas giant planet (in this case, Jupiter) can de-estabilise the material and throw it inwards (Raymond & Izidoro, 2017), towards the Earth.

These scenarios ruled out the cometary bodies as the main source of the Earth's water until recently, when it has been discovered that a subgroup of the Jupiter family comets (hyperactive comets) show similar D/H ratio to the water ratio on Earth (Lis et al., 2019). Comets are, therefore, viewed again as one of the main sources responsible of water delivery to the Earth on its past history.

So comets play an important role in the delivery of water to the inner regions of planetary discs that due to the high temperatures produced by stellar radiation should be devoided of it. These inner regions contain the habitable zones of most stars so the importance of comets is not minor regarding the astrobiology of planets. Furthermore, as early as in the late 19th century, it was hypothesised that life could have been originated outside the Earth (S. Arrhenius, and later Hoyle-Wickramasinghe theory of cosmic life), where small bodies such as comets and asteroids are the key as transport mechanisms. In this context, *lithopanspermia* suggests that material is ejected from the surface of a considerably large body, and then after a transit though the ISM or CS medium, enters the atmosphere of a planet (in this case, Earth). This implies that biological or organic material must survive a series of temperature changes, as well as high velocities and UV highly ionizing radiation in the absence of an atmosphere. In support of this general scenario is the fact that organic compounds not compatible with in situ formation have been found on Earth (Bell et al., 2015b). Furthermore, several studies have also proved that organic material could survive in the ISM when located in the inner layers of artificial meteorite-like material (Panitz et al., 2015). Moreover, the recent discoveries of 1I/'Oumuamua and 2I/Borisov confirm that different planetary systems are connected, as small bodies get ejected from one planetary system and delivered into another, at least in the case of inorganic material.

Not only comets carry a large amount of information of the first phases of planetary formation, but might as well deliver to planets the fundamental ingredients for life.

1.5 Objectives of the thesis

The exocometary research has slowly gone forwards since its beginning after the first detection carried out over 30 years ago. The lack of systematic observations and dedicated monitoring programmes and/or proper analysis of the context of cometary environments have led to a small number of detections and often to misreports of the presence of exocomets. Due to the small amount of data, it has not been possible until now, to perform any statistical analysis that could give hints on where and how exocomets arise.

The exponential growth of the exoplanet research field, the large number of exoplanets detected, and the need to understand their environmental and formation conditions has triggered research on the exocometary field, and thus this work. We aim first at increasing the number of minor bodies known in exoplanetary systems and second to study their relation to the planet formation processes. To do so, we present here the analysis of time series spectra obtained for a large number of stars and the gas features that indicate the potential presence of exocomets.

The main questions that are to be answered on this work are:

- Are there any common features shared by the stars that host exocometary activity?
- What is the correspondence between the presence of cold CS gas and the presence of exocomets? Are these small bodies the origin of gas in the outskirts of the system?
- What other physical mechanisms can explain exocomet-like variations?

Since September 2015 and during 14 observing campaigns, plus observations in service mode,$\sim$ 1500 spectra were obtained for 117 stars, candidates of harbouring circumstellar material. These stars have been analysed both individually and collectively. Most of the work presented here has already been published.

The structure of the thesis is as follows: Chapter 2 contains a full analysis of the sample observed, providing the first statistical results of exocometary host systems. Chapter 3 investigates the connection between hot gas, detected in optical spectra and cold gas in the outskirts of the system, detected via (sub-)mm and far IR observations. Chapter 4 summarises three conspicuous cases of variability in the Ca II lines and its possible origin. Finally, overall conclusions for this work are presented, as well as future work.

Chapter 2

Exocomets: A spectroscopic survey

This chapter is based on the paper:
"Exocomets: A spectroscopic survey"
by I. Rebollido et al.
submitted to A&A

2.1 Introduction

Main sequence (MS) stars are known to host a complex circumstellar (CS) environment populated by a plethora of planets, debris discs, and minor bodies, inherited from the physics that regulates the formation of stars. Later, the mutual dynamical interaction among those bodies and their host stars determines the evolution of the planetary systems.

Since the discovery of a giant planet orbiting the solar-type star 51 Peg (Mayor & Queloz, 1995), thousands of planets have been detected, which make up planetary systems with diversified architectures. (see e.g. The Extrasolar Planets Encyclopaedia[1]). Minor bodies, such as asteroids and comets, are expected in these planetary systems. Their study is relevant as they provide clues for understanding the formation and dynamical evolution of planetary systems (e.g. Armitage, 2010). However, evidences of their presence are practically limited to indirect observations, such as the detection of circumstellar dust and gas in debris discs and, to a considerable less extent, to more direct evidences such as observations of some metallic line absorptions.

Hundreds of debris discs are currently known to surround MS stars across practically all spectral types, and ages from around 10 Myr to several Gyr. Debris discs are detected as thermal emission at mid-/far-IR/(sub-)mm wavelengths, as well as scattered light in the optical and near-IR, from small dust particles, which are mainly originated in collisions among km-sized planetesimals and other destructive processes (e.g Matthews et al., 2014,and

[1] exoplanet.eu

references therein). It has been suggested that at least a fraction of debris discs possesses both warm (T $\sim$ 200 K) and cold (T $\lesssim$ 100 K) dust belts (e.g. Ballering et al., 2013; Chen et al., 2014; Kennedy & Wyatt, 2014; Pawellek et al., 2014; Morales et al., 2016), reminiscent of the Solar asteroid and Kuiper belts respectively. The two-belt structure could be created by a chain of planets, while comets scattered by those planets could constitute a relevant source feeding the warm exozodiacal belt (Schüppler et al., 2016; Geiler & Krivov, 2017; Marino et al., 2018). In our own solar system cometary material from Jupiter family comets is responsible for replenishing the exozodiacal cloud (Nesvorný et al., 2010).

Interferometric studies (Absil et al., 2006, 2013; Ertel et al., 2014; Nuñez et al., 2017) have revealed near-IR excesses also attributed in most cases to the combination of thermal emission and scattered light from small submicron-sized, hot (T $\sim$ 1500-2000 K) dust particles located within $\sim$ 0.01 - 1 AU from the stars (depending on the luminosity, see Kirchschlager et al., 2017), very close to the dust sublimation zone.

Again, cometary bodies scattered inwards from an outer reservoir is a likely scenario for the origin and persistence of the hot dust (Beust & Morbidelli, 2000; Thébault & Beust, 2001; Bonsor et al., 2014; Marboeuf et al., 2016; Faramaz et al., 2017; Marino et al., 2018; Sezestre et al., 2019).

Significant amounts of cold gas at several tens AU from the central stars (most young A-type stars) have been detected around $\sim$ 20 bright debris discs (e.g. Moór et al., 2015a, 2017; Riviere-Marichalar et al., 2012, 2014; Roberge et al., 2013; Greaves et al., 2016; Lieman-Sifry et al., 2016; Marino et al., 2016).

The cold gas most likely has a secondary origin (e.g. Marino et al., 2016; Matrà et al., 2017; Kral et al., 2018), but in some cases a remnant of the primordial protoplanetary disc has been suggested (Kóspál et al., 2013; Moór et al., 2015a; Kral et al., 2017). A variety of physical processes, including outgassing of cometary objects, have been invoked to explain the secondary cold gas, all of them related to the presence of planetesimals (e.g. Matthews et al., 2014,and references therein). In parallel, UV/optical high resolution spectroscopy reveals non-photospheric stable absorption features of elements such as C, O, Ca, Na or Fe at or close to the radial velocity of the star, as well as weak sporadic red- or blue-shifted absorption events with respect to the stellar radial velocity (Vidal-Madjar et al., 1994, 2017; Lagrange et al., 1998; Brandeker et al., 2004; Roberge et al., 2006; Iglesias et al., 2018; Rebollido et al., 2018, and Chap. 3). This gas would be hot with temperatures $\sim$ 1000 – 2000 K (Hobbs et al., 1988; Beust et al., 1998; Vidal-Madjar et al., 2017). The transient absorptions have been interpreted as hot gas released by the evaporation of exocomets grazing or falling onto the star, the "Falling Evaporating Bodies" scenario or FEBs (e.g. Ferlet et al., 1987; Beust et al., 1990), while additionally grain evaporation in the circumstellar disc has also been proposed to explain the stable absorption components (e.g. Fernández et al., 2006). A trend between the detection of this hot gas and the edge-on orientation of cold-gas-bearing debris discs has been found by Rebollido et al. (2018) (Chap. 3), who attributed it to a geometrical effect. It is remarkable that this hot gas would be located at distances $\lesssim$ 0.5 AU

from the star, i.e., at similar distances as the hot exozodiacal dust.

The first direct evidence for the presence of exocomets (FEBs) was found around β Pic, which remains unique and the best studied theoretically and observationally (e.g. Ferlet et al., 1987; Beust et al., 1991; Kiefer et al., 2014b; Vidal-Madjar et al., 2017,and references therein).

Several hundreds of cometary transits in β Pic have been detected, revealing two families of exocomets with distinct dynamical and compositional properties; one likely formed by old comets strongly depleted in volatiles, and a second one related to the recent fragmentation of one or few parent bodies (Kiefer et al., 2014b). It is worth to note that very recently β Pic transiting exocomets have likely been detected by means of $TESS$ broadband photometry (Zieba et al., 2019). Those exocomets would have been driven into the vicinity of the star by a larger body, i.e., a planet (Beust et al., 1991; Beust & Morbidelli, 2000). Thus, FEBs constitute an indicator of the plausible presence of planets; we recall that the Jupiter-like planet β Pic b, was later revealed by imaging (Lagrange et al., 2010).

In addition to β Pic, absorption events, mainly in the Ca II K line accompanied in most cases by a stable component, have been detected towards more than 20 stars (e.g. Redfield, 2007; Kiefer et al., 2014a; Welsh & Montgomery, 2015, 2018). Those stars are usually young ($<$ 100 Myr) A-type stars, but transient features have also been found around older stars. Also, Welsh & Montgomery (2019) have recently reported the first detection of an exocomet-like event with a 2.9σ signal around the F2 V type star η Crv. In addition, *Kepler* photometric light curves have been explained as due to transiting exocomets in a few F- and later spectral type stars (Rappaport et al., 2018; Ansdell et al., 2019) and maybe Boyajian's star (Boyajian et al., 2016). Exocomet-host stars have large projected rotational velocities, most with $v \sin i \gtrsim$100 km/s, in principle suggesting that the systems are viewed close to edge-on, which is the favoured orientation to detect non-photospheric absorptions from comet-like bodies passing in front of the star, and consistent with the trend suggested by Rebollido et al. (2018) (Chap. 3). In some cases, the stars hosting exocomets are associated with a debris disc. We note, however, that scattering of exocomets by eccentric planets can take place in planetary systems with low luminous, non-detectable debris discs with flux levels comparable to the Kuiper belt (Faramaz et al., 2017).

This work presents the observational results of a high spectral resolution survey of a large sample of stars with the primary aim of detecting and monitoring non-photospheric absorption features due to the passing of exocomets in front of the stars, and as secondary goal to assess any potential trend between the presence of exocomets and the properties of the host stars. The paper is structured as follows. Section 2.2 describes the sample of stars, the criteria to select them, and some basic properties. Section 2.3 presents our spectroscopic observations and data analysis. Section 2.4 presents our spectroscopic results concerning non-photospheric stable and variable features, their plausible interstellar (ISM) or circumstellar (CS) origin, and comments to some individual stars. Section 2.5 discusses the detection of the non-photospheric absorptions regarding some stellar properties, as well as with respect

to the selection criteria. Finally, Section 2.6 presents the conclusions of this work.

2.2 Sample

As mentioned above the primary goals of our study are the detection and monitoring of variable, non-photospheric absorption features that, as in the case of β Pic, could be attributed to the evaporation of solid bodies in the immediate surroundings of main-sequence stars. The observed stellar sample is formed by a heterogeneous and biased set of 117 MS stars in the spectral type range from B8 to G8, aiming at optimising those goals. The targets have been selected according to the following criteria: i) stars with previously reported Ca II H&K and/or Na I D events attributed to exocomets; ii) debris disc stars, seen edge-on when known; iii) debris disc stars where the presence of cold gas has been detected at far-IR and (sub-)mm wavelengths; iv) stars with near-IR excesses that could be due to hot dust; v) stars belonging to young associations, namely Upper Scorpius (UpSco), Tucana-Horologium (Tuc-Hor), and the β Pictoris moving group (BPMG); vi) shell stars with circumstellar Ti II absorptions; vii) λ Bootis stars. The Ti II stars have been selected because those lines denote the presence of discs seen at nearly right angles to the rotational axes (Abt & Moyd, 1973; Abt et al., 1997), i.e. hot discs seen near edge-on - we note that in general shell stars are a heterogenous group of late B- to early F-type with the distinct characteristic of enhanced lines of Fe II and Ti II denoting the presence of a gaseous circumstellar shell (Gray & Corbally, 2009,and references therein). In addition, λ Bootis stars are A and early F spectral type stars strongly depleted in heavier elements (such as Fe, Al, Mg, Ca...), and relatively normal abundances of volatile elements like C, N, O, and S (Paunzen, 2004), and some of them show clear evidences of accreting CS gas in their UV/optical spectra (Grady et al., 1996a; Holweger et al., 1999). The λ Bootis abundance pattern is most likely due to selective accretion of the volatile elements onto the star, material that could be provided by exocomets, although other sources could also be an alternative (Jura, 2015; Draper et al., 2016). We note that some stars in the sample share several of the selection criteria.

Table A.2 lists the observed stars. Columns 1 to 9 provide HD number, other names, 2000.0 equatorial coordinates, spectral types, distances, apparent V-magnitudes, $B-V$ colour indexes, and radial velocities v_{rad}, all taken from SIMBAD (Wenger et al., 2000a). In addition, column 10 gives ages; column 11 gives the fractional luminosity of the dust, L_{IR} /L_{star}, for those stars where a debris disc has been detected; column 12 gives the corresponding stellar association; and column 13 gives the primary selection criteria. The corresponding references for columns 10-13 are given within brackets. Fig. 2.1 shows the spatial distribution of the sample in galactic coordinates. Given the characteristics of the selection criteria, there is no preferencial location with the exception of stars in the UpSco and Tuc-Hor young associations, although most stars are in the Southern Hemisphere.

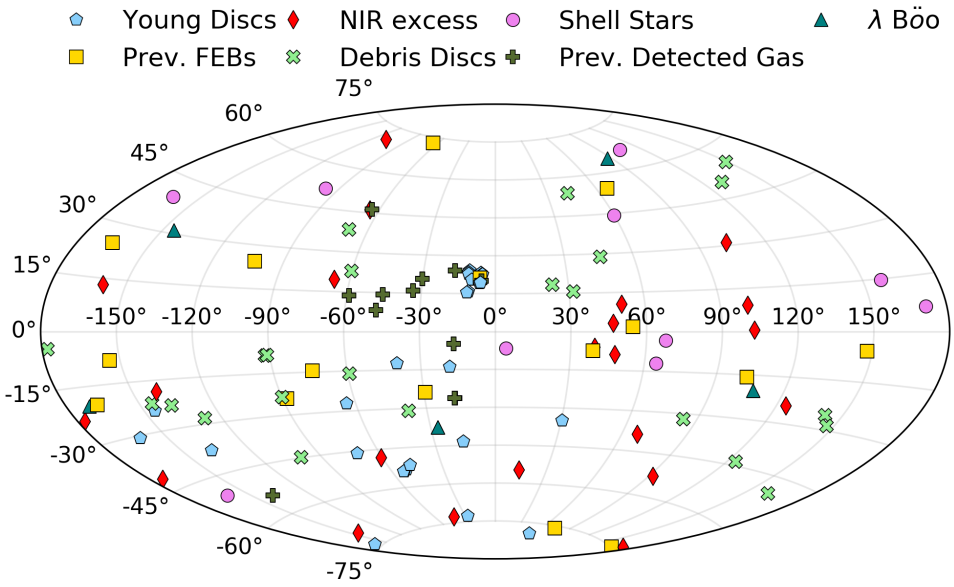

Figure 2.1: All sky plot of the sample in galactic coordinates. Although most stars are in the Southern Hemisphere, there is no preferential spatial location, with the exception of stars in the UpSco and Tuc-Hor young associations.

2.3 Observations and data analysis

High-resolution observations were taken in a series of campaigns from August 2015 to September 2017 from both the Northern and Southern hemispheres, using different fiber-fed spectrographs and telescopes. The spectrographs HERMES (Raskin et al., 2011a) attached at the 1.5 m Mercator Telescope, and FIES (Frandsen & Lindberg, 2000) at the 2.5 m Nordic Optical Telescope (NOT) were used in El Roque de los Muchachos Observatory (Canary Islands, Spain). In La Silla Observatory (Chile), the FEROS spectrograph (Kaufer et al., 1999) at the MPG/ESO 2.2 telescope was used. Complementary observations were obtained at La Luz Observatory (México) with the TIGRE telescope and the HEROS spectrograph (Schmitt et al., 2014). Table 2.1 summarises the resolutions and wavelength ranges of the various instruments, and the observing campaigns. A total of 1575 spectra for the 117 stars were obtained; a detailed observing log with the specific dates (UT) of the spectra for each star and the corresponding spectrograph is given in the Appendix in Table D. Due to the nature of the irregular, sporadic exocometary-like events, we aimed at obtaining time-series spectra, with at least one spectrum per night per object when possible. Integration times never exceeded 30 minutes and were mainly selected depending on the telescope and brightness of the star with the general goal of obtaining a S/N ratio $\gtrsim$ 100 in the Ca II H&K lines. That goal was not always achieved due to either poor weather conditions or the faintness of the star. Signal to noise (S/N) of the median spectra for each star measured in the continuum

Table 2.1: Instruments and observing campaings.

	HERMES	FIES	FEROS	HEROS[!]
Resolution	$\sim$ 85000	$\sim$ 67000	$\sim$ 48000	$\sim$ 20000
Range (nm)	377-900	364-736	352-920	374-884
Observations	03-06/Sep/2015	26-27/Jan/2016	21-24/Oct/2015	Aug 2015
	20-23/Dec/2015	16-19/Jul/2016	25-28/Mar/2016	Sept 2015
	27-30/Jan/2016	03/Mar/2016*	31/Mar-08/Apr/2017	Oct 2015
	03-06/Mar/2016	21/Mar/2016*	23/Sep-01/Oct/2017	Nov 2015
	08-11/May/2016			Dec 2015
	11-14/Jul/2016			Jan 2016
	06-03/Apr/2017			
	28/Mar-03/Apr/2017			

(*) On March 3^{rd} and 21^{st} during service mode only one spectrum was obtained each night. (!) HEROS spectra were taken in robotic mode during several months as complementary observations.

close to Ca II K line is given in Table D.

Data reduction was performed by the available pipelines of the different spectrographs. The reduction includes the usual steps for echelle spectra as bias subtraction, flat-field correction, cosmic ray removal, and order extraction; wavelength calibration is carried out by means of Th-Ar lamp spectra. In addition, barycentric corrections for the HERMES and FIES spectra were carried out as the corresponding pipelines do not include such correction. All spectra were normalised and the continuum set to 1.0 in the regions between spectral lines.

2.3.1 Telluric subtraction

The observed wavelength range includes regions of the visible spectra heavily affected by telluric lines; in particular the region around the 5890/5896 Å Na I D lines, which are highly relevant for both interstellar and circumstellar absorptions. Removal of telluric lines was performed by means of MOLECFIT[2](Smette et al. 2015a, Kausch et al. 2015a), a tool that generates an atmosphere model accounting for the most common absorbing molecules in the optical range (H_2O, O_2, O_3). Residuals after subtraction of the atmosphere model in the telluric line region are comparable to the noise level, and therefore negligible. An example of telluric subtraction is shown in Fig. 2.2.

2.3.2 Stellar parameters

Stellar parameters $T_{\rm eff}$, $\log g$ and $v \sin i$ for the early type stars (up to F2) in the sample were computed using the procedure described by Rebollido et al. (2018) (Chap. 3). Solar

[2]http://www.eso.org/sci/software/pipelines/skytools/molect

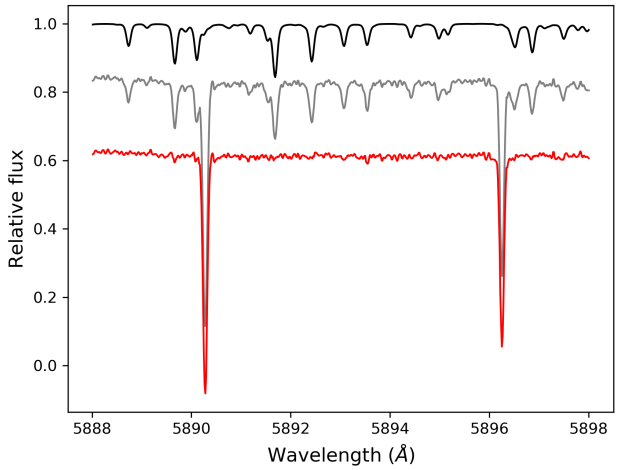

Figure 2.2: Example of telluric subtraction in HD 21620 in the Na I D spectral region. Black line shows the MOLECFIT atmospheric model; grey line shows the observed spectrum; and red line shows the final telluric-free HD 21620 spectrum.

abundances were used initially to iterate the solutions for all objects, the solutions being consistent with that metallicity for most of the stars. For the 15 objects with [M/H]$\leqslant -0.5$ according to our estimates, eight of them, namely HD 31295, HD 74873, HD 110411, HD 125162 (λ Boo), HD 183324, HD 198160 (HR 7959), HD 198161 (HR 7960) and HD 221756, were classified as λ Boo stars by Murphy et al. (2015a), consistently with their expected underabundace in heavier elements. For cooler stars (later than F2), a different approach was used to calculate parameters. In those cases we have followed the procedure described in detail by Maldonado & Villaver (2017) and Maldonado et al. (2018), which is based on the iron ionisation and excitation equilibrium, and match of the curve of growth conditions.

Radial velocities (v_{rad}) were estimated by measuring the shift between the synthetic spectrum, which is computed using a database of rest wavelengths, and the observed spectrum, corrected for barycentric velocity. Individual shifts were measured for the Balmer lines from Hγ to H9. Hϵ, which is blended with Ca II H, was excluded. Lines bluer than H10 were discarded since the lower part of the absorptions were usually noisy. Most of the stars have large values of the projected rotational velocity, $v \sin i$, therefore the cores of the lines, and in particular the Balmer ones, are fairly rounded; thus, a direct evaluation of the wavelength at which the minimum intensity occurs introduces large uncertainties. The procedure we have followed is to slightly smooth the spectra, and then take as the reference wavelength that of the bisector corresponding to 10% of the line intensity measured from the bottom of the absorption. The same was done on the synthetic profile and the difference was converted into v_{rad}; the results do not change significantly if instead of using the synthetic spectrum, the rest laboratory wavelength of the particular Balmer line was taken as reference. The v_{rad}

uncertainties come from the standard deviation of the set of displacements. Fig. 2.3 shows the method explicitly.

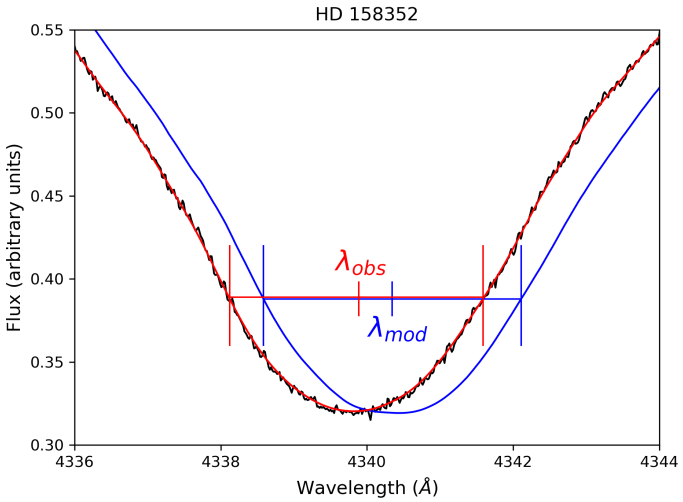

Figure 2.3: Radial velocities are measured as the difference between the synthetic model at rest (blue line) and the smoothed spectra at the radial velocity of the star (red line). The method is illustrated in the plot by means of the observed Hγ line in the star HD 158352 (black line). A detailed description is given in the text.

2.3.3 Non-photospheric absorptions

The Ca II H&K and Na I D lines were visually inspected to search for the presence of non-photospheric, stable or variable, absorption features at the core of the photospheric lines, which would suggest the presence of circumstellar gas. A median spectra (when data from different telescopes were available, all spectra were converted to the FEROS resolution in order to construct the median) was constructed for each star to improve the signal to noise ratio in order to analyse the potential stable absorption, This analysis has been carried out by estimating the photospheric contribution with splines fitted to the bottom of the lines, and then dividing the observed profiles by the estimated photospheric lines, and finally fitting Gaussians to the residuals.

A total of 60 stars show stable, non-photospheric Ca II and/or Na I absorptions (Table A.3); at the same time, irregular, variable features are seen in individual spectra of 18 stars (Table 2.2). For these latter stars, when no variations were detected in a range of hours/days, a median was constructed including all the consecutive non-variating spectra. The stable absorptions, when arising in the CS environment (see Sect 2.4.1), appear at the radial velocity (v_{rad}) of the stars or close to it, while the variable ones appear red- and/or blue-shifted.

In the following we present a separate analysis for stars only showing stable non-photospheric absorptions, and stars with variable components regardless of whether they also have stable

absorptions.

2.4 Results

2.4.1 Narrow, stable absorption features

As mentioned above, a total of 60 out of the 117 stars in the sample show narrow, stable absorption features superimposed on the photosphere, either in the Ca II and/or the Na I lines. Fig. A.1 shows the observed line profiles for both the Ca II H&K and Na I D lines of the 60 stars, along with their residuals, once the photosphere has been divided. Table A.3 lists radial velocities (RVs), equivalent widths (EWs), column densities (N), and the velocity dispersion (FWHM of the Gaussian fits) of the non-photospheric median stable absorptions, as estimated for the Ca II K and Na I D2 lines. EW were calculated with respect to the adjacent continuum, once divided the photospheric contribution. Column densities were estimated following Somerville (1988) in order to deal with the saturated lines.

Uncertainties for the features' radial velocities are estimated as two pixels of the median spectra corresponding to $\sim$2.5 km/s in Ca II lines and $\sim$1.5 km/s in Na I lines, and being this value consistent with the FWHM of the lines of the calibration lamps. In the case of the EWs, we estimate an uncertainty of 10% in our measurements. Uncertainties for column densities were calculated as propagation of the EW uncertainties according to the formulas for the non-saturation and saturation cases (Eq. 1 and 7 in Somerville, 1988, respectively). In some stars, most previously classified as shell stars, the Ca II K line has a sharp, very pronounced triangular-like profile consisting in a very narrow core and broader wings, which cannot be fitted by either a Gaussian or a Voigt profile; in those cases, we have measured the EWs of the excess absorption with respect to the photospheric line and the velocity dispersion as the FWHM of the mentioned excess absorption, i.e., the velocity dispersion at one half of the absorption depth.

Origin of the non-photospheric stable absorptions

Stable non-photospheric absorption features might originate in the close-in CS environment of the star, or in the warm and cold clouds of the local interstellar medium, ISM (e.g. Redfield & Linsky, 2008a). In order to try to decipher the origin, we have compared the radial velocity of those features with the radial velocities (v_{rad}) of the corresponding stars (Table A.1 and Table A.3) and with the velocity vectors of the local ISM (v_{ISM}) towards the line of sight of each star, as given for the ISM clouds in Redfield & Linsky's Colorado model[3]. Velocities and names of the clouds are also given in Table A.3. Nonetheless, a sound ascription to any of both CS or ISM origins is ambiguous in some cases; for instance, when the stellar v_{rad} and the ISM v_{ISM} along its line of sight are very close, or when there

[3]http://sredfield.web.wesleyan.edu/

is no identified ISM Colorado cloud along the line of sight towards some stars with narrow Ca II and Na I absorptions. Further, the properties of the non-photospheric absorptions do not clearly discriminate the plausible origin (Redfield et al., 2007) since the observed EWs in the ISM of the Ca II H&K and of the Na I D lines and their ratios vary by several orders of magnitude (e.g Welty et al., 1996; Redfield & Linsky, 2008a; Welsh et al., 2010). We note that Na I is found in cold ISM gas ($\sim$ 50 K) typically at distances larger than $\sim$ 80 pc (Welsh et al., 2010), although is also occasionally found at shorter distances (e.g. Bertin et al., 1993; Welty et al., 1994); whereas Ca II appears in much warmer medium ($\sim$ 5000 K) and is usually detected at much shorter distances (e.g. Redfield & Linsky, 2008b).

In this context, and taking into account the mentioned caveats, we identify stars with CS gas those that satisfy any of the following criteria: i) stars with variable absorptions (see section 2.4.2); ii) stars where the non-photospheric absorption shares its velocity with the radial velocity of the star but not with any ISM Colorado cloud; iii) stars with Ti II absorption lines and shell stars where the Ca II K line has a sharp, triangular-like profile. We point out that some stars have more than one non-photospheric feature that can be independently identified with the velocity of the star or of the ISM. Also, for some stars the absorptions neither coincides with v_{rad} nor with v_{ISM}. When possible, an inspection for nearby stars was made in a field of 5^o in radius and distances $\pm$ 20 pc around each star.

A column in Table A.3 shows our guess for the origin of the non-photospheric absorptions.

Comments on individual stars

In this section we discuss the plausible origin of the stable non-photospheric absorptions for some individual stars or group of stars. Stars with variable absorption features detected in this work are discussed in section 2.4.2. HD 9672 (49 Cet), HD 32297, HD 110058, HD 131488, HD 131835, HD 138813, HD 146897, HD 156623, HD 172555 and HD 181296 (η Tel) were analysed in Rebollido et al. (2018) (Chap. 3); therefore, we do not repeat the discussion here.

- HD 2884, HD 2885, and HD 3003 are members of the Tuc-Hor association. All three stars have similar proper motions, radial velocities and parallaxes. The projected angular separation between HD 2884 and HD 2885 is $\sim$ 27 while the one between HD 2884 and HD 3003 is $\sim$ 9. Thus, they likely form a physical multiple system (see also Eggleton & Tokovinin, 2008; Tokovinin, 2008; Howe & Clarke, 2009). HD 2885 itself is a binary candidate (Lagrange et al., 2009). Our spectra show a weak narrow Ca II K absorption in HD 2884, a weak Na I D absorptions towards HD 2885, and weak Ca II K and Na I D absorptions towards HD 3003 (see also Iglesias et al., 2018). All these absorptions are close to the velocity vector of the Vel cloud and do not coincide with the v_{rad} of the stars (Table A.3 and Fig. A.1). HD 224392 is another Tuc-Hor star located at a similar distance from the Sun as the multiple system and at an angular separation

of $\sim$ 4 deg. Its spectrum shows non-photospheric absorptions of both Ca II and Na I. The velocity of the Ca II feature is close to the Vel cloud and to the Ca II absorptions in HD 2884 and HD 3003; the velocity of the Na I is close to the Cet Colorado cloud that passes at $< 20^o$ the line of sight of HD 224392. All these facts suggest an ISM origin for the Ca II and Na I features; however, this ascription is controversial. First, we note that neither Ca II or Na I non-photospheric features appear simultaneously in HD 2884 and HD 2885. At the same time, Na I is detected towards HD 3003 but not towards HD 2884. Thus, since all three stars are located very close, in particular HD 2884 and HD 2885, a CS origin for the observed features cannot be excluded. Given all these facts, we find ambiguous to ascribe the non-photospheric features in all 4 stars to either a CS or ISM origin and further observations are needed to elucidate their origin.

- HD 5267 has two non-photospheric features in both Ca II and Na I lines. The velocity of the stable, strongest feature, $\sim$ –5.0 km/s, does not coincide with v_{rad} (9.5 km/s) or with the v_{ISM} of any Colorado cloud. At the same, time, the weakest, red-shifted feature at $\sim$10.0 km/s is close to the velocity vector, 11.44 km/s, of the LIC cloud (Table A.3). Unfortunately there are no spectra of field stars in the ESO archive that can be used to discriminate the origin of the component at –5 km/s. We note, however, that this feature is $\sim$15 km/s blue-shifted relative to the radial velocity of the star, and that HD 5267 has a similar effective temperature as HD 181296, T_{eff} $\sim$10500 K. HD 181296 has a stable component $\sim$20 km/s blue-shifted relative to the stellar velocity, most likely of CS origin as suggested in Rebollido et al. (2018) (see Chap. 3, and Chen & Jura, 2003, for other examples). Thus, while the origin of the $\sim$10 km/s component plausibly is ISM, the origin of the –5 km/s is dubious.

- HD 16978 is another Tuc-Hor star reported by Welsh & Montgomery (2018) as having a variable non-photospheric Ca II K profile within 3 observations. Our spectra show such absorption with a similar EW but does not show the mentioned variability. The radial velocity of the feature coincides with the stellar v_{rad}, and it differs $\sim$4 km/s from the v_{ISM} of the Vel cloud. Given the variability of the feature profile noted by Welsh & Montgomery (2018), which might be indicative of a transient event, the more plausible origin is CS, although we cannot definitively exclude an ISM origin.

- The stars HD 71043, HD 71722, and HD 105850, have Ca II and Na I features close to the velocity vectors of Colorado clouds, and far away form the stellar v_{rad}, supporting an ISM origin, in agreement with Iglesias et al. (2018). This is also the case for the star HD 188228 where only a weak Na I absorption is seen close to the velocity of the G and Vel clouds.

- HD 118232 (24 CVn), HD 125162 (λ Bootis), and HD 221756 have non-photospheric absorption features not coinciding either with the stellar radial velocities or any known ISM Colorado clouds. Due to their high declinations ($> +40^\circ$) we have not found any spectra of field stars in ESO archive which could help to elucidate the origin of the absorptions. Nonetheless, we find an ISM origin is the most plausible one given the

remarkable shift in velocity between the features and the photospheric lines.

- HD 145689 (HIP 79797) is a member of the Argus association and shows a weak Ca II absorption at a velocity of –11.9 km/s, between the radial velocity of the star at –7.1 km/s and the velocity of the G Colorado cloud at –17.21 km/s. The F0 V field star HD 147787, located at a distance of 40 pc and a projected separation of $\sim 4^{\circ}$ from HD 145689, does not show any non-photospheric feature in its spectrum. Thus, given this fact and since the difference between the Ca II feature and the stellar v_{rad} is $\sim 2\sigma$ we cautiously assign a CS origin to the Ca II absorption.

- HD 158352 (HR 6507) has two absorption Ca II H&K and Na I D components relatively close to the stellar v_{rad}. There are no Colorado clouds along the line of sight of the star, but it passes near ($< 20^{\circ}$) several clouds with similar velocity vectors. Our spectra reveal a faint narrow Ca II 8542 Å absorption, and several faint Fe II and Ti II lines characteristics of shell stars. Iglesias et al. (2018) assign the Ca II H&K absorptions an ISM origin based on two field stars, HD 156208 and V 2373 Oph, that have absorptions similar to those of HD 158352. We find, however, that the ISM origin is ambiguous. HD 156208 and V 2373 Oph are at distances $\sim$ 217 pc and $\sim$ 476 pc, respectively, i.e. considerably larger than the distance to HD 158352 of $\sim$ 63 pc. Therefore, while an ISM cloud could be located closer than 63 pc, it cannot be excluded that some ISM clouds responsible for the Ca II H&K and Na I D are located between HD 158352 and the other two stars. On the other hand, Welsh & Montgomery (2015) observed two Ca II K absorption components and attributed one of them a CS origin as it coincides with the stellar v_{rad}. Thus, while CS gas is certainly present around the star, the origin of the Ca II H&K and Na I D absorptions is not completely obvious. We note that Lagrange et al. (2009) identify this star as a binary candidate.

- HD 168646 (HR 6864) has a pronounced triangular profile in the Ca II at the bottom of the stellar line, as well as many strong shell lines of Ti II, Fe II, and strong cores in the Balmer lines. The Na I D lines present a strong feature close to the Ca II one, and a weaker one at a velocity of $\sim$ –22 km/s, away from the Aql cloud. A very weak third component might appear only in the D2 line at a velocity of $\sim$ 11 km/s. If real, this weak feature seems to have small variations in flux; we cannot make, however, any sound statement as we only have spectra taken in a single epoch. All features have velocities far away from any ISM Colorado cloud. In any case, the strong shell spectrum clearly traces the presence of CS gas.

- HD 177724 (ζ Aql) and HD 210418 have weak Ca II non-photospheric absorptions, each at their respective stellar radial velocities and close to some Colorado clouds. We have not found any useful field star in the ESO archive which could help to elucidate the origin of the features. Thus, the ascription to any of both CS or ISM origins is ambiguous .

- HD 196724 is a candidate shell star (Hauck & Jaschek, 2000) with low rotational velocity, which shows a weak Ca II K absorption at the stellar v_{rad} and also close to the

v_{ISM} of the Mic and Aql clouds. It might have weak Na I absorption but the spectra are too noisy to make a firm conclusion. The weak Ca II K feature does not reveal a sharp, pronounced profile as it is seen in the Ca II K&H lines in other shell stars. Thus, we find ambiguous the origin of the Ca II K (and Na I if real) absorptions.

- HD 198160 (HR 7959) is a λ Bootis type star with a very weak Ca II K absorption at the stellar v_{rad} and the Vel cloud v_{ISM}. It forms a binary system with another λ Bootis star, HD 198161 (Holweger & Rentzsch-Holm, 1995; Faraggiana & Bonifacio, 1999), both components at a projected angular separation of just 2.3. Weak Ca II K and Na I absorptions are detected towards HD 198161. We also note that a very weak Na I absorption is present towards HD 198160. Thus, while a CS origin cannot be excluded, we find an ISM origin more realistic given the fact that we detect very similar absorptions towards both stars. However, we note that Holweger & Rentzsch-Holm (1995); Holweger et al. (1999) favour a CS origin around the binary.

- Stars belonging to the Upper Scorpius subgroup in the Scorpius-Centaurus association deserve particular attention. There are 13 stars in our sample belonging to this subgroup (Table A.2). All of them are located in a region of 5 sq. deg., and between 110 and 150 pc. The stars show non-photospheric Ca II and Na I absorption components which tend to be grouped around ∼–9 km/s, ∼–15/–23 km/s, and ∼–28 km/s (Table A.3), in agreement with Welty et al. (1994). Most of the stars, with few exceptions, have two features with similar velocities in both Ca II and Na I lines; depending on the star those two features are distributed among the three mentioned velocity ranges. The more blue-shifted components at ∼–28km/s are close to the G cloud velocity vector; the least blue-shifted components at ∼–9 km/s are often close to the radial velocities of the stars. The fact that similar features, including those in the range ∼–15/–23 km/s, are shared in one way or another by all stars strongly suggests their ISM origin, as already noticed by Rebollido et al. (2018) (Chap. 3) for HD 138813 and HD 146897. In general, the strongest feature is the less blue-shifted one, i.e., the one close to the stars' v_{rad}; this trend holds irrespectively of whether one or two absorption features are detected in any of the Ca II and/or Na I; exceptions to this general trend are HD 146606, and HD 145964 - we refer to this star again in section 2.4.2 as it has a non-photospheric event identified by Welsh & Montgomery (2013). The above results point evidently out that the ISM towards Upper Scorpius is not homogeneous, but with a notorious complexity likely structured in clumps or relatively small cloudlets, with different properties and located at different distances, discernibles along very nearby lines of sight. Finally, we note that a faint emission feature at ∼–1.2 km/s is detected in both lines of the Na I doublet towards HD 138813. As shown in Fig. 2.4, the emission is not related to the telluric subtraction. The emission feature is at the radial velocity of the star, and is similar to the emission feature detected towards HD 156623, a star with Ca II variable events (Rebollido et al., 2018, 2019, Chap. 3). These emissions are most likely originated in the CS medium, as they are observed in every spectra, regardless of the observing campaign or atmospheric conditions.

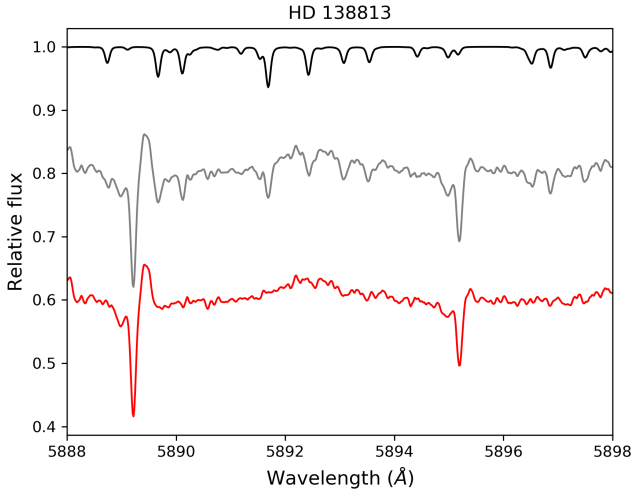

Figure 2.4: Na I D lines of HD 138813, where the emission near the radial velocity of the star is easily recognisable and clearly present in the uncorrected spectra (grey line), and not originated as an over subtraction of the atmospheric model (black line). Red line shows the telluric corrected spectrum.

2.4.2 Variable gas detection

Sixteen stars in our sample were selected because of variable, β Pic-like events of their Ca II H&K and/or Na I D lines. The stars HD 56537 (λ Gem), HD 108767 (δ Crv), HD 109573 (HR 4796), and HD 148283 (HR 6123) also present optical (or UV) events (e.g. Grady et al., 1996b; Welsh & Montgomery, 2015; Iglesias et al., 2018) although they were included on the basis of other criteria (Table A.2). These stars are listed in Table 2.2 together with five new stars showing variability in non-photospheric features found in the frame of this work - HD 36546, HD 37306, HD 39182 (HR 2025), HD 98058 (ϕ Leo), and HD 156623 (HIP 84881). We also include in Table 2.2 the star HD 132200; although this star was not included in our sample and has not directly been observed by us, a variable Ca II K absorption feature was found by Rebollido et al. (2018)(Chap. 3). Our results on HD 156623, ϕ Leo, and HR 10 have already been discussed in Rebollido et al. (2018, 2019)(Chap. 3) Eiroa et al. (2016) and Montesinos et al. (2019) (Chap. 4), respectively.

Comments on individual stars

- HD 9672 (49 Cet), HD 32297, HD 50241, HD 56537 (λ Gem), HD 64145 (ϕ Gem), HD 108767 (δ Crv), and HD 148283 (HR 6123) do not present any apparent transient event in our time series spectra (Table 2.2). Also, while we do not see any variability in HD 138629 (HR 5774) our spectra differ from previous ones (see below). Further, we note that the stars HD 56537, HD 64145, HD 110411, and HD 183324 do not present

Table 2.2: Stars with variable non-photospheric absorption features. References are within brackets.

Name	Prev. Detected	Det. in this work
HD 256 (HR 10)*	Yes (1,12,15)	**Yes**
HD 9672 (49 Cet)	Yes (2)	No
HD 21620	Yes (3)	**Yes**
HD 32297	Yes (4)	No
HD 36546	No	**Yes**
HD 37306	No	**Yes**
HD 39182 (HR 2025)	No	**Yes**
HD 42111	Yes (5,12)	**Yes**
HD 50241	Yes (5,11)	No
HD 56537 (λ Gem)	Yes (6)	No
HD 64145 (ϕ Gem)	Yes (6)	No
HD 80007 (HR 3685)	Yes (11,15)	**Yes**
HD 85905	Yes (7,15)	**Yes**
HD 98058 (ϕ Leo)*	No	**Yes**
HD 108767 (δ Crv)	Yes (6)	No
HD 109573 (HR 4796)	Yes (6,16)	**Yes**
HD 110411	Yes (3)	**Yes**
HD 138629 (HR 5774)	Yes (8)	No
HD 132200*	No	**Yes**
HD 145964	Yes (3)	**Yes**
HD 148283 (HR 6123)	Yes (5,13)	No
HD 156623 (HIP 84881)*	No	**Yes**
HD 172555	Yes (9)	**Yes**
HD 182919 (5 Vul)	Yes (2)	**Yes**
HD 183324	Yes (10,16)	**Yes**
HD 217782	Yes (2,5,14)	**Yes**

(*) Results have been presented by Rebollido et al. (2018) (Chap. 3), Eiroa et al. (2016) and Montesinos et al. (2019)(Chap. 4).

References: (1) Lagrange-Henri et al. (1990b); (2) Montgomery & Welsh (2012); (3) Welsh & Montgomery (2013); (4) Redfield (2007); (5) Roberge & Weinberger (2008); (6) Welsh & Montgomery (2015); (7) Welsh et al. (1998); (8) Lagrange-Henri et al. (1990c); (9) Kiefer et al. (2014a); (10) Montgomery & Welsh (2017); (11) Hempel & Schmitt (2003); (12) Lecavelier Des Etangs et al. (1997); (13) Grady et al. (1996b); (14) Cheng & Neff (2003); (15) Redfield et al. (2007); (16) Iglesias et al. (2018)

any stable, narrow absorption at the core of the photospheric line, although HD 110411 and HD 183324 seem to present variability at the bottom of the Ca II K line (Fig. 2.5, (see also Iglesias et al., 2018)).

- HD 21620 presents one stable non-photospheric absorption in both Ca II and Na I at $\sim$ 4 km/s (Fig. A.1 and Table A.3). This feature does not coincide either with the radial velocity of the star or any of the Colorado ISM clouds; it has, however, a plausible ISM origin as several neighbouring stars have similar Na I absorptions (Génova & Beckman, 2003; Welsh & Montgomery, 2013). A weak absorption detected in Ca II at $\sim$ 15 km/s is close to the ISM velocity of LIC cloud. Nonetheless the variability of this feature, also noted by Welsh & Montgomery (2013), is remarkable and we attribute it a CS origin. Fig. 2.6 shows the variations detected in HD 21620 during the campaigns of 2015 and 2016. As reported in the literature (Welsh & Montgomery, 2013, 2018) we detect mostly red-shifted variations in the range of $\sim$ 10-30 km/s, with only one weak blue-shifted event on 04-05/09/2015 at $\sim$ 0 km/s (top left panel of Fig. 2.6). Some dynamical evolution seems to be traced by the events detected in January 2016 as suggested by the changes in velocity and depth of the events detected along three consecutive nights. There is also a noticeable red-shifted event at $\sim$ 50 km/s in the NOT median spectra of 07/2016 (bottom left panel of Fig. 2.6).

- HD 36546 presents a narrow feature at a velocity of $\sim$ 15 km/ visible in both Ca II and Na I lines (Fig. A.1). The origin of the feature is most likely CS as it coincides with the radial velocity of the star and is far from the ISM cloud along the line of sight (Table A.3 and Fig. A.1). A red-shifted event at a velocity of $\sim$ 20 km/s is detected in the Ca II K spectrum of 6/3/2017, apparently evolving in the following dates and practically disappearing in the spectrum of 8/3/2017 (Fig. 2.7, left panel). A Gaussian deconvolution of the 6/3/2017 Ca II K absorption (Fig.2.8) gives an EW of 8.4 mÅ for the 20 km/s event and 24.8 mÅ for the narrow stronger feature centered at 15 km/s, which is similar to the EW of 27.1 mÅ of this narrow feature in the spectrum of 8/3/2017. The Na I D2 line presents as well an asymmetry in the red wing, with a small change of slope when comparing the different dates (Fig. 2.7, right panel).

  HD 36546 hosts a bright debris disc (Table A.2) seen near edge-on with an inclination angle $i \sim 70 - 75^{\circ}$ (Currie et al., 2017), following the trend suggested by Rebollido et al. (2018)(Chap. 3) between the disc inclination and the presence of narrow non-photospheric absorptions at the radial velocity of the star. Lisse et al. (2017) found evidence of a C-rich CS environment which makes HD 36546 similar to β Pic and 49 Cet (Roberge et al., 2006, 2014). Thus, it can be another example of an enhanced carbon abundance acting as a braking mechanism of the hot inner (¡1 AU) CS gas released by evaporation of exocomets, dust grains or grain-grain collisions (Fernández et al., 2006; Brandeker, 2011).

- HD 37306 presents two stable narrow Ca II and Na I absorptions (Fig. A.1) at velocities $\sim$11 km/s and $\sim$32 km/s, while the stellar v_{rad} is 25.1 km/s. Nonetheless, the most

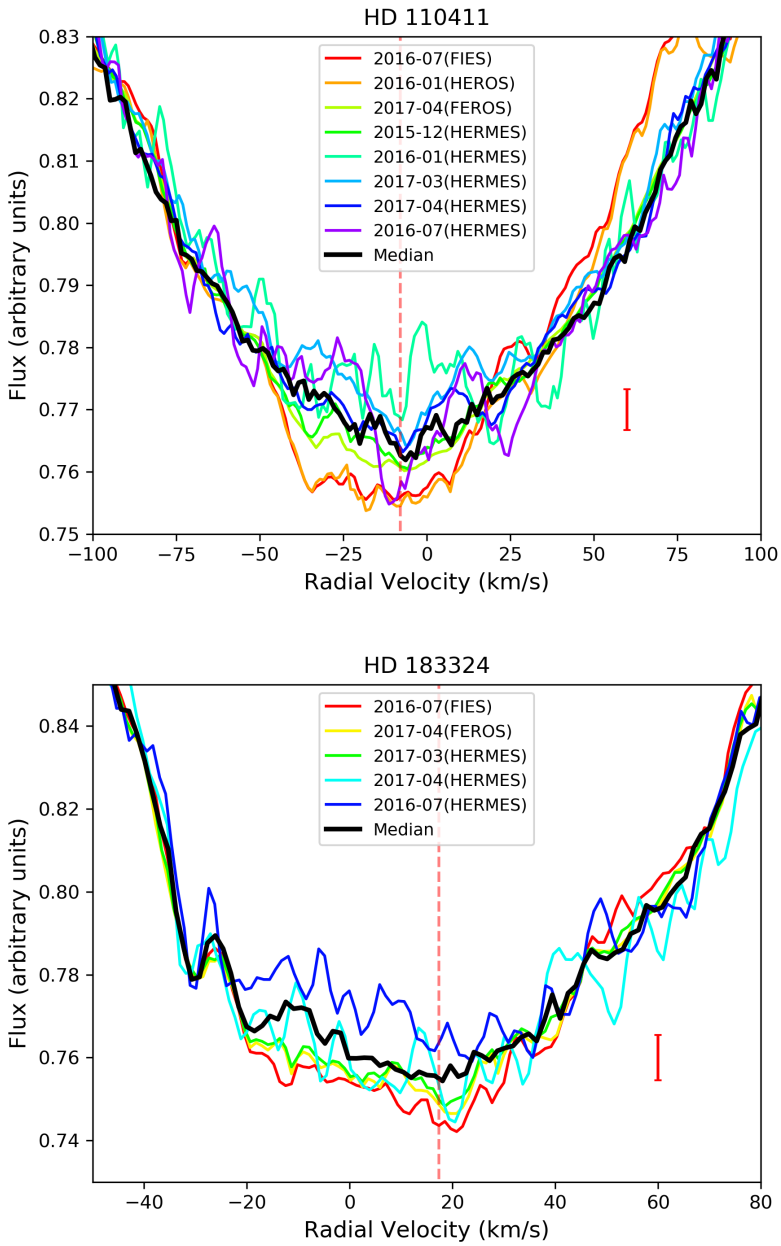

Figure 2.5: Photospheric profile of Ca II K spectra of HD 110411 and HD 183324. The core of the line varies although neither a narrow feature nor transient events are clearly distinguished. The red dashed vertical line marks the radial velocity of the star. The red error bar shows the 3-σ standard deviation in the region close to the bottom of the line. This applies to all upcoming figures.

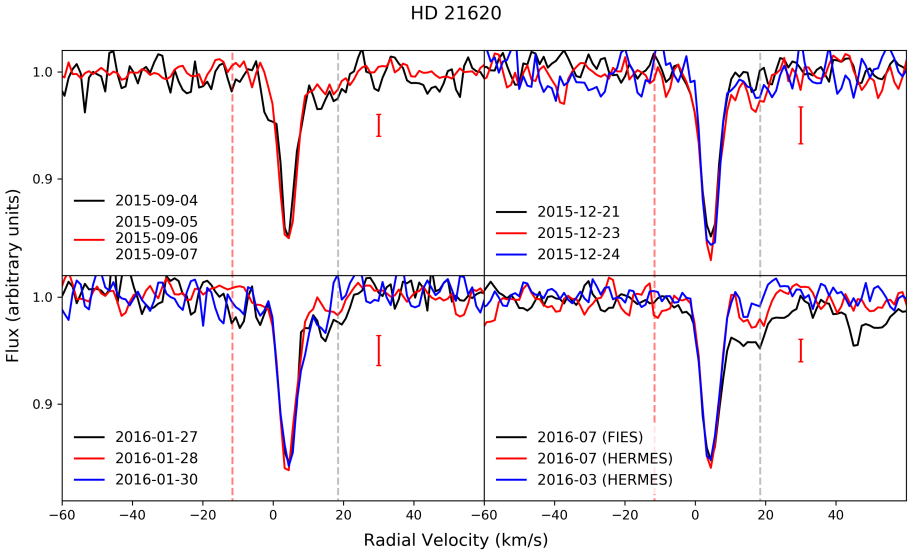

Figure 2.6: Ca II K line of different epochs of HD 21620. Panels at the top and lower left are from Mercator data. Lower right panel shows median spectra of indicated period and telescope. FEB-like events appear in ~ 0 (blue-shifted, top left panel), 15 and 50 km/s (red-shifted, bottom right). The events of January 2016 appears to present some dynamical evolution. Vertical red and grey dashed lines show the stellar and ISM radial velocities respectively.

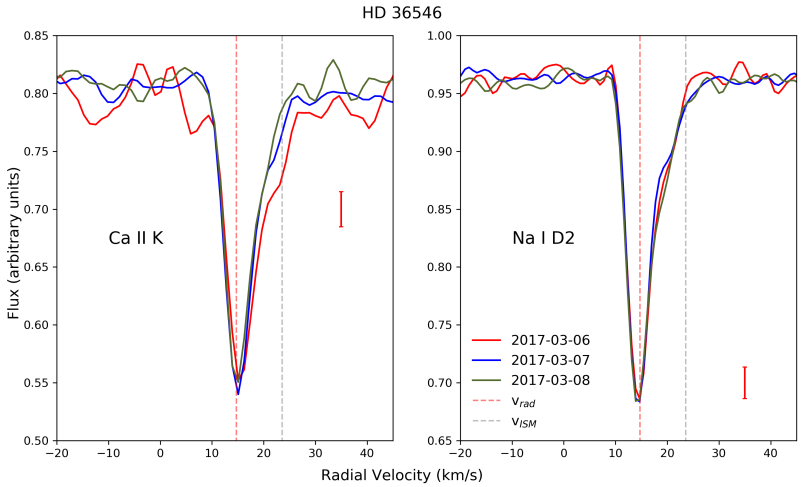

Figure 2.7: Left panel: Ca II K line. A transient event is seen at ~ 20 km/s superimposed on the red wing of the narrow non-photospheric absorption at $\sim$ 15km/s. No obvious event is seen in 08/03/2017. Right panel: Na I D2 line. Dates are as indicated. Red and grey vertical lines mark the radial velocity of the star and of the ISM respectively.

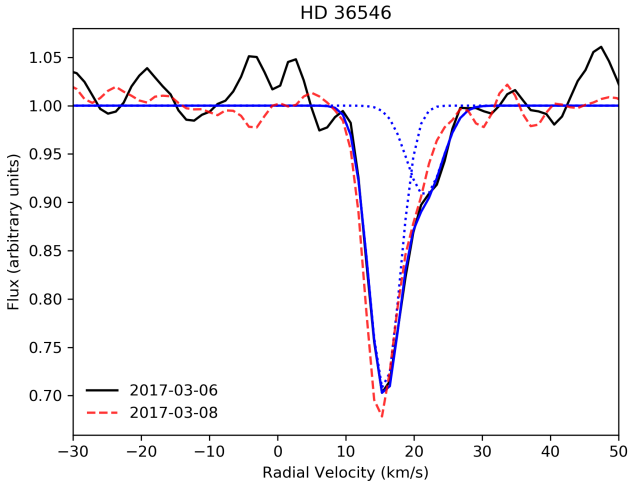

Figure 2.8: The Ca II K spectra of the HD 36546 non-photospheric absorption for the day where the event in the red wing is most conspicuous (06/03/2016, black line) and when it is practically undetectable (08/03/2016, red dashed line). Blue solid line shows a fit of the 06/03/2016 spectrum with two Gaussians, each one plotted as dotted blue lines.

remarkable and striking behaviour is the strong shell-like spectrum that appeared on the spectra of September 2017. The Ca II H&K lines developed a strong, symmetric, triangular profile superimposed on the photospheric lines and the two narrow interstellar features, together with narrow shell-like absorptions in the Ca II triplet or in several Fe II and Ti II lines (see Fig. 2.9). At the same time, photospheric lines as e.g. the Mg II 4481 Å or the O I triplet at 7750 Å remained constant, as well as the Na I D lines. Further, the strong shell spectrum fully vanished in additional spectra taken in November 28, 2018 with the CARMENES spectrograph in Calar Alto Observatory (Quirrenbach et al., 2016), and from December 14 to 18, 2018 with HERMES, that are still under deeper analysis. Due to the in principle unusual nature of this phenomenon, we have checked possible sources of contamination, such as instrumentation issues or additional sources in the fiber, but we have discarded these scenarios. Thus, the appearance/disappearance of the shell-like profiles does point out to the presence of CS gas, but no blue-/red-shifted FEB-like events are detected in any of our spectra. We note that variability of shell spectra and even its appearance/disappearance in some stars is well known (e.g. Jaschek et al., 1988). At the same time, and despite the lack of any identified ISM clouds in the line of sight, the fact that no remarkable changes are seen in the mentioned $\sim$11 km/s and $\sim$32 km/s narrow features during the 8 days of observations in September 2017, while drastic changes are seen in the CS (shell-type) environment, suggests an ISM origin as the more plausible alternative for those two absorptions, in agreement with Iglesias et al. (2018).

- HD 39182 (HR 2025), one of the selected Ti II stars, has a sharp triangular-like absorp-

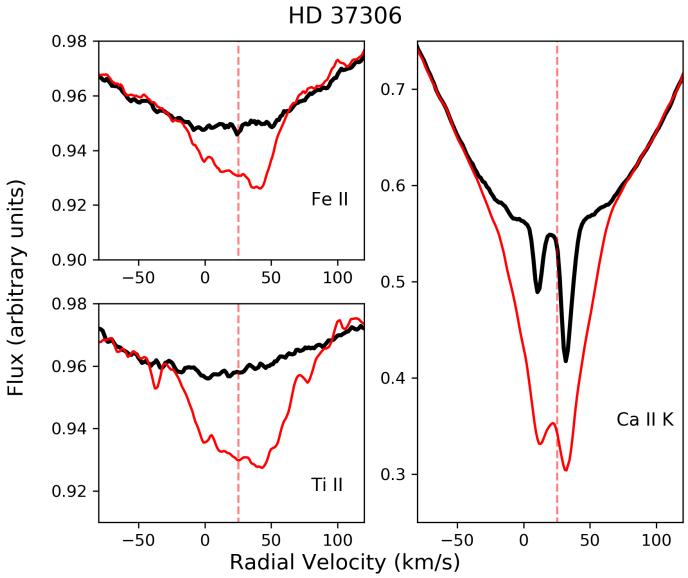

Figure 2.9: Fe II (4583.83 Å), Ti II (4549.62 Å) and Ca II K lines of HD 37306. While most of the spectra, represented by the median spectrum in the plot, do no vary and show two Ca II non-photospheric absorptions, a strong shell-like profile appeared in September 2017, while it was not observed again in later spectra of November and December 2018. Red vertical line marks the radial velocity of the star.

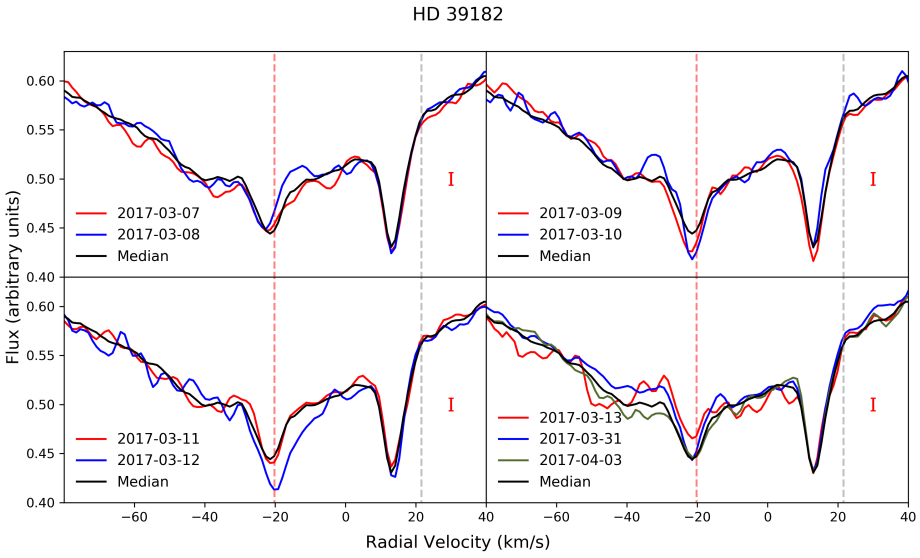

Figure 2.10: Ca II K spectra of HD 39182 grouped by observing dates. In all panels, the median spectra is also plotted. The red and grey vertical lines correspond to the radial velocity of the star and the velocity vector of the LIC Colorado cloud, respectively.

tion (Fig. A.1) with two narrow Ca II components; one is found at $\sim$ –22 km/s, centred in the photospheric line coinciding with the stellar v_{rad}, and varies significantly; the

second, strongest one at ∼ 13 km/s is clearly displaced from the line center (Fig. 2.10). A weak extra absorption at ∼ –41 km/s is present in some spectra, i.e., in the blue wing of the –22 km/s component (Figs. A.1 and 2.10). The Na I D lines only show a strong narrow absorption at ∼ 14 km/s, coinciding with the strongest Ca II component. None of the velocity components coincides with the velocity vector (v_{ISM} = 21.62 km/s) of the LIC cloud , which is seen along the line of sight to the star. Our spectra differ from the one reported by Lagrange-Henri et al. (1990d). Their spectrum shows a strong Ca II feature at the bottom of the stellar line, i.e., like our –22 km/s feature, but the strong 13 km/s absorption in our spectra, if present, is much weaker. Further, Lagrange-Henri et al. (1990d) do not report any Na I component. Thus, all these results suggest that the origin of all absorptions are CS.

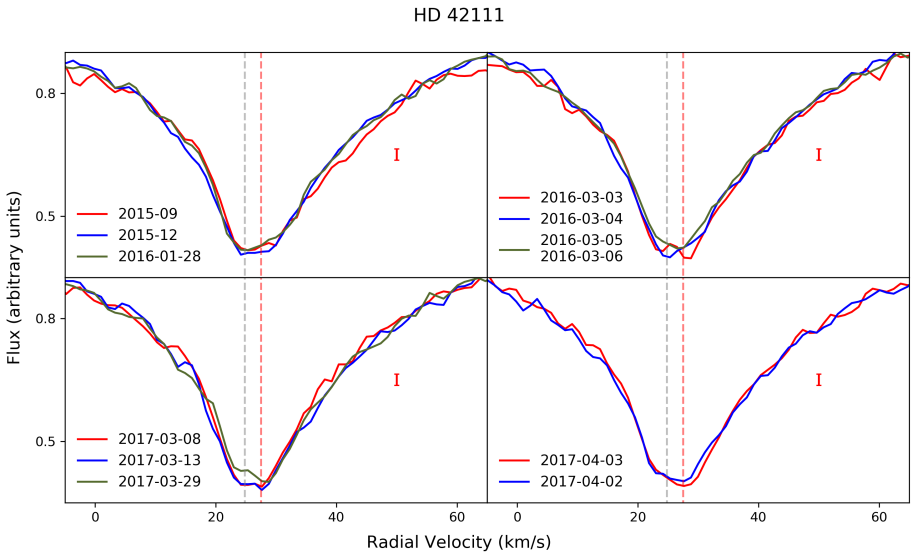

Figure 2.11: Ca II K spectra of HD 42111 grouped by observing dates. The red and grey vertical lines correspond to the radial velocity of the star and the velocity vector of the ISM in the line of sight.

- HD 42111 (HR 2174) is a shell star with seemingly one Ca II and two Na I features in the median spectrum (Fig. A.1 and Table A.3). The features are centred at the radial velocity of the star and close to the Aur cloud velocity. Individual spectra show that the Ca II feature is formed by two components at velocities ∼25 km/s and 27.5 km/s. The feature at ∼25 km/s varies in depth while the feature at ∼27.5 km/s appears distinctly only in some selected dates as a β Pic-like event, e.g. 03/03/2016 or 08/03/2017 (Fig. 2.11), likely with a small dynamical evolution, at least in the March 2016 spectra, (see top-right panel of Fig. 2.11). Thus, we attribute a CS origin to the more red-shifted component and at least partly to the one at 25 km/s. The inspection of nearby stars HD 40573 (B9.5) and HD 42299 (A3) showed absorptions at ∼ 30 km/s, that could be generated by the same cloud as the 25 km/s absorption. Welsh & Montgomery (2013) also detected a change in the EW of the main absorption, and a FEB-like event

at 75 km/s. Further, Grady et al. (1996b) and Lecavelier Des Etangs et al. (1997) detected gas in UV lines of Fe II, Mn II, and Mg II, interpreted as CS clumps falling onto the star. Moreover, the lines detected by Lecavelier Des Etangs et al. (1997) are asymmetric with low velocity red-shifted wings, somehow similar to the Ca II detected in our spectra.

- HD 80007 has weak Ca II and Na I absorptions at the stellar v_{rad} (Table A.3 and Fig. A.1). Hempel & Schmitt (2003) noticed a change in the equivalent width, shape, and velocity of the Ca II absorption. Redfield et al. (2007) also found variability in the velocity while the column density of the Ca II absorption remains relatively constant; in contrast, those authors found more remarkable variability in the velocity (two absorptions at $\sim$ –7 km/s and $\sim$ 7 km/s) and column densities of the Na I feature. Further, Welsh & Montgomery (2015) found a quasi two-component Ca II K feature in two consecutive nights and one single-component absorption in two other nights, with changes in the equivalent width. In addition, Wood & Hollis (1971) found a quasi-periodic oscillation in the strength of the Hβ Balmer line, and suggested it could be due to flares generated by acoustic oscillations of the stellar atmosphere.

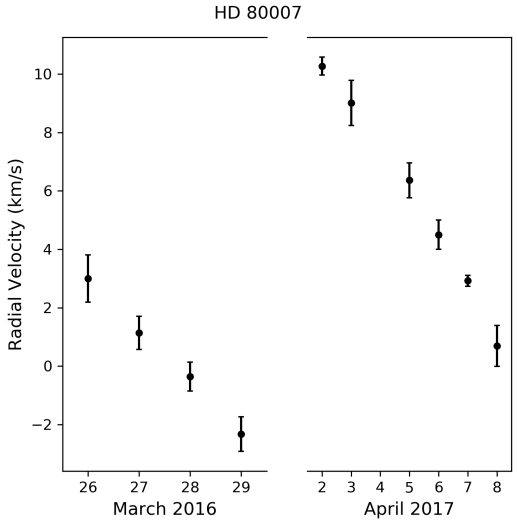

Figure 2.12: Radial velocity variation of HD 80007 in both observing periods. The observations suggest the presence of an unseen companion.

Our spectra show new aspects of both Ca II and Na I absorptions as well as in the stellar radial velocity. Firstly, the radial velocity of the star shows a regular variation of the order of $\sim$ 1.5 km/s per day in both 2016 and 2017 observing periods, Fig. 2.12. A possibility is that HD 80007 is a binary system and that the radial velocity variability is induced by an unseen companion. Secondly, the Ca II absorption shows a "central" feature with small changes in its strength accompanied in some spectra with blue- and red-shifted components (Fig. 2.13, top panel). At the same time the Na I D2 feature presents two components. One is a broad, variable feature centred at $\sim$ 2 km/s, i.e.,

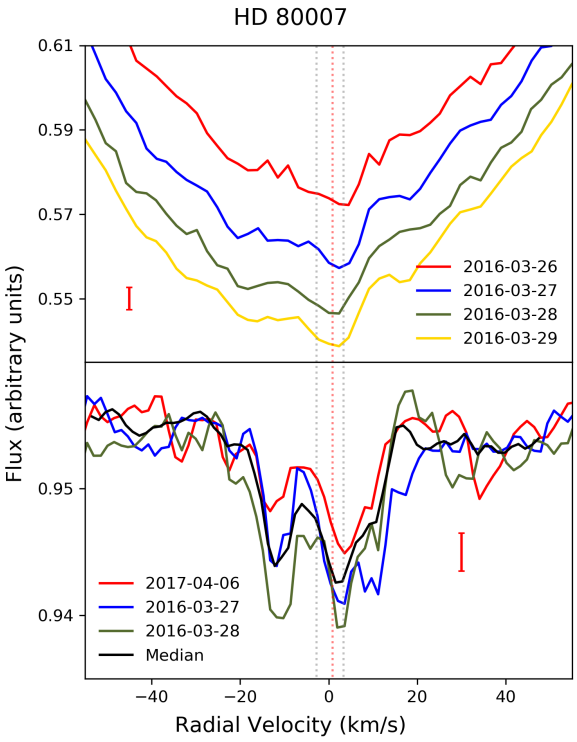

Figure 2.13: Top panel: Ca II K line of HD 80007 for the selected days. Spectra have been shifted in the Y-axis aiming to facilitate the visualisation of the variability. The central absorption is seen at $\sim$ 2 km/s, as well as blue- and red-shifted variable absorptions. Bottom panel: Na I D2 line of HD 80007 for the selected days. Variability is seen at $\sim$ -10 and $\sim$ 2 km/s.In both panels it is noticeable the slight shift at the bottom of the narrow absorptions presumably produced by a companion.

the velocity of the star and the Ca II feature, with a red-shifted wing up to $\sim$ 18.5 km/s even discernible in the median spectrum (Fig. 2.13, bottom panel). Further, one red-shifted event at $\sim$10 km/s and extending up to $\sim$22 km/s is present in the spectrum of 2016 March 27. The second Na I component at a velocity $\sim$ –11.5 km/s appears in all spectra but it varies its depth. We note that the velocity difference between both features is approximately the same as the ones sporadically observed by Redfield et al. (2007). We also note that while the component at the stellar velocity is detected in the Na I D1 line, the one at negative velocities is not.

- HD 85905 is a shell star whose median spectrum shows a sharp triangular-like Ca II absorption with two components at velocities at $\sim$8.4 km/s and $\sim$25.0 km/s, and one Na I feature at $\sim$8.1 km/s. The feature at $\sim$8 km/s coincides with the radial velocity of the star and is also close to the velocity vector of the G cloud (Fig. A.1 and Table A.3). Nonetheless, individual spectra from the different epochs show remarkable variability; Fig. 2.14 shows some examples. During December 2015 both Ca II components experienced noticeable variations, while the corresponding Na I 8.0 km/s feature remained

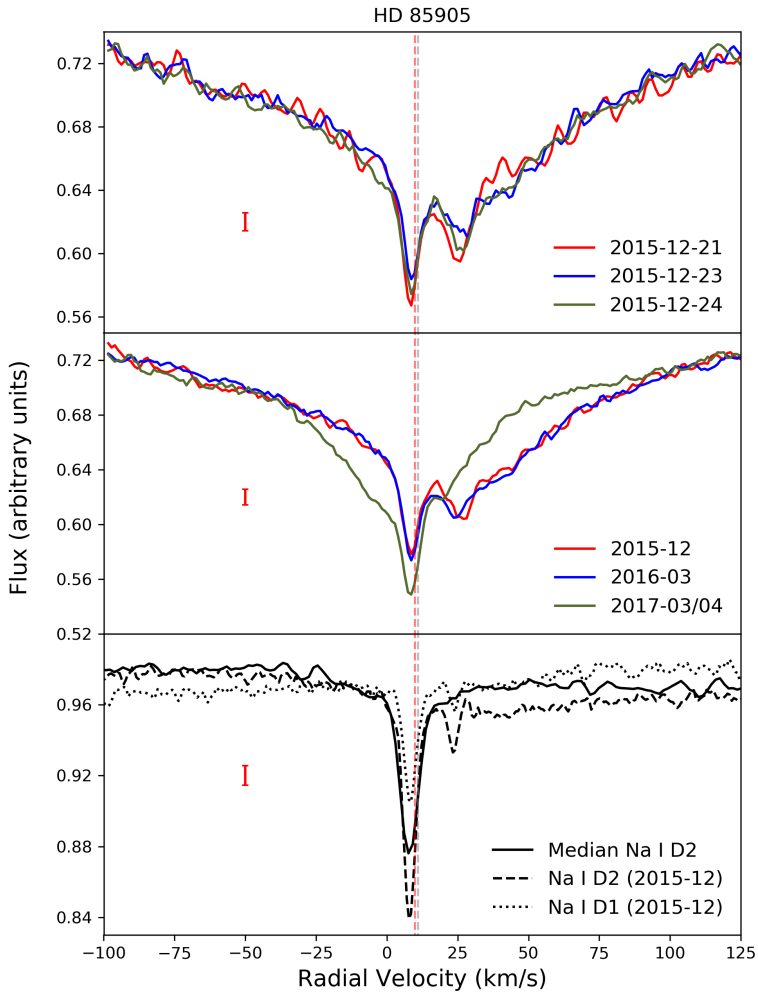

Figure 2.14: Top panel: Days 21, 23 and 24 of December 2015 where variability of the ∼ 25 km/s Ca II K feature can be seen. Middle panel: Ca II K median spectra of three different campaigns where the variability in the triangular profile is seen. The absorption at ∼ 25 km/s disappears in March 2017. Lower panel: Na I D lines of December 2015 where the absorption at ∼ 23 km/s is visible. The median of all spectra in the Na I D2 line where the absorption is no longer present is also shown.

constant. However, there is a relatively strong feature at a velocity of ∼23.7 km/s in both Na I D lines, (i.e. close to the Ca II 25.0 km/s component) visible in all dates of that period (December 2015) but not in any other of our observing epochs. The lower panel of Fig. 2.14 shows the median of December 2015 spectra of both Na I D lines

where this result can be appreciated. Further, while during the periods of December 2015, January and March 2016 both Ca II components were present, only the component at ∼8 km/s was visible during the two different campaigns of 2017 (March 8 to 11, and March 29 to April 8). During these campaigns, a strong absorption appeared as well in the blue wing of the Ca II K, while the red-shifted 25.0 km/s feature practically disappears. The above results clearly suggest a CS origin of the non-photospheric absorptions observed in HD 85905, maybe related to a variability of the CS shell as suggested by the variations observed in other shell lines of e.g. Fe II, but not in photospheric lines as Mg II 4481 Å or the O I triplet at 7775 Å (not shown). A detailed analysis will be published elsewhere. Welsh et al. (1998) and Redfield et al. (2007) also attributed a CS origin to the Ca II and Na I absorptions they detected.

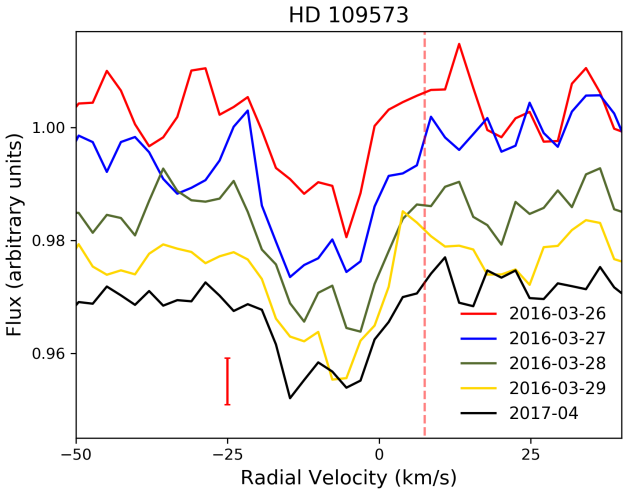

Figure 2.15: Ca II K line of HD 109573. A shift has been added to the Y-axis in order to help differentiate the variations. The red vertical line corresponds to the radial velocity of the star. Ca II K line shows two absorptions not coincident with the radial velocity of the star but with variations in their strength.

- HD 109573 (HR 4796) has two strong Ca II absorptions at ∼ –14.2 and –4.7 km/s in the median spectrum (Fig. A.1). The component at –4.7 km/s is also present in the Na I D lines. None of these components coincides with the radial velocity of the star. Fig. 2.15 shows details of the Ca II K line on different dates. Both components vary in depth and shape, in some cases close to the noise level. Nonetheless, a discernible variability is seen, e.g. the -14.2 km/s component of March 2016 26th and 29th is distinctively weaker than of March 2016 27th, 28th or the median of April 2017.

  Our spectra are similar to those in Welsh & Montgomery (2015), where a change in the profile of the ∼ –5 km/s feature is also apparent. Thus, we suggest that the non-photospheric features have a CS origin. Nonetheless, Iglesias et al. (2018) attribute the –5 km/s feature an ISM origin, as the field star 1 Cen (HD 110073; 30 pc behind HR 4796) also has a similar absorption feature. Welsh & Montgomery (2015) detected a

faint FEB-like event at $\sim$ 60 km/s in two spectra of a single night; and Iglesias et al. (2018) report a faint variable feature at the velocity of the star. None of these are apparent in our spectra.

- HD 138629 (HR 5774) has three non stellar Ca II features at velocities –31.8, –22.9, and –13.8 km/s with no sign of variability, none of them clearly coincident with v_{rad} or with v_{ISM}. The Na I D lines also present three absorptions, two of them coinciding with two Ca II ones (Fig. 2.16). Our spectra differ from the two and four Ca II components, and from one Na I feature, reported by Lagrange-Henri et al. (1990c). We attribute at least partially a CS origin due to the apparent changes with previous works, but an ISM origin can not be excluded at least for the features at $\sim$ –22 km/s and $\sim$ –12 km/s.

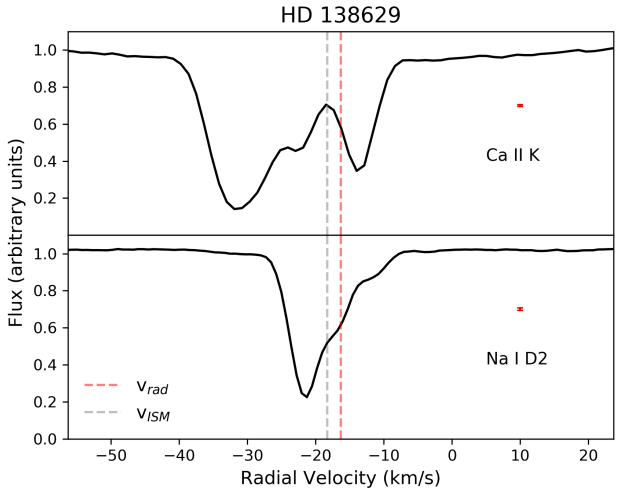

Figure 2.16: Ca II K and Na I D2 non-photospheric absorption features observed towards HR 5774. Dashed lines correspond to the radial velocity of the star (red) and the velocity vector of the interstellar NGP cloud (blue).

- HD 145964 is one of the Upper Scorpius stars. Two absorption components at velocities $\sim$ –9.5 km/s and $\sim$–25 km/s are detected in Ca II and Na I lines. Those components can be attributed to the ISM medium as they are also detected in many other UpSco stars (see Sect. 2.4.1). However, while the feature at –9.0 km/s, which is the velocity of the star, remains practically constant (variations below 3σ), the blue wing of the –25 km/s absorption shows a weak $\sim$ –30 km/s component in all observing runs, but not in both the Hermes and FEROS spectra taken during the same dates in April 2017. We also note that a marginal variation in the relative depth of the –9.0 km/s and –25 km/s features might be present. Thus, a CS contribution is suggested, in particular for the –25 km/s and –30 km/s absorptions. In the work by Welsh & Montgomery (2013), they observed a weak FEB-like event at a velocity of $\sim$ 50 km/s that is not detectable in our data.

- HD 172555 was already discussed by Rebollido et al. (2018)(Chap. 3) as one of the debris disc stars with both cold and hot gas in its circumstellar environment (see also the first paragraph of Sect. 2.4.1). Here we want to stress that a weak ISM feature is detected in both Ca II lines at a velocity of ∼–20 km/s, in good agreement with Kiefer et al. (2014a). In addition, our spectra reveal a weak, broad Na I D2 feature centred at ∼15.3km/s and extending from ∼–5 km/s up to ∼35 km/s. Although the individual spectra are relatively noisy we are confident on this detection as it appears in all spectra. The top panel of Fig. 2.18 shows spectra of 08/03/2016, 08/04/2017, and the median spectra for the Na I D2 line. The broad feature presents a clear variability, denoting its CS nature. The bottom panels of Fig. 2.18 shows the telluric subtraction for the indicated dates, where it is clear the variability is not related to telluric lines. Fig. 2.18 (top panel) also shows the median of all Na I D1 line spectra, where the ISM feature is clearly visible but not the broad CS one. We note that Grady et al. (2018) detected some UV broad, variable absorptions of ions like e.g. CII.

- HD 182919 (5 Vul) has a narrow absorption feature at ∼–18.5 km/s, close the velocity of the star and to the G, Mic, and Aql clouds (Table A.3 and Fig. A.1). The feature varies its depth (∼ 6.0σ) when analysing the median spectra of different epochs (Fig. 2.19); thus, it most likely has a CS origin, at least partly. During the 2016 July observing run at Mercator a weak blue-shifted absorption with an EW of 1.3 mÅ is apparent at a velocity of ∼ -35 km/s; in addition, the spectrum of 2016-07-14 shows a red-shifted event at ∼ 25 km/s and EW 1.6 mÅ. We note that Montgomery & Welsh (2012) also noticed the variability of the narrow absorption as well as the presence of a FEB-like event with a velocity range 15–60 km/s in one of their spectra.

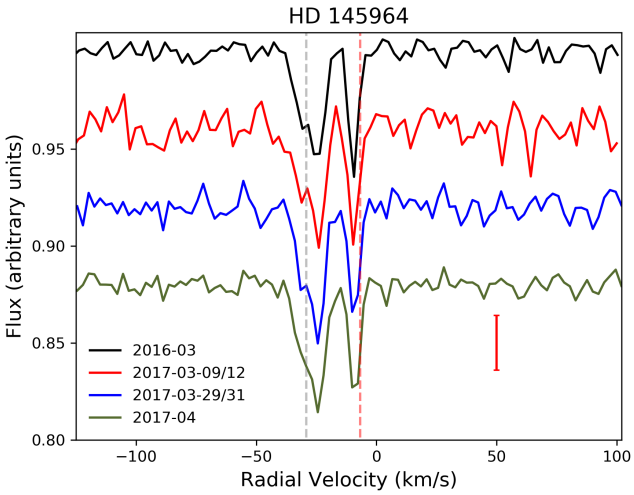

Figure 2.17: Spectra of HD 145964 as indicated in the labels. An offset was introduced in the Y-axis to better perceive the variations. The red and grey vertical lines correspond to the radial velocity of the star and the velocity vector of the G Colorado cloud, respectively

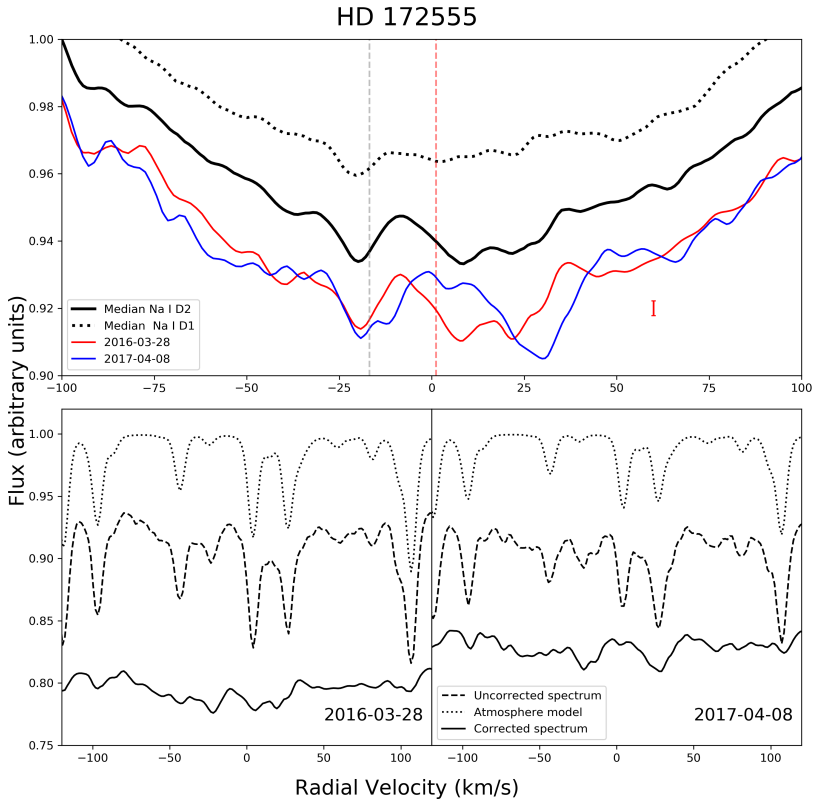

Figure 2.18: Top panel: Absorptions detected in the Na I D2 line of HD 172555. Black lines corresponds to the median of all spectra for Na I D2 (solid line) and D1 (dotted line). Blue and red lines correspond to two different dates, where the variations in the ∼15 km/s Na I D2 component can be perceived. Bottom panel: Examples of the telluric subtraction are plotted, in order to show that this process it is not the source of the variability. Red and grey vertical lines mark the stellar and ISM radial velocities respectively.

- HD 217782 (2 And) has three Ca II absorptions at velocities ∼ –17.1 km/s, –9.2 km/s, and 5.2 km/s (see Fig. A.1). Two of them, blue-shifted with respect to the radial velocity of the star, are also detected in Na I. The weakest feature at 5.1 km/s is at the stellar v_{rad} and the velocity vector of the Hyades ISM cloud (Table A.3). While the stronger and narrower -9.3 km/s feature remains unchanged (variations below 1σ), the -16.5 and likely the 5.1 km/s components present some variability (Fig. 2.20). Particularly, the -16.5 km/s feature experiences some dynamical evolution changing its depth and velocity within hours, e.g. up to 3 σ EW variation along the night $6^{th}/7^{th}$ September 2015, as well as a shape and depth change (Fig. 2.20, bottom left panel). Similar changes are also seen on other nights. These results suggest the presence of CS gas around 2 And. Cheng & Neff (2003); Montgomery & Welsh (2012); Welty et al. (1996) found similar UV/optical results.

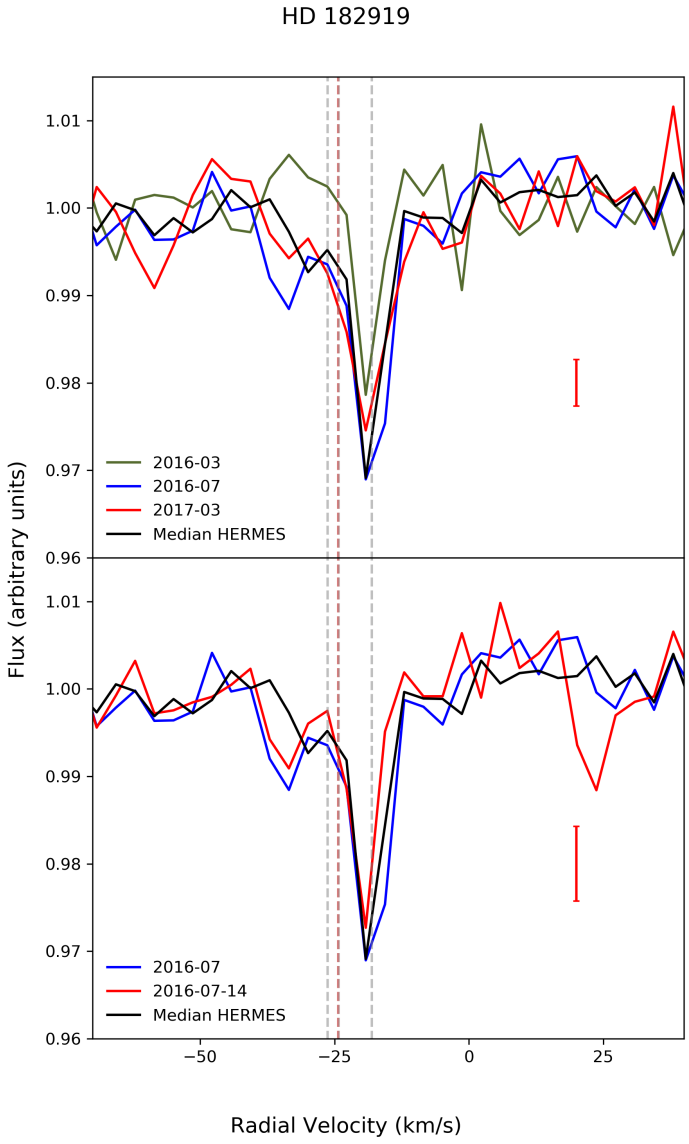

Figure 2.19: Spectra of HD 182919 (5 Vul) taken with Mercator in the dates indicated in the labels. Top panel shows the variation of the features at $\sim$ –18 and $\sim$ –35 km/s. In the bottom panel it is visible a possible FEB-like event at $\sim$ 25 km/s. The red and grey lines correspond to the radial velocity of the star and the velocity vector of Colorado clouds, respectively.

2.4.3 Summary of CS gas detections

Fig. A.1 shows the observed median Ca II K&H and Na I D lines and the non-photospheric residuals, once the stellar contribution has been subtracted, of the 60 stars that have narrow stable absorptions; radial velocities of the stars and the velocity vector of the ISM Col-

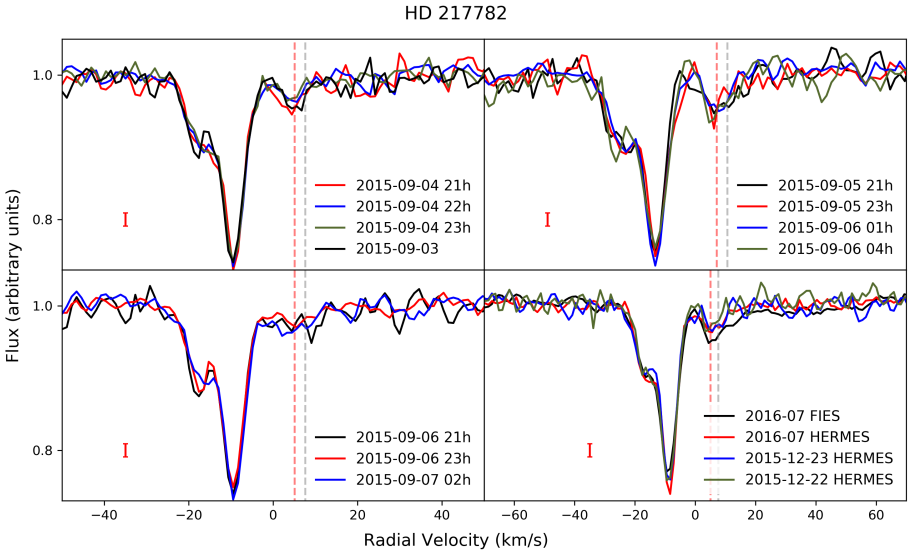

Figure 2.20: Spectra of HD 217782 as indicated in the labels. In the bottom right panel the labels indicate the instrument used in each case. The rest of the spectra were obtained with Mercator. The dashed and continuous lines correspond to the radial velocity of the star and the velocity vector of Colorado clouds, respectively

orado clouds velocities are also plotted. Table A.3 gives radial velocities, FWHM, equivalent widths, and column densities of the narrow features. Table 2.2 lists the stars showing variable absorptions detected in this work, and also the stars reported in the literature as hosting sporadic events but not detected by us.

We find evidence of hot CS gas in 32 objects out of the initial sample of 117 stars, being 30 in the form of stable non-photospheric components, and variable absorptions in the other two cases. Variable red- and/or blue-shifted events with respect to the radial velocity of the stars have been detected in 18 objects, including the serendipitous detection of HD 132200, which was not in the initial sample (Rebollido et al., 2018)(Chap. 3). Among those 18 objects, all but HD 110411 and HD 183324, also have stable narrow features. These figures mean we have found evidence of a close-in gaseous CS environment in $\sim$27% of the sample. We note, however, that it is not statistically significant as the selection criteria were highly biased, for instance including stars for which the presence of hot or cold CS gas was already known. Nonetheless, the figure does indicate that a non-negligible amount of stars, particularly A-type (see below), are surrounded by CS gas which can be detected by means of high resolution optical spectroscopy. We note that we are not considering the 8 stars where the detected narrow feature has a dubious origin as we are unable to soundly attribute it either to a CS or/and ISM environment.

The detected CS gas clearly has distinct origins. Red- and blue-shifted events are plausibly linked to the presence of FEBs, as in the well known case of β Pic; even in some cases our spectra likely trace the dynamical evolution of those exocomets, i.e., a change in depth and velocity. In none of the cases the exocomet activity is as rich as in β Pic, which re-

mains unique in this context. Stable absorption features in some stars are also likely related to exocomets and/or evaporation of grains in the immediate CS environment. In the case of shell stars, the non-photospheric stable features, including many metallic shell lines of species like Fe II or Ti II, are related to the shell itself, and likely arising from mass loss phenomena experienced by the central star. Nonetheless, some shell stars also present sporadic red- or blue-shifted absorption events in Ca II reminiscent of exocomets. HD 37306 represents an extreme case, where we detected the appearance and disappearance of a strong shell spectrum but no trace of any exocomet-like event.

2.5 Discussion

While our stellar sample is heterogeneous and highly biased we can still try to find some trends among the incidence of CS gas and some general properties of the stars, and the different groups of stars according to the selection criteria.

Fig. 2.21 shows the HR diagram of the sample where the absolute magnitude M_V and colour index B-V are estimated from the magnitudes and parallaxes given in SIMBAD; the MS track is taken from Pecaut & Mamajek (2013). To estimate M_V we have not taken into account the potential extinction towards the stars; nonetheless, the true loci of the individual stars in the HR diagram would not significantly alter the conclusions. Objects with evidence of hot CS gas (variable or stable) are A-type stars, and are therefore located in the upper-left region of the diagram. This is in line with previous works, although as far as we know they have only been concentrated in the study of A-type stars (e.g. Holweger et al., 1999; Welsh & Montgomery, 2018,and references therein). We only know of one later spectral type star, HD 109085 (η Crv, F2 V) for which one exocometary-like event has recently been reported although it requires confirmation (Welsh & Montgomery, 2019); While cold CO is most likely present in this system (Marino et al., 2017), we do not find any trace of CS gas associated with this star (Rebollido et al., 2018, Chap. 3,this work). In this respect, photometric transits are more efficient than spectroscopy to detect exocomets around later type stars (e.g. Rappaport et al., 2018; Ansdell et al., 2019). The inability, at least up to now, of spectroscopy to detect exocomet signatures in late-type stars might be due to the concurrence of several causes, e.g. stellar activity that makes it extremely difficult to detect faint variable events superimposed on the profiles of the chromospheric active Ca II and Na I lines; also, late type stars usually have small rotational velocities so that narrow stable absorptions are practically indiscernible from the core of the narrow stellar lines.

It is obvious from Fig. 2.21 that stars with both stable and/or sporadic CS features tend to be in many cases located above the main sequence, in the δ Scuti instability strip of the HR diagram (Breger, 1979; Rodriguez et al., 1994). A few of the hot-gas-bearing stars in our sample are identified as δ Scuti stars in SIMBAD - HD 110411, HD 183324, and HD 192518; recently, Mellon et al. (2019) have found that HD 156623 is also a δ Scuti star; we also point out that β Pic itself has δ Scuti pulsations (Koen, 2003; Mékarnia et al., 2017). In addition,

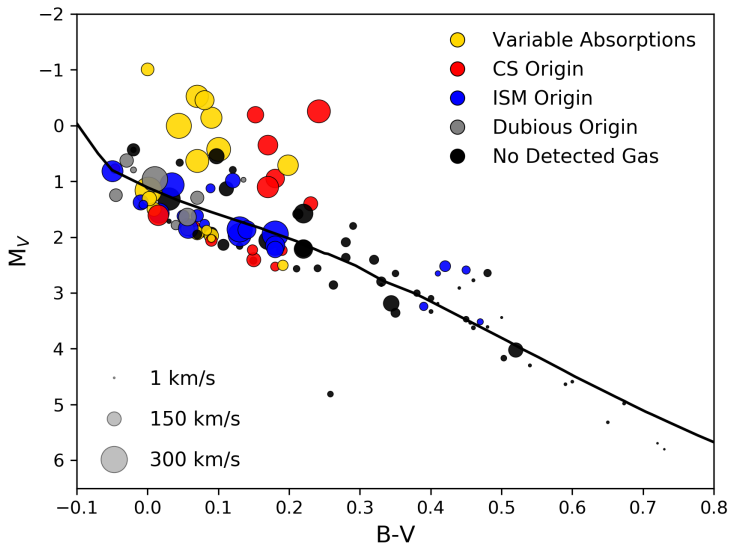

Figure 2.21: Colour-Magnitude diagram of the whole sample. Colours represent stars with different non-photospheric features while the size of the symbols is proportional to $v \sin i$.

the CS gas stars have distinctly larger $v \sin i$. As expected, (e.g. Nielsen et al., 2013), the highest $v \sin i$ values are found for the earlier spectral types (symbol sizes in Fig. 2.21 are proportional to v sin i). Excluding stars later than F2, Fig. 2.22 shows the cumulative distribution functions (CDF) of the projected rotational velocity of the early type stars without non-photospheric features, stars with features identified as ISM absorptions, and stars with variable events. It is evident from Fig. 2.22 that stars with non-photospheric ISM features or with variable CS events, have larger $v \sin i$ values than stars without non-photosperic features. Table 2.3 shows the results of a Kolmogorov-Smirnov test separating those three subsamples. We refer to Maldonado et al. (2012) for the meaning of the parameters D, p-value, and n_{eff} in that table. In particular, the p-value indicates that the subsample of stars with ISM absorptions differ with a probability of $\sim$97%, of the stars without non-photospheric absorptions; for the case of stars with variable events the probability is practically 100%. At the same time, the results of the Kolmogorov-Smirnov test indicates that the ISM and variable events subsamples do not differ significantly. Nonetheless, a visual inspection of Fig. 2.22 suggests that there might be a paucity of the variable hot-gas-bearing stars with $v \sin i$ up to $\sim$150 km/s with respect to the sample of stars with ISM absorptions, which is lost in the statistical test when comparing the whole range of $v \sin i$.

When considering the age of all stars with non-photospheric CS and ISM absorptions, $\sim$58% have ages below 100 Myr (Table A.2). If we just consider stars plausibly hosting CS features that figure is $\sim$51%, and reduces $\sim$42% (11 out of the 26 stars) when the stars with variable features are considered. Thus, although ages of field stars might be highly uncertain

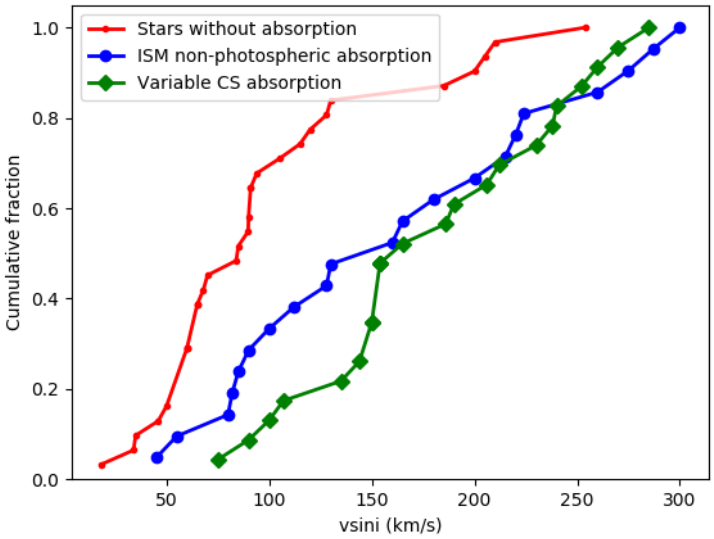

Figure 2.22: Cumulative distribution functions of the subsamples labelled in the plot.

Table 2.3: Kolmogorov-Smirnov test comparing the projected rotational velocity distribution of the subsample of stars earlier than F2 without non-photospheric features, stars with absorptions with an ISM origin, and stars with variable events.

Sample 1	Sample 2	D	p-value	n_{eff}
ISM absorp.	No absorp.	0.39	0.030	12.52
CS Var. absorp.	No absorp.	0.66	6.376×10^{-6}	12.20
ISM absorp.	CS Var. absorp.	0.30	0.222	10.98

and the nature of the variability of the features is not always due to exocomet-like events, e.g. the case of HD 37306, stars with FEB-like events do not tend to be young objects but they are distributed in a wide range of ages, from ∼10 Myr to ∼1 Gyr. All this is clearly recognised in Figure 2.23 where a plot of the rotational velocity of the stars (up to F2) versus age is shown. Stars with non-photospheric features are all younger than 1000 Myr, and its distribution is clearly modulated by stars in young clusters - mainly UpSco, UCL, BPMG and Tuc-Hor. Stars with CS features are found among the whole range of ages, and have higher rotational velocities than stars without non-photospheric features. They also appear to have higher rotational rotational velocities than stars with ISM features, in fact reflecting the results of the Kolgomorov-Smirnov test above, and the mentioned paucity of CS-feature stars with low $v \sin i$.

Out of the 32 stars in our sample with non-photospheric absorptions, we find in many cases coincident radial velocities (within the errors reported in Sect. 4.1) between the features observed in Ca and in Na. Fig. 2.24 shows the ratio of Ca II K and Na I D2 column

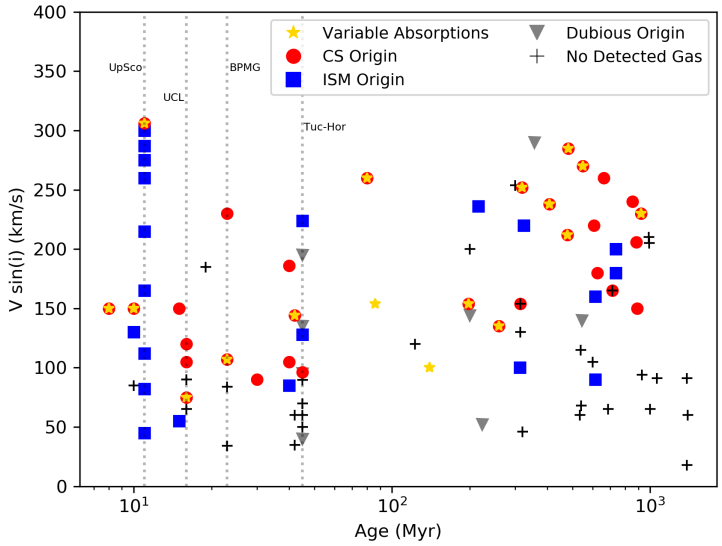

Figure 2.23: Age versus $v \sin i$ of the stars in the sample. Symbols mark the type of absorptions detected for each object. Vertical dotted lines mark the location of some of the young associations: Upper Scorpious, Upper Centaurus Lupus, Beta Pic Moving Group and Tucana-Horologium.

densities against the Ca II K column density, color coded for the attributed origin. In those cases where only one of the lines was detected, an upper limit was calculated using the EW uncertainty to compute the column density. The distribution of the stars in this diagram is consistent with other works (e.g. Welsh et al., 2010; Gudennavar et al., 2012). There is no clear separation between CS or ISM absorptions, i.e., the ratios of their column densities do not show any significant trend when comparing them regarding their origin, in agreement with previous results (see section 4.1.1, first paragraph). It is worth noticing though, that it seems that the presence of both Ca and Na components is more common in ISM absorptions. HD 42111 seems to behave as an extreme outlier in our sample as it has a large $N_{\mathrm{Ca\,II\,K}}$. However, this shell star has two practically blended narrow, absorptions (not discernible in the median spectrum), which might explain the large $N_{\mathrm{Ca\,II\,K}}$.

While objects in the sample are distributed in the sky without preferential locations (Fig. 2.1), we find a possible trend when examining distances. Stars without narrow absorptions (either CS or ISM) are located at < 50 pc, but there is no clear differentiation between stars with CS and ISM narrow absorptions. This could be due to the lower frequency of interstellar clouds at shorter distances, and the exponential growth of the number of stars with distance.

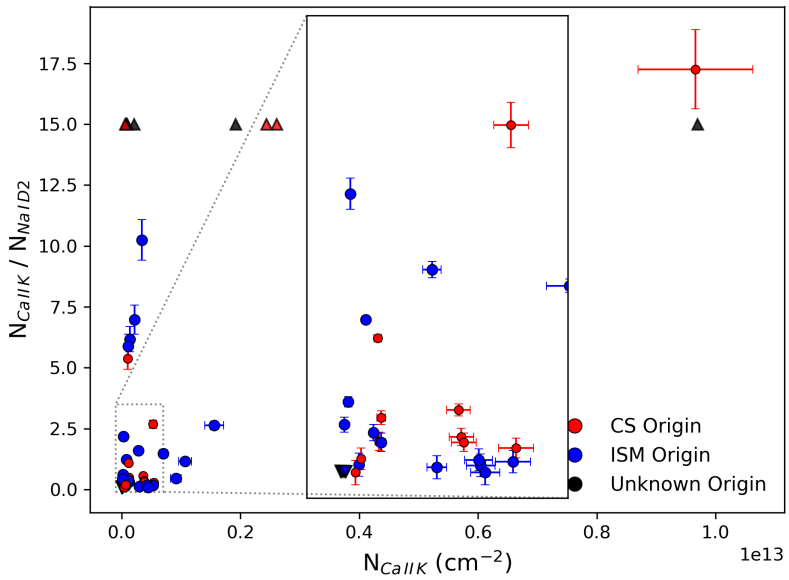

Figure 2.24: Column densities of Ca II K and ratio of column density of Ca II K and Na I D2 of those absorptions of similar radial velocities. For the case where an absorption was detected in only one of the lines, triangles pointing up are upper limits and triangles pointing down are lower limits. The outlier in the upper-left corner of the plot is HD 42111. Colour denotes the suggested origin as in the legend.

2.5.1 Stars with debris discs

To our knowledge, 76 out of the 117 stars in the sample are associated with a known debris disc (Table A.2). We find that 35 out of those 76 debris discs have at least a non-photospheric narrow feature (Table A.3 and Table 2.4), and 15 among these 35 debris disc stars plausibly have at least one CS component - this figure does not include stars with an ambiguous origin of the detected non-photospheric absorptions. Stable CS features at the velocity of the star have been interpreted as proof of a CS gas disc, and its persistence requires the presence of a braking mechanism that prevents the hot gas from being blown away by the strong radiation pressure from the star (e.g. Lagrange et al., 1998). Fernández et al. (2006) suggested that in β Pic such mechanism could be exerted by the observed enhanced carbon abundance (see also Roberge et al., 2006; Brandeker, 2011), a fact also suggested for HD 9672 (Roberge et al., 2014). Among the stars in our sample with stable features, in addition to HD 9672 and HD 36546 (see section 4.2), that scenario might be at work for HD 32297, where a carbon overabundance is suggested by the the 3.7σ Herschel detection of [C II] emission at 158 μm (Donaldson et al., 2013).

Concerning variable absorptions, 12 debris disc stars have shown at least variability either in the Ca II H&K lines or in the Na I D lines (Table 2.4 and Table 2.2); all these stars are younger than 200 Myr. In all cases, but HD 37306, transient red- or blue-shifted events attributed to exocomets have been observed. The observed variability in HD 37306 is due

Table 2.4: Debris disc stars in the sample with narrow non-photospheric features. Bold-faced stars have features of CS origin, and those in italics also have variable absorptions. HD 110411 and HD 183324 do not have narrow absorptions but have CS gas.

HD 3003	HD 118232	HD 146897
HD 5267	HD 125162	HD 147137
HD 9672	**HD 131488**	***HD 156623***
HD 21620	HD 131835	**HD 158352**
HD 32297	HD 138813	***HD 172555***
HD 36546	HD 142315	**HD 181296**
HD 37306	HD 144587	***HD 182919***
HD 71043	HD 144981	***HD 183324***
HD 71722	HD 145554	HD 188228
HD 105850	HD 145631	HD 198160
HD 109573	**HD 145689**	HD 221756
HD 110058	***HD 145964***	
HD 110411	HD 146606	

to the appearance, and later disappearance, of a strong shell spectrum (see above). Complementary to these results, the rest of the stars with variable features listed in Table 2.2, i.e. 14 stars, do not host a debris disc, and are older than 200 Myr. We point out, however, that in four cases - HD 39182, HD 64145, HD 132200, and HD 138629 - there is no observational information concerning the potential presence of a debris disc, and in two cases - HD 132200 and HD 138629 - we do not have information about their age.

In parallel, to our knowledge 36 out of the 76 debris discs have been spatially resolved after the compilations by N. Pawellek and A. Krivov[4], and C. McCabe, I.H. Jansen, and K. Stapelfeldt[5]. Further, 28 out of those 36 resolved debris disc stars have spectral types earlier than F2 and, therefore, sensitive to show the presence of exocometary signals. Also, Moór et al. (2017) reported inclinations for the A1 stars HD 121617 and HD 131488. Table 2.5 lists the early-type 30 resolved debris discs together with their corresponding inclination angles, taken from the mentioned catalogues. Among the resolved discs, 17 have non-photospheric features (Table 2.5). In 6 cases the absorption features are more plausibly interstellar or ambiguous - HD 71722, HD 125162, HD 131835, HD 138813, HD 146897, and HD 188228. In 11 stars, a CS origin seems to be the most reasonable one, for at least one of the observed non-photospheric absorption features; 8 out of these 11 stars have variable absorptions. Although based on a relatively low number of objects, an inspection of the inclination angles in Table 2.5 reveals: i) there is no a preferential distinction between discs seen edge- or polaron for those debris discs without non-photospheric absorptions; ii) similar result is seen for

[4]https://www.astro.uni-jena.de/index.php/theory/catalog-of-resolved-debris-disks.html
[5]https://www.circumstellardisks.org/

Table 2.5: Resolved debris discs and inclination angles. Bold-faced are those with narrow non-photospheric absorption features while those in italics have at least one component attributed to a CS origin. HD 110411 and HD 183324 do not have narrow absorptions but have CS gas.

Star	i^o	star	i^o	star	i^o
HD 9672	79	**HD 71722**	78	***HD 131488***[2]	82
HD 14055	83	HD 74873	27	**HD 131835**	75
HD 15115	80	HD 95418	84	HD 139006	80
HD 21997	26	HD 102647	30	***HD 138813***	28
HD 27290	69	HD 109085	35	**HD 146897**	84
HD 28355	76	***HD 109573***	76	***HD 156623***	30
HD 31295*,[1]		***HD 110058***†	50	***HD 172555***	75
HD 32297	90	*HD 110411*	70	***HD 181296***	90
HD 36546	75	HD 121617[2]	37	*HD 183324*	2
HD 38206	60	**HD 125162**	48	**HD 188228**	49

(*) resolved debris disc with unreported inclination angle; (†) Kasper et al. (2015) report an edge-on inclination. (1) Draper et al. (2016); (2) Moór et al. (2017)

those stars with ISM features; and iii) the trend is clearly different when we inspect debris discs with CS absorptions, i.e., most of them are clearly seen at $i > 70^\circ$ ($\sim 72\%$), and this trend is reinforced when only those discs with variable features are considered. In other words, debris discs associated with stars hosting CS absorptions tend to be seen edge-on, while debris discs associated with stars without non-photospheric absorptions or stars with ISM features do not show a preferential inclination. This result is consistent with the fact that the detection of CS features, i.e. hot gas, is favoured when the systems are seen close to edge-on, as well as with the large projected rotational velocities shown by the stars with CS gas compared to those without such gas. We note that the observed trend, which is just a geometrical effect, does not exclude the existence of hot gas, i.e. the eventual existence of comet-like bodies around the debris discs systems seen away from edge-on. A similar trend was already pointed out by Rebollido et al. (2018)(Chap. 3) in their analysis of debris discs with measurable amounts of cold gas seen in emission in the far-IR and (sub-) mm wavelength regimes.

2.5.2 Near infra-red excesses

There are 22 stars (Table A.2) in our sample explicitly taken from the literature searching for hot excesses in the H (1.6 μm) and K(2.2 μm) bands (Table A.2). In addition, HD 172555 also presents such excess (Absil et al., 2013; Ertel et al., 2014, 2016; Nuñez et al., 2017). Within the stars in our sample with near-IR excesses plausibly due to hot dust (i.e., excluding stars where binarity is the cause of the excess), 11 stars have spectral types earlier than F2, and 6 out of those 11 stars present non-photospheric features, either detected in this work or

Table 2.6: Stars showing near-IR excesses.

Name	Non-photospheric absorption	H/K excess
HD 2262	Yes*(1)	(2)
HD 28355	No	(2)
HD 40136	No	(1)
HD 56537	Yes(2)	(1)
HD 102647	No	(1)
HD 108767	Yes(2,3)	(2)
HD 172555	Yes(3,4)	(2)
HD 177724	Yes(3)	(1,3)
HD 187642	No	(1,3)
HD 203280	No	(1)
HD 210418	Yes(3)	(3)

*Not clear if exocomet-like or stellar mass loss events. References for non-photospheric absorptions: (1): Welsh & Montgomery (2018); (2): Welsh & Montgomery (2015); (3) This work ; (4) Kiefer et al. (2014a). References for H/K excess: (1): Absil et al. (2013), (2): Ertel et al. (2014), (3) Nuñez et al. (2017)

in previous ones (Table 2.6).

To assess the significance of the incidence of CS absorption around hot dust stars we consider all reported 31 near-IR excess stars (Absil et al., 2013; Ertel et al., 2014; Nuñez et al., 2017). Excluding the binaries, 14 stars - the 11 studied by us plus Vega, β Pic, and HD 210049 (μ PsA) - have spectral types earlier than F2. Among those 14 stars, 5 have variable absorptions features (HD 2262, HD 56573, HD 108767, HD 172555, and β Pic); 2 stars have an ambiguous CS/ISM narrow feature (HD 177724, and HD 210418); 2 stars are associated with pole-on debris discs (HD 102647 and Vega), i.e. an unfavourable orientation to detect CS features; 1 star (HD 28355) has a resolved debris disc with an inclination angle $i = 70^{\circ}$, but our spectra do no reveal any non-photospheric absorption; for the last 4 stars (HD 40136, HD 187642, HD 203280, and HD 210049) the orientation of the system is unknown. If we assume random orientations, the probability to observe a system with an inclination larger than 65°–70°, i.e., edge-on or close to it, lies between $\sim$42% and 34%, respectively, which is similar to the percentage of stars with hot CS gas among the hot dust stars. We also note that it agrees with the percentage of edge-on discs, either debris or other type of disc, that can be found in the Catalogue of Resolved Discs compiled by C. McCabe, I.H. Jansen, and K. Stapelfeldt. Given those figures, a relationship between hot dust and hot CS gas is suggested, which should be confirmed by increasing the sample of stars with the appropriate near-IR interferometric and UV/optical spectroscopic data.

Table 2.7: Shell stars. Stars with non-photospheric CS features are bold-faced while those with variability are emphasised.

Star	Star	Star
HD 256	***HD 50241***	***HD 148283***
HD 21688	HD 77190	***HD 158352***
HD 37306	***HD 85905***	**HD 168646**
HD 39182	***HD 98058***	**HD 192518**
HD 39283	HD 118232	HD 196724
HD *42111*	***HD 138629***	***HD 217782***

2.5.3 Ti II / Shell stars

In addition to the stars selected on the basis of their Ti II lines, there is a number of stars which have been classified as shell stars (Abt, 2008; Lagrange-Henri et al., 1990d; Hauck & Jaschek, 2000; Roberge & Weinberger, 2008). Table 2.7 lists, according to our knowledge, the shell stars in our sample. No Ca II or Na I non-photospheric absorptions are observed towards HD 39283 and HD 77190; in the cases of HD 118232 and HD 196724 the origin of the Ca II absorption is likely ISM or ambiguous. As a matter of fact, the spectra of these four stars do not reveal any prominent shell-like characteristics. The rest of the stars show triangular-like CS absorptions (bold-faced in the table) - those stars with variable features are also emphasised. Not all absorptions can be attributed to FEB-like events; for example, the stable absorption seen towards HD 192518 is clearly formed in a gaseous shell, while as already mentioned the variability in HD 37306 is due to the appearance/disappearance of a shell around this star. Nonetheless, 11 stars do present variable events, most of them attributable to exocomets; even, our spectra might be tracing their dynamical evolution of some events by changing their depths and velocities.

2.5.4 λ Boo stars

The sample contains 12 objects previously classified as λ Boo type stars (Table 2.8) although three of them - HD 39283, HD 210418, and HD 217782 - have recently been considered as non-members of this stellar class (Murphy et al., 2015b,and references therein). Several criteria have been used to classify λ Boo stars (e.g. Murphy et al., 2015b; Gray et al., 2017); among them, optical line ratios between volatiles, like CNO, and heavier elements (e.g. Mg) are useful to ascribe stars to this stellar class (Cheng et al., 2017). This criterion is based on the basic definition of the λ Boo stars, i.e. stars with a remarkable low abundance of heavy (e.g. Fe, Al, Mg) elements while volatiles as CNO have near solar abundances (Baschek & Slettebak, 1988,e.g.). In order to eventually find new λ Boo candidates, we have measured in all stars earlier than F2 in our sample the ratio of the Mg II 4481 Å and the O I 7774 Å triplet, which are strong and easy to measure in our spectra.

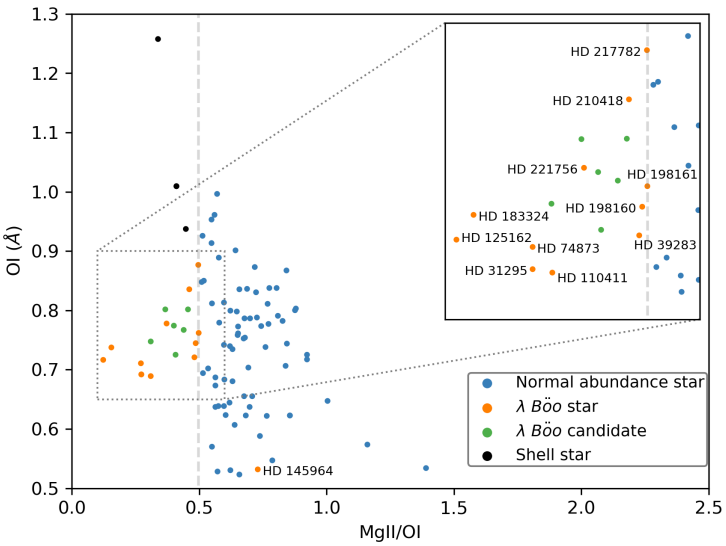

Figure 2.25: Ratio O I (7744 Å) and Mg II (4481 Å) versus the EW of O I. Orange dots mark stars previously classified as λ Boo stars; green dots mark new λ Boo candidates; and blue dots mark the stars with normal abundances. The vertical dashed line delimits the locus of bona fide λ Boo stars (see text).

Fig. 2.25 is a plot of the EW of the O I line versus the ratio of Mg II to O I lines. All identified λ Boo stars in the sample are clearly located to the left in that plot, well separated from the bulk of the stars. The exception is HD 145964 classified as *weak* λ Boo by Welsh & Montgomery (2013) based on the measurements of Abt & Morrell (1995). The identified λ Boo stars have low metallicities ([Fe/H] ¡ –0.25) excluding HD 145964 and HD 217782. A vertical dashed line at MgII /O I¡ 0.49 marks the limit for the identified λ Boo objects in our sample. This figure is the one for the λ Boo stars HD 198160 and HD 198161, and approximately the one for those removed from the class by Murphy et al. (2015b) stars. We note that 6 stars are additionally located at similar locations in Fig. 2.25 as the λ Boo stars, and they also have low metallicities (Table A.1). We consider that those stars are new candidates, Table 2.8. In addition, 3 shell stars -HD 39182, HD 42111, and HD 168646 - have low Mg II/O I ratio but a very high EW (O I), and metallicities ¿0.0.

With respect to the presence of non-photospheric narrow and/or variable features, 15 out of the 18 λ Boo stars (including the new candidates) listed in Table 2.8 present evidences of non-photospheric gas in their spectrum; in 5 cases the feature is interstellar, in 2 cases the origin is ambiguous; the rest of the stars, 8 stars (44% of the λ Boo stars), have exocometary-like events. Comparing this figure to the 26% incidence of exocometary-like events of the whole sample, there seems to be an enhanced probability for λ Boo stars to have such events. A connection between metal-poor stars and the presence of debris discs or remainings of planet formation processes has been suggested before in the literature (Jura, 2015; Murphy & Paunzen, 2017), as heavier elements are blown away by radiation pressure, while volatile

Table 2.8: EW of the Mg II 4481 Å and O I 7744 Å lines of previously known λ Boo stars, together with stars of the sample with similar characteristics. The new λ Boo candidates are indicated.

Star	EW Mg II (Å)	EW O I (Å)	λ Boo
HD 31295	0.188	0.692	Yes
HD 32297	0.336	0.767	New
HD 36546	0.231	0.748	New
HD 39182	0.413	1.010	Shell
HD 39283	0.347	0.720	Yes
HD 42111	0.424	1.258	Shell
HD 71722	0.294	0.802	New
HD 74873	0.192	0.711	Yes
HD 110058	0.310	0.774	New
HD 110411	0.213	0.689	Yes
HD 125162	0.087	0.717	Yes
HD 145964	0.388	0.532	Yes
HD 156623	0.366	0.802	New
HD 168646	0.418	0.937	Shell
HD 177724	0.294	0.726	New
HD 183324	0.114	0.738	Yes
HD 198160	0.362	0.745	Yes
HD 198161	0.378	0.762	Yes
HD 210418	0.385	0.836	Yes
HD 217782	0.435	0.877	Yes
HD 221756	0.289	0.778	Yes

elements are accreted onto the star (see Draper et al., 2016,and references therein). Therefore, exocomets represent a rather likely scenario, that could replenish the atmosphere of λ Boo stars of C, N, O and S elements.

2.5.5 Dependency on the stellar properties

All the detections of gas reported in this work are around A-type stars, in accordance with the literature. The high-rotational velocities, leading to wide spectral lines in earlier spectral types, could explain why it is easier to find variability in the bottom of photospheric lines. But this does not explain the lack of detections around B and O types. Furthermore, it has been argued that A-type stars host a richer environment, with a plethora of minor bodies and dust, favouring the presence of star-grazing bodies. However, studies like Eiroa et al. (2013); Montesinos et al. (2016) have shown that a fraction of FKG main sequence stars ($\sim$ 22%) also host debris discs, including material that could originate exocometary signals. Therefore, a richer environment is not the only condition that warrants the detection of exocomets.

Thus, before rulling out an observational bias we aim to explore the possibility that the properties of the system could be preventing or facilitating the presence of small bodies in the sublimation regions, close to the star.

Sizes

The smallest bodies in planetary systems are not hold by gravity, but rather by the yield strength of the material, that is, the force of gravity does not overcome the strength (i.e. the resistance of the material to undergo deformations) of the material in these bodies.

For the body to be spherical with radius r we need the overburden pressure to exceed the compressive yield strength, and therefore the pressure needs to be high enough so that the material deforms plastically. Following Lineweaver & Norman (2010), if we define the overburden pressure at radius r ($P(r)$), as that generated by the gravity over r ,

$$P(r) = \frac{2\pi}{3} G\rho^2 (R^2 - r^2) \tag{2.1}$$

where r is the radius where we evaluate the pressure, R is the radius of the body, G is the gravitational constant, and ρ is the density. Equallying Eq. 2.1 at half radius to the compressive strength σ_y,

$$P(r \approx R/2) = \sigma_{\rm y} \tag{2.2}$$

we can determine the maximum irregular radius that a self-gravitating body could have.

$$R_{\rm irr} = \frac{2\sigma_{\rm y}}{\pi G \rho^2} \tag{2.3}$$

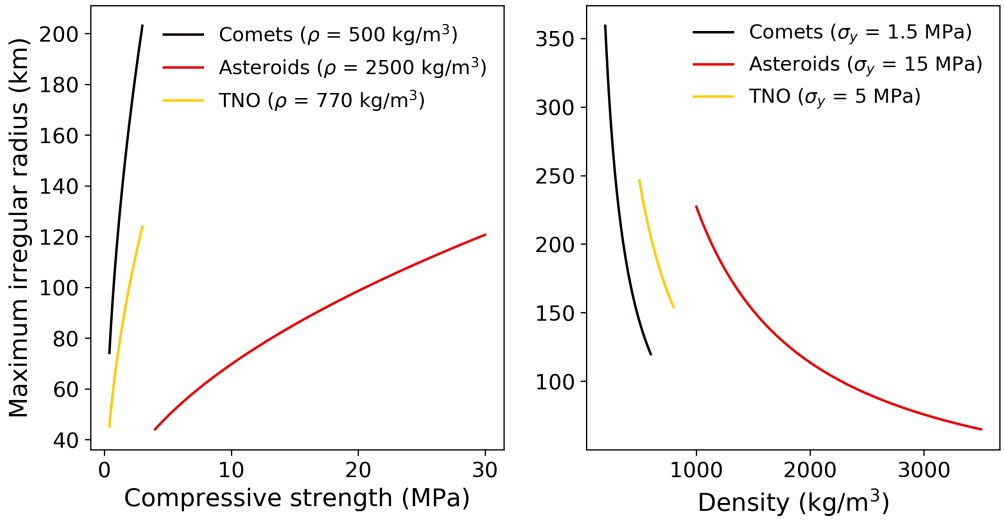

Figure 2.26: Maximum irregular (or minimum spherical) radius versus the compressive strength of the material (left) and densitiy (right). Different colours correspond to different types of bodies: comets (black), asteroids (red) and Trans Neptunian Objects (TNOs, yellow).

In Fig. 2.26 we explore the expected sizes for different objects with different compositions. Densities have been taken from Britt et al. (2006) and the yield strengths from Lineweaver & Norman (2010). We have made a distinction for three different cases: asteroids, comets and trans-neptunian objects (TNOs). All these are classified as small bodies, but have slightly different compositions, particularly when considering the amount of ices present, and the porosity of the materials (see e.g. Brown, 2012; Carry, 2012; Britt et al., 2006). From Eq. 2.3 we can see that the irregular radius is highly dependent on the yield strength and the density of the body with both being highly dependent on the composition of the material. Moreover, the inverse relation between the radius and the density implies that when the body contains large amounts of ice, a larger radius is needed to reach a spherical shape, as it is the case for comets.

Fig. 2.26 shows the range of sizes obtained for the different bodies. Due to the lower densities in comets, their maximum irregular size is the largest. There is a considerable difference between both panels of the figure, possibly due to the difficulties of properly estimating the yield strength of the material. Even so, the results are consistent with the sizes of comets ($\sim$ 200 km) observed in the solar system.

Temperatures

If we assume that the bodies are not self-gravitating, the compressive yield strength is the dominant force holding these minor bodies together. To determine how much mass of water ice –assuming that it is the most abundant volatile– is sublimated, we first need to get an approximation to the temperature reached by the cometary body at the distance from the star, that will be the equilibrium temperature $T_{\rm eq}$,

$$T_{\rm eq} = \left(I_\star \times \frac{(1 - A_{\rm g})}{4\sigma} \right)^{\frac{1}{4}} \tag{2.4}$$

where $A_{\rm g}$ is the geometric bond albedo, σ is the Stefan-Boltzmann constant and $I_\star$ is the intensitiy of the stellar radiation, obtained from:

$$I_\star = \frac{L_\star}{4\pi d^2} \tag{2.5}$$

for a body located at a distance d of a star with luminosity $L_\star$.

If we take the value estimated for Hale-Bopp ($A_{\rm g}$ = 0.04) as a typical albedo for comets, we can estimate using the luminosities for the different spectral types in the main-sequence, the variation of the equilibrium temperature with the distance to the stellar surface. These are shown in Fig. 2.27.

Now we consider the sublimation latent heat for water (L_{H_2O}) from (Rogers & Yau, 1989),

$$L_{\rm H_2O} = 2834.1 - 0.29 \times T - 0.004 \times T^2 \tag{2.6}$$

The latent heat is negative for temperatures below T = 806.29 K, which means that for higher temperatures the sublimation process becomes exotermic, and therefore all the water will be in the gas phase. According to Eqs. 2.1 and 2.5, this temperature corresponds to a stellar luminosity of 7×10^4 $L_\odot$ (B-type) at 100 AU. For larger luminosities, or closer distances, water is no longer in solid state on the surface of a comet (grey line in Fig. 2.27).

The latent heat for sublimation of water can be used to calculate the mass loss rate ($\dot{m}$) of water per unit of area and time (Steckloff et al., 2015) as,

$$m_{\rm H_2O} = (1 - A_{\rm g}) \frac{I_\star}{L_{\rm H_2O}} \tag{2.7}$$

As they evaporate, water molecules will be thermalized, and reach a velocity consistent with the Boltzmann distribution,

$$v_r \simeq \sqrt{\frac{3k_{\rm B}T_{\rm eq}}{m_{\rm H_2O}}} \tag{2.8}$$

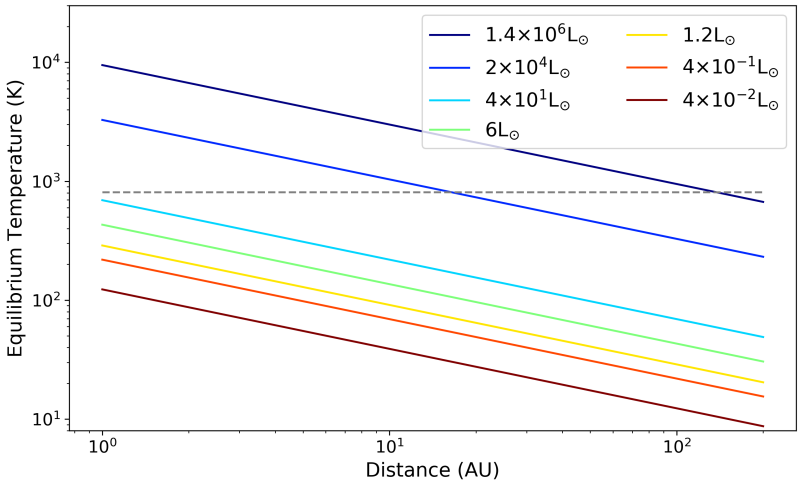

Figure 2.27: Equilibrium temperature for a body with the typical albedo, 0.04, of cometary bodies in the solar system plotted against the distance to the stellar surface. T_{eq} has been computed for different luminosities considering spectral types between O ($L_\star \sim 1.4\times 10^6$ $L_\odot$) to M ($L_\star \sim 4\times 10^{-2}$ $L_\odot$) (colour codes are shown in the legend). The grey dashed line marks the maximum surface temperature for water sublimation.

where k_B is the Boltzmann constant, T_{eq} is the temperature from Eq. 2.4, and m_{H_2O} is the water mass lost, as obtained from Eq. 2.7.

Water sublimation is a mechanism capable to drag the dust in the surface. Thus, if we assume that the sublimated water carries an amount of dust of $\sim 20\%$ of its mass as it leaves the surface of the comet (from the estimations from Fink & Rubin, 2012, for 67P/Churyumov-Gerasimenko), and considering $M_{\mathrm{Ca\,II}} \simeq 0.01\ M_{\mathrm{dust}}$ (Beust et al., 1990), we can estimate the mass of Ca II, the most common exocomet tracer, for different luminosities.

Figure 2.28 shows the evaporation rate of water (solid line) and ionized calcium (dashed line). The result obtained for a G-type star (yellow line, $L_\star \sim 1\ L_\odot$) is consistent with the mass loss rates given by Fink & Rubin (2012) for comets in the solar system, if we assume a size of 100-200 km for the sublimating body, and only half of the area is releasing gas ($\sim$ 100 kg/s). There is no water sublimation in the inner region of the systems for O and B-type stars ($L_\star \gtrsim 10^4\ L_\odot$), preventing transits deep enough to be detected in photometry or spectroscopy. In order for the transits to be detectable, the evaporation distances should lie within 1 au from the star (see e.g. Kiefer et al., 2014b). For F-type ($L_\star \sim 6\ L_\odot$), the production of dust drops to 5% of that of A-type ($L_\star \sim 40\ L_\odot$), where exocomets are detected in spectroscopy. Therefore, this simple estimate points that the most favourable conditions for detection of Ca in the spectra are found around A stars.

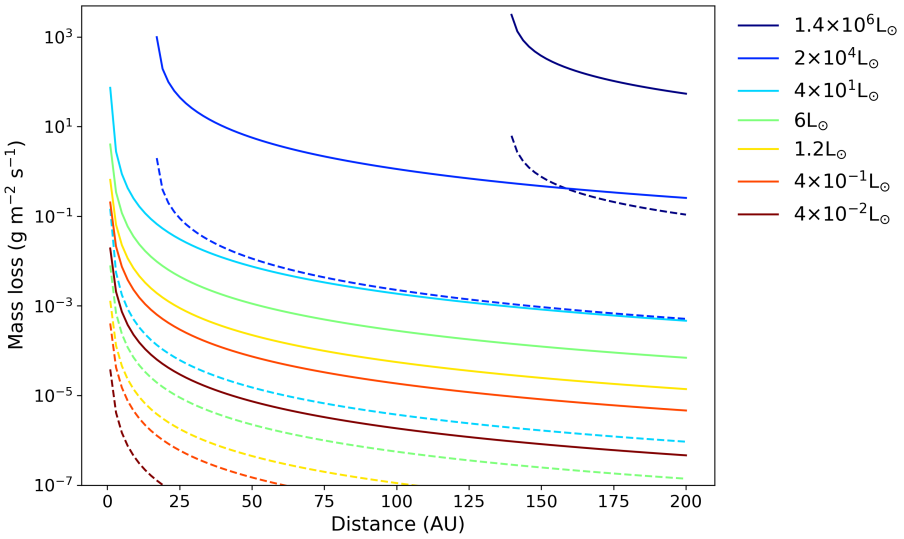

Figure 2.28: Evaporation rate per unit of area and time, for different luminositites plotted against the distance to the star. For large luminosities and small distances, all water is already sublimated, and therefore there is no mass loss. Solid and dashed lines show the mass loss of water and Ca, respectively.

Tidal gravitational disruption

The passing of a small body close to a large planet or its host star, might lead to gravitational disruption, causing the release of gas and dust, that could also be detected as an exocometary variable absorption. We obtain the maximum distance from the star (or planet) before disruption of the small body, $d_{\rm tidal}$ from Raymond et al. (2018b),

$$d_{\rm tidal} \approx R \left(\frac{M_\star}{m} \right)^{1/3} \tag{2.9}$$

where $M_\star$ is the mas of the main gravitational body, and m and R are the mass and radius of the small body.

We have explored the tidal distance dependency with different stellar masses and small bodies densitites, and obtained the results showed in Fig. 2.29. Each color line represents different stellar spectral types (marked as masses in the figure), and vertical lines indicate the radius of the star for each mass. Horizontal lines correspond to the densities of comets (solid), asteroids (dashed) and TNOs (dotted). For larger stars, i.e., O and B-type ($M_\star \gtrsim 10$ $M_\odot$), the disruption process will not take place for densities above 750 kg/m^3, correspondent to TNOs, as they will be engulfed first. This is also the case for $M_\star \gtrsim 20$ $M_\odot$ (O-type stars) and cometary densities. For stars cooler than A-type ($M_\star < 1.5$ $M_\odot$) bodies within the densities range considered will suffer gravitational tidal disruption, and therefore could originate a cloud of material that would be observed as a transient absorption in the spectra.

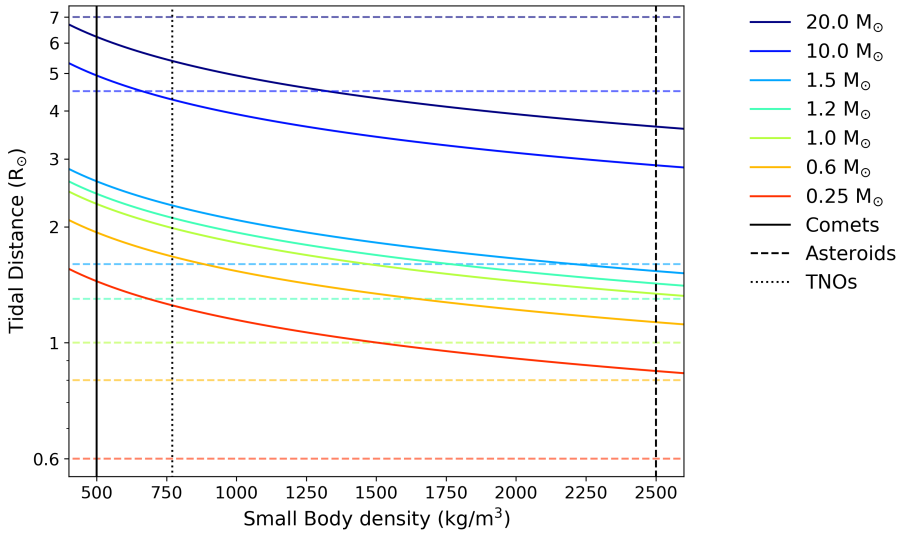

Figure 2.29: Tidal distance for disruption versus density of the small body. Different line colous represent different spectral types. The horizontal lines correspond to different densities for comets, asteroids and trans neptunian objects (TNOs). The vertical lines indicate the radius of the stars for different stellar masses.

Overall, there are hints of a possible connection between the stellar properties and the sublimation of material, but this deserves further and intensive study, that we intend to continue in the near future.

2.6 Conclusions

We have presented the observational results of a systematic study aiming at detecting and monitoring hot gas attributed to the presence of exocomets in the CS environment. The study has been based on the analysis of the Ca II K&H and Na I D lines in a heterogeneous and biased sample of 117 main-sequence late B to G type stars. This is the largest systematic study searching for exocomets carried out so far. The main results are the following:

Narrow non-photospheric ISM or CS absorptions have been detected towards ∼50% of the sample (60 stars). Among the stars with those absorptions, at least one of the detected narrow features can be attributed to CS gas in 30 objects, i.e., 26% of the whole sample. This figure is not statistically significant as the studied sample included stars with previously detected CS gas, but it does show that gas in the CS environment of A-type stars is relatively common. In some stars, the gas is originated in a CS shell surrounding the stars; in some other cases, the narrow absorptions can be attributed to the evaporation of exocomets or to gas released by dust grain collisions or evaporation.

Sporadic red-shifted, and in a less degree blue-shifted, events that can be attributed to β

Pic-like exocomets have been found in the CS environment of 18 stars, out of which 6 are new to the literature. In a few cases, our spectra seem to trace the dynamical evolution of such events as suggested by changes in their velocity and depth. Nonetheless, the exocometary-like activity in our stars, maybe with the exception of ϕ Leo (see Eiroa et al., 2016, and Chap. 4), is very poor compared with β Pic, which remains a unique object.

The variability of the CS features in HR 10 is mainly due to the binary character of this star. A detailed analysis was carried out in a separated paper (**?**).

In the particular case of HD 37306, our spectra have witnessed the appearance and disappearance of a strong shell around this star. There are no hints in our data of exocometary events in this star, although we point out that some shell stars in our sample do show such events.

Hot CS gas is only detected towards stars earlier than A9, in line with previous works. The F2 V star η Crv is the only star for which β Pic-like events with a 2.9σ detection have been claimed (Welsh & Montgomery, 2019). This paucity in detecting exocometary events around late type stars might be due to the inability of spectroscopy to detect faint non-photospheric absorptions on top of cool photospheres. In this respect, photometric transits have demonstrated to be competitive and successful in detecting exocomets around late type stars.

Hot gas-bearing main sequence stars have distinctly higher projected rotational velocities, and spread over a large range of ages, from $\sim$10 Myr up to at least $\sim$1 Gyr. Some of them are also known to present δ Scuti pulsations, as β Pic itself.

Exocometary-like events are often associated with edge-on debris disc stars, in particular towards those with cold gas (see also Rebollido et al., 2018, Chap. 3). This result is interpreted as a geometrical effect, but it does suggest that debris disc stars with non-photospheric absorptions (i.e. hot gas) are excellent targets to search in the far-IR and (sub-)mm spectral range for the presence of cold gas released by the evaporation of solid bodies at distances relatively far from the central star. We note that not all stars with FEB-events are associated with a debris disc. It cannot be excluded that this is due to the current, limited sensitivity to detect debris discs, $L_{dust}/L_{*} \sim 10^{-6}$.

We find that FEB-like events are detected towards 17% of stars with near-IR excesses denoting the presence of hot exozodies. Both hot dust and gas might be related phenomena, although more observations are needed to confirm or deny the trend pointed out in our study.

Our sample includes 18 λ Bootis stars, with 6 new candidates found in this work. A relevant fraction of them, 8 out the 18 stars, have FEB-like events, suggesting again that both phenomena could be related.

Chapter 3

The co-existence of hot and cold gas in debris discs

This chapter is based on the paper:
"The co-existence of hot and cold gas in debris discs"
by I. Rebollido et al.
published in A&A 614, A3 (2018)

3.1 Introduction

Debris discs are second-generation dusty discs produced by collisions among planetesimals leftover from planet formation. They are observationally characterised by the thermal infrared excess observed in main-sequence stars (e.g. Backman & Paresce, 1993; Wyatt, 2008,and references therein). Debris discs have been described as gas-poor discs, since in contrast with the "canonical" gas-to-dust ratio 100:1 in primordial discs, that ratio, although unconstrained, should be significantly lower (Liseau, 2003; Matthews et al., 2014). However, following the first detection of CO in β Pic (Vidal-Madjar et al., 1994; Roberge et al., 2000; Dent et al., 2014), and in 49 Ceti (Zuckerman et al., 1995; Hughes et al., 2008), a number of cold-gas-bearing debris-disc systems - currently 17 objects to our knowledge - have been detected through emission lines of O I, C I, C II and CO at far-infrared (FIR) and (sub-)millimetre wavelengths, mainly thanks to Herschel, APEX, JCMT and ALMA (e.g. Moór et al., 2011a, 2015a, 2017; Riviere-Marichalar et al., 2012, 2014; Roberge et al., 2013; Donaldson et al., 2013; Cataldi et al., 2014; Dent et al., 2014; Greaves et al., 2016; Lieman-Sifry et al., 2016; Marino et al., 2016). We note, nevertheless, that the CO emission associated with η Crv requires confirmation (Marino et al., 2017). The gas in emission detected in these 17 stars is cold, T $\sim$ 10-20 K, and located at distances from tens to more than 100 au from the central star. It is also remarkable that numerous optical emission lines of Ca II, Na I, Fe I, Cr I+II, Ti I+II, and other metals, were detected towards the archetypical β Pic debris disc

(Olofsson et al., 2001; Brandeker et al., 2004). A detailed analysis of the optical data by those authors reveals that the optical atomic gas seen in emission is in Keplerian rotation and coexisting with the dust.

Stars with debris discs bearing cold gas tend to be young (ages <50 Myr), but at least two of them, Fomalhaut and η Crv, are significantly older; $\sim$ 400 and $\sim$ 1400 Myr, respectively (Mamajek, 2012; Marino et al., 2017). Most of them, 14 out of 17, surround A-type stars - the three remaining objects are F-type stars. All 17 systems have high fractional dust luminosities compared to other debris discs, $L_{\rm dust}/L_{\star} > 10^{-4}$ (e.g. Kennedy & Wyatt, 2014; Thureau et al., 2014; Moór et al., 2017,and references therein); and their spectral energy distributions (SEDs) have been fitted with two-temperature (warm and cold) components (e.g. Ballering et al., 2013; Melis et al., 2013; Chen et al., 2014; Kennedy & Wyatt, 2014; Thureau et al., 2014; Cotten & Song, 2016; Ballering et al., 2017). One exception is HD 172555, where only a warm component is present, at least up to the current detection limits (e.g. Riviere-Marichalar et al., 2012; Thureau et al., 2014).

The origin of the cold gas is a matter of debate. In the cases of HD 21997 and HD 131835 the gas could predominantly be a remnant of the primordial protoplanetary disc (Kóspál et al., 2013; Moór et al., 2015a). However, in most cases, for example, β Pic or HD 181327 (Matrà et al., 2017; Marino et al., 2016), the observed gas most likely has a secondary origin. In primordial discs, CO is maintained against photodissociation as long as self-shielding is high enough to maintain a substantial CO mass, but the relatively low content of gas in the cold-gas-bearing debris discs suggests that self-shielding is low, and CO should be photodissociated on timescales of hundreds of years (van Dishoeck & Black, 1988; Roberge et al., 2000; Moór et al., 2011a), requiring therefore a continuous replenishment to explain the observed emission in debris discs. A variety of physical processes have been proposed to explain the secondary origin of the cold gas, all of them in some way related to the presence of planetesimals - vaporization of solids in dust-dust collisions, photon-stimulated desorption of dust, collisions of volatile-rich dust grains, and outgassing of comet-like objects. Those mechanisms could even operate concurrently to explain the observed amount of gas (Matthews et al., 2014,and references therein).

In parallel, thanks to the favourable edge-on orientation of the β Pic disc, stable and variable UV/optical absorption features in metallic lines have been known for several decades (Slettebak, 1975; Kondo & Bruhweiler, 1985; Hobbs et al., 1985; Ferlet et al., 1987; Lagrange-Henri et al., 1988; Roberge et al., 2000). The variable, transient events, mainly traced in the Ca II K line (λ 3933.66 Å), appear red- and, to a much less degree, blue-shifted with respect to the radial velocity of the star, and might vary on timescales as short as hours. They have been interpreted as due to the gas released by the evaporation of exocomets grazing or falling onto the star, *the Falling Evaporating Bodies* scenario or FEBs (Ferlet et al., 1987; Beust et al., 1990; Kiefer et al., 2014b); Those FEBs would have been driven into the vicinity of the star by the perturbing action of a larger body, a planet (Beust et al., 1991; Beust & Morbidelli, 2000). Similar transient absorption events have been observed towards more than 20 A-type stars (e.g. Redfield et al., 2007; Roberge & Weinberger, 2008; Kiefer et al., 2014a; Welsh

& Montgomery, 2015; Eiroa et al., 2016; Welsh & Montgomery, 2018, and see Chap. 4). Related to this, evidence of exocomet transits based on Kepler light curves of the F2 V stars KIC 3542116 and KIC 11083727 have recently been presented by Rappaport et al. (2018).

With respect to the stable absorption in β Pic, in addition to the Ca II H&K lines at the core of the photospheric lines that share the radial velocity of the star, similar absorption features appear in UV/optical lines of elements such as C, O, Na, Fe, and many other metallic species (Vidal-Madjar et al., 1994, 2017; Lagrange et al., 1998; Brandeker et al., 2004; Roberge et al., 2006). This gas would be located at distances of $\sim$ 0.5 au, would be relatively hot with temperatures of $\sim$ 1000–2000 K (Hobbs et al., 1988; Beust et al., 1998; Vidal-Madjar et al., 2017), and could be generated by evaporation of comet-like bodies or dust grains in the disc (Fernández et al., 2006). However, this hot gas should rapidly be blown away by the strong radiation pressure from the star unless a braking mechanism is at work. Fernández et al. (2006) have suggested a solution to this problem, showing that the gas affected by the radiation pressure is largely ionised and couples into a single ionic fluid. As a consequence, the radiation pressure is reduced and the fluid could be self-braking if it has enhanced carbon abundance. Such a scenario is supported by the observed overabundance of C in β Pic (Roberge et al., 2006; Brandeker, 2011). A similar mechanism could be acting in the case of 49 Ceti (Roberge et al., 2014).

This work presents high-resolution optical spectra of the currently known cold-gas-bearing debris-disc stars. Our aim is to search for signposts of hot gas, which would suggest the presence of close-in cometary-like material around those stars. Thus, the analysis is mainly centered on the Ca II K (λ 3933.66 Å) line as it is the most sensitive one to trace both transient and stable absorptions, but we also refer to the Ca II H (λ 3968.47 Å) and Na I D ($\lambda\lambda$ 5889.95/5895.92 Å) lines. The spectra have been obtained in the working frame of a large survey aiming at detecting and monitoring cometary-like absorption events in a sample of main-sequence stars, most of them A-type but also some FG-type (Chap. 2).

3.2 Observations

High-resolution optical spectra of 15 out of the currently known 17 cold-gas-bearing debris-disc stars were obtained with several fibre-fed high-resolution spectrographs and telescopes located at different observatories (Table 4.1) . Namely, the spectrographs HERMES at Mercator and FIES at NOT (Roque de Los Muchachos, La Palma, Spain), FEROS at MPG/ESO 2.2 m (La Silla, Chile), and HEROS at the robotic telescope TIGRE (La Luz, Mexico). A series of observing runs were carried out at each telescope: Mercator (2015 September/December; 2016 January/March/July; 2017 March/April), NOT (2016 January/July); MPG/ESO 2.2 m (2015 October; 2016 March; 2017 April); TIGRE (2015 September/November). The number of spectra per star and telescope is given in Table 4.1; a more detailed log with the specific dates (UT) of the observations of each star and the corresponding instrument is given in Appendix D. Spectral range and resolution of the different

Table 3.1: Log of observations. Number of spectra per instrument and signal-to-noise ratio (S/N) in brackets of the median spectra.

Star	Number of Spectra (S/N)
HD 9672	31 H (296) + 7 FI (161)
HD 21997	13 H (133) + 3 FE (281) + 9 HE (130)
HD 32297	15 H (98), 4 FI (97)
HD 109085	3 H (85)
HD 110058	8 FE (280)
HD 121191	1 FE (90)
HD 121617	2 FE (103)
HD 131488	2 FE (110)
HD 131835	13 FE (390)
HD 138813	20 H (205) + 13 FE (447) + 4 FI (102)
HD 146897	2 H (7) + 4 FE (112)
HD 156623	13 FE (314)
HD 172555	17 FE (380)
HD 181296	16 FE (373)
HD 181327	5 FE (241)

H: HERMES; FE: FEROS; FI: FIES; HE: HEROS.

spectrographs are: HERMES, spectral resolution R$\sim$85000 covering the range $\lambda\lambda$ $\sim$370–900 nm (Raskin et al., 2011b); FIES, R$\sim$67000 covering $\lambda\lambda$ $\sim$370–830 nm (Frandsen & Lindberg, 2000); FEROS, R$\sim$48000 and $\lambda\lambda$ $\sim$350–929 nm (Kaufer et al., 1999); and HEROS, R$\sim$20000 and $\lambda\lambda$ $\sim$350–880 nm (Schmitt et al., 2014). The spectra have been reduced using the available pipelines of the corresponding instrument; they include the usual steps for echelle spectra, such as bias subtraction, flat-field correction, cosmic ray removal, and order extraction. Wavelength calibration is carried out by means of Th-Ar lamp spectra taken at the beginning and end of each night. Finally, barycentric corrections have been applied to all of them. Telluric lines heavily affect the wavelength range around the Na I D lines. To correct for them we have taken advantage of the fact that the spectra were obtained at many different epochs of the year. Thus, it is easy to identify and remove telluric lines, as they shift in wavelength when the barycentric correction is applied but the stellar Na I D lines remain at the same wavelength; furthermore, both lines of the Na I doublet share the same radial velocity. Table 4.1 also gives the signal-to-noise ratio (S/N) of the median spectra achieved for each instrument in two "continua" at each side of the Ca II K line. Those values, and those of the individual spectra, are mostly affected by the observing weather conditions.

Table 3.2: Stellar properties of the observed cold-gas-bearing debris-disc stars

Star	SpT	d (pc)	V (mag.)	B (mag.)	$T_{\rm eff}$ (K)	$\log g$	vsin i (km/s)	Age[a] (Myr)	Cold gas detection [b]
HD 9672	A1V	59.4	5.61	5.67	9110	4.25	186	40 (1)	(1) CO
HD 21997	A3IV/V	68.3	6.37	6.50	8610	4.10	60	42 (2)	(2) CO
HD 32297	A0V	136.2	8.14	8.32	7910	4.05	90	$<$ 30 (3)	(3) CO
HD 109085	F2V	18.3	4.31	4.69	6950	4.20	60	1400 (4)	(4) CO
HD 110058	A0V	188.7	7.97	8.12	9720	4.45	150	15 (5)	(5) CO
HD 121191	A5IV/V	135.9	8.16	8.40	7970	4.25	65	16 (5)	(6) CO
HD 121617	A1V	128.2	7.29	7.36	9285	4.45	90	16 (5)	(6) CO
HD 131488	A1V	150.0	8.00	8.09	9050	4.21	120	16 (5)	(6) CO
HD 131835	A2IV	145.6	7.86	8.05	8610	4.35	105	16 (5)	(7) CO
HD 138813	A0V	134.4	7.30	7.37	9685	4.45	130	10 (5)	(5) CO
HD 146897	F2/3V	122.4	9.11	9.58	6700	4.30	55	15 (6)	(5) CO
HD 156623	A0V	118.3	7.26	7.35	9580	4.10	80	16 (5)	(5) CO
HD 172555	A7V	28.6	4.77	4.97	7900	4.05	120	23 (7)	(8) OI
HD 181296[c]	A0V+M7	48.2	5.02	5.04	10400	4.30	230	23 (7)	(9) CII
HD 181327	F6V	48.6	7.04	7.50	6650	4.40	28	23 (7)	(10) CO

[a] References for ages: (1) Torres et al. (2008); (2) Bell et al. (2015a) ; (3) Kalas (2005); (4) Marino et al. (2017); (5) Pecaut & Mamajek (2016); (6) Pecaut et al. (2012); (7) Mamajek & Bell (2014). [b] References for cold gas detection: (1) Zuckerman et al. (1995); (2) Moór et al. (2011a); (3) Greaves et al. (2016); (4) Marino et al. (2017); (5) Lieman-Sifry et al. (2016); (6) Moór et al. (2017); (7) Moór et al. (2015a); (8) Riviere-Marichalar et al. (2012); (9) Riviere-Marichalar et al. (2014); (10) Marino et al. (2016) [c] The M7 brown dwarf companion of η Tel is located at an angular distance of $\sim$ 4 (Neuhäuser et al., 2011).

3.3 Stellar properties of the observed sample

Table 3.2 shows some of the observational and fundamental properties of the sample of stars presented in this work. Names, spectral types, and B and V magnitudes have been taken from SIMBAD (Wenger et al., 2000b), while the distances are estimated from the revised Hipparcos parallaxes (van Leeuwen, 2007) and/or the Gaia archive (Lindegren et al., 2016), except for HD 131488 taken from Melis et al. (2013). We note that there is a large discrepancy between the Gaia distance of HD 110058 of 188.7 pc and the Hipparcos one of 107.4 pc. Ages from the literature and the corresponding references are also given in Table 3.2, as well as the list of papers reporting the cold gas detection.

$T_{\rm eff}$, $\log g$, and $v \sin i$ have been estimated using the spectral synthesis programs ATLAS and SYNTHE (Kurucz 1993), fed with the models describing the stratification of the stellar atmospheres (Castelli & Kurucz 2003). A grid of models with temperatures from 6000 to 10500 K, step 100 K, and log g= 3.5, 4.0, 4.5 was created and prepared to be broadened with any value of $v \sin i$. Solar abundances were used for all objects, with the exception of HD 32297 and HD 146897 as the fits clearly pointed towards a metallicity different from solar. For these two stars, metallicities [Fe/H] -0.5 and -0.2 were used, respectively (Gebran et

al. 2016 give a value -0.7 for HD 32297).

For stars hotter than $\sim$ 8000 K, the first step was to find the three models whose temperatures match the depth of the photospheric Ca II K line for the three values of $\log g$. The widths of Hγ, Hδ, H[8-2] and H[9-2] were measured in the stellar spectra and in the models. Values of stellar gravities were found for each line by interpolating the width of the stellar lines in the models' measurements. The final value of the gravity, $\log g$, is the average of the individual determinations for each line, the uncertainty in the gravity being the standard error of the mean. The value of $\log g \pm \Delta \log g$ is then interpolated in the three models mentioned above to obtain the best fit value $T_{\rm eff} \pm \Delta T_{\rm eff}$. The uncertainties in $v \sin i$ have been estimated by comparing the width of the Mg II 4481 Å absorption in the stellar spectrum with that of models computed with a range of rotation rates so as to allow the relative differences between star and model to be the order of 5%.

For the F stars, the approach, being qualitatively similar, accounts for the different dependence of the calcium and hydrogen lines on temperature and gravity as compared with late-B or A-type stars. Once an acceptable model fitting the Ca II HK and the hydrogen lines is found, uncertainties are estimated by changing model parameters until the departures from the best fit are $\sim$ 10%. The value of $v \sin i$ is estimated for this kind of stars by comparing the widths of weak photospheric lines with those of models and following a similar criterion as for hotter stars. Final typical errors are $\sim$100 K, $\sim$0.20, and $\sim$ 5 km/s for $T_{\rm eff}$, $\log g$ and $v \sin i$, respectively.

3.4 Results

Narrow, stable, non-photospheric absorption features at the centre of, or slightly blue-/red-shifted with respect to, the photospheric Ca II K absorption line have been detected in 10 out of the 15 observed debris-disc systems (Table 3.3). The non-photospheric absorption profile of some stars presents a red wing, suggesting that the observed profile is a blend of independent absorptions. In addition, a few stars show transient absorption events. In the following we describe the results of the stars with and without non-photospheric absorptions separately.

3.4.1 Stars with non-photospheric Ca II absorptions

Figure 3.1 shows the observed Ca II K line profiles of the observed stars with narrow, stable central absorptions, superimposed to the rotationally broadened photospheric line. The plotted, observed profile is the median of the spectra of each star. As far as we know, this is the first time that the Ca II K absorption feature is reported towards HD 32297, HD 131488, HD 131835, HD 138813, HD 146897, HD 156623, and HD 181296 (η Tel). Welsh & Montgomery (2019) have also recently detected the narrow absorption towards η Tel. Previous narrow absorption detections have been published in the cases of 49 Ceti, HD 110058, and

Table 3.3: Radial velocities and equivalent widths (EWs) of the Ca II H&K and Na I D non-photospheric absorptions, radial velocities of the stars, and projected velocities of ISM clouds in the Colorado model. The FWHM velocity dispersion of the Ca II K lines is also given.

Stars with non-photospheric absorptions							
Star	v_{CaIIK} (km/s)	EW(K/H) mÅ	Δv_{CaIIK} (km/s)	v_{NaID} (km/s)	EW(D2/D1) [c] mÅ	v_{rad} (km/s)	v_{ISM} [d] (km/s)
HD 9672[a]	13.5±2.3	10.6/6.0	7.4	11.5±2.3	16.4/9.3	11.0±2.0	11.01 (LIC)
HD 32297[a]	22.7±3.0	19.4/8.9	9.7	23.8±2.5	93.0/84.0	19.7±2.0	23.59 (LIC)
HD 110058	12.7±3.3	27.0/24.1	6.8	12.5±2.8	46.0/39.1	12.6±2.4	–14.46 (G)
	1.2±3.3	19.9/10.0	12.6	0.9±2.8	34.0/18.9		
HD 131488	4.0±2.7	5.7/–	9.6	5.3±2.2	42.1/34.2	5.8±1.5	–23.91 (G)
	-3.2±2.7	4.0/–	4.2	–13.88±2.2	7.2/–		
HD 131835	2.2±2.7	0.7/–	2.3	–	<0.9	2.6±1.4	–18.56 (GEM)
	–5.9±2.7	2.1/1.4	7.9	–	<0.9		
	–13.8±2.7	8.3/4.1	7.4	–11.8±2.0	41.0/32.1		
HD 138813	–27.5±3.0	5.6/–	18.7	–22.2±2.2	5.9/3.1	–0.4±2.0	–27.82 (G)
				–12.0±2.5	18.0/15.4		
				0.1±2.0	–7.55/–5.2		
HD 146897	–8.0±2.7	12.4/–	7.2	–8.8±2.1	118.2/80.0	–4.0±1.5	–29.19 (G)
	–30.0 ±2.7	5.9/–	4.6	–	<0.8		
HD 156623[a]	–15.0±2.7	9.0/3.7	18.7	–1.8±2.6	–10.6/–8.5	–0.2±1.5	–24.89 (G)
	8.1 ±2.7	4.3/–	6.0 [e]	–	<0.7		
HD 172555[a]	2.3±3.0	9.9/4.0	9.7	15.3±2.1	8.0/–	2.6±1.9	–16.84 (G)
				–20.4±2.1	3.2/1.8		
HD 181296[b]	–22.8±3.8	3.9/2.2	8.4	–22.9±2.4	4.0/–	–3.0±3.0	–18.51 (G)
Stars without non-photospheric absorptions							
HD 21997	–	–	–	–	–	17.3±2.0	15.87 (LIC)
HD 109085	–	–	–	–	–	–0.4±1.0	–0.11 (GEM)
HD 121191	–	–	–	–	–	12.0±1.4	–18.34 (G)
HD 121617	–	–	–	–	–	7.8±1.6	–19.84 (G)
HD 181327[b]	–	–	–	–	–	0.2±1.5	–18.51 (G)

[(a)] Stars with FEBs.[(b)] The line of sight towards these two stars does not traverse any ISM cloud in the Colorado model but it passes within 20 of several clouds. Among these, cloud G is the closest one in velocity to these stars. [(c)] Upper limits are shown for those stars without Na non-photospheric absorption. [(d)] Names within parentheses are ISM clouds in the Colorado model (Redfield & Linsky, 2008a). [(e)]The velocity dispersion for this absorption is highly variable, and the value shown here is the value obtained from the median spectra.

HD 172555 (Montgomery & Welsh, 2012; Kiefer et al., 2014a; Hales et al., 2017). Table 3.3 gives equivalent widths (EWs), radial velocities, and velocity dispersion (full width at half maximum (FWHM)) of all non-photospheric Ca II K features. The table also gives EWs of the Ca II H line in those cases where the line can be distinguished from the strong Hϵ Balmer line, as well as EWs and velocities of the Na I D lines when detected. In the case

of non-detection in Na I, upper limits of the D2 line (the strongest one of the doublet) were calculated as EW of Gaussians with parameters determined by the instrumental resolution (width) and the 3σ rms noise in the wavelength region (depth). In case of detection, EWs are the average of independent measurements made with three different software packages - MIDAS, dipso and Gaussian fits made with Python. Estimated uncertainties are of the order of 10%. Velocity dispersions in Table 3.3 were calculated in the median spectra as the FWHM of fitted Gaussians. Radial velocities were measured as the central value of the non-photospheric absorption. Uncertainties were estimated as the square sum of the uncertainties in the radial velocity of the star (see below) and the size of the pixel in velocity.

Stable absorptions might originate in CS discs sharing the radial velocity of the central star, or in the complex local ISM (e.g. Redfield & Linsky, 2008a). In order to try to decipher which of these alternatives corresponds to reality, radial velocities of the stars were estimated using the Balmer lines and the velocity shift of the Kurucz models to fit the observed Ca II K photospheric line (Table 3.3). Quoted v_{rad} errors correspond to the difference between both methods. For the sake of completeness, radial velocities of the stars and of the corresponding ISM velocity vectors are also given in Table 3.3 for those stars without non-photospheric absorptions. Our stellar radial velocity estimates are in good agreement with previous ones (e.g. de Bruijne & Eilers, 2012; Melis et al., 2013; Hales et al., 2017). For the ISM velocity vectors, we have used Redfield & Linsky's Colorado model[1] (Redfield & Linsky, 2008a) to estimate them along the line of sight towards the stars. Names of the corresponding ISM clouds are also indicated in Table 3.3. In the cases of HD 181296 and HD 181327, their lines of sight do not traverse any cloud in the Colorado model, although they pass within 20deg of several clouds. A complementary search of ISM absorption features has been conducted in the cases of HD 131488, HD 131835, HD 138813, and HD 146897. This search was motivated since, based on previous results and on our own spectra, the origin of the observed non-photospheric absorptions was highly ambiguous. In this context, we have analysed the Ca II and Na I lines of field stars surrounding those four cold-gas-bearing debris discs. We note that these stars are located in the line of sight of the G or Gem Colorado clouds (Table 3.3), and are members of the Scorpius-Centaurus OB association (Pöppel et al., 2010; Lieman-Sifry et al., 2016). Details of this search are given in Appendix B. The remaining 11 objects in the sample were excluded from this study due either to the presence of variable non-photospheric absorptions, or the unambiguous determination of a CS absorption.

Individual stars

HD 9672 (49 Ceti): A Ca II K narrow, stable absorption at the bottom of the photospheric line at $\sim$13.5 km/s and EW(Ca II K) $\sim$10.6 mÅ is detected. This feature coincides with the radial velocities of the star and of the local ISM (Fig. 3.1 and Table 3.3). Our result is similar to the stable component observed by Montgomery & Welsh (2012). Using the high-resolution spectrograph STIS at the HST, Malamut et al. (2014) detected two partially blended, near-

[1] http://sredfield.web.wesleyan.edu/

UV Mg II and Fe II features with velocities 9.0 and 14.4 km/s (Mg II), and 11.0 and 13.65 km/s (Fe II), and suggested the second one could be attributed to the CS disc. Thus, it is most likely that the absorption we detect is a blend of both the CS and the ISM components. The Ca II H line is detected with EW(Ca II) ∼6.0 mÅ, which suggests that the Ca II lines are optically thin. None of our spectra show any transient Ca II absorption in contrast with the FEBs detected by Montgomery & Welsh (2012). A Na I D absorption is coincident with the Ca II K feature and the radial velocity of the ISM.

HD 32297: The radial velocity of the star (19.7 km/s) is very close to that of the local ISM. The velocity and EW of the detected Ca II K stable absorption is ∼22.7 km/s and ∼19.4 mÅ, respectively (Fig. 3.1 and Table 3.3). The Ca II H line is detected with EW(Ca II H) ∼8.9 mÅ. Very high-resolution spectra, R ∼240000, of the Na I doublet show two components at ∼20.5 km/s and ∼24.5 km/s, attributed to the CS medium and the ISM, respectively (Redfield, 2007). This suggests again that the Ca II absorptions we detect are a blend of both CS and ISM components. Redfield (2007) detected variability in the Na I lines; in our case, no apparent variability is detected either in the Ca II lines or in the Na I ones.

HD 110058: Two Ca II K components at velocities of 12.7 and 1.2 km/s are detected with EW ∼27 mÅ and ∼20 mÅ, respectively (Fig. 3.1 and Table 3.3). The 12.7 km/s absorption coincides with the radial velocity of the star, while the ISM velocity towards this line of sight is -14.46 km/s. The same velocity components have been reported by Hales et al. (2017) and Iglesias et al. (2018). However, while both features remain stable in our spectra (taken in the same campaign), a comparison with those of similar spectral resolution (Hales et al., 2017) suggests that the strength of the blueshifted component varies. Hales et al. (2017) ascribe this absorption to the ISM because of the presence of a similar feature in the spectra of close-by stars. However, the fact that its strength might vary suggests that it might well have a CS origin. Further monitoring of this star is required to elucidate this apparent controversy. Both features are detected in the Ca II H line with EW ∼24.0 and ∼10.0 mÅ, respectively. This result suggests that the stronger 12.7 km/s absorption is optically thick, while the weaker one at 1.2 km/s is optically thin. A similar behaviour is present in the Na I D lines (Table 3.3, Hales et al., 2017; Iglesias et al., 2018).

HD 131488: The non-photospheric Ca II K profile shows a narrow absorption with a red wing extending up to ∼12.0 km/s, suggesting a blend of two independent features (Fig. 3.1). The Ca II K profile can be fit with two Gaussians centred at 4.0 and –3.2 km/s, and EWs ∼5.7 and ∼4.0 mÅ, respectively (Fig. 2). While both features are far away from the expected ISM velocity in the Colorado model, the 4.0 km/s feature coincides with the radial velocity of the star (Table 3.3, and Melis et al., 2013). A Ca II H absorption is indistinguishable from the noise. The Na I doublet appears at a velocity of 5.3 km/s, that is, at the radial velocity of the star and one of the Ca II K components (Fig. 2). Their EWs are ∼42 mÅ (Na I D2) and ∼ 34 mÅ (Na I D1), which suggests that the Na I lines are optically thick. There is also an absorption at –13.9 km s^{-1} in the D2 line, most likely interstellar. Among the field stars aroundHD 131488 (see Appendix B), HD 132200, located at a distance of 165 pc and at an angular distance from HD 131488 of 1.24deg, shows two non-photospheric Ca II K

absorptions at velocities -6.9 km/s and 4.6 km/s, which are similar to the velocities of the observed features in HD 131488. As mentioned before, both stars belong to the complex Scorpius-Centaurus OB association, and both show a feature at negative velocities close to the mean velocity of $\sim$ –6.6 km/s that characterise the approaching face, located at a distance $\leqslant$ 76 pc, of the large expanding bubble around the OB association (Pöppel et al., 2010). Thus, the negative velocity feature of both stars is likely of ISM origin. At the same time, the 4.6 km/s feature of HD 132200 is variable, suggesting a relation to the star (see Fig. A.1, Appendix B). This fact also suggests that the HD 131488 4.0 km/s absorption, which coincides with the stellar radial velocity, is likely circumstellar.

HD 131835: This star shows a non-photospheric absorption in both Ca II H&K lines with a weak red wing extending up to $\sim$ 0.0 km/s (Figs. 3.1 and 3). The feature profiles can be fit with two (Gaussian) components at $\sim$ –13.8 km/s and EW $\sim$ 8.3 mÅ, and –5.9 km/s and EW $\sim$ 2.1 mÅ. The corresponding Ca II H EW values are $\sim$4.1 mÅ and $\sim$ 1.4 mÅ, respectively. A third very weak component, $\sim 3\sigma$ level, is present only in Ca II K at a velocity of 2.2 km/s and EW $\sim$0.7 mÅ (Table 3.3, Figs.3.1 and 3). This weak feature, which would require further confirmation, coincides with the radial velocity of the star. The Na I D lines show a narrow feature at $\sim$ –11.8 km/s, approximately at the velocity of the strongest Ca II component (Fig. 3). The estimated EWs are $\sim$41 mÅ (Na I D2) and $\sim$32 mÅ (Na I D1), suggesting they are partly optically thick. We note that stars in the field show a non-photospheric absorption at $\sim$ –13 km/s (Appendix B), close to the one observed in HD 131835, and that the -5.9 km/s feature is close to the mentioned mean velocity of the approaching face of the expanding bubble around the Scorpius-Centaurus association. Thus, both features are likely to be interstellar, while the weak 3σ one has an ambiguous origin (see Appendix B.)

HD 138813: A clear, very broad (Δv (FWHM) $\sim$18.7 km/s) Ca II K absorption at -27.5 km/s is detected, coinciding with the ISM velocity (Fig. 3.1), but it is hardly recognisable in the Ca II H line. The Na I D lines (Fig. 4) show narrow features at $\sim$ –12 km/s and $\sim$ –22 km/s and EWs of 18 and 5.2 mÅ (D2 line) and 15.4 and 3.1Å (D1 line), suggesting that they are partly optically thick. There is also an emission feature at the radial velocity of the star ($\sim$ 0.1 km/s) Field stars show Na I D absorption features at similar velocities (Appendix B). Neither Ca II nor Na I features are detected at the radial velocity of the star.

HD 146897: This star presents a narrow Ca II K absorption at the bottom of the photospheric line with an EW of $\sim$12.4 mÅ and a velocity of $\sim$ –8.0 km/s, close to the radial velocity of the star (Fig. 3.1, Table 3.3). A second weaker feature is detectable at a velocity of $\sim$ –30.0 km/s, that is, the ISM velocity vector. No absorption is recognisable in the Ca II H line. Narrow strong Na I D absorptions are detected with the same velocity as the strong Ca II K feature (Fig. 5); their EWs are $\sim$ 118 mÅ (D2 line) and $\sim$ 80 mÅ (D1 line), suggesting that they are at least partly optically thick. Field stars around HD 146897 show absorption features with similar velocities in the Ca II and/or Na I lines (Appendix B).

HD 156623: Two Ca II K absorptions at velocities of $\sim$ –15.0 and $\sim$ 8.1 km/s and with EWs

of $\sim$ 9.0 mÅ and $\sim$ 4.3 mÅ, respectively, are detected superimposed on the photospheric line. Neither feature exactly coincides either with the Colorado model ISM velocity vector or with the radial velocity of the star (Fig. 3.1 and Table 3.3). While the strongest, very broad feature remains practically constant, the weaker one shows variability. As an example, Fig. 6 shows three Ca II K spectra of HD 156623 taken at different epochs where it is distinguished that the $\sim$8.1 km/s absorption is clearly a FEB-like event. A Ca II H feature at the velocity of the strongest Ca II K with EW $\sim$ 3.7 mÅ is present in our spectra. There is an emission feature in the Na I D lines, most likely related to the star (see Fig. 3.6).

HD 172555: A narrow Ca II K absorption with a velocity of 2.3 km/s and an EW of $\sim$ 9.9 mÅ at the core of the stellar line is detected (Fig. 3.1 and Table 3.3). A similar absorption is detected in the Ca II H line with an EW(Ca II H) of $\sim$ 4.0 mÅ. Two narrow features are detected as well in the Na I D lines, at $\sim$ –20.4 km/s, possibly related to the ISM (also reported in Kiefer et al. (2014a)) and at $\sim$ 15.3 km/s, of attributed CS origin, as it does not coincide with the ISM. Kiefer et al. (2014a) did not detect this last feature in Na II D lines, but reported some Ca II FEBs not present in any of our spectra.

HD 181296 (η Tel):. A narrow absorption is observed in both Ca II H&K lines at a velocity of ~ -22.8 km/s with EWs of $\sim$3.9 mÅ (K-line) and $\sim$2.2 mÅ (H-line), and coincident with the absorption detected in Na I D2 line. The velocity of the feature is very different from the estimated radial velocity of the star of -3 km/s. The line of sight to this star does not traverse any identified local cloud in the Colorado model, but it is close ($<$ 20 deg) to some of them; in particular to the G and Vel clouds which have a projected velocity of –18.51 and –27.6 km/s, respectively.

3.4.2 Stars without narrow absorption components

Neither stable nor variable Ca II or Na I absorption features, which could be attributed to the ISM or CS medium, have been detected in any of our spectra towards the cold-gas-bearing debris-disc stars HD 21997, η Crv, HD 121191, HD 121617, and HD 181327. For the sake of completeness, Fig. 7 shows the observed median Ca II K profile of these stars together with the Kurucz synthetic profiles. A clear emission due to stellar activity at the core of the photospheric line is apparent in the spectrum of the F6 V star HD 181327. At the same time, the observed Ca II K line of η Crv (HD 109085, F2 V spectral type) is not as deep as predicted by the synthetic line. We have tested the effects of changing the metallicity and Ca abundance in the Kurucz models without finding a satisfactory fit between the observed Ca II K line and the synthetic one. However, we have achieved satisfactory fits between Kurucz models and stars with similar properties as η Crv. These results lead us to conclude that η Crv most likely presents some level of chromospheric activity.

Table 3.4: Summary of the non-photospheric absorption features of the observed cold-gas-bearing debris-disc stars. Columns 2 to 4: Coincidences of the Ca II velocity components with the radial velocity of the star, Colorado model ISM clouds along the line of sight, or none of both. Columns 5 to 7: Coincidences of the Na I velocity components with Ca II features, the radial velocity of the star, or ISM absorptions. Column 8 gives the inclination angle of the debris disc associated with the stars. Empty spaces signify non-detections.

Stars with non-photospheric absorptions							
	Ca II			Na I			Angle (deg.)[e]
Star	V_{star}	V_{ISM}	Neither	V_{CaII}	V_{star}	V_{ISM}	
HD 9672[a]	Y	Y		Y	Y		70-90 (1,2,3)
HD 32297[a]	Y	Y		Y	Y		80-88 (4,5)
HD 110058	Y		Y	Y	Y		∼90 (6)
HD 131488	Y	Y		Y	Y		82 (7)
HD 131835	Y	Y		Y		Y[c]	75-83 (8,9,14)
HD 138813		Y		Y	Y[d]	Y[c]	32 (10)
HD 146897	Y	Y		Y	Y	Y[c]	84 (11)
HD 156623[a]			Y		Y[d]		34 (10)
HD 172555[a]	Y					Y	75 (12)
HD 181298[b]			Y	Y			>70 (13)

Stars without non-photospheric absorptions					
Star	HD 21997	HD 109085	HD 121191	HD 121617	HD 181327
Angle (deg.)[e]	24 (15)	35 (16)	unresol. (7)	37 (7)	30 (17)

[a] Stars with FEBs. [b] See text Sec. 5.2. [c] ISM absorptions from field stars. [d] Features in emission. [e] References for inclination angle: (1) Hughes et al. (2008); (2) Moór et al. (2015b); (3) Choquet et al. (2017); (4) Schneider et al. (2005); (5) Asensio-Torres et al. (2016); (6) Kasper et al. (2015); (7) Moór et al. (2017); (8) Hung et al. (2015); (9) Moór et al. (2015a); (10) Hales et al. (in preparation); (11) Thalmann et al. (2013); (12) Smith et al. (2012); (13) Smith et al. (2009); (14) Feldt et al. (2017);(15) Moór et al. (2013); (16) Marino et al. (2017); (17) Marino et al. (2016) .

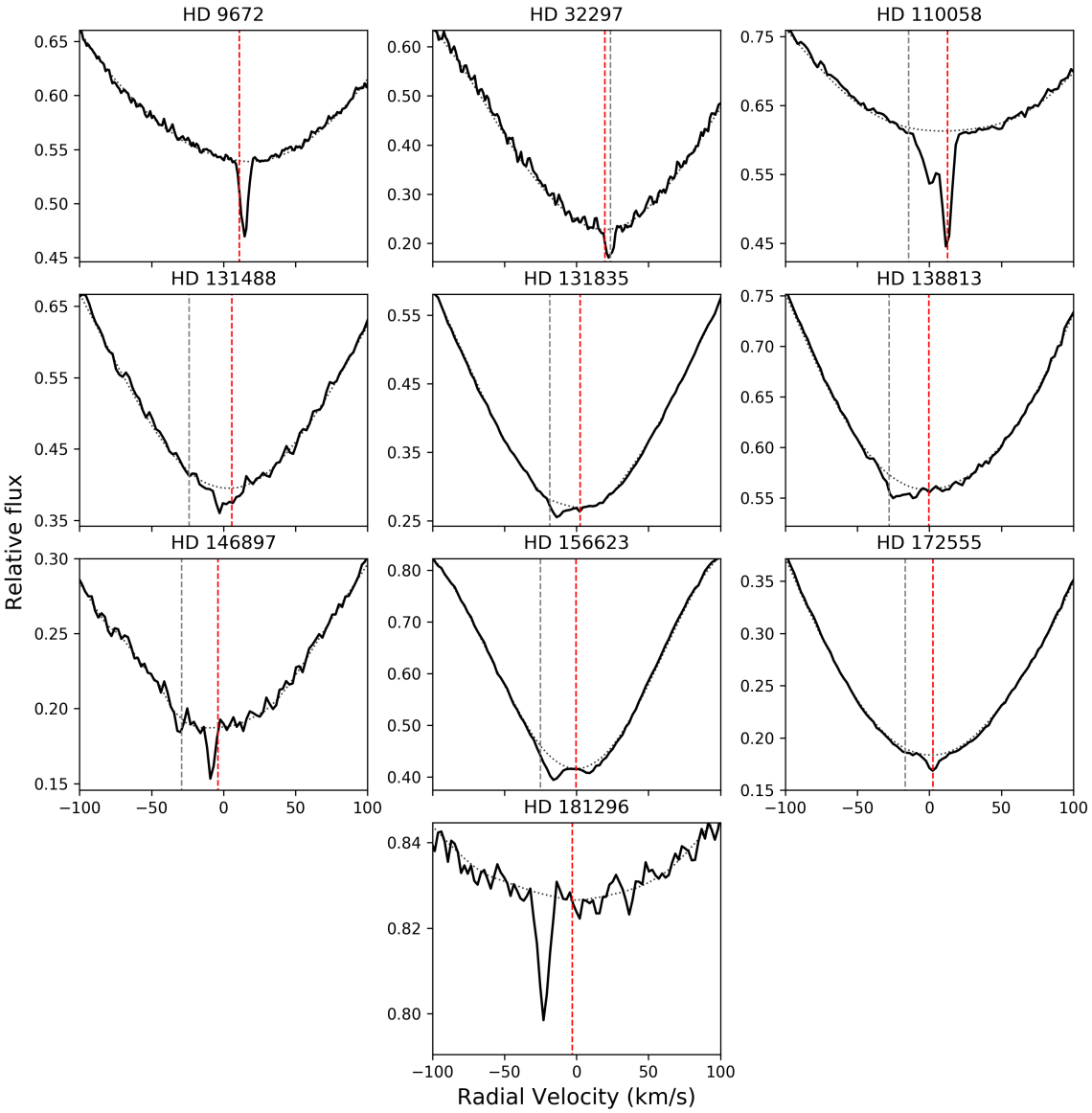

Figure 3.1: Median Ca II K line profiles of the gas-bearing debris-disc stars with non-photospheric absorption (black solid line) together with a Kurucz photospheric model (black dotted line) with stellar parameters according to Table 3.2. Dashed lines in all panels indicate the corresponding radial velocities of the stars (red), and the projected velocities of the local ISM (grey) after the Colorado model (Redfield & Linsky, 2008a). Velocities are in the reference frame of the Ca II K line. v_{rad} and v_{ISM} are coincident for HD 9672 (see Table 3.3). HD 181296 has no ISM lines in the line of sight (see Table 3 and Sect 5.2 for a discussion). The same convention for v_{rad} and v_{ISM} is used in all further figures.

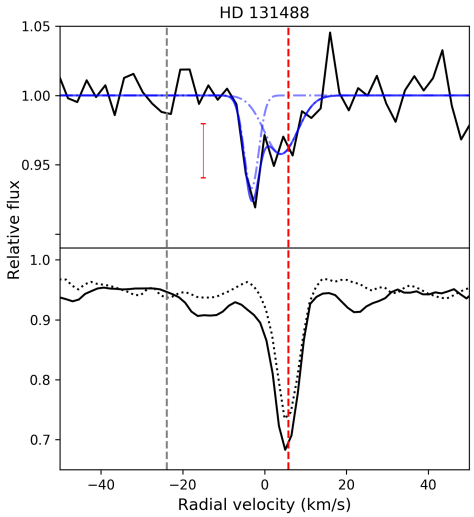

Figure 3.2: Top: Non-photospheric Ca II K feature profile of HD 131488. The observed spectrum is plotted with a black solid line. The Ca II K feature is fit with two Gaussians, plotted with a blue dash-dotted line; the blue continuous line is the sum of both Gaussians . A 3-σ error bar is plotted in red. Bottom: both Na I D2 (continuous line) and Na I D1 (dotted line) components.

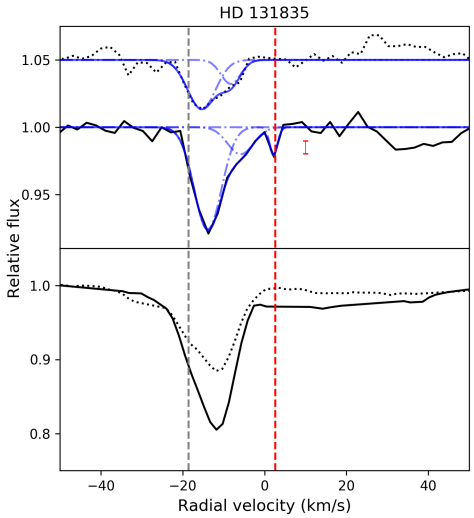

Figure 3.3: Top panel: Non-photospheric Ca II K (black continuous line) and H (black dotted lined) feature profiles of HD 131835. Ca II H has been displaced 0.05 relative units for clarity. Both Ca II features are fit with three and two Gaussians, respectively, plotted with blue dash-dotted lines; the blue continuous lines are the sum of the Gaussians in each case. A 3-σ error bar is also plotted in red. Bottom panel: Na I D2 (black continuous line) and D1 (black dotted line) profiles.

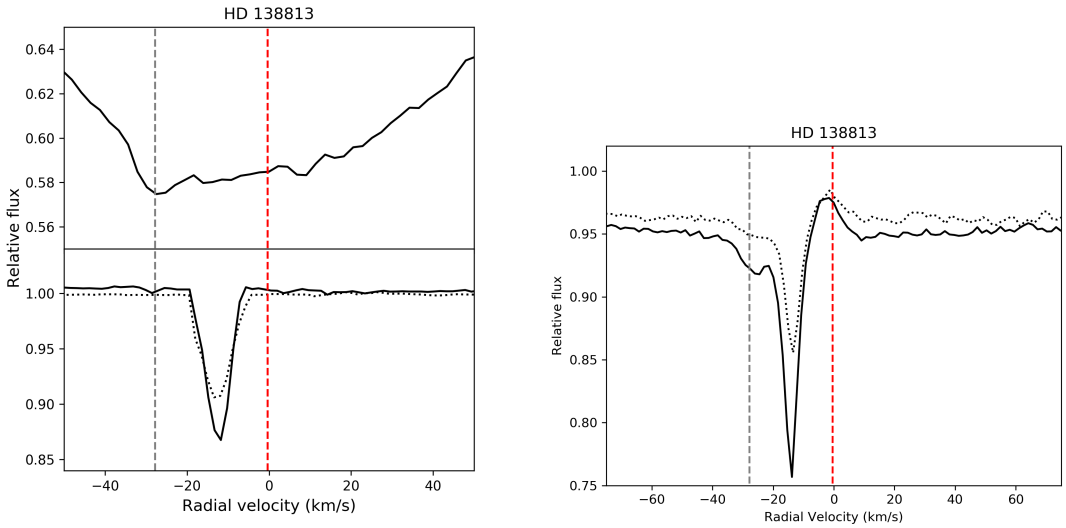

Figure 3.4: Top panel: Ca II K line profile of HD 138813. An absorption feature is detected at the ISM velocity. Bottom panel: Non-photospheric Na I D2 (black continuous line) and Na I D1 (black dotted line) absorption features.

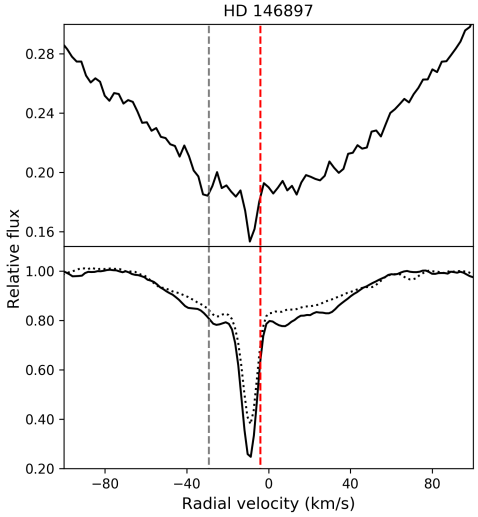

Figure 3.5: Top panel: Ca II K line profile of HD 146897. Bottom panel: Na I D2 (black continuous line) and Na I D1 (black dotted line).

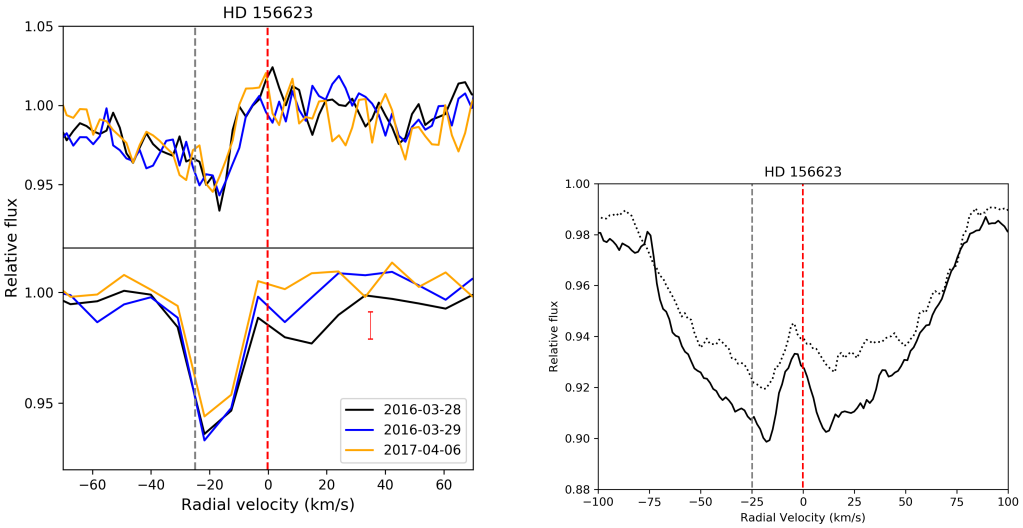

Figure 3.6: Top panel: Individual non-photospheric Ca II H absorption features of HD 156623. Bottom panel:Ca II K line. The variable redshifted absorption at $\sim$ 8.1 km/s is a clear FEB-like event. A 3-σ error bar is plotted in red. Dates are indicated with different colours in both panels.

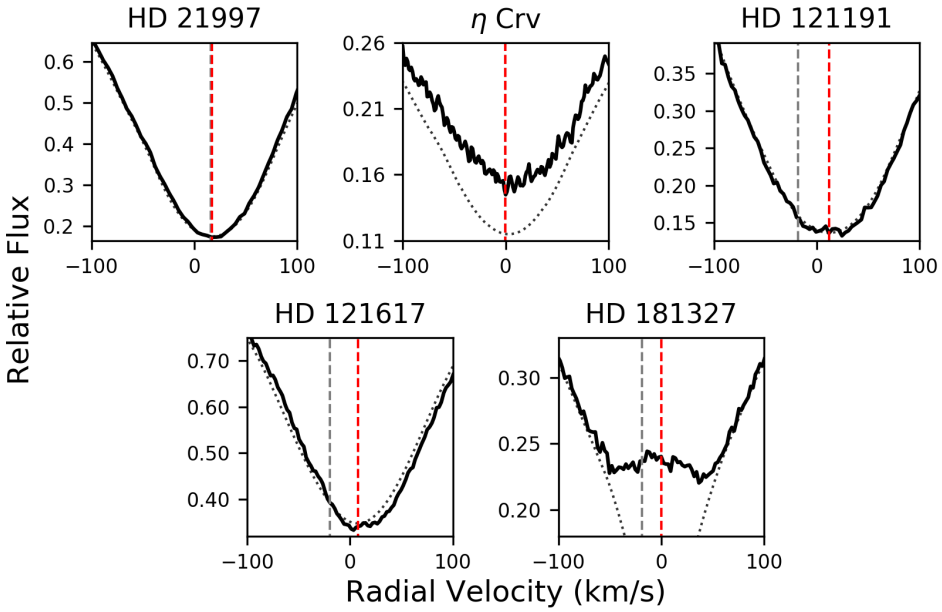

Figure 3.7: Observed median Ca II K line profiles of cold-gas-bearing debris-disc stars without non-photospheric absorption features.

3.5 Discussion

Before discussing plausible origins of the observed non-photospheric features and their potential correlations with the properties of the cold-gas-bearing debris discs and their host stars, it is useful to globally evaluate the observational results of the whole cold-gas-bearing debris-disc sample, that is, including the two systems not observed by us, β Pic and Fomalhaut.

3.5.1 Global overview of the observational results

As pointed out before, 10 out of the 15 observed gas-bearing debris-disc stars show at least one non-photospheric Ca II absorption feature. Table 4 summarises these observational findings, where we indicate the stars with non-photospheric Ca II and Na I features at the velocities of the star, ISM clouds of the Colorado model, and/or plausible ISM absorptions as suggested by their detection in field stars. We have conservatively assumed that the observed features have a stellar or ISM counterpart if the velocity difference is less than 5 km/s. The table also shows those stars with FEB-like events.

When considering the whole sample of 17 cold-gas-bearing debris-disc stars, we find that 11 of them (including β Pic) show at least one non-photospheric Ca II K absorption. That leaves 6 objects with no traces of any extra absorption superimposed on the photospheric line. Fomalhaut has been added to the observed stars in this work since neither Ca II nor Na I extra absorptions in the core of the stellar lines have been detected (Hobbs, 1986; Lagrange-Henri et al., 1990d; Holweger & Rentzsch-Holm, 1995). Furthermore, we have downloaded UVES spectra from the ESO archive confirming the lack of a non-photospheric absorption feature in the Fomalhaut spectrum.

3.5.2 Origin of the non-photospheric absorption features

There is some ambiguity concerning the CS or ISM origin of the stable Ca II and Na I absorptions as they can originate in warm and cold clouds of the local ISM. The observed line EWs, their ratios, and (in most cases) the velocity dispersion of the Ca II K line are not different from what is detected in the ISM (Redfield & Linsky, 2002; Welsh et al., 2010), where different lines of sight with or without Ca II or Na I absorptions are found, as well as a large range of Ca II-to-Na I ratios (Redfield et al., 2007; Welsh et al., 2010). Nonetheless, a CS origin has been attributed to at least one velocity component in the cases of 49 Ceti, HD 32297, HD 110058, and HD 172555 (e.g. Montgomery & Welsh, 2012; Redfield, 2007; Hales et al., 2017; Kiefer et al., 2014a), respectively. HD 156623 shows a variable FEB-like event. The feature at the stellar radial velocity of HD 131488 is likely CS (Sect. 4.1.1). The weak 3σ feature, if confirmed, at the radial velocity of HD 131835 might also be circumstellar. At the same time, an ISM origin is the most plausible case for the non-photospheric

absorptions in HD 138813 and HD 146897, although even in these two stars the Ca II K FWHM dispersion velocities, ∼18.7 km/s, are larger than typical ISM values (e.g. Redfield & Linsky, 2002).

HD 181296 (η Tel) merits particular attention. This star has a stable feature blueshifted by $\sim$ 20 km/s with respect to the stellar radial velocity (Fig. 3.1 and Table 3.3); its line of sight does not cross any of the Colorado model clouds, although it passes within 20deg of several clouds. η Tel is located at a projected angular distance of $\sim$ 7 arcmin from HD 181327, which corresponds to $\sim$ 0.1 pc at the distance of both stars (Table 3.2). HD 181327 is another cold-gas debris disc but without non-photospheric absorption features (Table 3.3 and Fig. 7). Both stars are members of the β Pic moving group, and form part of a triple system (Neuhäuser et al., 2011), sharing distances, radial velocities, and proper motions. Thus, although an ISM origin cannot be totally excluded from being the η Tel Ca II absorption feature, those data strongly suggest that the feature is CS. We note that similar blueshifted CS absorptions in UV-excited lines of C II and N II are found around the debris-disc star σ Her, which has a similar $T_{\rm eff}$ as η Tel (Chen & Jura, 2003). Those authors suggest that the blueshifted features arise in a radiatively driven wind, and that the gas could be generated by the sublimation of comets or collisions between solid bodies.

The previous arguments strongly suggest the presence of hot Ca II and Na I gas in the CS environment of at least eight (including β Pic), or possibly nine (if the feature at the stellar radial velocity of HD 131835 is confirmed) of the cold-gas-bearing debris-disc stars. Furthermore, the presence/absence of Ca II and Na I suggests that there are differences in the CS gas composition around the debris-disc stars. We note that Kiefer et al. (2014b) suggest the presence of two families of exocomets in β Pic, one of them strongly depleted in volatiles. Assuming, therefore, the plausible circumstellar-hot-gas scenario as suggested by some of the non-photospheric features, the permanence of such gas in the surroundings of the stars would require a continuous replenishment as it would be subject to a strong radiation field overcoming the gravitational force (Beust et al., 1989). These authors, and Lagrange et al. (1998), Liseau (2003), and Fernández et al. (2006) have estimated the ratio $\beta = F_{\rm rad}/F_{\rm grav}$ in the case of β Pic for lines of many different atoms/species, including the Ca II H&K and Na I lines, and shown that the atomic gas would disappear unless a braking mechanism is at work. This would also be the scenario of the stars in this work as their radiation fields are similar to that of β Pic.

Thus, a braking mechanism should be at work to explain the hot, inner ($<$ 1 au) CS gas around these gas-bearing debris-disc stars. Such a mechanism could be the one suggested by Fernández et al. (2006) - acceleration of an ionic fluid produced by an enhanced carbon abundance. In this sense, it would be interesting to search for carbon lines around these stars, for example in the UV spectral range (Roberge et al., 2006, 2014).

3.5.3 Correlation of the non-photospheric features with the inclination of the debris discs

We have checked if any observational property of the stars or of the gas/dust components in their debris discs correlate in some way with the presence/absence and strength of the Ca II/Na I absorptions at the core of the stellar lines. We note that CS features are only detected in the A-type stars of the sample and in none of the three F-type stars, but we cannot identify any trend with other properties like rotational velocity or age.

Concerning the debris disc properties, the only trend we find is that non-photospheric CS absorptions are predominantly detected when the discs are oriented close to edge-on. This is the case in at least 7 (possibly 8 if HD 131835 is included) out of 9 objects. On the contrary, discs seen close to face-on (8 objects) do not show non-photospheric absorptions, with the exception of HD 156623 that shows evidence of hot gas as suggested by the FEB-like absorption (Table 4). β Pic and Fomalhaut are included in those figures, as the β Pic disc is seen edge-on, $\sim$ 90deg (Smith & Terrile, 1984), but not the Fomalhaut disc, $\sim$ 65deg (Acke et al., 2012). Thus, at least $\sim$ 78% (possibly 88%) of edge-on cold-gas-bearing debris-disc stars show evidence of hot CS gas, while only $\sim$ 12 % of the face-on cold-gas-bearing debris-disc stars show such evidence. While this result is not surprising as such, it suggests that the non-detection is most likely due to geometrical effects, that is, the disc inclination with respect to the line of sight, but not to the absence of hot gas in those discs. In the case of HD 156623, the detection of the FEB-like Ca II event, in addition to the very broad stable absorption (Table 3), might indicate a significant scale height of the hot gas, since such gas would be located very close to the star. Based on the CO gas detection in β Pic, Kral et al. (2017) have recently developed a model predicting the detection with ALMA of cold gas around debris-disc stars assuming that the gas arises from icy, volatile-rich planetesimals.

From the observational perspective presented in this work, our results strongly suggest that debris discs with central absorptions indicative of hot CS gas would be good targets to search for a cold-gas counterpart with ALMA.

With respect to other debris-disc properties, all but HD 121191 have been resolved either in their dust thermal emission, gas emission, and/or scattered light (e.g. Asensio-Torres et al., 2016; Schneider et al., 2005, 2014; Feldt et al., 2017; Choquet et al., 2017; Moór et al., 2017,see also the Catalogue of Resolved Debris Disc[2] and references therein). Concerning the cold gas, neither the detected species nor the flux/luminosity of the lines show any trend with the optical absorption lines - see e.g. Moór et al. (2017) for CO line luminosities. With regard to the dust, all systems but HD 172555 present two-temperature SEDs. Kennedy & Wyatt (2014) and Geiler & Krivov (2017) have analysed large samples of two-temperature debris-disc systems, and have shown that most of them likely have a two-belt disc structure, similar to the solar system's zodiacal and Kuiper belts. There are, however, a small number of exceptions. In particular, HD 181327 seems to be surrounded by an extended disc with a range of dust temperatures and properties (Lebreton et al., 2012; Kennedy & Wyatt, 2014;

[2]http://www.astro.uni-jena.de/index.php/theory/catalog-of-resolved-debris-disks.html

Ballering et al., 2017). Several works postulate an exo-asteroid belt and/or cometary sources as the possible origin of the warm disc (Kennedy & Wyatt, 2014; Ballering et al., 2017; Geiler & Krivov, 2017). In any case, although both dust belts and hot gas likely share a similar, comet-related origin, we cannot identify any trend of the dust-disc properties - fractional luminosities, radii, and temperatures - with the presence or strength of the hot-gas absorptions. It is interesting to note that the prototype FEB host β *Pic* also harbours species of very hot dust in addition to hot gas (Defrère et al., 2012). HD 172555 also harbours both hot dust and gas (Ertel et al., 2014, 2016). The origin of this hot dust is still unclear. Although the samples of stars checked for hot dust and those for hot gas have little overlap so far, and thus a correlation cannot be seen, it seems conceivable that both phenomena might be related.

3.6 Conclusions

In this work we present high-resolution optical spectra of the currently known cold-gas-bearing debris-disc systems. The observations show Ca II and Na I non-photospheric absorptions in at least $\sim$ 78 %, and possibly 88%, of the discs seen edge-on, and in only $\sim$ 12% of the face-on discs. Those absorptions are usually interpreted as signposts of hot gas released by exocomets or small grains in the close vicinity of the central stars. Thus, these detection rates suggest that the non-detections in some discs seen close to face-on are most likely due to geometrical effects, that is, the inclination of the CS disc. At the same time, hot gas is only detected in A-type debris-disc systems, but it does not correlate either with any other stellar or disc properties.

The optical, infrared and submillimetre observations suggest that planetesimals/cometary bodies often populate gas-bearing debris-disc systems, from a few stellar radii up to hundreds of au. Collisions among those large bodies, as well as among small dust grains, and their evaporation are the agents, possibly accompanied by planets, as in the case of β Pic, structuring the CS environments and planetary systems of main-sequence stars. Choquet et al. (2017) have recently outlined a scenario to interpret the gas and dust structure of the 49 Ceti system; the authors suggest physical mechanisms for the production of gas at different distances from the central star. That scenario is likely at least roughly applicable to the systems studied in this work.

Chapter 4

Highlights of three remarkable objects in the sample

This chapter is based on the papers:
"Exocomet signatures around the A-shell star Leo?"
by C. Eiroa et al.
published in A&A 594, L1 (2016)
and
"HR 10: a main-sequence binary with circumstellar envelopes around both components"
by B. Montesinos et al.
published in A&A 629, A19 (2019)

4.1 Introduction

While exoplanets are now routinely detected and hundreds of debris discs provide indirect evidence of planetesimals around main-sequence (MS) stars (Matthews et al., 2014), little is directly known about minor bodies around stars other than the Sun. Only detections of variability in metallic lines of refractory elements, such as Ca II, point towards the presence of evaporating bodies, resembling solar system comets, around stars other than the Sun, called Falling Evaporating Bodies (FEBs) or exocomets (Ferlet et al., 1987; Kiefer et al., 2014b; Welsh & Montgomery, 2018). Up to date, only a few systems (~ 20, see Chapter 2) have shown such exocomet-like variations, all of them around A-type stars. But there are other physical explanations for this phenomenon, including the (unlikely) case of chromospheric activity in hot stars (Böhm et al., 2015). Out of the 117 objects contained in the original sample (see Chapter 2), and while there are several of them with remarkable variations in the Ca II K line in their spectra (e.g. HD 80007 or HD 85905), three were selected for individual analysis due to the singular shapes and periodicities observed : HD 98058(ϕ Leo), HD 256 (HR 10) and HD 37306.

These three A-type stars showed prominent variations, and in the following we will investigate whether the origin could be exocomets, or the result of other different processes.

Sect. 4.2 examines the high level of variations observed in the Ca II K line of ϕ Leo from the observations obtained in five observing runs from December 2015 to December 2016. In sect. 4.3, we confirm the non-exocometary origin for the variations observed in the classical exocomet-host star HR 10 (Redfield et al., 2007), and the evidences of its binarity. Finally, Sect. 4.4 analyses the shell-like profile absorptions observed in the metallic lines of HD 37306 in a single campaign in September 2018.

4.2 Exocomet-like variations in ϕ Leo

4.2.1 ϕ Leo: properties and astrophysical parameters

The source ϕ Leo is an A7IVn shell star (Jaschek et al., 1991) located at a distance of 56.5 pc. The star is seen close to edge-on with a very high rotational velocity, $v \sin i$ ~220 - 254 km/s (Lagrange-Henri et al., 1990d; Royer et al., 2007). It is surrounded by a gaseous CS disc detected in the Ti II 3685, 3759, 3762 Å lines and in the Ca II H/K lines (e.g., Jaschek et al., 1988; Abt, 2008). The star ϕ Leo is close to the center of the local interstellar bubble, a cavity of low density, which makes it unlikely that its shell –or disc– is formed by accretion of the interstellar medium, as conjectured for other A-shell stars (Abt, 2015). The Ca II K profile shows a triangular shape probably due to the combination of the photospheric and disc absorptions (Lagrange-Henri et al., 1990d). The star does not possess a warm debris disc (Rieke et al., 2005), although a cool debris disc cannot be excluded since data at $\lambda > 25$ μm are not available, to our knowledge. The best Kurucz photospheric model fitting our spectra is $T_{\rm eff}$ = 7500 K, $\log g$ = 3.75, $v \sin i$ = 230 km/s, v_{rad} = – 3 km/s in good agreement with previous estimates (e.g., David & Hillenbrand, 2015). Its bolometric luminosity is ~ 45 $L_\odot$ (Zorec & Royer, 2012), and age estimates are in the range ~ 500-900 Myr (David & Hillenbrand, 2015; De Rosa et al., 2014; Zorec & Royer, 2012).

4.2.2 Observations

High-resolution spectra of ϕ Leo were obtained with the high-resolution fiber-fed échelle spectrographs HERMES and FEROS attached to the Mercator (La Palma, Spain) and MPG/ESO 2.2 m (La Silla, Chile) telescopes, respectively. A total of 60 spectra of ϕ Leo were taken. Observing dates, telescope, and number of spectra per night are given in Table 4.1. HERMES has a spectral resolution of ~ 85000 (high-resolution mode) covering the range $\lambda\lambda$ ~370-900 nm (Raskin et al., 2011b). Exposure times ranged from 260 to 600 seconds. Some spectra were taken consecutively and combined after reduction. FEROS has a spectral resolution R~48000 covering the range from ~350 to 929 nm (Kaufer et al., 1999). Exposure times ranged from 120 to 360 seconds. The HERMES and FEROS spectra were reduced using the available pipelines of the two instruments. Barycentric corrections were also made for all spectra.

4.2.3 Results

Distinct changes are observed in the Ca II H and K lines of ϕ Leo; these affect the line profile as well as the wavelength and depth of the absorption peak. Variations occur on timescales of hours, days, and months. All the spectra show the triangular shape noted by Lagrange-Henri et al. (1990d) , modulated in most cases by an additional redshifted absorption. Furthermore, no temporal variability pattern is found. In the following we refer to the

Table 4.1: Log of observations

Observing run	Dates	Spectra per night
2015 December[1]	20, 22, 23	1, 4, 1
2016 January[1]	27, 28, 30	1, 3, 3
2016 March[1]	3, 4, 5, 6	4, 4 ,2 ,3
2016 March[2]	25, 26, 27, 28	4, 4, 3, 3
2016 May[1]	11	20

[1] HERMES, [2] FEROS

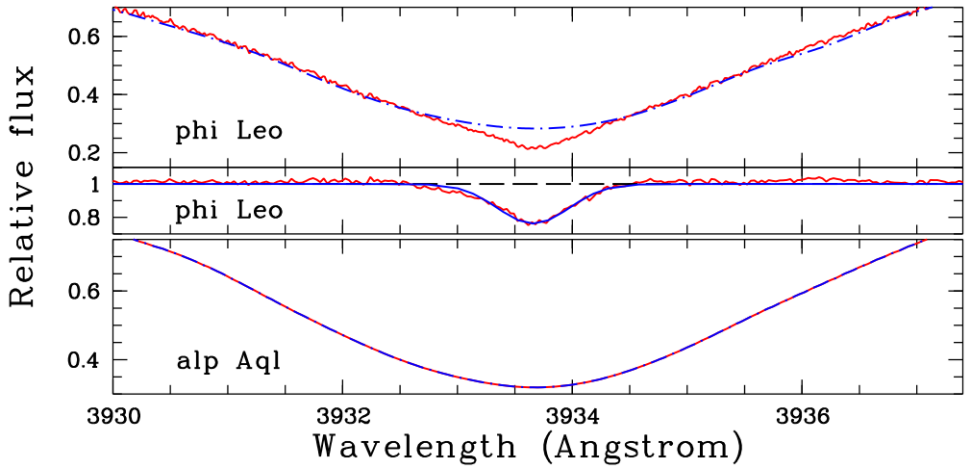

Figure 4.1: Top: Average Ca II K line of ϕ Leo from 2015 December 20 and 23 (red continuous line), together with a Kurucz photospheric model (blue dash-dotted line). See text for stellar parameters. Middle: residuals of the average of the spectra obtained on 20 and 23 December 2015 with respect to the photospheric line. The blue continuum line is a Gaussian with FWHM = 56 km/s. Bottom: observed Ca II K line (red line) of α Aql compared with a Kurucz model (blue dash-dotted line) with stellar parameters $T_{\rm eff}$ = 7900 K, $\log g$ = 4.25, $v \sin i$ = 210 km/s.

Ca II K line alone, although we also comment on some Ca II H line spectra to illustrate the results for this line in comparison with the K line.

Stable Ca II K component

The Ca II K line spectra taken on 20 and 23 December 2015 are identical with their absorption peaks at the stellar radial velocity, $v_{\rm rad}$ = -3 km/s (de Bruijne & Eilers, 2012). The remaining spectra are either deeper, with the absorption peak shifted to longer wavelengths, or with obvious additional redshifted absorption components superposed on the December 20 and 23 spectra. The exceptions are the spectra of 3 and 5 March 2016, which show small differences with those of December 20 and 23 (see below).

Figure 4.1 shows the average of the 20 and 23 December Ca II K line together with

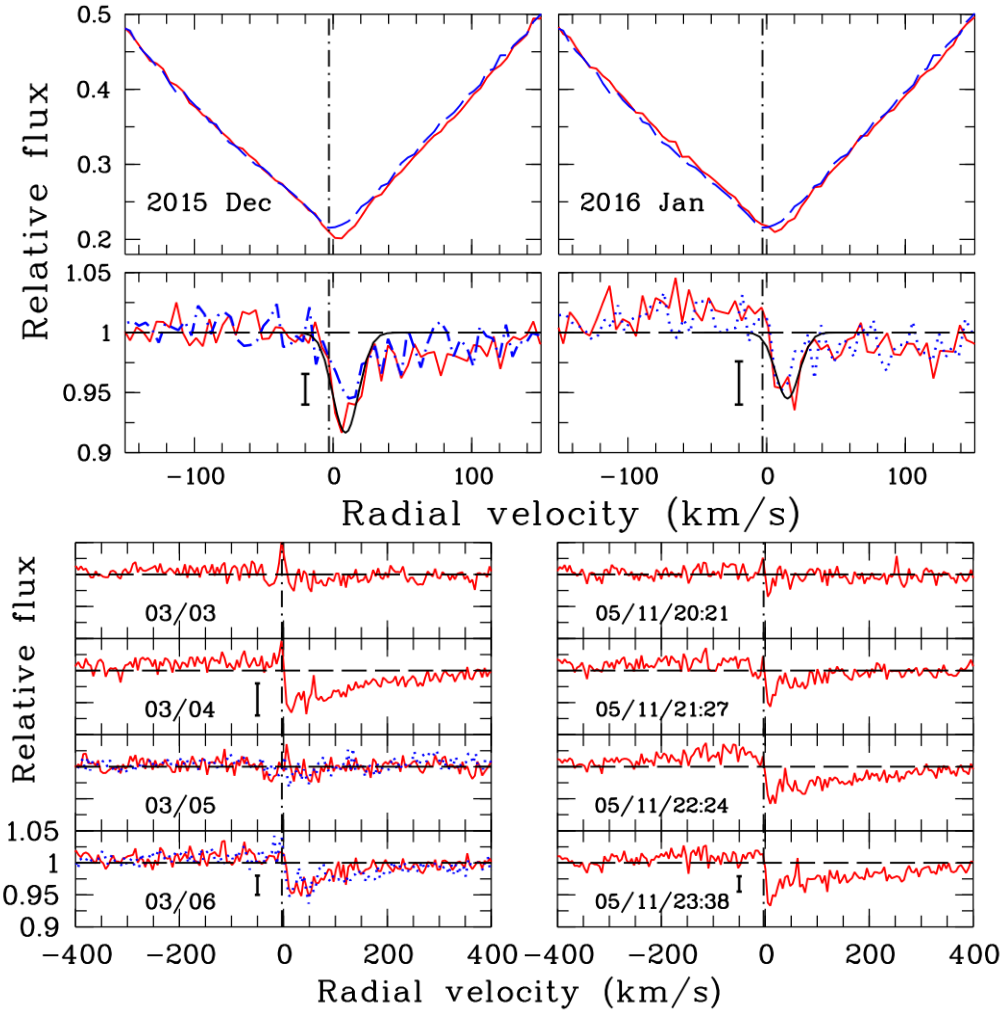

Figure 4.2: From left to right the Ca II K line from the observing runs with Mercator. At the top of the December and January panels the average of the four spectra obtained on 22 December and the average of the January spectra are plotted (red continuous lines) together with the template spectrum (blue dashed line). At the bottom the corresponding residuals are shown in red. To guide the eye, two Gaussians with FWHM 25 km/s (December) and 20 km/s (January) are plotted (black continuous line). The March panel shows the residuals of the average spectrum of each night. The May panel shows the average of five consecutive spectra of May 11 starting at the UT indicated in the panel. Some panels show the residuals of the Ca II H line for comparison (blue dotted line). A 3-σ error bar is plotted in some panels. The dash-dotted line at -3.0 km/s corresponds to the radial velocity of the star.

the photospheric line of the Kurucz model with the stellar parameters mentioned in Sect. 4.2.1. The broad additional absorption with a FWHM = 56 km/s at approximately the stellar radial velocity produces the triangular shape of the line profile. Its depth and equivalent width are 0.238 and 0.22 Å, respectively. This corresponds to a column density $N(\mathrm{Ca\ II}) \sim 2.3 \times 10^{12}$ cm^{-2}. To ensure that this additional absorption is real, we synthesised a photospheric model for α Aql, a star with similar spectral type (A7Vn) and rotational velocity, and compared it to spectra taken with the same instrument and configuration as for ϕ Leo. Figure 4.1 shows the excellent fit between the α Aql model and the observed spectra.

These results suggest that during December 20 and 23 we detected the contribution of a CS gas disc superimposed on the stellar photosphere, while the remaining spectra are affected by additional gas absorptions, although other causes producing the triangular absorption cannot be excluded (see below). In the following we assume that the additional absorption seen on December 20 and 23 is a stable component in addition to the ϕ Leo photospheric absorption and take the average of the two spectra as a template to analyse other contributions to the gas components.

Variable Ca II K components

Mercator 2015 December. The four spectra of December 22 show no appreciable changes, but their absorption is redshifted and deeper than the average December 20 and 23 template spectrum. Figure 4.2 shows the average of these four spectra and the residuals, taking the template spectrum as a continuum for the spectrum of December 22. An obvious absorption event occurs at v ∼6.0 km/s, that is, ∼9.0 km/s redshifted from the stellar radial velocity, and depth ∼0.083. A second event might be present at a velocity ∼16 km/s and depth ∼0.060. The equivalent width of both events together is ∼23 mÅ, and its FWHM is ∼25 km/s. The figure also shows the residuals corresponding to the Ca II H; in this case, only one event with a depth of ∼0.054 is clearly seen.

Mercator 2016 January. These spectra appear slightly redshifted with respect to the template spectrum, but their depth is lower than the one of December 22. There might be tiny changes among the spectra taken on different nights, although we consider only their average because poor weather conditions produced relatively low signal-to-noise (S/N) ratios. Figure 4.2 shows the 2016 January spectrum and its residual compared to the template. An event at ∼15 km/s, that is, redshifted by ∼18 km/s with respect to the stellar radial velocity, is clearly discernible. Its equivalent width is 20 mÅ, the depth is 0.055, and the FWHM is ∼20 km/s.

Mercator 2016 March. No detectable variations were recorded during the individual nights, but the Ca II K line clearly varied from night to night. Figure 4.2 shows the nightly residuals. The spectra of March 3 and 5 are similar to the template, but a clear flux depression is evident on March 4 and 6 at ∼16 km/s, the March 4 depth of ∼0.065 is deeper than the depth on March 6 of ∼0.047. In both cases, a broad wing extending up to ∼200 km/s might be present. The corresponding Ca II H line depths are 0.052 and 0.047 for March 4 and 6,

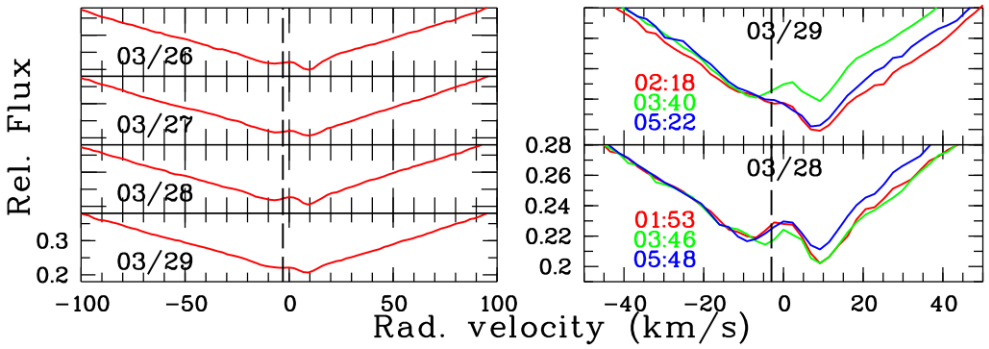

Figure 4.3: Ca II K spectra obtained with the MPG/ESO 2.2 m telescope from March 26 to March 29. Right: average of the nightly spectra. Left: individual spectra taken during the nights March 28 and March 29. colours correspond to the spectra obtained at different times (UT are shown).

respectively.

Mercator 2016 May. Twenty spectra were taken consecutively during four hours on 2016 May 11. Figure 4.2 shows the Ca II K residuals with respect to the template spectrum grouped in four one-hour periods. The residuals smoothly change in one hour, and an event at ∼9 km/s develops. Its deepest observed intensity of 0.068 depth is achieved during the last hour. A broad red wing seems to develop during the four observing hours.

MPG/ESO 2016 March. The Ca II K line exhibited a pronounced variation from night to night and within individual nights on timescales shorter than two hours. No regular pattern can be inferred from the variations. Figure 4.3 shows the average of the spectra taken during each of the four nights. All nights show a distinct redshifted event with respect to the template spectrum. Furthermore, the strength of the events changes strikingly from one spectrum to another, with time differences as short as 90 minutes. To exemplify this behaviour, Fig. 4.3 shows the individual spectra from March 28 and March 29. Events at ∼9 km/s and depths of 0.118 (March 28) and 0.093 (March 29) are detected. There might exist some blueshifted absorptions, at least on March 28, which vary in velocity, -4 to -9 km/s, and tiny changes in the depth of 0.04–0.05.

4.2.4 Discussion

The variable absorptions at 10-20 km/s from the star, with velocity dispersions of ∼10-20 km/s, depths of ∼0.05-0.1, and equivalent widths of ∼20 mÅ, that were observed in ϕ Leo behave similarly to those attributed to exocomets in β Pic. Nonetheless, it is reasonable to consider other alternatives because a remarkable difference between the two stars is that ϕ Leo does not have a massive debris disc. This might be due to the age of ϕ Leo because warm debris discs decline rapidly for stars older than a characteristic time of ∼150 Myr (Rieke et al., 2005). In addition, as noted before, it is unknown whether the star is surrounded by a cold debris disc, which in any case would decline rapidly for stars older than a characteristic

time of ∼400 Myr (Su et al., 2006). Furthermore, some relatively old stars with exocomet signatures do not possess a debris disc (Roberge & Weinberger, 2008).

For β Pic, phenomena involving the stellar atmosphere as the origin of the events were soon excluded (Lagrange-Henri et al., 1990d). This seems also to be the case of ϕ Leo, since we would expect a similar behaviour in other photospheric lines, which is not the case. Moreover, given the very short timescales of the variations, an origin in the interstellar medium is not plausible. Mass-loss rates resulting from weak radiatively driven winds in A stars are not expected to be significant around late-type A stars such as ϕ Leo. A wind origin like this was excluded for β Pic (Lagrange-Henri et al., 1992), although it has not been ruled out for events in other stars (Redfield et al., 2007). Sporadic mass-loss events, that is, clumps generated in a hypothetical stellar wind and rotating with the star, or moving outward with the wind, are expected to produce emission lines moving from blue to red across the center of the line, or be present in the blue and red wings of the wind lines. This is typically observed in relatively hot stars, like Be stars (Porter & Rivinius, 2003). However, this behaviour is not observed in ϕ Leo.

The ratio of the event depths observed in the Ca II K and H lines, ∼1-1.5, differs from the oscillator strength ratio of these lines (=2), suggesting that the variable absorptions arise at least partly from optically thick clumpy gas that covers a small fraction of the stellar surface, again similar to β Pic or HD 172555 (Lecavelier Des Etangs et al., 1997; Kiefer et al., 2014a). These results, together with the high-velocity broad line wings measured in some spectra, makes it plausible that the ϕ Leo events trace the evaporation of comet-like bodies in the CS environment. In this scenario, the broad wings could be produced by a sort of comet-like coma or by several unresolved events.

Assuming a cometary origin, the similar dynamical properties of the events could point to a disruption of a larger primordial body by tidal forces in a near-stellar encounter, or to a family of comets (Beust et al., 1996) driven into the vicinity of the star by a planet. Several not mutually exclusive mechanisms might deliver the bodies: Kozai-Lidov (Naoz, 2016), secular resonances (Levison et al., 1994), mean motion resonances (Beust & Morbidelli, 1996), or direct scattering by an eccentric planet (Beust et al., 1991). We note that only a future improvement of the event statistics in ϕ Leo will help to better constrain these dynamical mechanisms. The orbit of the infalling bodies can only be roughly estimated since the radial velocity is degenerated between the pericenter distance and the angle formed between the axis of the orbit and the line of sight (true anomaly). Thus, the largest pericenter distances at which the bodies can originate (for a 3.25 $M_\odot$ star, estimated from the stellar parameters in Sect. 4.2.1) is ∼20-70 au. The observed infall velocities, ∼0-20 km/s, possibly with some wings of up to 200 km/s, are much lower that the free-fall velocity at reasonable pericenter distances, 79 km/s and 177 km/s at 50 and 10 $R_\star$, respectively. The most plausible option apparently is that the potential exocomets follow parabolic to hyperbolic orbits that cross the line of sight, in which case the main absorption event and the broad wings at larger velocities can be explained. The crossing distances must be close enough to the star to allow refractory material to sublimate. Following Beust et al. (1998), the shortest crossing distance would

be ∼0.21 au using a FWHM of 20 km/s and assuming that the source of line broadening is Keplerian. Alternatively, if we assume thermal equilibrium (Beust et al., 1996), the distance at which dust sublimates, taking as a typical value $T_{\rm sub} = 1500$ K, would be ∼0.46 au or ∼0.33 au for albedos 0.0 and 0.5, respectively. These values depend on the composition of the grains.

With respect to the stable Ca II component, we can exclude to be originated in the local interstellar medium since interstellar lines are considerably narrower, the line of sight traverses the Leo cloud, which has a centroid radial velocity of 1.75 km/s (Redfield & Linsky, 2008a), and its equivalent width gives a lower limit for the column density of $N(H) \gtrsim 10^{20}$cm^{-2}, much higher than the expected interstellar column densities in the Leo direction (Redfield & Linsky, 2000). This means that the component might originate in one of the scenarios suggested for the stable CS gas disc in β Pic: stellar winds, star-grazing comet evaporation, or grain evaporation near the star or in the disc (see Fernández et al., 2006), although we note that the stable ϕ Leo component is broader and not as sharp as in β Pic (Lagrange-Henri et al., 1992). On the other hand, practically all stars showing an absorption photospheric profile with a triangular shape rotate at very high velocities, $v \sin i \gtrsim 200$ km/s. At these velocities the structure of the rotating stars and the inclination angle with respect to the line of sight affect their location on colour-magnitude diagrams (Bastian & de Mink, 2009), and the induced oblateness of the star produces a gravity darkening that results from the temperature gradient from the stellar equator to the poles. A preliminary test for which Kurucz models were combined with a temperature gradient from the equator to the poles indicated that the strength of the additional triangular absorption decreases with temperature.

4.2.5 Summary

Our intensive monitoring of ϕ Leo showed that its spectrum is very rich in redshifted absorption events, which might be accompanied in some cases by broad wings and even blueshifted absorptions. These sporadic events are similar to those in β Pic and can be most plausibly explained as exocomets that graze the star or fall onto the stellar surface. Assuming this scenario, it is intriguing how a relatively old 500-900 Myr star such as ϕ Leo, which does not have any known associated debris disc, possesses such a rich environment that hosts minor bodies. Another interesting aspect is the origin of what might be a triangular-shaped stable CS absorption component in the Ca II lines. Additional monitoring is clearly needed to better characterise the sporadic events and the stable component by comparing them with similar stars.

4.3 The binary nature of HR 10

4.3.1 Previous work on HR 10

HR 10 (HD 256, HIP 602) is a bright "shell star" ($V = 6.23$) (Cheng et al., 1991; Jaschek et al., 1991), also labelled as a "disc star" by Abt (2008) under the assumption that due to the large rotation velocity, the CS Ti II lines must originate in a disc. The spectral type classification of the object in the literature varies from A0 to A6, and luminosity classes IV or V. The current most accepted classification is A2 IV/V (see e.g. Wright et al., 2003,VizieR catalogue `III/231`). The spectrum of HR 10 resembles that of a rapidly rotating early A star ($v \sin i$=294 km/s, Mora et al., 2001).

Observations taken since the late 1980s show high spectroscopic variability in the narrow absorption components superimposed on the photospheric Ca II K line. Lagrange-Henri et al. (1990d) and Welsh et al. (1998) interpreted those variations within the FEB model, which is similar to that devised for β Pic.

Redfield et al. (2007) carried out a detailed study of the presence of narrow components superimposed on the photospheric Ca II and Na I lines, and their potential short- and long-term variability. The origin of the narrow Ca II K absorption was attributed to CS material, with no interstellar contribution, the variability being caused by the closeness of the gas to the star. No significant absorption was detected in Na I after water vapour lines were removed.

Abt (2008) pointed out the singularity of HR 10 as the only star in a sample of 20 objects analysed showing double Ti II narrow absorptions in the doublet around 376.0 nm. The redshifted components were interpreted as being caused by infalling material onto the star.

Concerning the spectral energy distribution (SED), Cheng et al. (1991) reported a weak IR excess at 12 and 25 μm from Infrared Astronomical Satellite (*IRAS*) data, whereas Redfield et al. (2007) did not detect any significant IR excess in *Spitzer* Infrared Array Camera (IRAC), Multiband Imaging Photometer (MIPS), or Infrared Spectrograph (IRS) measurements. An upper limit of $L_{\rm IR}/L_* < 6.1 \times 10^{-6}$ (consistent with the *Spitzer* upper limits at the longest IR wavelengths) was given by these latter authors, a value to be compared with $L_{\rm IR}/L_* \simeq 3.0 \times 10^{-3}$ (Backman & Paresce, 1993), or $\simeq 2.4 \times 10^{-3}$(Heinrichsen et al., 1999) for β Pic. There are no traces of accretion or emission lines in the spectra, and therefore the star is most likely not in the pre-MS phase.

So far, HR 10 has been treated in the literature as a single object. In retrospect, this fact has been a tight constraint not only in interpreting the observed variability, but also in determining its absolute parameters and its position in the HR diagram. The single-star assumption yielded some controversial results; the V magnitude, and the *Gaia* DR2 distance, $\varpi = 6.8882 \pm 0.1184$ mas, $d = 145.18^{+2.54}_{-2.45}$ pc (*Gaia* Collaboration, 2018), imply an absolute magnitude of $M_V \simeq +0.42$, which would put the star closer to luminosity class ~III/IV; Redfield et al. (2007) found a value $L_*/L_\odot = 63.8$ which corresponds to a typical ~A2 III (Aller

et al., 1982), both results being in contrast with the spectral classification IV/V. Montesinos et al. (2009) estimated the stellar gravity from the width of the wings of the Balmer lines and derived the mass and age from a $\log g_*$– $\log T_{\rm eff}$ HR diagram and evolutionary tracks, and then the luminosity from the corresponding point in the $\log L_*/L_\odot$–$\log T_{\rm eff}$ HR diagram; the fact that the Balmer lines – and the whole spectrum – are actually the composite of profiles from two stars invalidates the initial measurement of $\log g_*$ and then the set of parameters derived. The discovery of the binarity of HR 10 makes a complete reassessment of the stellar parameters compulsory.

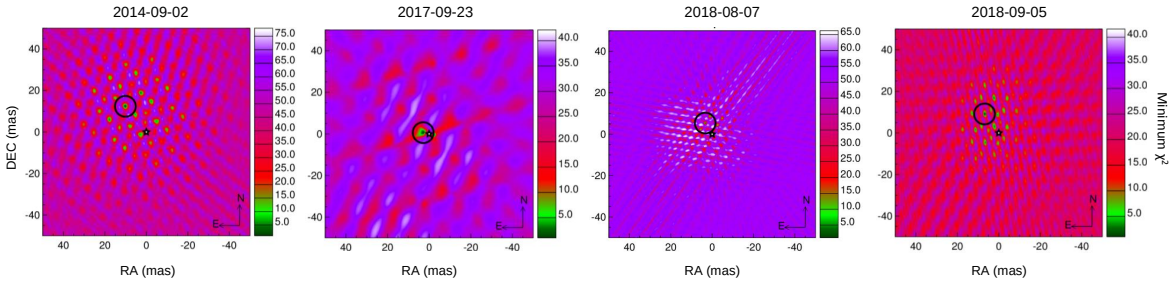

Figure 4.4: Normalised χ-square maps of the combined cp+V^2 for the four PIONIER/VLTI observations. The maps are centred at the brightest component. The black circles indicate the positions of the minima in the maps and the star marks the position of the bright component.

4.3.2 PIONIER/VLTI observations

Interferometric observations of HR 10 were first performed in September 2014 as part of a search for hot exozodiacal dust (see details of the programme in Ertel et al., 2014, 2016) and three more times in September 2017, and August-September 2018, for a total of four epochs. The Precision Integrated Optics Near-Infrared ExpeRiment (PIONIER, Le Bouquin et al., 2011) on the Very Large Telescope Interferometer (VLTI) was used. PIONIER is a four-telescope beam combiner allowing the user to simultaneously obtain squared visibility (V^2) measurements on six baselines and closure phase (cp) measurements on four telescope triplets. A log of the observations is provided in Table 4.2.

PIONIER operates in H band; the light was dispersed over three (in 2014) and six spectral channels (later) across this band. Chains of alternating observations of a calibration star (CALs) and the science target (SCI) were executed in order to characterise the interferometric transfer function (TF) and calibrate the V^2 and cp measurements of the science target. Each chain started and ended with a CAL, and various CALs were used within a chain in order to minimise the impact of imperfect knowledge of the calibration stars (e.g. uncertain stellar diameters or unknown companions).

Data reduction and calibration were performed with the PIONIER pipeline `pndrs` (Le Bouquin et al., 2011) version 3.79 using standard parameters. In particular, we calibrated

a whole sequence of CAL and SCI observations at once using the smooth TF interpolation method provided by the pipeline.

The binary signature is obvious in both the calibrated and uncalibrated V^2 and cp data, making for a strong detection with each observation. In order to extract the astrometric information (separation and position angle) and contrast (secondary-to-primary flux ratio) of the binary, we follow the method outlined by Absil et al. (2011) and Marion et al. (2014). We compute the χ^2 goodness of fit to the V^2 and cp data, both separately and jointly, for a series of binary star models with a range of positions and flux ratios. The resulting χ^2 cubes (one for the V^2, one for the cp, and one for the combination of both) were used to identify the best-fit model and evaluate the significance of the detection. The results are listed in Table 4.2. Figure 4.4 shows the normalised χ-square maps of the combined $cp + V^2$ for the four PIONIER/VLTI observations of HR 10.

Table 4.2: PIONIER observations of HR 10.

Date	2014-09-02	2017-09-23	2018-08-07	2018-09-05
Starting time [UT]	06:13:06	02:55:38	09:15:56	07:50:37
BJD [TDB] mid observation	2456902.7803	2458019.6773	2458337.8991	2458366.8422
Programme	093.C-0712(B)	099.C-2015(A)	0101.C-0182(B)	0101.C-0182(B)
VLTI array	D0-G1-H0-I1	A0-B2-C1-D0	A0-G1-J2-J3	A0-G1-J3-K0
# SCI observations[a]	3	4	2	2
Significance in cp	1435	50	283	247
Significance in V^2	8271	1378	1623	4948
Significance combined	1038	963	1046	654
Separation [mas]	15.98±0.35	2.94±0.56	6.34±0.16	11.43±0.27
Position angle [deg][b]	39.3±1.2	77.7±2.5	32.1±0.3	37.0±2.7
Contrast (%)	32.0±1.5	35±13	31.9±3.9	31.9±2.8

Notes: (a) Number of observations (observing blocks) executed on the science target and bracketed by observations of calibrators. (b) The position angle is measured east of north, i.e. counterclockwise from the north.

4.3.3 Spectroscopic observations

In this section we describe the sets of high-resolution spectroscopic observations of HR 10 that have been used in this work to analyse the CS narrow absorption features superimposed on the photospheric lines, decompose their complex profiles, and measure the corresponding RVs of the components. We built a historical record covering the period 1986–2019 in order to complete what is to date the most comprehensive study of the CS variability of this object.

4.3.4 Dedicated campaigns

Table C.1 (upper block) summarises the information of the campaigns coordinated by our team since September 2015 to observe HR 10, among other stars, looking for transient exo-

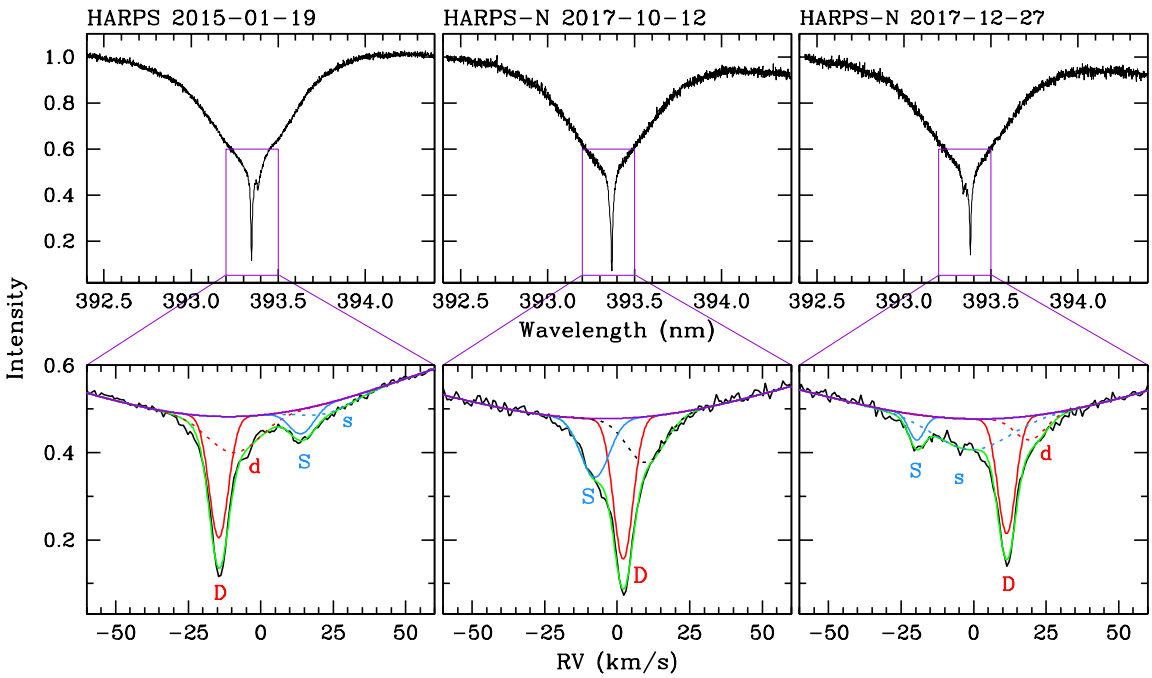

Figure 4.5: Top: Profiles of the broad photospheric Ca II K line of HR 10 of spectra obtained on 19 Jan 2015, 12 Oct 2017 and 27 Dec 2017. Superimposed on the lower part of the lines, narrow absorption features are remarkably conspicuous. Bottom: Narrow CS components corresponding to the spectra at the top, plotted in velocity space. The velocity RV = 0 km/s corresponds to the rest wavelength of the Ca II K line. The letters D and S label the deep and shallow components of each CS absorption, respectively; these are present in all the spectra analysed in this work. Solid red and blue lines correspond to the Gaussian decomposition of those two main components, the bottom of the photospheric profile is plotted in purple and the whole fit in green. Dotted lines are the additional Gaussians d and s required to complete the decomposition of the absorption. See text for details.

cometary events around MS stars, and campaigns targeted exclusively at HR 10. Signal-to-noise ratios (S/Ns) of the spectra at the bottom of the Ca II K line were always above 100. The spectra used in this work come from the corresponding reduction pipelines.

Archival and published data

In Table C.1 (lower block) we give the relevant information for the observations obtained prior to September 2015, when we started our own monitoring campaigns. The data come from the literature, were provided by one of the authors (Prof. Seth Redfield), or were taken from observatory archives. Direct measurements on the reduced spectra, corrected for barycentric velocity, were done for the observations obtained with UES/WHT, CS21/2.7-m HJS, UVES/VLT, HIRES/Keck, and HARPS/3.6-m La Silla, and on the spectrum taken on 15 Jun 2005 with UHRF/3.6-m AAO. The spectra from Lagrange-Henri et al. (1990a)

were not available in readable format, and were therefore scanned from the paper itself and digitised. The data on radial velocities from the observations obtained on 30 Nov 1996 and 20 Jun 1997 were taken directly from the work by Welsh et al. (1998).

4.3.5 The circumstellar absorption features

The Ca II K line

Figure 4.5 (top) shows the profiles of the broad photospheric Ca II K line of spectra of HR 10 obtained on 19 Jan 2015, 12 Oct 2017, and 27 Dec 2017. Superimposed on the lower part of the lines, narrow absorption features are remarkably conspicuous. The insets delimited with purple boxes are blown up and plotted in velocity space at the bottom row; RV = 0 km/s corresponds to the rest wavelength of the Ca II K line, namely, 393.366 nm.

These three observations are representative of what we see in the *whole set* of spectra analysed in this work. The decomposition of the profiles in Gaussian components was carried out using the `Emission Line Fitting (ELF)` package of `dipso`, a spectrum analysis program developed by the Starlink Project (Howarth et al., 2004). The common feature of all the narrow absorptions is the presence of two main components: one deep and one shallow, hereafter plotted as red and blue solid lines, respectively, when the absorption is decomposed into Gaussian functions and labelled 'D' and 'S'. The origin of these narrow absorption features is clearly CS, their variability being attributed in previous works to β Pic-like phenomena (see Sect. 4.3.1), however the interpretation of their dynamical behaviour, as we see below, when analysing the RV series over a long time span turns out to be related to the binarity of HR 10 rather than to transient phenomena.

The profiles of the observations taken on 19 Jan 2015 and 27 Oct 2017 (left and right panels of Fig. 4.5) show two cases where the D and S components appear well separated, whereas the observation taken on 12 Oct 2017, plotted in the middle, shows a case where the separation in radial velocity between D and S is small. The pattern observed during the ~ 32 years of observations collected is that component D moves to the blue (red), as component S moves to the red (blue), crossing each other at certain times.

When the profile was such that the two main components appeared well separated, a four-Gaussian fit was needed to reproduce the whole narrow absorption. The two additional components, plotted as dotted red and blue lines, are placed to the red side of the main D and S components, respectively; these latter have been labelled as 'd' and 's', to stress the fact that each one seems to be associated with D and S. When the profile showed an appearance similar to that plotted in the middle graph of Fig. 4.5, a three-Gaussian fit was accurate enough to reproduce the absorption. Whereas in the four-Gaussian fittings the d and s components, redshifted with respect to D and S, seem to have a physical relationship with their corresponding main component, in the case of three-Gaussian fits, the parameters of the additional component probably embed the contribution of the two dotted components

of the four-Gaussian decomposition. In Fig. 4.5 the pseudocontinuum tracing the bottom of the broad photospheric line is plotted in purple and the fit to the whole profile is plotted in green. For the three-Gaussian fit the additional component has been plotted as a dotted black line.

Figure 4.6 shows the results of a well-sampled monitoring carried out between 5 Oct 2017 and 3 Jan 2018 (21 spectra obtained with FIES/NOT and HARPS-N/TNG), where the gradual dynamical evolution of D and d moving to the red, and S and s moving to the blue, is very clear. The colour code is the same as in Fig. 4.5.

We quantitatively analyse the behaviour of all these components in Sects. 4.3.6 and 4.3.7.

Circumstellar absorption features in other photospheric lines

In this work we concentrate on the analysis of the Ca II K line for two main reasons: the first one is that this line is the most important and clear tracer of CS activity, as has been proved in β Pic and other stars (see references in the Introduction); the second is that for some of the early spectroscopic observations, which have been crucial for the completion this study, only data for this particular line were available. However, HR 10 presents narrow CS absorption features superimposed on many other photospheric lines.

Figure 4.7 shows the CS components superimposed on 24 photospheric lines of the spectrum of HR 10. Since some of these components are fairly weak, in order to increase the S/N, five FIES/NOT spectra – those taken between 26 Dec 2018 and 8 Jan 2019, see Table C.2 – were averaged. These were chosen because the separation in RVs of the Ca II K narrow absorption features is large, almost 30 km/s, and therefore the CS components present in other lines would appear well separated. The photospheric profile of each line has been subtracted and the residual narrow absorption features have been scaled between intensities 0.5 and 1.0. The red and blue solid lines are the average RVs of the D and S components of the Ca II K absorption, and the dashed line marks the RV of the system. The Ca II K CS absorption is plotted with a thicker line type.

In most cases, the CS narrow absorption features follow the same pattern of intensity as in Ca II K, with the remarkable exception of the IR Ca II triplet, where a strong component is seen in the three lines at the velocity of the shallow component of the Ca II K absorption. Conversely, a weak absorption at the velocity of the Ca II K strong component is clearly visible in the central and most intense line of the triplet (854.21 nm), but does not appear in the other two. On the other hand, the appearance of the absorption features at the Na I D doublet is complex due to the many telluric lines in that spectral range; these were removed using the package `MOLECFIT`[1] (Smette et al., 2015b; Kausch et al., 2015b).

Figure 4.8 shows the narrow CS components superimposed on the photospheric Ca II K and H lines, the Ti II 375.93 + 376.13 nm and the Fe II 423.32 nm lines; in the case of the

[1] http://www.eso.org/sci/software/pipelines/skytools/molecfit

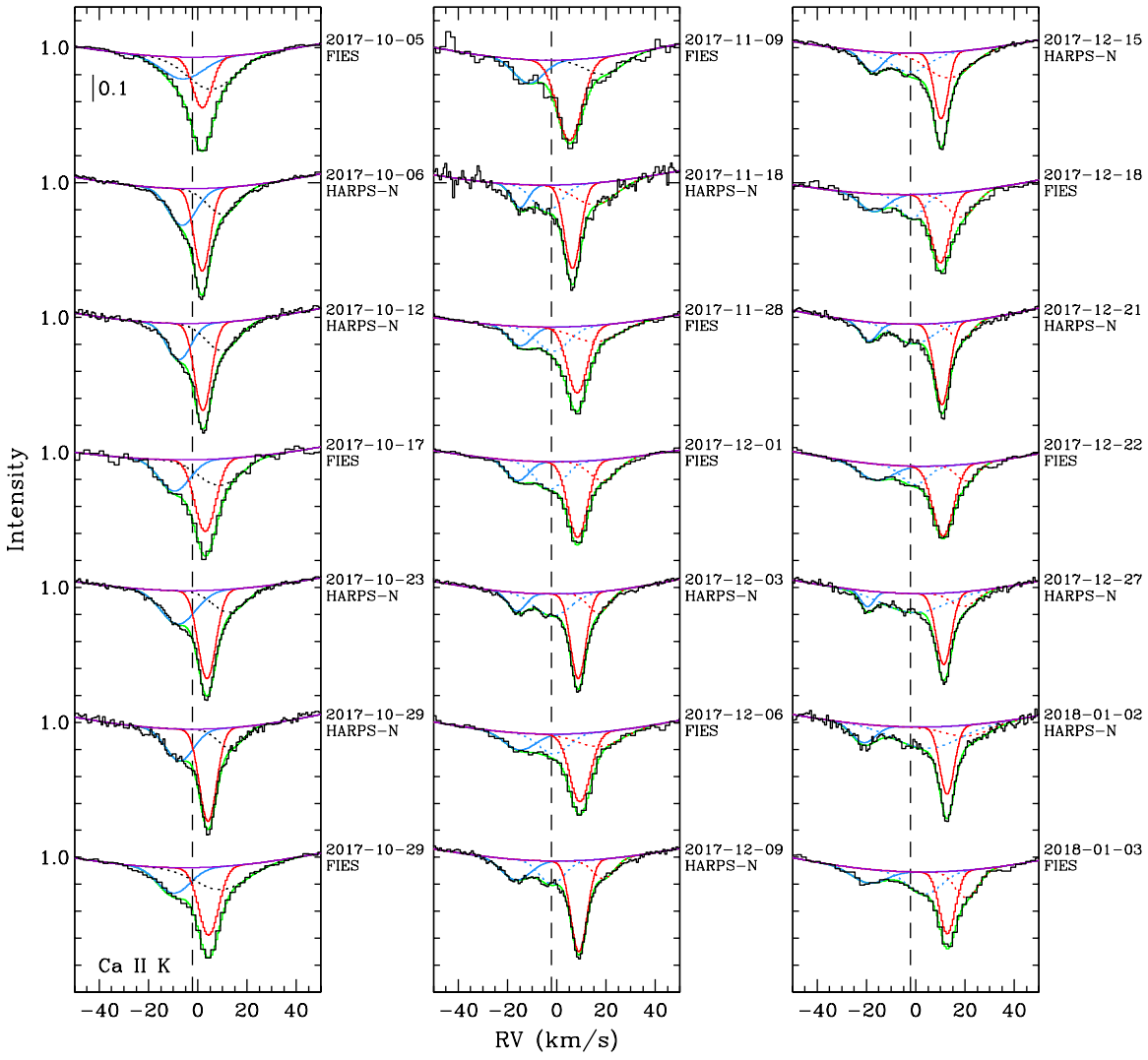

Figure 4.6: The Ca II K CS profile for 21 observations obtained with FIES/NOT and HARPS-N/TNG between 5 Oct 2017 and 3 Jan 2018. The profiles have been decomposed with three or four Gaussians, plotting D (d) and S (s) as solid (dotted) red and blue lines. The pseudocontinuum tracing the bottom of the broad photospheric line is plotted in purple and the fit to the whole profile is plotted in green. For the three-Gaussian fit the additional component has been plotted as a dotted black line. The dashed line marks the RV of the system -2.18 ± 0.32 km/s (see Sect. 4.3.6 and Table 4.3).

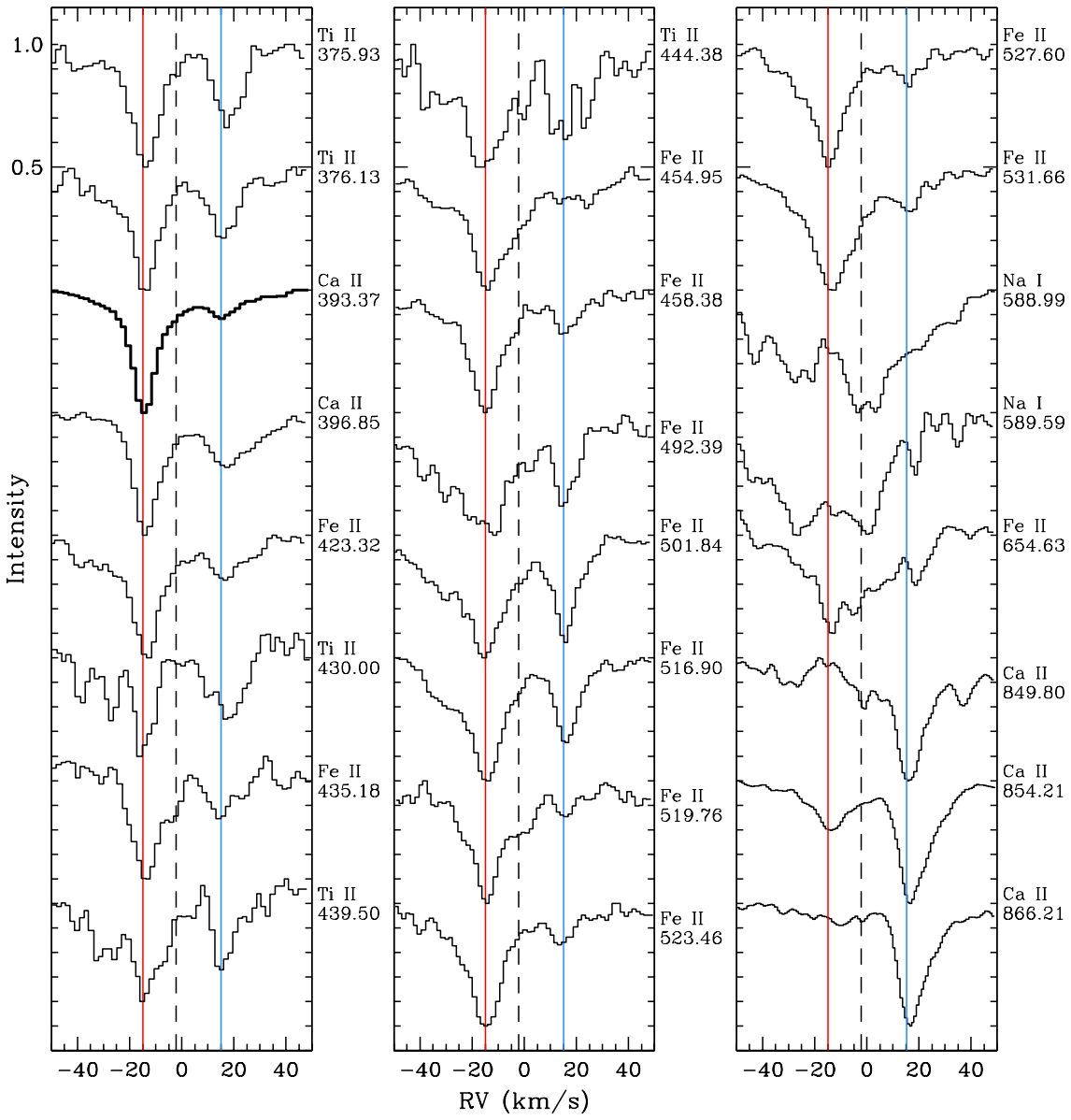

Figure 4.7: Circumstellar components in 24 lines of the optical spectrum of HR 10. The photospheric profiles have been subtracted and, for the sake of clarity, the narrow absorption features have been scaled to the same size. The red and blue lines mark the radial velocities of the D (deep) and S (shallow) components, -14.80 ± 0.50 $+15.16 \pm 1.54$ km/s, respectively, of the Ca II K narrow absorption, which has been plotted with a thicker line. The dashed line marks the RV of the system, -2.18 ± 0.32 km/s. The line identification with the wavelength in nm is included. See text for details.

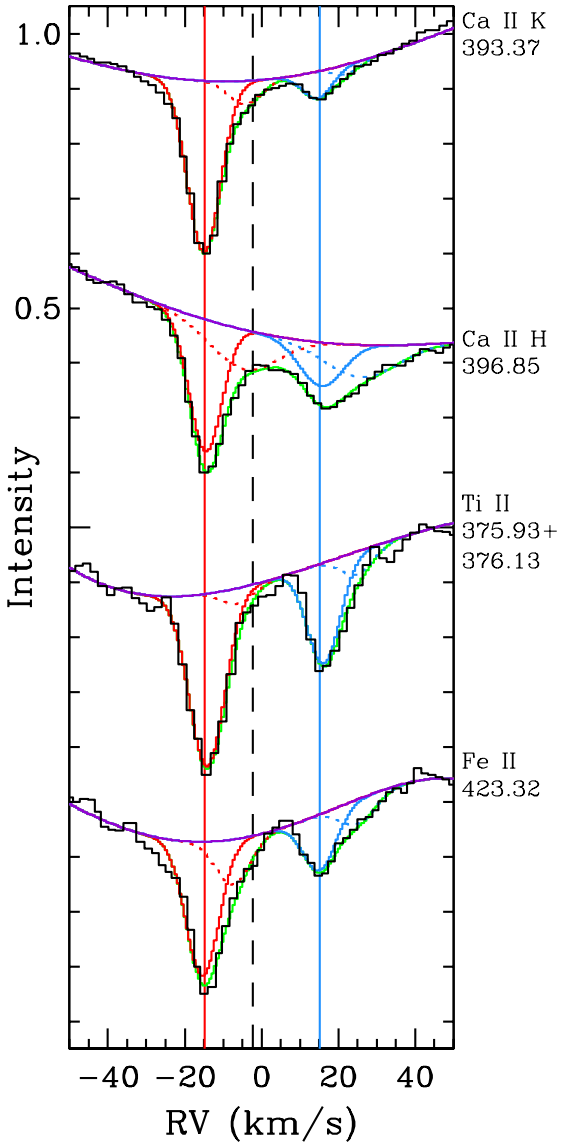

Figure 4.8: Circumstellar components of the narrow absorption features superimposed to the photospheric Ca II K and H lines, the Ti II doublet around 376.0 nm, and the Fe II line at 423.32 nm, for the same set of observations as in Fig. 4.7; the vertical solid red and blue lines and the dashed black line mark the same radial velocities as in that figure. The Gaussian decomposition clearly shows the presence of the S, D (solid red and blue lines), s, and d (dotted red and blue lines) components. The line identification with the wavelength in nm is included. See text for details.

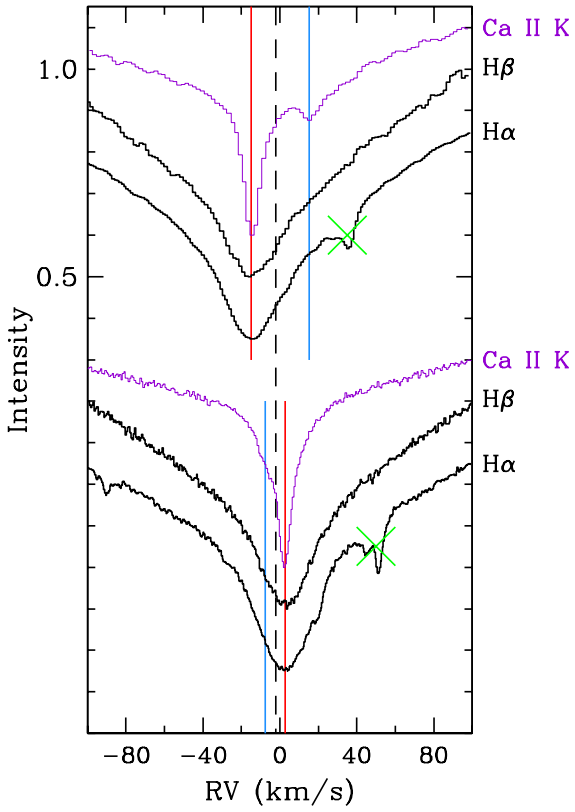

Figure 4.9: Bottom of the Balmer lines Hα and Hβ for observations corresponding to a configuration where the difference in RVs is large (top) and small (bottom). The red and blue lines mark the radial velocities of the D and S components, measured on the Ca II K narrow absorption features, plotted in purple as references. Those RV are -14.80 ± 0.50 (D), $+15.16 \pm 1.54$ km/s (S) (top), and $+2.75 \pm 0.73$ (D), -7.72 ± 1.38 (S) km/s (bottom). The dashed line marks the RV of the system, -2.18 ± 0.32 km/s. The two green crosses mark the position of telluric lines.

Ti II doublet, the profiles of the two CS absorptions of the two lines, in velocity space, were merged and converted into a single profile. Colour codes and the meaning of the vertical lines are the same as in Figs. 4.5, 4.6, and 4.7. It is remarkable that components s and d, which appear in the Gaussian decomposition of the Ca II K narrow absorptions, are also present in other species.

Figure 4.9 shows the bottom of the photospheric Balmer lines Hα and Hβ for two situations with the D and S components of Ca II K – plotted in purple as a reference – appear well separated (top) and blended (bottom). The profiles at the top correspond to the same spectra used in Fig. 4.7, whereas the profiles at the bottom are extracted from an average of the HARPS-N spectra obtained on 6 Oct 2017 and 24 Oct 2017. The vertical red and blue lines mark the RVs of components D and S and the dashed black line marks the RV of the system; three telluric features on the Hα profiles are marked by green crosses. It is very clear that the minima of the Balmer profiles are located at the RV of component D. The profiles at the top are clearly asymmetric. In the following section it becomes clear why this happens, the binarity being the origin of the variable shape and position of the bottom of these lines.

We defer to a forthcoming paper a more detailed analysis of the CS absorption features in lines other than Ca II K, and also of the Balmer lines.

4.3.6 Results

Radial velocities and velocity dispersions.

Table C.2 shows the RVs and velocity dispersions, b, of the deep, D, and shallow, S, components of the narrow CS absorption features superimposed on the bottom of the photospheric Ca II K line, measured for all spectra. In those cases where a four-Gaussian fit was feasible, the same results for the d and s components are listed. The RVs correspond to the minimum of the main Gaussian components of the absorption (see Sect. 4.3.5) and the dispersion velocities are the full widths of the Gaussian profiles. All the values correspond to spectra obtained on individual nights; only in three cases were the measurements carried out over averaged spectra obtained on consecutive nights, namely 28-29 Aug 2004 (CS21), 4 to 7 Sep 2015 (HERMES), and 23-24 Oct 2017 (HARPS-N), to increase the S/N of the profile.

Uncertainties were assigned in a very conservative way taking into account those provided by the ELF package after the Gaussian decomposition of the profiles, and the effect of potential offsets between the wavelength calibrations provided by the pipelines of the different instruments. The quantitative effects of these offsets can be estimated by measuring the position of the telluric lines in spectra from the different spectrographs; differences in velocities were found to be less than ~ 0.2 km/s.

Figure 4.10 shows a plot of the whole set of RVs for the D (red) and S (blue) components given in Table C.2 with the corresponding error bars. With the only purpose of guiding

Table 4.3: Median and 68.7% confidence intervals for the RV parameters analysed in Sect. 4.3.6. Prior distributions are also given.

Parameter	Prior	Posterior
$V_{\rm sys}$ [km/s]	$\mathcal{U}(-30.0, 30.0)$	$-2.18^{+0.34}_{-0.31}$
$P_{\rm orb}$ [days]	$\mathcal{G}(747.0, 20.0)$	$747.60^{+0.61}_{-0.70}$
$T_{\rm c,A}$ [BJD-2400000]	$\mathcal{G}(57562.4, 20.0)$	$57563.5^{+8.0}_{-7.2}$
$K_{\rm A}$ [km/s]	$\mathcal{U}(0.0, 40.0)$	$16.45^{+0.76}_{-0.79}$
$e_{\rm A}$	$\mathcal{U}(0.0, 0.9)$	$0.254^{+0.036}_{-0.039}$
$\omega_{\rm A}$ [$^\circ$]	$\mathcal{U}(-180.0, 180.0)$	$38.0^{+4.0}_{-4.0}$
$T_{\rm c,B}$ [BJD-2400000]	$\mathcal{U}(57562.0, 58309.0)$	$58022.3^{+6.4}_{-8.6}$
$K_{\rm B}$ [km/s]	$\mathcal{U}(0.0, 40.0)$	$20.35^{+0.69}_{-0.72}$
$e_{\rm B}$	$\mathcal{U}(0.0, 0.9)$	$0.209^{+0.030}_{-0.026}$

Note: $\mathcal{U}(a, b)$ stands for uniform prior between a and b, while $\mathcal{G}(\mu, \sigma)$ represents a Gaussian prior with mean μ and standard deviation σ.

the eye, we have included in the graph two sinusoidal curves, plotted in pale red and blue, without any quantitative physical meaning, to show that the behaviour of the RV of each component seems to follow a periodic pattern over decades. The most plausible scenario is that each component, D and S, traces the orbit of each individual star in the binary. In the following sections we prove, by means of robust calculations of a spectrometric binary solution (Sect. 4.3.6) and an orbital solution (Sect. 4.3.6), that this hypothesis is consistent.

Spectrometric binary solution

In this section we derive the spectrometric solution for the binary under the assumption mentioned in the last paragraph. We assign component D to HR 10-A, and component S to HR 10-B, the reason for this being, as we show in the following, that component D originates in the more massive of the two stars (component A) as it displays a smaller amplitude in the RV variation than component S.

We first computed the Lomb-Scargle periodogram of the measured RVs for each star using the `astroml` package (Ivezić et al., 2014) based on the methodology described in Zechmeister & Kürster (2009). This periodogram is shown in the upper panel of Fig. 4.11. The result clearly shows a common peak above the 0.1% false-alarm probability (FAP) corresponding to a periodicity of ≈ 747 days, indicating that both are gravitationally bound. Although the periodogram shows other peaks above the 0.1% FAP level, we attribute their origin to the different offsets between the many different instruments used, which are not

taken into account in this periodogram computation but are in the modelling of the RV.

We analyse the RV sets obtained from each component, D and S, – corresponding to stars A and B – by modelling the whole system. The model includes two Keplerian orbits described by

$$\begin{aligned} V_{\mathrm{rad\,A}} &= V_{\mathrm{sys}} + K_{\mathrm{A}}\left[\cos(\nu_{\mathrm{A}} + \omega_{\mathrm{A}}) + e_{\mathrm{A}}\cos(\omega_{\mathrm{A}})\right] \\ V_{\mathrm{rad\,B}} &= V_{\mathrm{sys}} + K_{\mathrm{B}}\left[\cos(\nu_{\mathrm{B}} + \omega_{\mathrm{A}} + \pi) + e_{\mathrm{B}}\cos(\omega_{\mathrm{A}} + \pi)\right] \end{aligned} \tag{4.1}$$

where V_{sys} is the systemic velocity of the binary system, ω is the argument of the periastron of star A, e_{A} and e_{B} are the eccentricities of the orbits of stars A and B, respectively, and ν_{A} and ν_{B} are the true anomalies of each star, which implicitly include the times of conjunction $T_{\mathrm{c,A}}$ and $T_{\mathrm{c,B}}$. We used uninformative priors for all the parameters except for the orbital period, P_{orb}, and the conjunction passage. For P_{orb}, we used a normal distribution around the highest peak of the RV periodogram. The prior for the conjunction passage was set after a first exploration with an uninformative prior. The boundaries of the priors for all parameters are specified in Table 4.3. Additionally, we included N_{inst}-1 additional parameters to account for RV offsets between the different instruments, with N_{inst} being the number of instruments used. We set uninformative priors for these parameters between -1 and $+1$ km/s. In total, 19 parameters were explored.

In order to sample the posterior probability distribution of each of those parameters, we used the implementation of Goodman & Weare's affine invariant Markov chain Monte Carlo (MCMC) ensemble sampler `emcee` developed by Foreman-Mackey et al. (2013). We used 50 walkers and 5000 steps per walker. This turned out to be enough due to the quick convergence of the chains. In order to compute the final posterior distributions, we discarded the first half of the chains and combined the second half to build the marginalised posteriors, finally composed of 1.25×10^5 steps. The median and 68.7% confidence intervals for each parameter are shown in Table 4.3. The results of the final fitting are displayed in Fig. 4.12 showing the whole time span and Fig. 4.13 showing the phase-folded RV curves; this figure also includes the RVs of components d and s, the behaviour of which is described in Sect. 4.3.7.

Orbital solution

The four PIONIER astrometric positions of the two stellar components of the binary system were analysed following the equations of motion described in Mede & Brandt (2017,see their Eqs. 7-15). Given the low number of epochs, we assumed Gaussian priors on the orbital period, P_{orb}, and the eccentricities of the two orbits, e_{A} and e_{B}, as obtained from the RV analysis. For the rest of the parameters (namely the argument of the periastron of star A, ω_{A}, the longitude of the ascending node of star A, Ω_{A}, orbital inclination, i, time of periapsis T_0, and the total semi-major axis, $a_{\mathrm{tot}} = a_{\mathrm{A}} + a_{\mathrm{B}}$, we used uninformative priors as stated in Table 4.4. The posterior distribution of these parameters was explored using again the `emcee` code. We

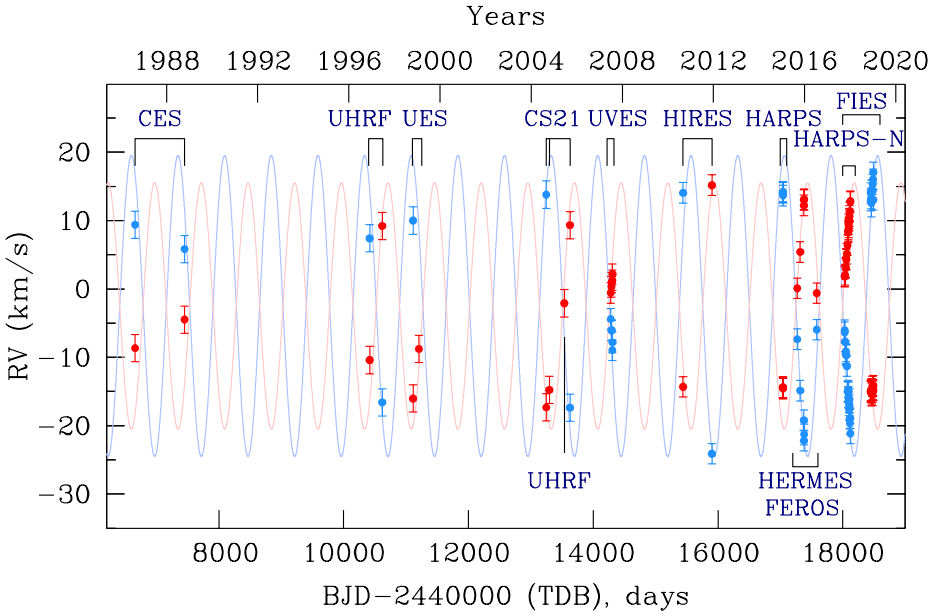

Figure 4.10: Radial velocities of the components D (red) and S (blue) of the CS Ca II K narrow absorption features for all the observations. The sinusoidal curves plotted as pale red and blue have the only purpose to show, in a qualitative way, that the behaviour of the RVs shows a periodic pattern during the $\sim$ 32-yr interval covered by the observations. The exact treatment of the data is explained in Sect. 4.3.6. The labels indicate the instruments with which the observations were obtained (see Sect. 4.3.3).

Table 4.4: Median and 68.7% confidence intervals for the orbital parameters analysed in Sect. 4.3.6. Prior distributions are also displayed

Parameter	Prior	Posterior
$P_{\rm orb}$ [days]	$\mathcal{G}(747.58441074, 0.67)$	$747.36^{+0.67}_{-0.64}$
T_0 [BJD-2400000]	$\mathcal{U}(57200.0, 57600.0)$	57453^{+22}_{-44}
$a_{\rm tot}$ [mas]	$\mathcal{U}(10.0, 50.0)$	$10.58^{+0.60}_{-0.37}$
$\Omega_{\rm A}$ [°]	$\mathcal{U}(0, 360)$	$137.65^{+0.83}_{-0.84}$
$\omega_{\rm A}$ [°]	$\mathcal{U}(-180.0, 180.0)$	17^{+11}_{-22}
i [°]	$\mathcal{U}(90.0, 100.0)$	$93.34^{+0.60}_{-0.63}$
$e_{\rm A}$	$\mathcal{G}(0.24, 0.03)$	$0.242^{+0.017}_{-0.012}$
$e_{\rm B}$	$\mathcal{G}(0.207, 0.03)$	$0.208^{+0.015}_{-0.011}$

Note: $\mathcal{U}(a, b)$ stands for uniform prior between a and b, while $\mathcal{G}(\mu, \sigma)$ represents a Gaussian prior with mean μ and standard deviation σ.

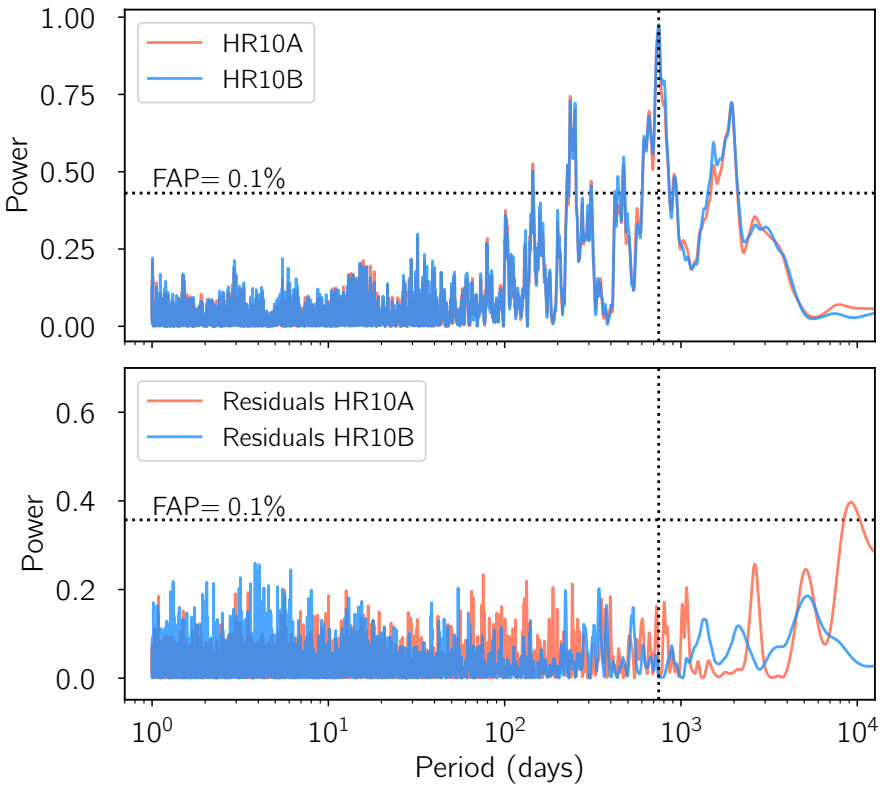

Figure 4.11: Top: Periodogram corresponding to the RV measurements for each of the two components of the binary system in HR 10. The 0.1% FAP is shown as a horizontal dotted line and the final orbital period is displayed as a vertical dotted line. Bottom: Periodogram of the residuals of the RV modelling.

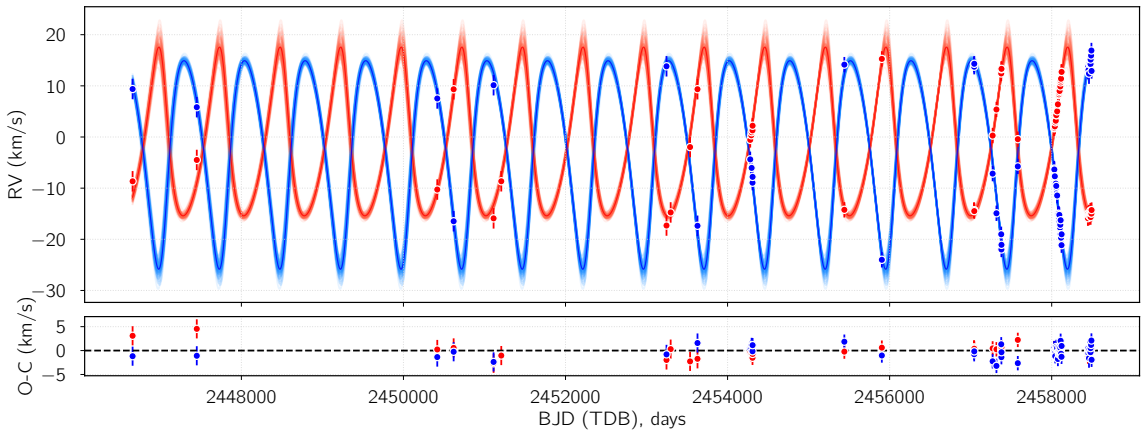

Figure 4.12: Radial velocity measurements of the two stars along the $\sim$ 32 years of observations. Red and blue symbols and lines correspond to components D and S from the Gaussian fittings of the narrow Ca II K absorptions, which in turn correspond to stars A and B, respectively. The upper panel shows the model corresponding to the median values of the posterior distributions of the parameters as thick lines and 100 random samples drawn from the final MCMC chain; the lower panel shows the residuals.

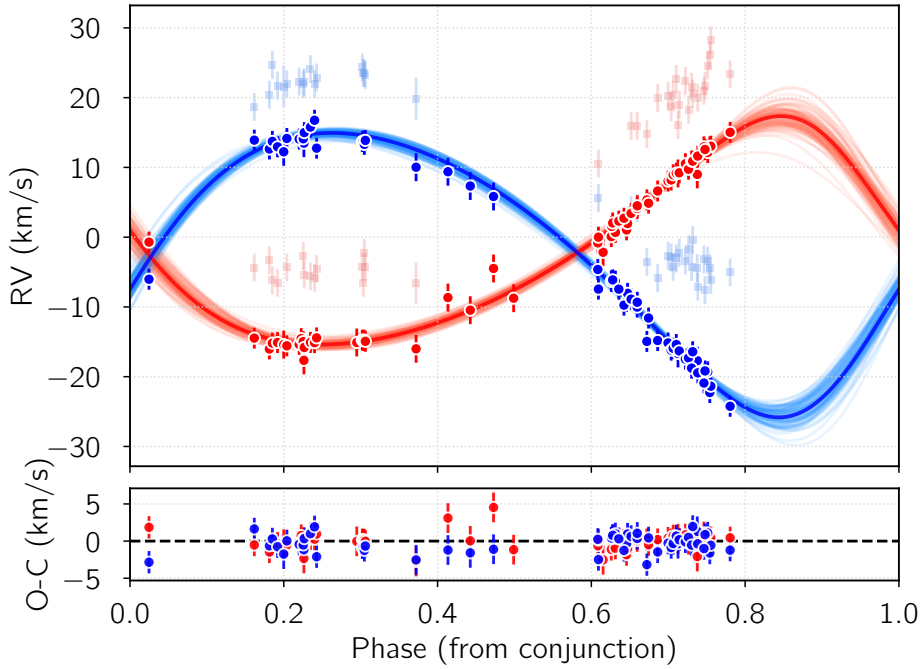

Figure 4.13: Phase-folded RV curves of the two stellar components of HR 10. Red and blue circles and lines follow the same colour code as in Fig. 4.12. Pale red and blue squares correspond to the RVs of components d and s; further details of their behaviour are given in Sect. 4.3.7.

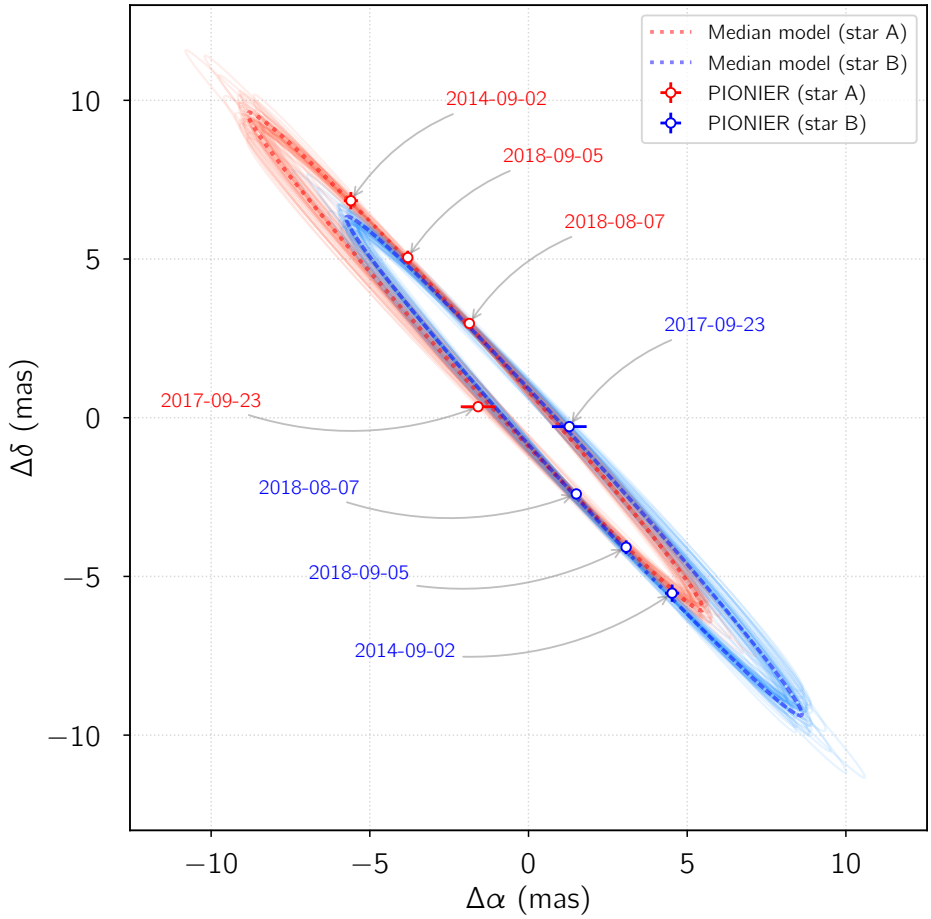

Figure 4.14: PIONIER/VLTI astrometric positions for the two components of the HR10 resolved binary system (circle symbols include error bars). The date for each observation is specified. A sample of 100 orbital solutions obtained from the posterior distributions derived in Sect 4.3.6 (see Table 4.4), are represented by the colour-coded thin lines. The median models are represented by thick dashed lines.

used 20 walkers and 10 000 steps per walker to widely explore the parameter space and then ran a second exploration in a smaller parameter space centred on the maximum likelihood set of parameters as obtained from the first phase. In this second run, we used 20 walkers and 5 000 steps. The first 20% of the steps for each walker were removed and the posterior distributions were built from a total of 80 000 steps. All chains converged nicely into the values presented in Table 4.4, including the median and 68.7% confidence intervals. As an example, the result for the argument of the periastron obtained from this analysis is in perfect agreement (within 2σ) with the result from the RV analysis (see Table 4.3). Figure 4.14 shows the positions of the stars in the plane of the sky according to the four PIONIER/VLTI observations, and the solutions for the projected orbits of HR 10-A (red) and HR 10-B (blue) around the centre of mass.

Stellar parameters

In order to compute a consistent set of stellar parameters, the observed photometry, spectra, and some of the quantities extracted from the binary solution, must be matched by the combination of the individual synthetic photometry and spectra of each component. The following inputs have been used:

1. High-resolution optical spectra.
2. Low-resolution ultraviolet spectra: HR 10 was observed with the International Ultraviolet Explorer (*IUE*, Kondo & Wamsteker, 1987). A merged spectrum covering the interval 115.0–332.0 nm was built from spectra SWP38943 and LWP18015 extracted from the *IUE* Newly Extracted Spectra (INES) database[2].
3. Photometry: Optical and NIR photometry of HR 10 collected from several sources is given in Table 4.5. Johnson *BV* are from the SIMBAD database, and PAN-STARSS DR1 *grizy* and 2MASS JHK_s are taken from VizieR catalogues `II/349/ps1` (Chambers et al., 2016) and `II/246` (Cutri et al., 2003), respectively. The calibration from magnitudes into fluxes was carried out using the zero points from Bessell (1979) and Cohen et al. (2003) for *BV* and JHK_s, respectively; *grizy* are AB magnitudes and a value of $F_0 = 3631.0$ Jy has been adopted. The effective wavelength, $\lambda_{\rm eff}$, for each filter is provided. An uncertainty of 0.02 mag was assigned to the optical magnitudes, since no value is given in the corresponding catalogues.
4. Relative brightness of the stars constrained by the contrast in H-band ($F_H(\mathrm{B})/F_H(\mathrm{A}) \simeq 0.32$) from the PIONIER observations (see Table 4.2).
5. Masses derived from the binary solution: Provided the inclination of the system is known, the individual masses of the components can be estimated with the following expression:

[2]http://sdc.cab.inta-csic.es/ines/

Table 4.5: HR 10: Optical and NIR photometry.

Magnitude	$\lambda_{\rm eff}$ [nm]	Filter
6.33	440.0	*B* Johnson/Bessell
6.25	477.6	PAN-STARRS/PS1.*g*
6.230	550.0	*V* Johnson/Bessell
6.328	612.9	PAN-STARRS/PS1.*r*
6.434	748.5	PAN-STARRS/PS1.*i*
6.507	865.8	PAN-STARRS/PS1.*z*
6.539	960.3	PAN-STARRS/PS1.*y*
5.858 ± 0.019	1235.0	2MASS *J*
5.831 ± 0.033	1662.0	2MASS *H*
5.747 ± 0.027	2159.0	2MASS $K_{\rm s}$

$$M_{\rm A(B)}\ \sin^3 i\ =\ \frac{P_{\rm orb}}{2\pi G}\ (1-e^2_{\rm A(B)})^{3/2}\ (K_{\rm A}+K_{\rm B})^2\ K_{\rm B(A)}. \tag{4.2}$$

Using the data in Tables 4.3 and 4.4 we obtain $M_{\rm A} = 1.94 \pm 0.15$, and $M_{\rm B} = 1.62 \pm 0.13$ $M_\odot$.

The starting point of the estimation of the stellar parameters is a one-model fitting of the optical high-resolution spectrum, using Kurucz synthetic models; the method is described in Rebollido et al. (2018) (Chap. 3); the programmes SYNTHE and ATLAS (Kurucz, 1993) fed with models describing the stratification of the stellar atmospheres (Castelli & Kurucz, 2003) have been used for the spectral synthesis. Since the computation of the effective temperature hinges on the match of the depth of the photospheric Ca II K profile, we derived a model that slightly underestimates that depth, measured on a spline fitted to the line profile, avoiding the CS components. The reason for this is that the final fit will be composed of two models, therefore the addition of the synthetic Ca II K profiles of both stars should match the observed profile. The spectral fit was made on observations obtained with the stars almost in conjunction, to avoid large shifts between the spectral lines of both components. After some iterations, the result is $T_{\rm eff} = 9000 \pm 100$ K, $\log g_* = 3.8 \pm 0.1$; the model was broadened with $v \sin i = 294$ km/s (Mora et al., 2001). We make the initial hypothesis that the parameters of star A are close to these ones; this hypothesis is tested at the end of the fitting process.

Since the contrast in *H*-band between the two components is 0.32, it is trivial to deduce that $\Delta H({\rm A}-{\rm B}) = -1.24$. Magnitudes $B_{\rm A}$, $V_{\rm A}$, $J_{\rm A}$, $H_{\rm A}$ and $K_{\rm s,A}$ for star A, with $T_{\rm eff}$(A)=9000 K and $\log g_*$(A)=3.8 have been computed. In order to estimate the parameters of star B, a grid of magnitudes $B_{\rm B}$, $V_{\rm B}$, $J_{\rm B}$, $H_{\rm B}$ and $K_{\rm s,B}$ was created, covering a range of $T_{\rm eff}$ from 7500 to 9000 K (step 50 K), and $\log g_*$ from 3.8 to 4.3 (step 0.1 dex). The empirical colour–temperature calibration by Worthey & Lee (2011) and the code `mash3.f` provided by these

authors were used[3]. The sets of magnitudes were computed from the corresponding colours keeping $\Delta H(\mathrm{A}-\mathrm{B}) = -1.24$.

Combined colours $B-V$, $V-H$, $J-H$ and $J-K_\mathrm{s}$ were computed using the magnitudes of both stars and reddened with values of $E(B-V)$ between 0.0 and 0.2; the coefficients A_λ/A_V were taken from Wang & Chen (2019,Table 3); independent extinctions were allowed for each star in order to take into account potential differences caused by the individual CS envelopes. These synthetic colours are compared with the observed ones, this process yielding a subset of solutions [9000 K, 3.8] + [T_eff(B), $\log g_*$(B)] for which the observed and synthetic colours are in agreement, within the uncertainties.

In order to break the degeneracies and further constrain the parameters for star B, the observed SED, which includes the available photometry and the *IUE* spectrum, is compared with composite Kurucz low-resolution models, built as the sum of the model for star A, [9000 K, 3.8], and those for [T_eff(B), $\log g_*$(B)] obtained in the previous step. The models for stars A and B, reddened with the corresponding values of $E(B-V)_\mathrm{A}$ and $E(B-V)_\mathrm{B}$ are scaled so that $F_H(\mathrm{B})/F_H(\mathrm{A}) = 0.32$ at the H-band, and the sum is normalised to the observed SED.

A further constraint can be obtained from the HR diagram, by imposing that the point [T_eff(B), $\log g_*$(B)] falls on the same isochrone as the point [9000 K, 3.8]. PARSEC V2.1s evolutionary tracks and isochrones[4] (Bressan et al., 2012) with solar metallicity, $Z = 0.017$, were used.

Once all these requirements are taken into account and fulfilled, a solution for each star is found. Table 4.6 shows the parameters of the individual stars, and the observed colours compared with the synthetic ones. The synthetic magnitudes of the combined pair A+B, computed by imposing $H = 5.83 \pm 0.03$, are $B = 6.35 \pm 0.06$, $V = 6.22 \pm 0.05$, $J = 5.89 \pm 0.05$, and $K_\mathrm{s} = 5.81 \pm 0.06$; both these magnitudes and the synthetic colours are in excellent agreement with the observed photometry (see Table 4.5).

Two sets of values for the masses and luminosities of the stars are given in Table 4.6. Regarding the masses, those labelled "from tracks" were derived by locating the points [T_eff, $\log g_*$], [9000 K, 3.8] (A), and [8750, 4.2] (B), which are direct results of the above analysis, on the HR diagram $\log g_* - T_\mathrm{eff}$, whereas those labelled "from eq. (4.2)" are computed using that equation, which contains parameters obtained from the binary solution. The corresponding mass ratios are 0.72 ± 0.05 and 0.84 ± 0.09, which agree with each other within the uncertainties; there is however a discrepancy between the two values of the mass for star A, the reason could be the strong dependence of the stellar mass on $\sin^3 i$ (see eq. 4.2).

Regarding the luminosities, the first set of values is found by 'translating' the points [9000 K, 3.8] (A) and [8750 K, 4.2] (B) into the tracks in the $L_*/L_\odot - T_\mathrm{eff}$ HR diagram. Figure 4.15 shows the HR diagrams $\log g_*$ (top) and $L_*/L_\odot$ (bottom) – T_eff with the positions of the individual components of HR 10, plotted as black dots with the corresponding error

[3]http://astro.wsu.edu/models/

[4]https://people.sissa.it/ sbressan/parsec.html

Table 4.6: HR 10: Stellar parameters and colours.

Parameters of the individual components

Parameter	Star A	Star B
$T_{\rm eff}$ [K]	9000 ± 100	8250 ± 100
$\log g_*$ [cgs]	3.8 ± 0.1	4.2 ± 0.1
$L/L_\odot$ [from tracks]	64.9 ± 10.0	12.6 ± 4.0
$L/L_\odot$ [from SED fit]	57.3 ± 2.0	13.7 ± 0.5
$M/M_\odot$ [from tracks]	2.5 ± 0.1	1.8 ± 0.1
$M/M_\odot$ [from eq. (4.2)]	1.94 ± 0.15	1.62 ± 0.13
$v \sin i$ [km/s]	294 ± 9	200 ± 20
Age [Myr]	530 ± 50	
$E(B-V)$	0.10	0.05

Observed and synthetic colours

Colour	Observed	Synthetic (A+B)
$B-V$	$+0.10 \pm 0.04$	$+0.13 \pm 0.04$
$V-H$	$+0.40 \pm 0.04$	$+0.40 \pm 0.04$
$J-H$	$+0.03 \pm 0.04$	$+0.06 \pm 0.04$
$J-K_{\rm s}$	$+0.11 \pm 0.04$	$+0.08 \pm 0.04$

bars. The PARSEC V2.1s evolutionary tracks and isochrones are plotted in red and green, respectively. The stretch of the tracks plotted in a more intense red tone correspond to the time span where hydrogen is actively burning in the core.

The estimate of the age of the system is derived from the position of the stars in the HR diagram. Below, we give details about the second set of values for the luminosities in Table 4.6, plotted as magenta triangles in the bottom panel of Fig. 4.15.

Figure 4.16 shows the SED of HR 10 composed of the ultraviolet *IUE* spectrum and the photometry converted into fluxes together with the composite model solution A+B (green) and the individual Kurucz models for stars A (red) and B (blue) reddened with values of $E(B-V)$ 0.10 and 0.05, and scaled so that $F_H({\rm B})/F_H({\rm A}) = 0.32$. The plot shows the contribution of each star to the total SED very clearly. Individual luminosities for each component have been computed by dereddening each model, integrating – which provides values of $F_{\rm obs}$ (erg cm^{-2} s^{-1}) at Earth – and converting the results into luminosities using the expression $L_* = 4\,\pi\,F_{\rm obs}\,d^2$ where $d = 145.18^{+2.54}_{-2.45}$ pc (*Gaia* DR2). These luminosities are shown as two magenta triangles at the bottom HR diagram of Fig. 4.15. The agreement between the values of the two sets of luminosities is excellent.

Figure 4.17 shows the comparison of the observed high-resolution spectrum of HR 10 with the composite synthetic model. The spectrum is the median of 14 UVES/VLT spectra

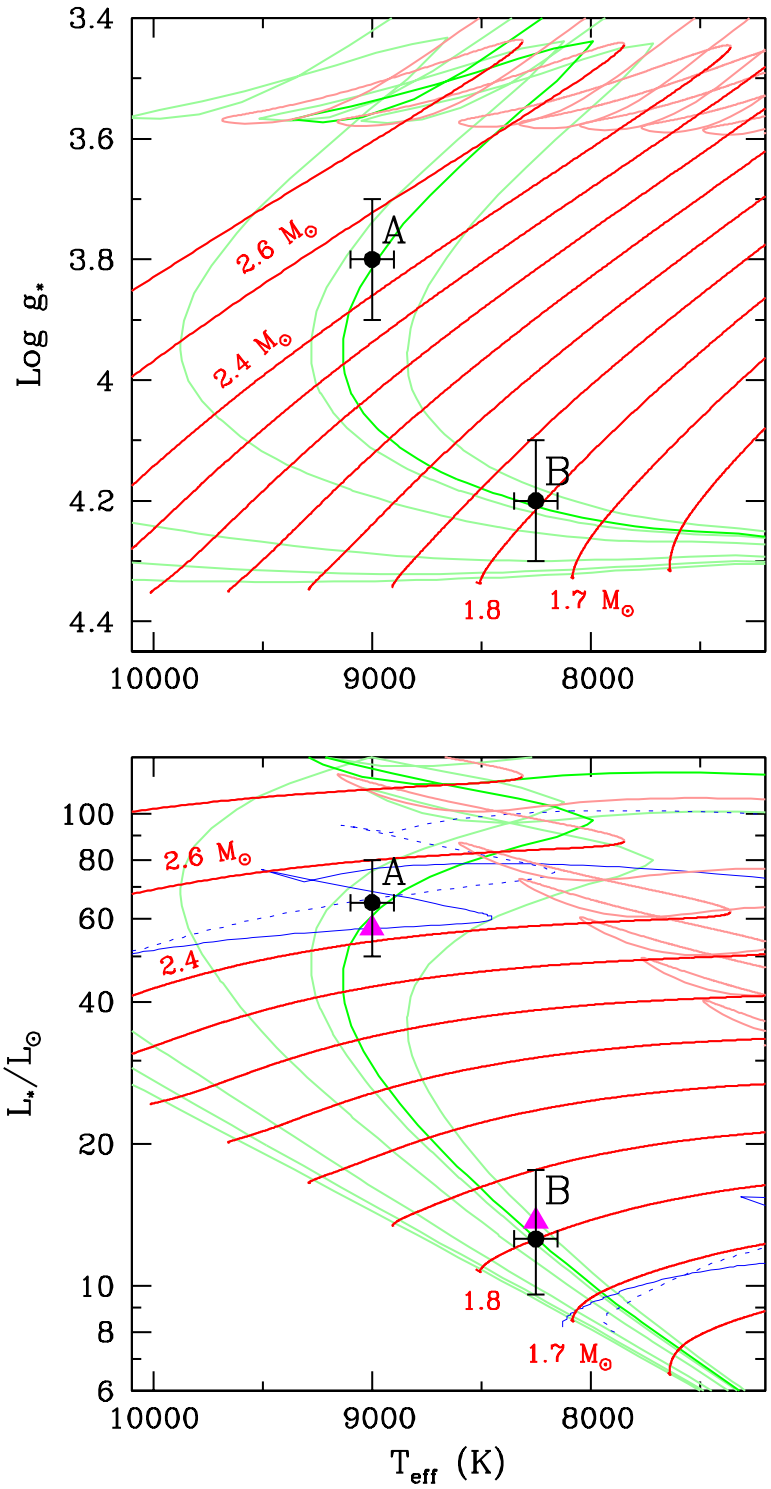

Figure 4.15: HR diagrams $\log g_* - T_{\rm eff}$ (top) and $L_*/L_\odot$ (bottom) and the positions of the individual components of HR 10. PARSEC V2.1s evolutionary tracks (red) and isochrones (green) are used. Isochrones correspond to 50, 100, 200, 400, 500, 530 (highlighted) and 600 Myr. Solid (dotted) blue lines in the lower panel are the evolutionary tracks with no rotation (rotation) for stars with 1.7 and 2.5 $M_\odot$ from Ekström et al. (2012) (see Sect. 4.3.7). The two magenta triangles in the lower HR diagram show luminosities, described below in the main text.

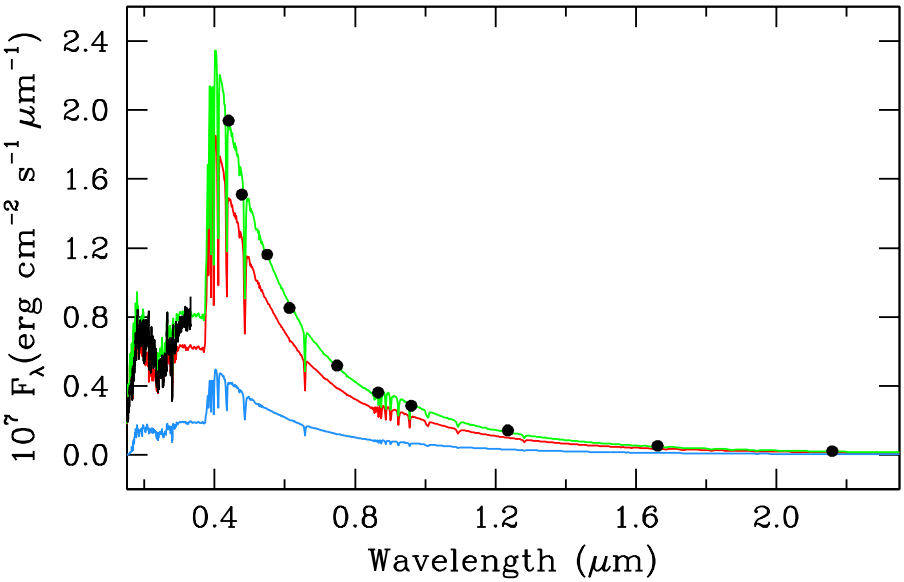

Figure 4.16: Spectral energy distribution (SED) of HR 10 and the adopted solution. The observed optical and NIR photometry and the ultraviolet *IUE* spectrum SWP38943 + LWP18015 are plotted in black. The models for stars A and B and the combined solution are plotted in red, blue, and green, respectively.

obtained on 2007-06-28, and three HARPS-N spectra obtained on 2017-10-06 and 2017-10-23/24. These spectra were selected because the radial velocities of the stars are small (see Table C.2), and therefore we can consider that the stars are almost in conjunction, and no substantial broadenings of the lines due to large differences between the RVs of the stars are present. Model for star A [9000 K, 3.8] was rotationally broadened with $v \sin i = 294$ km/s (Mora et al., 2001). The projected rotational velocity of 200 km/s used for star B has been assigned after some iterations and comparison with some observed photospheric features, although this value has to be taken with caution because there is no formal way to obtain a more robust result. The depth and full width at half depth of the photospheric Ca II K profile, measured on a spline traced on the observed line are 0.40 ± 0.02 and 484 km/s, respectively, whereas the values in the composite A+B model are 0.39 ± 0.02 and 465 km/s. It is interesting to point out that the bottom of the Balmer lines shows a profile that cannot be reproduced by the synthetic spectrum, that yields a slightly more rounded shape as a consequence of the high values of the projected rotational velocities of the stars.

Given the excellent agreement between the observed quantities and those extracted during the above thorough analysis, we can consider that the initial hypothesis made about the parameters $T_{\rm eff}$ and $\log g_*$ for star A being close to the first estimate is consistent.

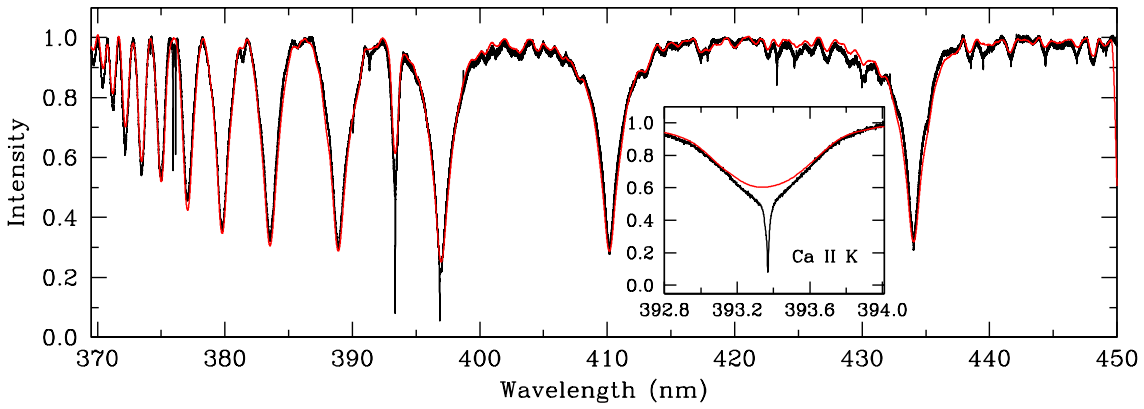

Figure 4.17: The spectrum of HR 10 (black) and the spectral fit (red) computed for the composite model for the stellar parameters given in Table 4.6. The inset shows a blow-up of the Ca II K profile and the fit. The main narrow features that are not reproduced by the synthetic model – which only accounts for the photospheric spectrum – are the Ti II lines at 375.93 and 376.13 nm, and the Ca II HK lines at 393.37 and 396.85 nm (see Sect. 4.3.5).

4.3.7 Discussion

Interpretation of the D, S, d, and s profiles

We have shown that the RVs of the D and S narrow absorption features trace the movements of the primary and secondary components, HR 10-A and -B. The important result that immediately comes out of this is that both stars hold individual CS envelopes. Should the star have a unique, circumbinary shell, we would only observe a single narrow absorption.

In Fig. 4.13, already described in Sect. 4.3.6, we have included the RVs of components d and s, plotted as pale red and blue squares. As mentioned above, these components appear redshifted with respect to D and S, and do not seem to be transient phenomena, since they are clearly apparent at any time when the difference in RVs between D and S is large enough. In addition, we show (see Fig. 4.8) that these weak components are also present in the CS narrow absorptions of species other than Ca II.

In what follows we carry out a quantitative analysis of components d and s for the narrow CS absorptions of the Ca II K line. Figure 4.18 shows the behaviour of the RVs of D, S, d, and s for all the observations where a four-Gaussian decomposition was feasible[5]. The issue is to ascertain whether or not there is a physical link between the main components D and S, and the redshifted components d and s.

The upper panel of Fig. 4.18 shows s – d plotted against S – D, that is, the difference

[5]To avoid a tedious notation, we use the nomenclature S – D, s – d, d – D, and s – S to express the differences in radial velocities RV(S) – RV(D), RV(s) – RV(d), RV(d) – RV(D) and RV(s) – RV(S), respectively.

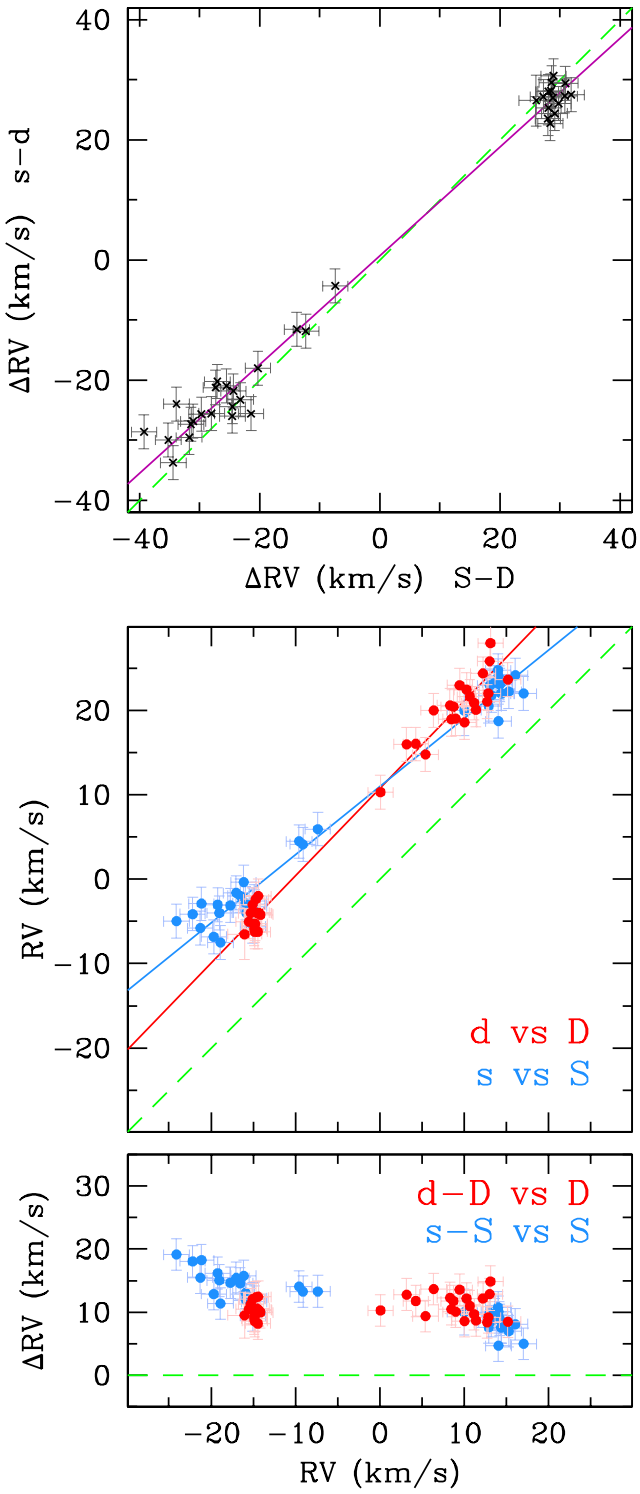

Figure 4.18: Top: Difference between the RVs of components s and d for each observation, s – d, plotted against the difference between the corresponding RV of components S and D, S – D. Middle: RV of components d and s, plotted against the corresponding RV of components D and S; the dashed green line is the 1:1 relationship. Bottom: Differences in RVs d – D and s – S plotted against D and S, respectively.

between the radial velocities of the weak components, compared with the same quantity for the main ones. The diagonal of the diagram is plotted as a dashed green line whereas a linear fit, plotted in purple, yields a slope 0.91 ± 0.02 (an orthogonal fit, giving both variables a symmetric treatment, was chosen, Isobe et al., 1990). This shows that, on average, the differences in RVs between the weak components s – d and the main components S – D behave quantitatively in the same way.

Some differences are apparent when individually analysing the behaviour of components d and s with respect to D and S. In the middle panel of Fig. 4.18 the RVs of d (s) are plotted against the RVs of D (S) in red (blue), the slopes of the linear fits being 1.04 ± 0.02 and 0.81 ± 0.02, respectively. As a general feature, components d and s are always redshifed with respect to the main components D and S; however it is interesting to note that whereas for the whole range of RVs of component D, the distance d – D is always within a narrow range of 10.72 ± 1.72 km/s (see lower panel of Fig. 4.18), in the case of component S, the mean distance s – S is 8.29 ± 1.79 for positive values of S and 14.18 ± 2.47 for negative values; the overall trend seems to be a decrease of s – S as the RV of component S increases.

After this quantitative analysis, the physical link between D, S, d, and s seems fairly clear, but once the transient nature of the phenomenon is discarded, the real origin of the weak components is uncertain.

Evolutionary status of HR 10

In Fig. 4.15 it can be seen that the components of HR 10 lie on the stretches of the tracks starting at the beginning of the MS and ending at the first turning point, where almost all hydrogen in the core is totally exhausted. During that time span, the stars are actively burning hydrogen. According to the individual PARSEC V2.1s track models, the ratio H/He (by mass) is ~ 0.34 for HR 10-A and ~ 1.36 for HR 10-B; the initial ratio being ~ 2.51. The stars lie on the ~ 530-Myr isochrone, whereas the turning points occur at ~ 630 Myr and ~ 1.6 Gyr for A and B, respectively, away in both cases of the red giant branch phase, especially for star B. Taking all this into account, HR 10-A would be in an evolutionary stage close to subgiant, where HR 10-B is still very close to the MS. Since a star remains on the main sequence as long as there is hydrogen in the core that it can fuse into helium, we can consider that HR 10 is still in the MS, although speaking more precisely, it would be a very early post-MS binary.

Binarity and shell/discs

The value of $a_{\rm tot}$ (10.58 mas, Table 4.4) at the distance to HR 10 (145.18 pc) is equivalent to ~ 3.08 au, which implies, according to the value of the masses and eccentricities, a minimum separation between the stars – when both components are at the corresponding pericentres – of ~ 2.39 au. The simple sketch of Fig. 4.19 illustrates that particular configu-

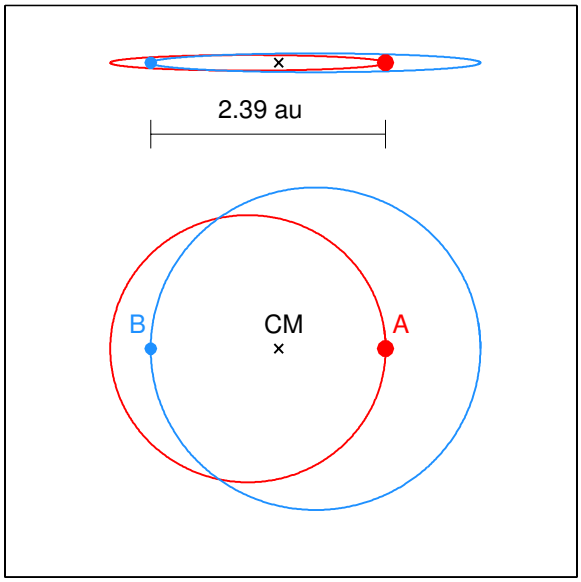

Figure 4.19: Simple sketch of the orbits of HR 10-A and -B around the centre of mass of the system plotted at scale as they are observed (top) and deprojected onto a plane using the value of the inclination, i, from Table 4.4. The stars have been located at the corresponding pericentres, i.e. the points where the distance between components A and B is a minimum ($\sim$2.39 au).

ration, showing the orbits of HR 10-A and -B around the centre of mass as they are observed and seen pole-on, deprojecting the orbits using the inclination, i (93.34°, Table 4.4). That minimum separation is a small value, and leaving aside a dynamical and evolutionary study of the binary, which is out of the scope of this paper, it is remarkable to point out that i) both stars maintain their individual envelopes or shells, and ii) the absence of a stable narrow absorption component at the systemic velocity of the system implies that no circumbinary envelope is present. Some studies on binarity and discs have been carried out in other contexts; for example, Herbig AeBe stars (see e.g. Duchêne, 2015), T Tauri stars (Harris et al., 2012), and debris discs around solar-type and intermediate-mass stars (Rodriguez & Zuckerman, 2012). However, to the best of our knowledge, there have been no studies devoted to the MS or early post-MS binary systems with shells. Therefore, this system is the first of its class to be discovered and studied.

TESS photometry: rotation and pulsations

For the sake of completeness, we would like to mention the observations of HR 10 obtained by the Transit Exoplanet Survey Satellite mission (*TESS*) during Sector 2 in Camera 1 and CCD 3 (TIC 289592423). The photometric observations span a total of 27.4 days with a short cadence of 2.15 min. The data were downloaded from the Mikulski Archive for Space

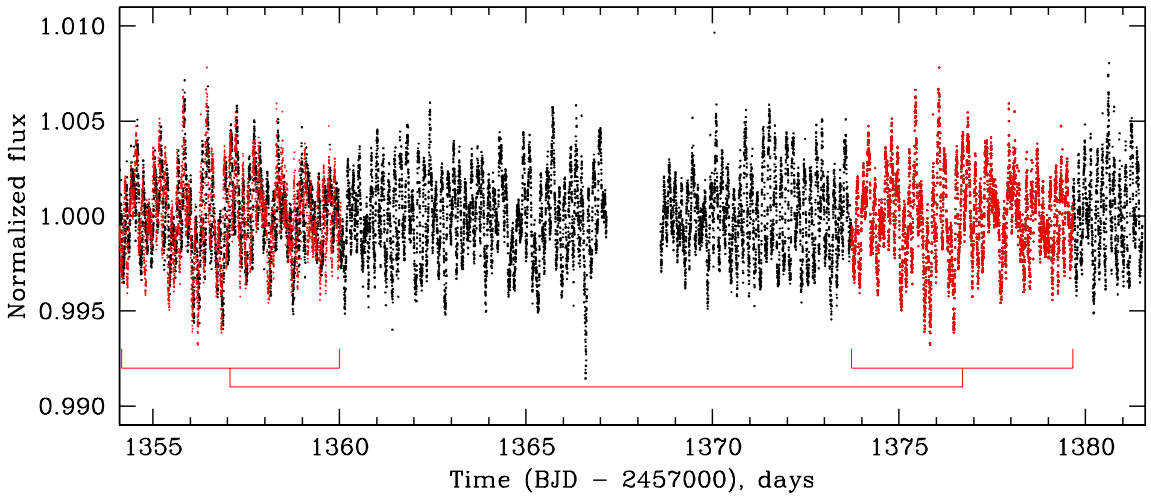

Figure 4.20: *TESS* photometric time series, showing the very short-time variability of the HR 10 system. As an example of the repeatibility of the pattern, the observations between days 1373.72 and 1379.66 (in BJD–2457000) highlighted in red have been shifted to the interval 1354.11 – 1360.05, where they are overplotted in red on the original set of data. See text for details.

Telescopes[6] (MAST), including the extracted light curve by the Science Processing Operations Center (SPOC) pipeline. The median photometric uncertainty per datapoint for the pre-search data conditioning simple aperture photometry (known as PDCSAP) is 140 parts per million. Given the large pixels and apertures used to extract the light curve, the binary system is not resolved by *TESS*. In Fig. 4.20 the light curve shows clear periodic photometric variations with ∼5 mmag semi-amplitude. As an example of how the variability pattern repeats itself, the observations corresponding to ∼ 6 days at the end of the observing window – highlighted in red – have been shifted in time by ~ -19.630 days and superimposed on the original data at the beginning of the observing run, fine-tuning the shift and causing the maxima and minima to coincide. The residuals between the shifted and the original data are less than 5.0×10^{-3}, the average of the absolute values being 1.0×10^{-3}. The analysis of these data, which include effects of rotation, pulsation, and gravitational darkening from the two components of HR 10, will be presented in another paper (Barceló-Forteza et al., in preparation).

Caveats

Finally, we would like to point out explicitly some caveats that must be taken into account when using and interpreting the results presented here.

The projected rotational velocities of the stars are large, and therefore they must produce geometrical distortions which imply an oblateness of the objects, which in turn results in

[6] http://archive.stsci.edu

a larger (smaller) gravity and temperature at the poles (equator), the so-called gravitational darkening. Further phenomena, such as differential rotation, prevent us from assigning a single temperature, gravity, or rotation velocity to the stars (see e.g. Zorec et al., 2017,and references therein).

Even if each component can be characterised by a single magnitude and colour, its position in colour–magnitude diagrams, and hence in the HR diagram, when translating magnitudes and colours into luminosities and temperatures, can be altered by rotation (see e.g. Bastian & de Mink, 2009).

The PARSEC V2.1s tracks used during the computation of the stellar parameters do not include rotation. For comparison purposes we plotted the evolutionary tracks with no rotation (rotation) for stars with 1.7 and 2.5 $M_{\odot}$ and $Z = 0.014$ from Ekström et al. (2012) as solid (dotted) blue lines in the lower HR diagram of Fig. 4.15. This grid only includes models for stars with 1.5, 1.7, 2.0, and 2.5 $M_{\odot}$, in the range of interest for this work, an overly scarce sampling for our purposes, and are computed for rotation velocities that do not correspond to those of HR 10. Therefore, we were not able to use them for the analysis. In any case the deviation with respect to the PARSEC V2.1s tracks does not seem to be dramatic.

4.3.8 Summary

Here we present a complete analysis of the star HR 10 in the context of a large programme aimed at detecting and monitoring variable metallic features superimposed on the photospheric lines that could be attributed to exocometary events (Rebollido et al., 2019, Chap. 3). HR 10 was singled out because of its peculiar variability, the availability of a large amount of high-resolution spectra in archives and publications, and the hints of a first interferometric PIONIER/VLTI observation obtained in 2014 that suggested that HR 10 could be a binary. Dedicated campaigns, both with that instrument and with spectrographs in several telescopes, together with all the archival material have allowed us to carry out a thorough study whose main results can be summarised as follows.

1. Four interferometric PIONIER/VLT observations have provided solid evidence that HR 10 is a binary, the contrast between the components being $\sim 32\%$ in H-band.
2. The analysis of more that 32 years of high-resolution spectroscopic observations from archives, publications, and since 2015, from our dedicated campaigns, shows that narrow CS absorption features are present in at least 24 metallic lines of Ca II, Ti II, and Fe II.
3. Particular attention has been paid in this work to the strong Ca II K CS narrow absorption features, which can be decomposed into two main components, labelled ‘D’ and ‘S’ – for ‘deep’ and ‘shallow’. These components show a periodic behaviour, with component D moving to the blue (red) as component S moves to the red (blue), crossing each other at certain times; this pattern being kept over decades.

4. In those situations where the separation in RVs of components D and S is large, two additional weaker components, labelled 'd' and 's' are very apparent, each one to the red side of components D and S, respectively. These weaker d and s absorption features seem to accompany the main D and S in their periodic movements and not only appear in the Ca II K narrow absorptions, but also in lines of other species, like Ti II and Fe II.

5. Each star holds its individual shell or envelope. The detailed analysis of the time evolution of components D and S shows that they trace the orbit of each individual star in the binary. This is strongly confirmed by the spectrometric binary solution. The orbital period is $P_{\rm orb} = 747.6$ days, the mass ratio $q = M_{\rm B}/M_{\rm A} \simeq 0.72 - 0.84$, and the eccentricity of the orbits is $e \simeq 0.23$.

6. The complete orbital solution was obtained using the results of the RV analysis and the four PIONIER/VLTI astrometric points. This allowed us to compute the inclination of the system, $i = 93.34^{\circ}$ and the total semimajor axis, $a_{\rm tot} = a_{\rm A} + a_{\rm B} = 10.58$ mas, which at the distance to HR 10 (145.18 pc) is equivalent to ~ 3.08 au; this implies a minimum distance between the stars – when both are located at their pericentre – of ~ 2.39 au, a remarkably small value.

7. Stellar parameters for HR 10-A and -B were estimated making use of observable quantities – photometry, optical and ultraviolet spectra, and the constraint imposed by the PIONIER observations – and synthetic low- and high-resolution spectra and evolutionary tracks.

8. To our knowledge, this is the first case studied of a (slightly off)-MS binary where both components have individual envelopes or shells. The current analysis does not show any variability in the CS components that could be attributed to exocometary events. The absence of a narrow absorption component at the systemic velocity rules out the presence of a circumbinary envelope.

As a final remark, we would like to explicitly mention the fact that there is a chance that other stars that exhibit variability attributed to FEB phenomena might actually be binaries and behave in a way qualitatively similar to HR 10. Marion et al. (2014) estimated that when using interferometry and single-aperture imaging, about half the population of nearby A-type stars could be resolved as binaries, and suggested that a number of them remain undetected. In the case of HR 10, the key point that drove the whole analysis presented in this paper was the first PIONIER observation obtained in 2014 that showed strong evidence that the star was a binary.

In a generic case, should the interferometric observations not be feasible, spectroscopy alone would be able to unveil the binarity, provided that observations obtained during a well-sampled and long time interval can be collected; the binarity would show up in the structure of the photospheric lines provided the projected rotation velocities of the stars were low enough, and/or in the periodic shifts of the narrow absorption component (components), if it

(they) were present and found to show a similar shape during timescales long enough to rule out the FEB scenario. Otherwise, if the orbital period of the binary is of the order of months or years, the analysis of the variability of the narrow absorptions during shorter intervals (days or weeks) can be misinterpreted as originating from an exocometary event.

4.4 A transient shell-like absorption around HD 37306

4.4.1 Parameters and characteristics of HD 37306

HD 37306 is an A2V star, located at 70.4 pc (*Gaia* Collaboration, 2018). It hosts an unresolved debris discs with a fractional luminosity of 1.2×10^{-4} and an excess in the IR compatible with two temperatures of grain distribution $T_{dust,1}$ = 399 K and $T_{dust,2}$ = 94 K, similar to our asteroid and Kuiper belt respectively (Chen et al., 2014). The spectral energy distribution of the star is shown in Fig. 4.21, along with the black body models corresponding to the star and the two temperature belts. The photometric values were obtained from SIMBAD (Wenger et al., 2000a). There is also evidence of silicate at 10 and 20 μm features in its IRS spectra (Mittal et al., 2015). This star belongs to the Columba association (Zuckerman & Song, 2012), and has a reported age of 42 Myr (Bell et al., 2015a). Its line of sight does not traverse any known Colororado interstellar medium (ISM) cloud, but within 20 deg of its location there are four ISM clouds that are worth taking into account (Redfield & Linsky, 2008a).

The fitting of a photospheric spectral model, as described in Chapt. 2 and 3, gave values for its stellar parameters of T_{eff} = 9600 K; log(g) = 4.48 [cgs]; [M/H] = 0.0; v_{rad} = 25.7 km/s; and $v \sin i$ = 144 km/s, consistent with a large inclination angle. The median spectrum obtained, as shown in Chap. 2, is plotted along the model in Fig. 4.22. The stellar spectrum is well reproduced by the model, with the exception of the narrow absorptions present in the Ca II and Na I D lines. Fig. 4.22 shows a zoomed inset of the Ca II K to illustrate the absorptions. These features were reported in Chap. 2 and in Iglesias et al. (2018) as originated in the interstellar medium (ISM) - even if no ISM clouds in the line of sight were reported by Redfield & Linsky (2008a) -, since no remarkable variability is detected, and they are not coincident with the radial velocity of the star.

4.4.2 Observations and data reduction

Observations for this object were obtained in eight different observing campaigns. In total, 37 high-resolution spectra were obtained with HERMES (Raskin et al., 2011a), located at the Mercator telescope in La Palma (Spain); FEROS (Kaufer et al., 1999), at the MPG/ESO 2.2 in La Silla (Chile); FIES (Frandsen & Lindberg, 2000), at the NOT telescope in La Palma (Spain); and CARMENES (Quirrenbach et al., 2016), at the 3.5 Telescope in Almería (Spain). The spectra obtained, the instruments and dates are summarised in Table 4.7. The log of the observations is available in Appendix D. The reduction of the data was performed with the pipelines of the instruments, with the exception of the barycentric corrections for the HERMES and FIES data, that was added afterwards. Telluric contamination was removed by using the tool MOLECFIT [7] (Smette et al., 2015a; Kausch et al., 2015a), that provides

[7] http://www.eso.org/sci/software/pipelines/skytools/molect

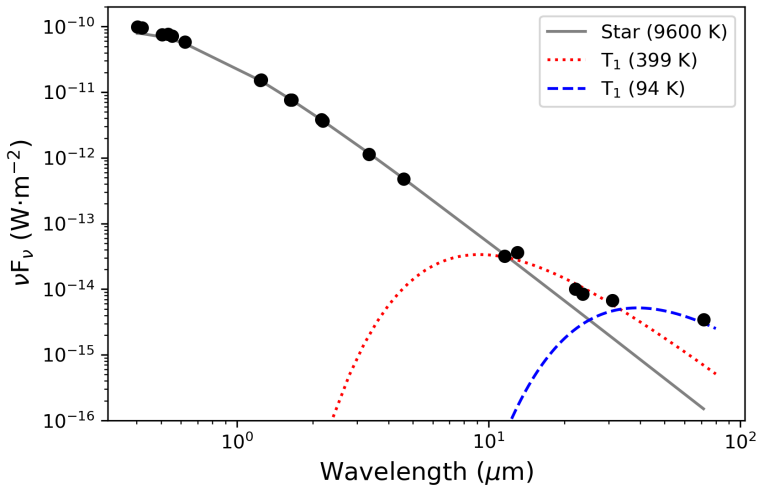

Figure 4.21: Spectral energy distribution of HD 37306. The gray line shows the black body corresponding to the temperature derived for the star. The two temperature estimates for the debris disc model are plotted as a red dotted line (T=399 K) and a dashed blue line (T=94 K).

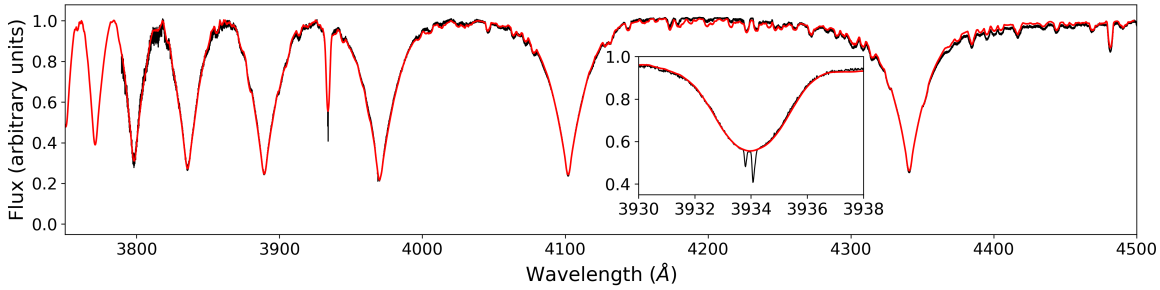

Figure 4.22: The median spectrum of all the observations obtained with HERMES (black) is plotted along with the synthetic model (red) computed with the parameters specified in the text. The inset shows the Ca II K profile, where two narrow non-photospheric absorptions are clearly visible.

Campaign	Instrument	Number of Spectra
October 2015	FEROS	2
March 2016	HERMES	8
March 2016	FIES	1
March 2017	FEROS	2
March 2017	HERMES	7
September 2017	FEROS	8
November 2018	CARMENES	2
December 2018	HERMES	7

Table 4.7: Dates, instruments and number of spectra obtained for HD 37306.

Ca II K			Ca II H			Na I D2			Na I D1		
RV (km/s)	FWHM (km/s)	EW mÅ	RV (km/s)	FWHM (km/s)	EW mÅ	RV (km/s)	FWHM (km/s)	EW mÅ	RV (km/s)	FWHM (km/s)	EW mÅ
11.0	6.91	13.1	10.6	6.75	6.3	10.6	6.41	4.6	10.7	5.22	2.2
32.3	8.71	31.6	32.5	9.39	19.3	31.2	7.95	6.7	31.6	8.08	3.2

Table 4.8: Characteristics of the narrow stable non-photospheric absorptions superimposed on the Ca II and Na I doublets.

an atmosphere model considering the night conditions. An example of its performance is shown in Sect. 2.3.1.

4.4.3 Results

An analysis of the 37 spectra obtained for this star showed the presence of a narrow non-photospheric absorption in the Ca II and Na I D lines, pointing towards the presence of gas in the ISM along its line of sight. At the same time, a broad non-photospheric absorption was observed only in the data of September 2017, superimposed on the photospheric lines of metallic elements, and coincident with the radial velocity of the star. Here we present the results of the analysis of the non-photospheric absorptions observed in the metallic lines inspected: Ca II K & H, Ti II and Fe II.

Narrow absorption features

As shown in Fig. 4.22, the Ca II K profile shows two narrow non-photospheric absorptions superimposed on the photospheric line. These are also detected in the Ca II H and Na I D doublet (see Fig. 4.23). These lines were analysed in Chap. 2, and are suggested to be of ISM origin, due to the lack of variability detected, and also to the fact that their radial velocities do not coincide with the radial velocity of the star. The radial velocities, full widths half maximum (FHWM) and equivalent widths (EW) of the absorptions are given in Table 4.8.

The line ratios (K/H) for the Ca II absorptions are lower than 2, its expected value considering the oscillator strengths, whereas the ratios for the Na D case (D2/D1), are exactly 2. Still, the values for both cases are consistent with a partially optically thin gas, i.e., the optical depth of the gas is smaller than 1 ($\tau_0 < 1$) The column densities obtained according to the prescription by Somerville (1988) are: $N_{Ca\,II} = 1.4 \times 10^{11}$ and 3.4×10^{11} cm^{-2}; and $N_{Na\,I} = 2.3 \times 10^{10}$ and 3.3×10^{10} cm^{-2} for the absorptions at 11 and 32 km/s respectively. The ratios of column densities $N_{Ca\,II}/N_{Na\,I}$, 6 and 10, are compatible with the results obtained by Welsh et al. (2010) for the ISM.

The appearance of a shell-like absorption

During the last campaign of our set of observations, in September 2017, a large absorption appeared superimposed on some of the metallic lines of HD 37306, resembling those of a shell-like profile. For all the nine days the campaign lasted, the absorption was present and not varying in intensity and velocity. Observations taken in November and December 2018 with CARMENES and HERMES spectrographs respectively, showed the absorption had completely disappeared. A median spectrum for the September 2017 spectra was constructed in order to compare with data previously obtained.

In Figs. 4.24, 4.25, 4.28, 4.27, the median of the data obtained in the September 2017 campaign is plotted in black, whereas the red line shows the median of the FEROS (October 2015 and March 2017) and HERMES spectra, with the exception of the 3760 Å Ti II range, where no data from HERMES are available. Each figure also shows the residual of the ratio between the HERMES and the FEROS September 2017 median. The spectra obtained with FIES in service mode did not improve significantly the SNR of the median, and has lower resolution, therefore, it was omitted from the figures and analysis. Table 4.9 summarises the characteristics of the absorption feature. Errors were estimated as in Chap. 2, as 10% for the EW, and two pixels for the radial velocities, corresponding to $\sim$2 km/s.

The Ca doublet is shown in Fig. 4.24, for both lines, the FHWM have values of $\sim$ 22 km/s in both cases, and the central velocities are 22.5 and 26.2 km/s for the K and H lines respectively. There is an apparent displacement between the lines, possibly due to the blend of the H line with Hϵ. The resultant absorptions have an EW ratio of $\sim$ 1.3, so wa can say the absorption is partially optically thick ($\tau_0 > 1$). The column densities obtained according to Somerville (1988) are shown in Table 4.9. The Ca II infrared triplet (Fig. 4.25) also shows the broad absorption superimposed on the photospheric lines. Due to the configuration of FEROS, the 8542 Å line profile is not fully observed, and the values obtained for the absorption are estimations based on a gaussian fit for the observed part; even so, the EW is not provided to avoid the large uncertainties. The ratios of EW of the lines, point towards to, at least, partial saturation as well.

There are several Fe II lines (listed in Table 4.9) that show an absorption feature. All of them are plotted in Fig. 4.27, along with their residuals. Considering their oscillator

Element	Line Å	Radial Velocity km/s	FWHM km/s	EW mÅ	N cm^{-2}
	3933.6	22.5	22.0	259.1	
	3968.4	26.2	22.0	196.9	
Ca II	8498.0	24.5	24.3	95.6	5.17×10^{12}
	8542.1*	24.9	21.0	-	
	8662.1	24.1	22.6	240.5	
	4508.3	26.3	21.8	8.8	
	4515.3	23.8	24.9	8.1	
	4522.6	26.9	24.1	13.9	
	4583.8	26.4	22.6	24.6	
Fe II	4629.3	24.6	22.6	7.8	$> 7 \times 10^{13}$
	4923.9	23.7	22.0	21.9	
	5018.4	25.5	23.7	37.3	
	5169.0	23.2	21.8	40.8	
	5197.5	28.0	16.4	10.5	
	3759.3	29.1	21.5	42.6	
Ti II	3761.3	20.1	24.6	32.9	$> 3 \times 10^{11}$
	4549.6	26.6	22.8	23.5	

Table 4.9: Characteristics of the absorption observed in September 2017 in several lines.* The values for the Ca II 8542 are just estimations based on a gaussian fit, due to the lack of wavelength coverage in that region.

strengths, there is saturation as well . Ti II is detected in the 3760 Å range and 4549 Å line, possibly blended with an Fe II line (see Fig. 4.26). Due to the lack of coverage of the FEROS spectrograph, the comparison spectrum for the 3760 Å doublet is the median of the FEROS data from October 2015 and March 2016. The column density for both elements was calculated with Eq. (1) of Somerville (1988), but since the gas is optically thick, the values are lower limits.

There is no evidence in Na I D lines for an absorption, with the exception of the ISM narrow features shown in Fig. 4.23. The plot with the September 2017 median is still shown for comparison in Fig. 4.28. Other photospheric metallic lines such as Mg I in 4481 Å, or Fe I lines in the range 4400-4600 Å are present in the spectra, and were inspected as well, but showed no evidence of any extra absorption.

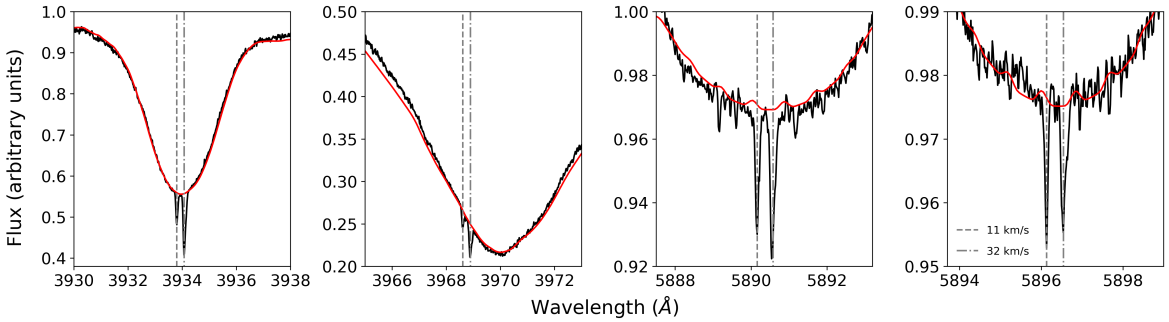

Figure 4.23: Lines Ca II K & H and Na I D2 and D1. The median spectra for all campaigns except September 2017 is shown in black, and the modelled spectra is shown overplotted in red. All four lines show absorptions at the same velocity, and an ISM origin is suggested for them.

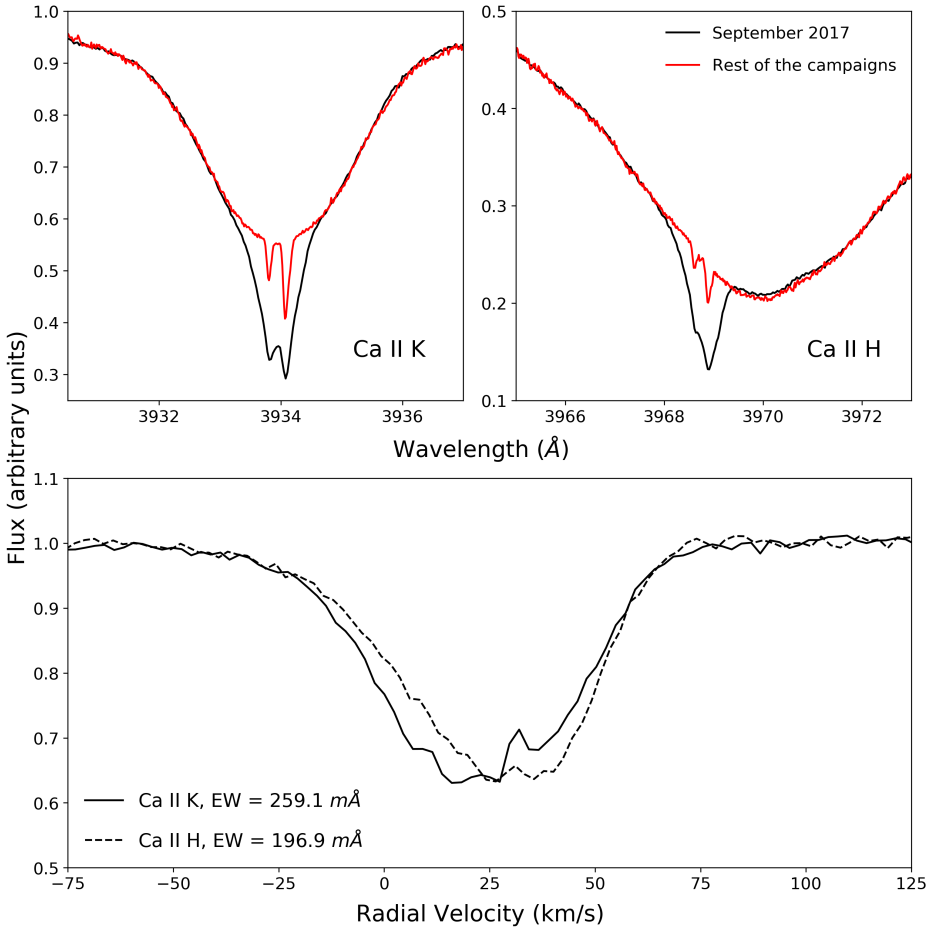

Figure 4.24: Top panels: Ca II K & H lines for the median spectra of September 2017 where the absorption is present (black), and the median for the rest of the campaigns(red). Bottom panel: Residuals of the ratio between the spectra in the top panels. The EW for both Ca II K and H residuals are also given. This description applies to the following figures.

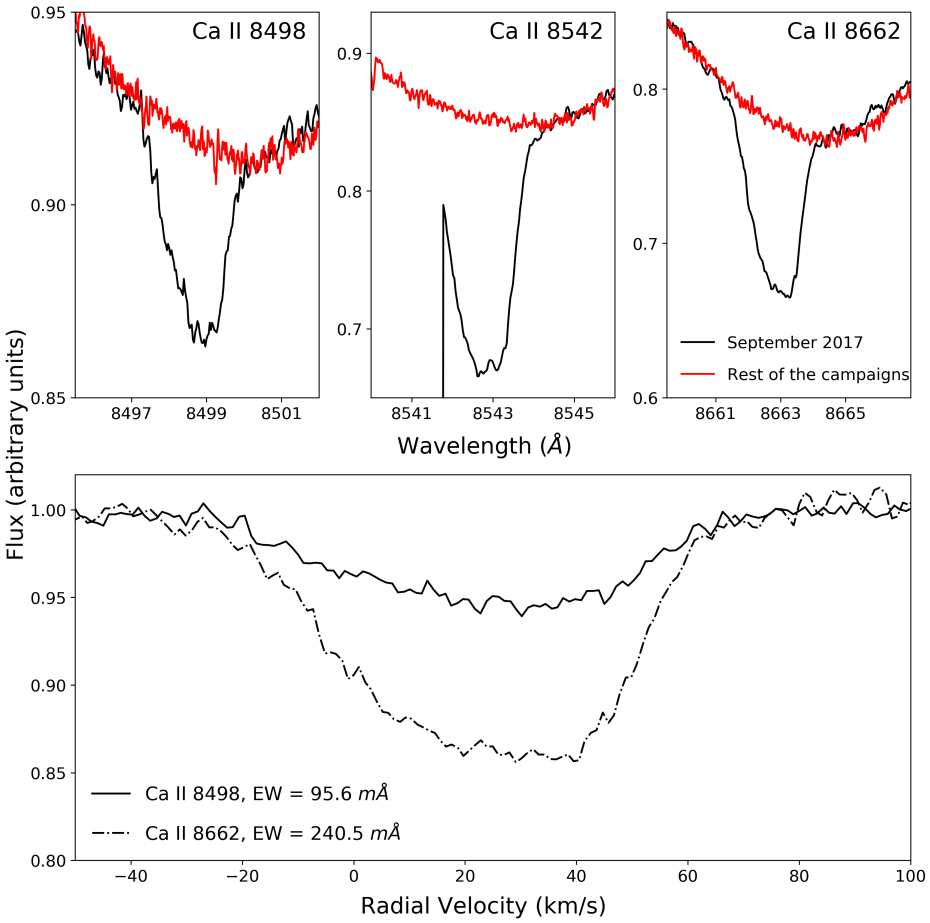

Figure 4.25: Ca II triplet lines. The 8542 line does not have a full wavelength coverage, and therefore only part of the line is shown for the FEROS spectra.

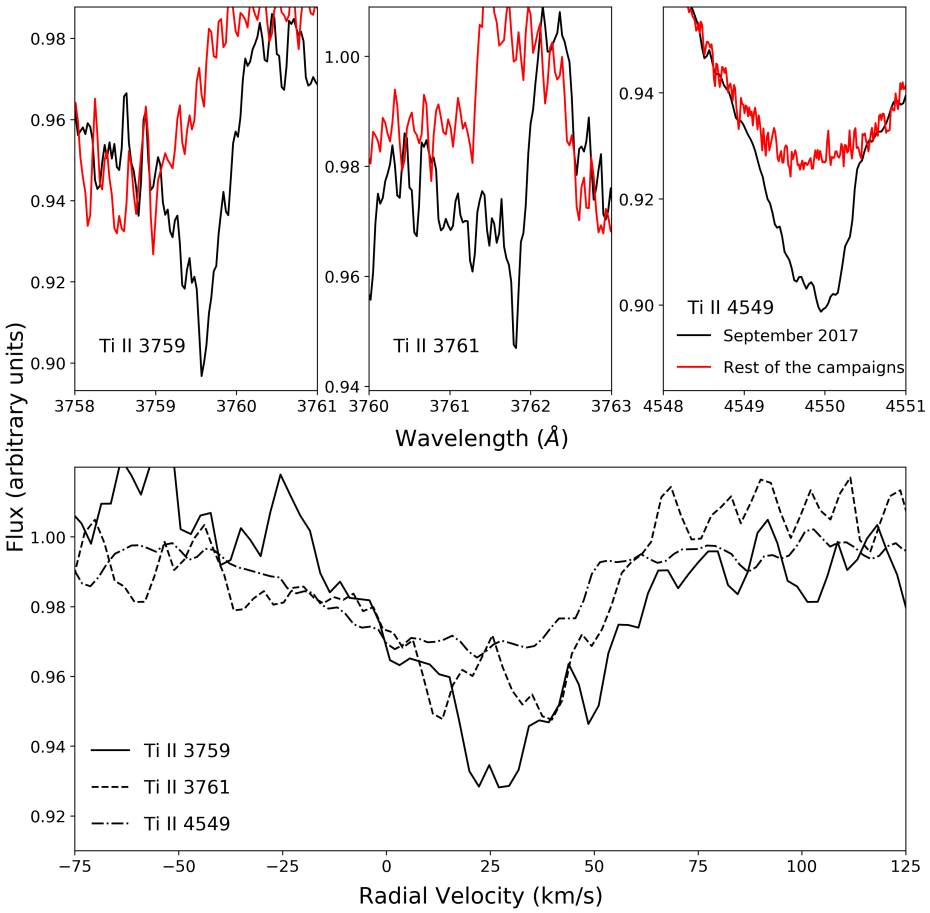

Figure 4.26: Ti II lines. Due to the lack of coverage of HERMES in the 3760 Å range, in the first two panels the black spectrum corresponds to the median of the FEROS spectra from October 2015 and March 2017.

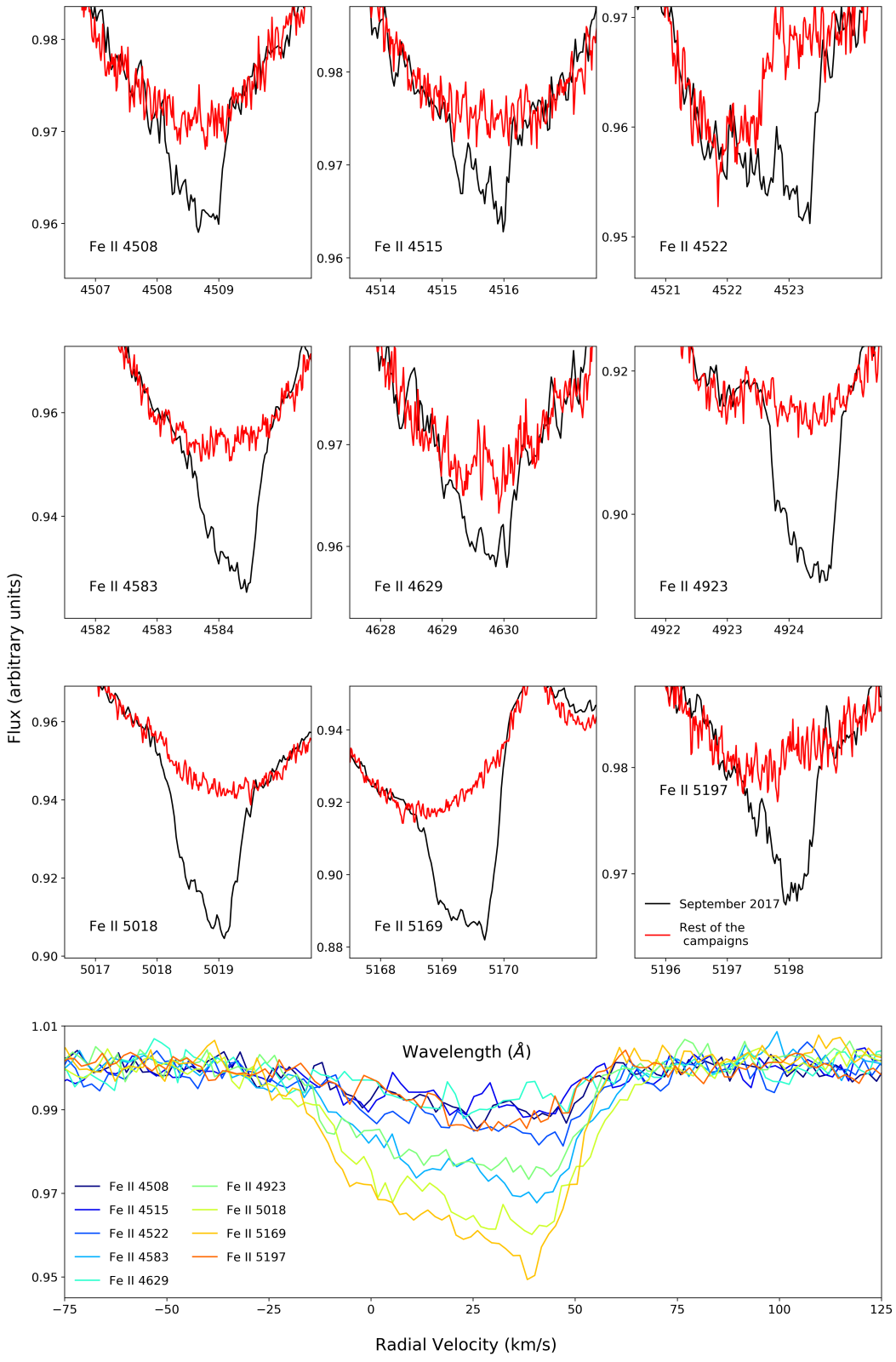

Figure 4.27: All Fe II lines showing broad shell-like absorption.

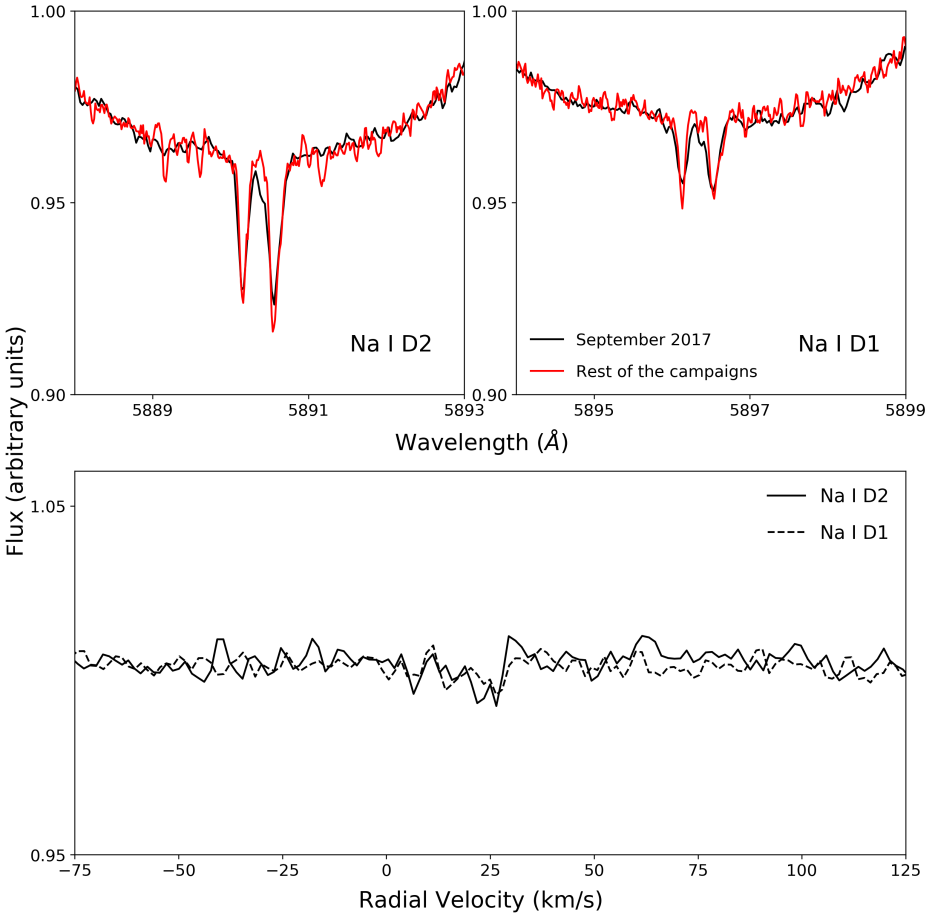

Figure 4.28: Na I D2 & D1 lines. The absorptions are due to the ISM, but there is no evidence of the broad shell-like absorption.

4.4.4 Discussion

The non-variable, non-photospheric broad absorption that appeared in September 2017 does not resemble the *typical* narrow absorption features observed in the exocomet host stars. Also, the lack of variability through several days is not consistent with the exocomet scenario, where variations occur within hours, or at most, few days (e.g. Kiefer et al., 2014a; Welsh & Montgomery, 2015, 2018, or Chap. 2).

The possibility of instrumental or background contamination was considered, but observations of other stars taken in the same days do not show any similar feature, and with the exception of the lines mentioned in Table 4.9, there are no other variations in the spectra.

The large velocity dispersion in every observed line, consistent with the mean velocity dispersion in Abt (2015), suggests a large structure. The presence of ionised metals requires high temperatures, and therefore a location close to the star. Such structures, either discs or spherical shells, have been suggested as an explanation for the so called "shell stars" (Slettebak, 1982; Gray & Corbally, 2009). The shell absorptions would be generated by gas, very close to the star, and possibly having some of its material accreted (Abt, 2015). These stars show a broad core absorption in some metallic lines such as Ti II or Ca II, and sometimes in H lines. These cores tend to have variations in their depth, reported in up to 57% of stars (Jaschek & Andrillat, 1998), and in some cases periodic (Abt, 2008; Abt et al., 1997), possibly related to variations in the material of the disc, or accretion episodes, as the star transverses the ISM, that would lead to material expelled from the stars by stellar winds (Abt, 2015).

An alternative analysis of our data is done in Iglesias et al. (2019). They suggest that broad absorption would be caused by a break up of small bodies, or exocomets, releasing large amounts of gas, but without a detected photometric counterpart. The shell scenario is ruled out due to the lack of variations detected in the Balmer lines, and the low rotational velocity of the star, despite there are reports of shell stars without hydrogen features (e.g. Abt, 2015), and the star having $v \sin i \sim 140$ km/s. They also report observations taken in 2019, where the broad absorption was no longer present, pointing towards an sporadic event.

4.5 Conclusions

While the presence of variable features in the Ca II K line in A-type stars has been interpreted as transiting gaseous comae, resembling solar system comets, other physical effects should be considered, as well as the analysis of different metallic lines. The cases we have shown here represent particularities that can only be analysed after intensive monitoring. The case of HR 10, a star classically classified as an exocomet-host (Welsh et al., 1998; Lagrange-Henri et al., 1990d; Redfield et al., 2007) is a representative example of the need for exhaustive time series analysis.

Radial velocities, EWs and velocity dispersions are very diferent in each star, indicating different scenarios. Lines in ϕ Leo are narrower, and the variations are redshifted and more frequent, pointing towards a β-Pic like star. The case of HR 10, where the absorptions are also narrow but appear shifted both to the red and blue, is a clear example of the need of larger time series of data, to rule out other possible explanations, and determine whether there is periodicity in the radial velocity patterns of the absorptions.

The serendipitous detection of the absorption in HD 37306 has similarities with the exocometary scenario, but the duration of the event, and the lack of variation in depth, EW or velocity for several days, is more likely compatible with a more stable phenomenon, such as the presence of a gaseous disc, similar to those suggested for shell stars.

The bottom line of this chapter is that the presence of exocomets is relatively common around A-type stars, but there are other phenomena that could act as false positives in the detection surveys, that must be considered when looking for evidences of small bodies.

Chapter 5

Conclusions and future work

Summary and conclusions

The work presented in this thesis focuses on the study of the signatures of small bodies detected around A-type main sequence stars, i.e. what is interpreted as exocomets. Due to their small surface area and low brightness, it is not possible to observe them directly, however, they leave absorption fingerprints in the stellar spectra as they evaporate while passing in front of the star, and become detectable in the form of non-photospheric, variable absorptions.

High-resolution spectroscopic observations were obtained with four telescopes, located in both hemispheres, during two years, in order to construct a large sample to identify new exocomet-host stars, and perform a study of the characteristics of the systems. A total of 117 stars were observed with appropriate time cadences aimed at identifying variable features. A total of 1575 high resolution spectra were obtained and analysed for the purpose of the work performed in this thesis.

In the following, the conclusions reached in this work are summarised.

1. The bulk of this PhD thesis focuses on the analysis of the 1500 spectra obtained between September 2015 and September 2017 for the set of 117 stars with spectral types ranging from G to B. The selection criteria were highly biased towards i) stars with rich circumstellar environments, including stars with exocomet-like variations previously detected, ii) stars showing traces of hot –detected with optical spectroscopy– or cold –detected in the sub-mm and mm wavelength ranges– gas in their circumstellar environments, iii) stars with debris discs oriented edge-on, iv) stars with near-infrared excesses related to hot dust, and v) stars belonging to young associations (e.g. Upper Scorpius, Tucana-Horologium or the β Pic moving group).

   All the available spectra were inspected looking for evidence of circumstellar gas in

the Ca II and Na I D lines. This represents the largest systematic study performed so far in the search for exocomets. The analysis of the whole sample revealed:

- The presence of narrow stable non-photospheric absorptions, compatible with the presence of hot circumstellar gas, superimposed on the photospheric profiles of the Ca II and/or Na I lines, in 60 stars ($\sim$50% of the sample). An inspection of the characteristics of those features, and the possible relation with clouds of interstellar gas in the line of sight, was carried out in order to discern whether the narrow absorptions have a circumstellar or interstellar origin. In 30 stars, a circumstellar origin seems to be the most plausible explanation, either due to variations detected in the absorption, a correspondence between the radial velocity of the star and that of the absorption, or evidence for absence of gas in the interstellar medium in the line of sight. The origin of this gas could be related to outgassing small bodies, or to gas released in collisions of dust or planetesimals. In those cases where shell-like triangular profiles are identified superimposed to the photospheric metallic lines of the spectra, narrow stable absorptions are also detected, pointing towards a gaseous-rich circumstellar environment.
- The column densities of these narrow non-photospheric absorptions were computed, but no apparent differences were found, when comparing their $N_{Ca\,II}/N_{Na\,I}$ ratios, between the two populations of gas with interstellar or circumstellar origin. Still, it should be noted that the presence of absorption features both in Ca II and Na I is more common for lines of interstellar origin lines.
- Variable non-photospheric features were detected in 18 stars, representing 15% of the sample, out of which six are new. These variations are simultaneously present in the spectra along with stable features in 16 cases, most of which cab be attributed to a circumstellar origin. The variations detected show a wide range of changes in depth and radial velocity, all of them within $\pm$100 km/s of the stellar radial velocity. Most of these detections are consistent with a gaseous tail transiting in front of the stars, i.e. exocomets. In addition, there are another eight stars in the sample that showed exocomet-like variations in their spectra, reported in previous works, for which we do not observe any variability, rising to a percentage of 22% of the sample the number of objects showing exocomet-like variations.
- We have found, in total, 32 stars with non-photospheric absorption features attributed to circumstellar gas, all of them have spectral types earlier than A9, consistent with previous works, and a wide spread of ages, between $\sim$ 10 Myr and $\leqslant$1 Gyr. They have higher projected rotational velocities, possibly indicating high inclination angles, and therefore a favoured geometry for the detection of transiting gas.
- Near-infrared excesses, related in some cases to the presence of hot dust, have been reported for 22 stars in our sample. The detection rate of non-photospheric absorptions for these stars is $\sim$27%, while if we consider only those with spectral types earlier than F2, it grows up to $\sim$50%. Considering the obvious fact that these

stars have random inclinations, the probabilities of observing one of these systems edge-on, and therefore, being favourable for the detection of transiting gas, is around $\sim$40%, consistent with the fraction of hot-dust host stars with reported hot gas. This points towards a correlation between the presence of gas and dust in a region close to the star, and a possible common origin.

- The presence of gas is also remarkable around the stars with anomalous metallic abundances, namely, the λ Boo objects included in the sample. The difference in abundances of lighter –C, N, O– and heavier –Fe, Al, Mg– metals, has been explained in the literature as differential accretion from the circumstellar medium, a scenario that could involve the presence of small bodies in the system. By comparing the equivalent widths of Mg and O lines, we have identified six additional objects with λ Boo characteristics, that had not been reported before in the literature. Out of a final sample of 18 λ Boo stars, we have identified exocomet-like variability in 44% of them, a much larger fraction than that obtained for the sample ($\sim$ 22%), reinforcing the scenario of differential accretion from the circumstellar medium.
- There is no apparent relation between the presence of a detected debris disc ($L_{dust}/L_{\star} \geqslant 10^{-6}$) and the presence of circumstellar gas in the system. Only a fraction of 45% of stars with exocomet-like variations and 50% of stars with narrow stable components originated in the circumstellar medium show infrared excesses compatible with a debris disc. Nevertheless, stars in the sample with resolved discs show a clear trend of detections of circumstellar spectroscopic features when the discs are seen near edge-on.

2. A separate analysis was performed for the early-type stars with debris discs, where cold gas, observed in the far-infrared or (sub-) millimetric wavelengths, is also present; most of these stars are included in our sample, with the exception of β Pic and Fomalhaut, that were taken into account for this particular study. Narrow stable non-photospheric components were identified in the Ca II K line of 11 out of 17 stars, being hot circumstellar gas the most likely origin for eight of them. When considering the inclination of the discs, known for 16 out of 17 objects, the presence of a circumstellar narrow absorption feature is detected in eight out of nine objects with edge-on inclinations; and there is evidence of circumstellar gas absorptions in only one out of eight face-on discs, HD 156623, where variations compatible with an exocomet-like event are detected. This hints at a correlation between the detection of hot, circumstellar gas, and the inclination angle of the system. It also suggests that hot and cold gas are coexisting, and possibly share a common secondary origin, related to the presence of small bodies in the system. This result could be key in the search for new systems with cold gas, more difficult to detect than the stable optical spectroscopic features.

3. Individual studies of three remarkable stars from the sample are included. The objects were selected due to peculiarities in their variable features.

- The A7 star ϕ Leo is the most variable object in the sample, showing changes in its Ca II K line in timescales as short as less than one hour. The Ca II K line shows a triangular shell-like profile, and there are prominent absorptions in the Ti II 3760 Å doublet, indicative of the presence of gas in its circumstellar environment. The high frequency of the variations of the narrow absorptions in the Ca II K line suggests that they could be originated by evaporating bodies, i.e. exocomets, close to the star. This object might be one of the oldest stars –$\sim$900 Myr– known to be an exocometary rich environment.
- HR 10 has been repeatedly studied in the literature, and considered before our work one of the most important exocomet-host stars. Prominent narrow non-photospheric absorptions in many metallic lines of Ca II, Fe II and Ti II were observed in all the spectra obtained during our monitoring campaigns, the common feature being that each narrow absorption had two narrower components. The joint analysis of all the available spectroscopic data –our own observations plus archival and published data, covering a time span of $\sim$32 years– showed a clear periodicity pattern in the radial velocities of the two narrow components of each line, which is not expected for exocomets. This, along with the interferometric observations made with the infrared instrument PIONIER on the Very Large Telescope Interferometer (VLTI), led to the conclusions that HR 10 is actually a binary, and the absorptions were caused by individual circumstellar envelopes surrounding each star of the binary system, ruling out the hypothesis of an exocometary origin. The observations allowed us to make a complete characterization of the stars and the orbit.
- HD 37306 has been studied separately due to the unusual variation observed in its metallic lines. This A2 star shows in every spectra two narrow non-photospheric absorption components attributed to the interstellar medium due to the lack of variability, and the fact that the absorptions have radial velocities not coincident with the radial velocity of the star. In one of the campaigns, lasting for at least 8 days without any variations, a shell-like profile absorption in Ca II, Ti II and Fe II was detected. The broad triangular-shaped absorption is produced by optically thick ionised material, since there are no detections in neutral species (e.g. Mg I), and the equivalent width ratios are consistent with an optically thick medium. The origin of the absorptions in shell stars is uncertain, but an spherical shell or a disc around the star has been suggested .

As a general conclusion, the work contained in this PhD thesis provides general and individual results of a large high-resolution spectroscopic survey to search for exocomets, and investigates the gaseous environment of main-sequence stars. Circumstellar gas has been detected in 32 objects, all of them A-type stars. Results point towards higher detection rates if the system is edge-on, and a possible correlation between the presence of cold gas and the gas detected in optical spectroscopy. Six new objects have been found to host exocomet-like variability, and the connection between the presence of exocomets and the environment, and

the stellar properties hints at higher probabilities of detection of exocomets around edge-on A-type λ Boo stars, or showing near-IR excesses due to hot dust, while the presence of a debris disc has, in principle, no clear connection with the exocomet phenomenon. Still, the detection of variable non-photospheric absorption features superimposed on the photospheric profiles should be carefully analysed before attributing an undoubted exocometary origin, since there is a number of processes, related to the star or the circumstellar medium, that could be responsible for them. Ongoing work, already presented in this thesis, suggests that the detection of exocomets and/or circumstellar stable gas only around A-type stars might not be an observational bias, but is more likely related to physical mechanisms preventing for the detection of exocometary features in other spectral types.

Future work

The results obtained during the course of this PhD thesis point towards new lines of work and further monitoring of the stars in the sample showing variability.

Spectroscopic follow up is needed for the exocomet-host stars, in order to discard false positives. The available and upcoming high-resolution instruments designed for radial velocity search of exoplanets, will allow us to detect features with smaller velocity dispersions, and to better constrain the radial velocities of the absorptions, identifying possible cases of periodicity, that could arise from binarity, or spectroscopic signatures of stellar activity.

The finding of a correlation between the presence of both hot and cold circumstellar gas has led to the selection of a sample of objects with narrow stable non-photospheric absorptions with circumstellar origin that will be observed with the Atacama Large Millimiter Array (ALMA) in Cycle 7 in order to search for a cold counterpart of the gas. If our hypothesis is confirmed, this will also open the possibility of a new selection method for possible cold gas bearing stars. Not only facilities working in the millimetric and submillimetric ranges should be considered when looking for cold gas, but also the available high-resolution spectrographs working at infrared wavelengths, that are able to detect rotational lines of CO, and give initial estimates of the presence and amount of gas in the outskirts of the systems.

The detection of exocomet signatures in the light curve of β Pictoris, and the capabilities of new space missions such as *TESS* and *CHEOPS* are starting points for photometric studies of stars with exocomet signatures in their spectra. Simultaneous observations in spectroscopy and photometry are needed in order to perform a better characterization of exocomets.

Further studies are needed to clearly determine whether the detection of exocomets only around A-type stars is an observational bias, or, on the contrary, has a physical explanation, related to the characteristics of the star and/or the environmental conditions of the system. Particularly, the photometric search for exocometary signals in stars of later spectral types, which has already given some results, or the search for variability in lines of species different from Ca II could shed light on this matter.

In general, the exocometary field has a lot of possibilities for further explorations, in different wavelength ranges and with different techniques, that would help to expand the current knowledge. Research focused on small bodies is essential in the study of the formation mechanisms and the configuration of planetary systems, and could have a non-negligible impact in the search for life and its origin.

Chapter 6

Conclusiones y trabajo futuro

Resumen y conclusiones

El trabajo presentado en esta tesis se centra en el estudio de las evidencias de cuerpos pequeños detectadas alrededor de estrellas de secuencia principal de tipo A, es decir, interpretadas como exocometas. Debido a la pequeña superficie, y a la baja cantidad de luz que reflejan, no es posible observarlos directamente. Sin embargo, a medida que pasan frente a la estrella se pueden detectar las absorciones del gas evaporado superpuestas al espectro de la propia estrella. Con el fin de identificar nuevas estrellas con exocometas, y realizar un estudio de las características de los sistemas en los que se encuentran, se obtuvieron 1575 espectros de alta resolución para 117 estrellas. Para ello, se utilizaron cuatro telescopios, ubicados en ambos hemisferios, durante dos años de trabajo. A continuación, se resumen las conclusiones alcanzadas en esta investigación.

1. La mayor parte de esta tesis doctoral se centra en el análisis de los 1500 espectros obtenidos entre septiembre de 2015 y septiembre de 2017 para el conjunto de 117 estrellas con tipos espectrales que van desde G hasta B. Los criterios de selección fueron muy sesgados hacia i) estrellas con entornos circunestelares ricos, incluyendo aquellas que presentaban variaciones similares a las producidas por exocometas detectadas previamente, ii) estrellas que muestran rastros de gas caliente –detectado con espectroscopía óptica– o frío –detectado en los rangos de longitud de onda sub-mm y mm– en sus entornos circunestelares, iii) estrellas con discos de *debris* con inclinaciones cercanas a 90 grados, iv) estrellas con excesos en infrarrojo cercano relacionados con la presencia de polvo caliente, y v) estrellas que pertenecen a asociaciones jóvenes (por ejemplo, Upper Scorpious, Tucana-Horologium o el grupo de β Pic). Todos los espectros disponibles fueron inspeccionados en busca de evidencias de gas circunestelar en las líneas Ca II y Na I D, lo cual representa el estudio sistemático más grande realizado hasta ahora en la búsqueda de exocomets. El análisis de toda la muestra reveló:

- La presencia de absorciones estrechas, no fotosféricas y estables, compatibles con la existencia de gas circunestelar caliente, superpuestas en los perfiles fotosféricos de las líneas Ca II y / o Na I, en 60 estrellas ($\sim$ 50% de la muestra). Se realizó una inspección de las características de esas absorciones, y su posible relación con las nubes de gas interestelar en la línea de visión, para discernir si las absorciones estrechas tienen un origen circunestelar o interestelar. Debido a variaciones detectadas en la absorción, correspondencia entre la velocidad radial de la estrella y la de la absorción, o la evidencia de ausencia de gas en el interestelar, se atribuyó origen circunestelar para 30 estrellas. El origen de este gas podría estar relacionado con la evaporación de cuerpos pequeños, o con el gas liberado en colisiones de polvo o planetesimales. En aquellos casos en los que se identifican perfiles triangulares en forma de *shell* superpuestos a las líneas metálicas fotosféricas de las estrellas, también se detectan absorciones estables estrechas, que apuntan hacia un entorno circunestelar rico en gas.
- Se calcularon las densidades de columna de estas absorciones no fotosféricas estrechas, pero no se encontraron diferencias aparentes, al comparar sus relaciones N_{CaII} / N_{NaI}, entre las dos poblaciones de gas con origen interestelar o circunestelar. Aún así, debe tenerse en cuenta que la presencia de absorciones tanto en Ca II como en Na I es más común para las líneas de origen interestelar.
- Se detectaron absorciones no fotosféricas variables en 18 estrellas, que representan el 15% de la muestra, de las cuales seis son nuevas (no aparecen como tal en literatura anterior). Estas absorciones variables están presentes simultáneamente junto con absorciones estables en 16 casos, la mayoría de los cuales pueden atribuirse a un origen circunestelar. Las variaciones detectadas muestran una amplia gama de cambios en la profundidad y la velocidad radial, todas ellas en un rango menor de $\sim$ 100 km/s con respecto a la velocidad radial estelar. La mayoría de estas detecciones son consistentes con el tránsito de una nube (o coma) de gas frente a una estrella, es decir, exocometas. Además, hay otras ocho estrellas en la muestra que presentaron variaciones similares a exocometas en trabajos previos, para los cuales no observamos ninguna variabilidad, siendo el porcentaje final de objetos con variabilidad tipo exocometaria de un 22% en toda la muestra.
- Hemos encontrado, en total, 32 estrellas con algún tipo de absorción no fotosférica, atribuida a gas circunestelar. Todas aparecen en estrellas con tipos espectrales anteriores a A9 (consistente con trabajos previos) y una amplia distribución de edades, entre $\sim$ 10 Myr y $\sim$ 1 Gyr. Con respecto al resto de la muestra, tienen velocidades de rotación proyectada más elevadas, posiblemente indicando ángulos de inclinación altos (cercanos a 90 grados) y, por lo tanto, una geometría adecuada para la detección de gas en el disco.
- En 22 estrellas de la muestra hay detecciones de excesos en el infrarrojo cercano, relacionadas en algunos casos con la presencia de polvo caliente, muy cerca de la estrella. La tasa de detección de absorciones no fotosféricas para estas estrellas es del $\sim$ 27%, mientras que, si consideramos solo aquellas con tipos espectrales ante-

riores a F2 (consistentes con las detecciones de exocometas), crece hasta $\sim 50\%$. Teniendo en cuenta el hecho de que estas estrellas tienen inclinaciones aleatorias, las probabilidades de observar uno de estos sistemas con inclinaciones cercanas a 90 grados y, que por lo tanto, la orientación del sistema sea favorable a la detección de gas en el disco, son de alrededor del 40%, consistente con la fracción de estrellas con polvo caliente detectado. Esto apunta hacia una correlación entre la presencia de gas y polvo en las regiones internas del sistema, cerca de la estrella, y un posible origen común.

- Las estrellas con abundancias anómalas, también conocidos como λ Boo incluidos en la muestra, también presentan una fracción alta de detecciones de gas. La diferencia en la abundancia de metales más ligeros –C, N, O– y más pesados –Fe, Al, Mg–, se ha explicado en la literatura como acreción diferencial del medio circunestelar, un escenario que podría involucrar la presencia de cuerpos pequeños en el sistema. Comparando las anchuras equivalentes de las líneas de Mg y O, hemos identificado seis objetos con características λ Boo, que no aparecen en trabajos previos como tal. De una muestra final de 18 estrellas con características λ Boo, hemos identificado variabilidad de tipo exocometario en el 44% de ellas, una fracción mucho mayor que la obtenida para la muestra ($\sim 22\%$), lo que refuerza el escenario de acreción diferencial del medio circunestelar .
- No existe una relación aparente entre la presencia de un disco de *debris* en torno a la estrella ($L_{\rm dust}$ / $L_\star \geqslant 10^{-6}$) y la presencia de gas circunestelar en el sistema. Solo el 45% de las estrellas con variaciones de tipo exocometario y el 50% de las estrellas con componentes estables estrechas originadas en el medio circunestelar muestran excesos infrarrojos compatibles con un disco de *debris*. Sin embargo, las estrellas en la muestra cuyos discos han sido resueltos espacialmente presentan una clara tendencia hacia detecciones de absorciones de origen circunestelar cuando los discos tienen orientaciones cercanas a 90 grados.

2. Se realizó un análisis separado para todas las estrellas de tipo temprano (tipo A) con discos de *debris* detectados, donde también está presente gas frío, observado en longitudes de onda de infrarrojo lejano o (sub-) milimétrico. La mayoría de estas estrellas están incluidas en nuestra muestra, con la excepción de β Pic y Fomalhaut, que aun así se tuvieron en cuenta para este estudio en particular. Se identificaron componentes no fotosféricos estables estrechas en la línea de Ca II K en 11 de 17 estrellas, para ocho de las cuales la presencia de gas en el entorno circunstelar es el origen más probable. Al considerar la inclinación de los discos, conocida para 16 de 17 objetos, se detecta la presencia de una absorción estrecha circunestelar en ocho de nueve objetos con inclinaciones en torno a 90 grados; y existe evidencia de absorciones de gas circunestelar en solo uno de los ocho discos que tienen inclinaciones pequeñas, HD 156623, donde se detectan variaciones compatibles con un evento de tipo exocometario. Esto sugiere una correlación entre la detección de gas caliente y circunestelar y el ángulo de inclinación del sistema. Este resultado también apunta hacia una correlación entre la

presencia de gas frío y gas caliente, que posiblemente comparten un origen secundario común, relacionado con la presencia de cuerpos pequeños en el sistema. Esto podría ser clave en la búsqueda de nuevos sistemas con gas frío, más difíciles de detectar que las absorciones espectroscópicas ópticas.

3. Tres estrellas fueron seleccionadas de la muestra general para su estudio individual debido a peculiaridades en las absorciones detectadas, originadas mediante diferentes mecanismos.

   - La estrella ϕ Leo, de tipo espectral A7, es el objeto más variable de la muestra, presentando cambios en la línea de Ca II K en escalas de tiempo menores a una hora. También se detecta en la linea de Ca II K un perfil triangular, similar a los observados en estrellas tipo *shell*, y absorciones prominentes en el doblete de Ti II en 3760 Å, lo que indica la presencia de gas en el entorno circunestelar. La alta frecuencia de las variaciones de las absorciones en la línea Ca II K sugiere que podrían originarse por cuerpos que se evaporan, es decir, exocometas, cerca de la estrella. Este objeto podría ser una de las estrellas con un entorno rico en exocometas más viejas, $\sim$ 900 Myr.
   - HR 10 ha sido repetidamente estudiado en la literatura y considerado antes de nuestro trabajo como una de las estrellas con exocometas más importantes. Se detectaron absorciones estrechas no fotosféricas en muchas líneas metálicas de Ca II, Fe II y Ti II en todos los espectros obtenidos durante nuestras campañas de observación, con la característica común de que cada absorción estrecha tenía dos componentes. El análisis conjunto de todos los datos espectroscópicos disponibles (nuestras propias observaciones y datos de archivo y publicados) que cubren un lapso de tiempo de 32 años, mostró un claro patrón de periodicidad en las velocidades radiales de las dos componentes estrechas observadas en cada línea, lo cual, no se espera para absorciones de tipo exocometario. Esto, junto con las observaciones realizadas con el instrumento infrarrojo PIONIER en el interferómetro del Very Large Telescope (VLTI), llevó a la conclusión de que HR 10 es en realidad un sistema binario, y las absorciones están originadas en las envolturas circunestelares individuales que rodean cada estrella, descartando la hipótesis de un origen exocometario. Además, las observaciones permitieron hacer una caracterización completa de las estrellas y sus órbitas.
   - HD 37306 se ha estudiado por separado debido a la variación inusual de sus líneas metálicas. Esta estrella A2 muestra en cada espectro dos componentes de absorción no fotosféricos atribuidos al medio interestelar debido a la falta de variabilidad y al hecho de que las absorciones tienen velocidades radiales que no coinciden con la velocidad radial de la estrella. En una de las campañas, y durante 8 días, se detectó una absorción superpuesta a las líneas fotosféricas de la estrella similar a las observadas en estrellas *shell* en las lineas de elementos metálicos, como Ca II, Ti II y Fe II. Debido a que no se detectó la variación en especies neutras (por ejemplo, Mg I), y las proporciones de las anchuras equivalentes de

las líneas no son consistentes con un medio ópticamente delgado, la absorción debe estar producida por material ionizado ópticamente grueso. El origen de las absorciones en las estrellas tipo *shell*, y particularmente en este caso, es incierto, pero se ha sugerido la presencia de una envoltura esférica o un disco alrededor de la estrella.

Como conclusión global, el trabajo contenido en esta tesis doctoral proporciona resultados generales e individuales a través de un gran estudio espectroscópico de alta resolución para buscar exocometas, y de la investigación del entorno gaseoso de las estrellas de secuencia principal. Se ha detectado gas circunestelar en 32 objetos, todos ellos estrellas de tipo A. Los resultados apuntan hacia tasas de detección más altas si el sistema está de canto (inclinaciones en torno a 90 grados) y una posible correlación entre la presencia de gas frío y el gas detectado en la espectroscopía óptica. Se han encontrado seis nuevos objetos que muestran variabilidad similar a la producida por exocometas, y la conexión entre la presencia de exocomets y su entorno, o las propiedades estelares, apuntan hacia una mayor probabilidad de detección de eventos tipo exocometario alrededor de estrellas Boo de tipo A, con inclinaciones en torno a 90 grados, o con evidencias de la presencia de polvo caliente (excesos en el infrarrojo cercano), mientras que la presencia de un disco de *debris* no muestra, en principio, una conexión clara con el fenómeno exocometario. Aún así, la detección de absorciones variables no fotosféricas superpuestas a las líneas fotosféricas de la estrella, debe analizarse cuidadosamente antes de atribuir un origen exocometario, ya que hay una serie de procesos, relacionados con la estrella o el medio circunestelar, que podrían generar absorciones similares. Los primeros resultados preliminares del trabajo en curso presentado en esta tesis acerca de la relación entre el tipo espectral y la presencia de exocometas en el espectro, sugiere que este tipo de detecciones podría ser más probable en torno a estrellas tipo A debido, no solo debido a un sesgo observacional, sino que probablemente esté relacionado con mecanismos físicos que impiden la detección de características exocometarias en otros tipos espectrales.

Trabajo futuro

Los resultados obtenidos durante el desarrollo de esta tesis doctoral apuntan hacia nuevas líneas de trabajo y la necesidad de continuar las observaciones de las estrellas en la muestra que presentan variabilidad.

Se necesita un seguimiento espectroscópico para las estrellas que muestra evidencias de presencia de exocometas, para descartar falsos positivos. Los instrumentos de alta resolución disponibles y futuros diseñados para la búsqueda en velocidades radiales de exoplanetas, nos permitirán detectar características con dispersiones de velocidad más pequeñas y restringir mejor las velocidades radiales de las absorciones, identificando posibles casos de periodicidad, que podrían surgir como consecuencia de la binariedad del sistema, o evidencias espectroscópicas de la actividad estelar. El hallazgo de una correlación entre la presencia

de gas circunestelar frío y caliente ha llevado a la selección de una muestra de objetos con absorciones no fotosféricas estables estrechas con origen circunestelar que se observarán con el Atacama Large Millimiter Array (ALMA) en el ciclo 7 para buscar una contrapartida de gas frío. Si se confirmara nuestra hipótesis, esto también abrirá la posibilidad de un nuevo método de selección para la búsqueda de estrellas con gas frío. Además de las instalaciones que trabajan en los rangos milimétrico y submilimétrico, los nuevos espectrógrafos de alta resolución en rango infrarrojo también permitirán la detección de los modos rotaciones del CO, que servirían como estimación inicial de la presencia y cantidad de gas en las zonas externas del sistema.

La detección de variaciones compatibles con exocometas en la curva de luz de β Pictoris, y las capacidades de nuevas misiones espaciales como TESS y CHEOPS, representan el punto de partida para estudios fotométricos de estrellas con evidencias de la presencia de exocometas en sus espectros. Además, se necesitan observaciones simultáneas en espectroscopía y fotometría para realizar una mejor caracterización de los exocometas.

La realización de un estudio teórico en profundidad acerca de la presencia de exocometas solo alrededor de estrellas de tipo A es fundamental para determinar si esto es un sesgo observacional o, por el contrario, tiene una explicación física, relacionada con las características de la estrella y/o las características del sistema . En particular, la búsqueda en fotometría de señales exocometarias en estrellas de tipos espectrales tardíos, que ya ha dado algunos resultados, o la búsqueda de variabilidad en líneas espectrales distintas al Ca II podrían arrojar luz sobre este asunto.

En general, la investigación de exocometas tiene muchas posibilidades para exploraciones futuras, en diferentes rangos de longitud de onda y con diferentes técnicas, que ayudarían a expandir el conocimiento actual. La investigación centrada en cuerpos pequeños es esencial en el estudio de los mecanismos de formación y la configuración de los sistemas planetarios, y podría tener un impacto no despreciable en la búsqueda de vida y su origen.

Chapter 7

Conclusións e traballo futuro

Resumo e conclusións

O traballo presentado nesta tese céntrase no estudo das evidencias de corpos pequenos detectadas arredor de estrelas de secuencia principal de tipo A, é dicir, interpretadas como exocometas. Debido á súa pequena superficie, e á baixa cantidade de luz que reflexan, non é posible observalos directamente. Porén, a medida que pasan fronte á estrela pódense detectar as absorcións do gas evaporado superpostas ao espectro da propia estrela. Coa fin de identificar novas estrelas con exocometas, e realizar un estudo das características dos sistemas nos que se atopan, obtivéronse 1575 espectros de alta resolución para 117 estrellas. Para acadar este obxectivo, empregáronse catro telescopios, situados en ambos hemisferios, durante dous anos de traballo. A continuación, resúmense as conclusións acadadas nesta investigación.

1. A maior parte da presente tese de doutoramento céntrase na análise dos $\sim$ 1500 espectros obtidos entre setembro de 2015 e setembro de 2017 para o conxunto de 117 estrelas con tipos espectrais que van dende G ata B. Os criterios de selección privilexiaron i) estrelas con contornas circunestelares ricas, incluíndo aquelas que presentaban variacións similares ás producidas por exocometas detectadas previamente, ii) estrelas que amosan rastros de gas quente –detectado con espectroscopía óptica– ou frío –detectado nos rangos de lonxitude de onda sub-mm e mm– nas súas contornas circunestelares, iii) estrelas con discos de *debris* con inclinacións próximas a 90 graos, iv) estrelas con excesos en infravermello próximo relacionados coa presenza de polvo quente, e v) estrelas que pertencen a asociacións novas (por exemplo, Upper Scorpious, Tucana-Horologium ou o grupo de β Pic). Tódolos espectros dispoñibles foron inspeccionados na procura de evidencias de gas circunestelar nas liñas Ca II e Na I D, o cal representa o estudo sistemático máis grande realizado ata o de agora na busca de exocometas. A análise de toda a mostra revelou:

    - A presenza de absorcións estreitas, non fotosféricas e estables, compatibles coa

existencia de gas circunestelar quente, superpostas nos perfís fotosféricos das liñas Ca II e/ou Na I, en 60 estrelas (50% da mostra). Realizouse unha inspección das características desas absorcións, e a súa posible relación coas nubes de gas interestelar na liña de visión, para discernir se as absorcións estreitas teñen unha orixe circunestelar ou interestelar. Debido a variacións detectadas na absorción, correspondencia entre a velocidade radial da estrela e a da absorción, ou a evidencia de ausencia de gas no medio interestelar, atribuíuse orixe circunestelar para 30 estrelas. A orixe deste gas podería estar relacionada coa evaporación de corpos pequenos, ou co gas liberado en colisións de polvo ou planetesimais. Naqueles casos nos que se identifican perfís triangulares en forma de *shell* superpostos ás liñas metálicas fotosféricas das estrelas, tamén se detectan absorcións estables estreitas, que apuntan cara unha contorna circunestelar rica en gas.

- Calculáronse as densidades de columna destas absorcións non fotosféricas estreitas, pero non se atoparon diferenzas aparentes, ao comparar as súas relacións N_{CaII}/N_{NaI}, entre as dúas poboacións de gas con orixe interestelar ou circunestelar. Aínda así, salientamos que a presenza de absorcións tanto en Ca II como en Na I é máis común para as liñas de orixe interestelar.

- Detectáronse absorcións non fotosféricas variables en 18 estrelas, que representan o 15% da mostra, das cales seis son novas (non aparecen como tal na literatura anterior). Estas absorcións variables están presentes simultaneamente con absorcións estables en 16 casos, a maior parte das cales poden atribuírse a unha orixe circunestelar. As variacións detectadas amosan unha ampla gama de cambios na profundidade e na velocidade radial, todas elas nun rango menor de $\sim$ 100 km/s respecto da velocidade radial estelar. A maioría destas detección son consistentes co tránsito dunha nube (ou coma) de gas fronte a unha estrela, é dicir, exocometas. Ademais, hai outras oito estrelas na mostra que presentaron variacións similares a exocometas en traballos previos, para os cales non observamos ningunha variabilidade, sendo a porcentaxe final de obxectos con variabilidade tipo exocometaria dun 22% en toda a mostra.

- Atopamos, en total, 32 estrelas con algún tipo de absorción non fotosférica, atribuída a gas circunestelar. Todas aparecen en tipos espectrais anteriores a A9 (consistente con traballos previos) e unha ampla distribución de idades, entre $\sim$ 10 Myr e $\sim$ 1 Gyr. Respecto do resto da mostra, teñen velocidades de rotación proxectada máis elevadas, posiblemente indicando ángulos de inclinación altos (próximos a 90 graos) e, polo tanto, unha xeometría axeitada para a detección de gas no disco.

- En 22 estrelas da mostra prodúcense detección de excesos no infravermello próximo, relacionadas nalgúns casos coa presenza de polvo quente, moi preto da estrela. A taxa de detección de absorcións non fotosféricas para estas estrelas é do $\sim$ 27%, mentres que, se consideramos só aquelas con tipos espectrais anteriores a F2 (consistentes coas detección de exocometas), a taxa de detección medra ata o $\sim$ 50%. Tendo en conta o feito de que estas estrelas teñen inclinacións aleatorias,

as probabilidades de observar un destes sistemas con inclinacións próximas a 90 graos e, que polo tanto, a orientación do sistema sexa favorable á detección de gas no disco, son de arredor do 40%, consistente coa fracción de estrelas con polvo quente detectado. Isto apunta cara unha correlación entre a presenza de gas e polvo nas rexións internas do sistema, preto da estrela, e unha posible orixe común.

- As estrelas con abundancias anómalas, tamén coñecidas como Boo incluídas na mostra, tamén presentan unha fracción alta de detección de gas. A diferenza na abundancia de metais máis lixeiros –C, N, O– e máis pesados –Fe, Al, Mg–, tense explicado na literatura como acreción diferencial do medio circunestelar, un escenario que podería involucrar a presenza de corpos pequenos no sistema. Comparando as anchuras equivalentes das liñas de Mg e O, identificamos seis obxectos con características Boo, que non aparecen como tal en traballos previos. Dunha mostra final de 18 estrelas con características Boo, identificamos variabilidade de tipo exocometario no 44% delas, unha fracción moito maior que a obtida para a mostra ($\sim$ 22%), o que reforza o escenario de acreción diferencial do medio circunestelar.

- Non existe unha relación aparente entre a presenza dun disco de *debris* en torno á estrela ($L_{\rm dust}$ / $L_\star$ ¿ 10^{-6}) e a presenza de gas circunestelar no sistema. Só o 45% das estrelas con variacións de tipo exocometario e o 50% das estrelas con compoñentes estables estreitas orixinadas no medio circunestelar amosan excesos infravermellos compatibles cun disco de *debris*. Porén, as estrelas na mostra cuxos discos teñen sido resoltos espacialmente presentan unha clara tendencia cara detección de absorcións de orixe circunestelar cando os discos teñen orientacións próximas a 90 graos.

2. Realizouse unha análise separada para tódalas estrelas de tipo temperán (tipo A) con discos de *debris* detectados, onde tamén está presente gas frío, observado en lonxitudes de onda de infravermello afastado ou (sub-) milimétrico. A maior parte destas estrelas están incluída na nosa mostra, coa excepción de β Pic e Fomalhaut, que aínda así tivéronse en conta para este estudo en particular. Identificáronse compoñentes non fotosféricas estables estreitas na liña de Ca II K en 11 de 17 estrelas, para oito das cales a presenza de gas na contorna circunstelar é a orixe máis probable. Ao considerar a inclinación dos discos, coñecida para 16 de 17 obxectos, detéctase a presenza dunha absorción estreita circunestelar en oito de nove obxectos con inclinacións en torno a 90 graos; e existe evidencia de absorcións de gas circunestelar en só un dos oito discos que teñen inclinacións pequenas, HD 156623, onde se detectan variacións compatibles cun evento de tipo exocometario. Isto suxire unha correlación entre a detección de gas quente e circunestelar e o ángulo de inclinación do sistema. Este resultado tamén apunta cara unha correlación entre a presenza de gas frío e gas quente, que posiblemente comparten unha orixe secundaria común, relacionado coa presenza de corpos pequenos no sistema. Este feito podería ser clave na procura de novos sistemas con gas frío, máis difíciles de detectar que as absorcións espectroscópicas ópticas.

3. Tres estrelas foron seleccionadas da mostra xeral para o seu estudo individual debido a peculiaridades nas absorcións detectadas, orixinadas mediante diferentes mecanismos.

   - A estrela ϕ Leo, de tipo espectral A7, é o obxecto máis variable da mostra, presentando cambios na liña Ca II K en escalas de tempo menores a unha hora. Tamén se detecta na liña de Ca II K un perfil triangular, similar aos observados en estrelas tipo *shell*, e absorcións prominentes no dobrete de Ti II en 3760 Å, o que indica a presenza de gas na contorna circunestelar. A alta frecuencia das variacións das absorcións na liña Ca II K suxire que poderían orixinarse por corpos que se evaporan, é dicir, exocometas, preto da estrela. Este obxecto podería ser unha das estrelas cunha contorna rico en exocometas máis vellas, $\sim$900 Myr. - HR 10 ten sido repetidamente estudada na literatura e considerado antes do noso traballo como unha das estrelas con exocometas máis importantes. Detectáronse absorcións estreitas non fotosféricas en moitas liñas metálicas de Ca II, Fe II e Ti II en tódolos espectros obtidos durante as nosas campañas de observación, coa característica común de que cada absorción estreita tiña dúas compoñentes. A análise conxunta de tódolos datos espectroscópicos dispoñibles (as nosas propias observacións e datos de arquivo e publicados) que cobren un lapso de tempo de 32 anos, amosou un claro patrón de periodicidade nas velocidades radiais das dúas compoñentes estreitas observadas en cada liña, o cal, non se agarda para absorcións de tipo exocometario. Isto, xunto coas observacións realizadas co instrumento infravermello PIONIER no interferómetro do Very Large Telescope Interferometer (VLTI), levou á conclusión de que HR 10 é, en realidade, un sistema binario, e as absorcións están orixinadas nas envolturas circunestelares individuais que rodean cada estrela, descartando a hipótese dunha orixe exocometaria. Ademais, as observacións permitiron facer unha caracterización completa das estrelas e as súas órbitas. - HD 37306 estudouse por separado debido á variación inusual das súas liñas metálicas. Esta estrela A2 amosa en cada espectro dúas compoñentes de absorción non fotosféricas atribuídas ao medio interestelar debido á falla de variabilidade e ao feito de que as absorcións teñen velocidades radiais que non coinciden coa velocidade radial da estrela. Nunha das campañas, e durante 8 días, detectouse unha absorción superposta ás liñas fotosféricas da estrela similar ás observadas en estrelas *shell* nas liñas de elementos metálicos, como Ca II, Ti II e Fe II. Debido a que non se detectou a variación en especies neutras (por exemplo, Mg I), e as proporcións das anchuras equivalentes das liñas non son consistentes cun medio opticamente delgado, a absorción debe estar producida por material ionizado ópticamente groso. A orixe das absorcións nas estrelas tipo *shell*, e particularmente neste caso, é incerta, pero tense suxerido a presenza dunha envoltura esférica ou un disco arredor da estrela.

Como conclusión global, o traballo contido nesta tese de doutoramento proporciona resultados xerais e individuais a través dun gran estudo espectroscópico de alta resolución na procura de exocometas, e da investigación da contorna gaseosa das estrelas de secuencia

principal. Detectouse gas circunestelar en 32 estrelas, todas elas de tipo A. Os resultados apuntan cara taxas de detección máis altas se o sistema está de canto (inclinacións en torno a 90 graos) e unha posible correlación entre a presenza de gas frío e o gas detectado na espectroscopía óptica. Atopáronse seis novos obxectos que amosan variabilidade similar á producida por exocometas, e a conexión entre a presenza de exocometas e a súa contorna, ou as propiedades estelares, apuntan cara unha maior probabilidade de detección de eventos tipo exocometario arredor de estrelas λ Boo de tipo A, con inclinacións en torno a 90 grados, ou con evidencias da presenza de polvo quente (excesos no infravermello próximo), mentres que a presenza dun disco de *debris* non amosa, en principio, unha conexión clara co fenómeno exocometario. Aínda así, a detección de absorcións variables non fotosféricas superpostas ás liñas fotosféricas da estrela, debe analizarse coidadosamente antes de atribuír unha orixe exocometaria, xa que hai unha serie de procesos, relacionados coa estrela ou o medio circunestelar, que poderían xerar absorcións similares. Os primeiros resultados preliminares do traballo en curso presentado nesta tese acerca da relación entre o tipo espectral e a presenza de exocometas no espectro, suxire que este tipo de detección podería ser máis probables en torno a estrelas tipo A, no só debido a un sesgo observacional, senón que, probablemente, estea relacionado con mecanismos físicos que impiden a detección de características exocometarias noutros tipos espectrais.

Traballo futuro

Os resultados obtidos durante o desenvolvemento desta tese de doutoramento apuntan cara novas liñas de traballo e a necesidade de continuar as observacións das estrelas na mostra que presentan variabilidade.

Precísase un seguimento espectroscópico das estrelas que amosan evidencias de presenza de exocometas, para descartar falsos positivos. Os instrumentos de alta resolución dispoñibles e futuros deseñados para a busca de exoplanetas en velocidades radiais, permitirannos detectar características con dispersións de velocidade máis pequenas e restrinxir mellor as velocidades radiais das absorcións, identificando posibles casos de periodicidade que poderían xurdir como consecuencia da binariedade do sistema, ou evidencias espectroscópicas da actividade estelar. O achado dunha correlación entre a presenza de gas circunestelar frío e quente levou á selección dunha mostra de obxectos con absorcións non fotosféricas estables estreitas con orixe circunestelar que se observarán co Atacama Large Millimiter Array (ALMA) no ciclo 7 na procura dunha contrapartida de gas frío. De confirmarse a nosa hipótese, isto tamén abriría a posibilidade dun novo método de selección para a busca de estrelas con gas frío. Ademais das instalacións que traballan nos rangos milimétrico e submilimétrico, os novos espectrógrafos de alta resolución en rango infravermello tamén permitirán a detección dos modos rotacións do CO, que servirían como estimación inicial da presenza e cantidade de gas nas zonas externas do sistema.

A detección de variacións compatibles con exocometas na curva de luz de β Pictoris,

e as capacidades de novas misións espaciais como *TESS* e *CHEOPS*, representan o punto de partida para estudos fotométricos de estrelas con evidencias da presenza de exocometas nos seus espectros. Ademais, necesítanse observacións simultáneas en espectroscopía e fotometría para obter unha mellor caracterización dos exocometas.

A realización dun estudo teórico en profundidade acerca da presenza de exocometas só arredor de estrelas de tipo A é fundamental para determinar se isto é un sesgo observacional ou, polo contrario, ten unha explicación física, relacionada coas características da estrela e/ou as características do sistema. En particular, a procura en fotometría de sinais exocometarias en estrelas de tipos espectrais tardíos, que xa ten dado algúns resultados, ou a busca de variabilidade en liñas espectrais distintas ao Ca II poderían clarificar este asunto.

En xeral, a investigación de exocometas ten moitas posibilidades para exploracións futuras, en diferentes rangos de lonxitude de onda e con diferentes técnicas, que axudarán a expandir o coñecemento actual. A investigación centrada en corpos pequenos é esencial no estudo dos mecanismos de formación e a configuración dos sistemas planetarios, e podería ter un impacto non desprezable na procura de vida e da súa orixe.

Appendix A

Exocomet Survey: Figures & Tables

A.1 Figures: Narrow Stable Absorptions

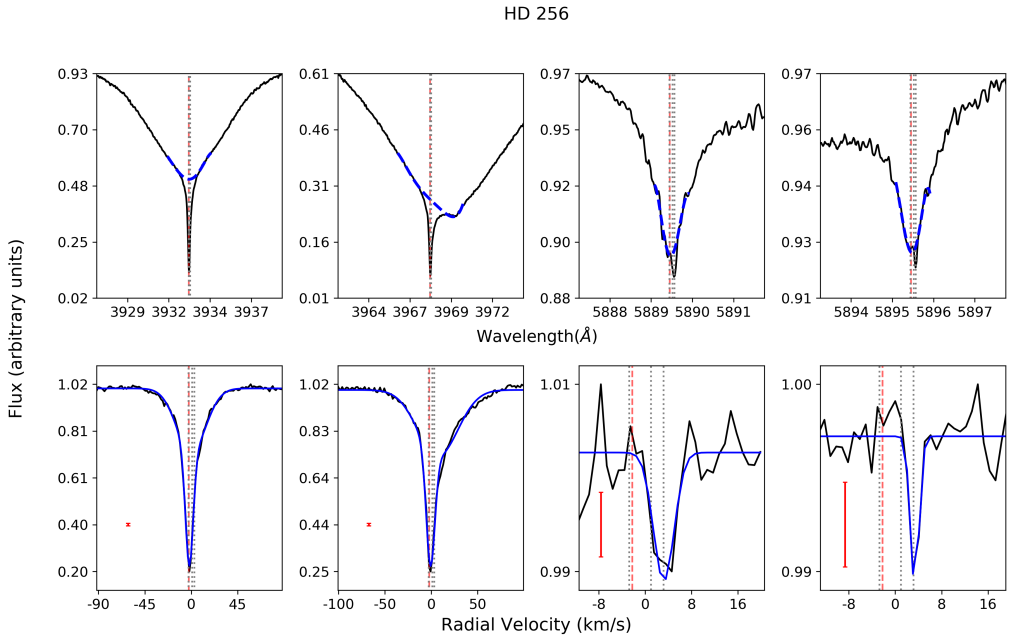

Figure A.1: Stars showing narrow non-photospheric absorptions. Top panels: Photospheric Ca II H & K and Na I D lines with fitted modeling dashed blue line, x-axis shows the wavelength. Bottom panels: Residuals once the spectrum is divided by the photosphere, x-axis in velocity. Blue lines mark the fits to the non-photospheric absorptions. Vertical red dashed and grey dotted lines represent the stellar radial velocity and the ISM velocities respectively. Red error bars show three sigma value measured in the continuum adjacent to the photospheric line.

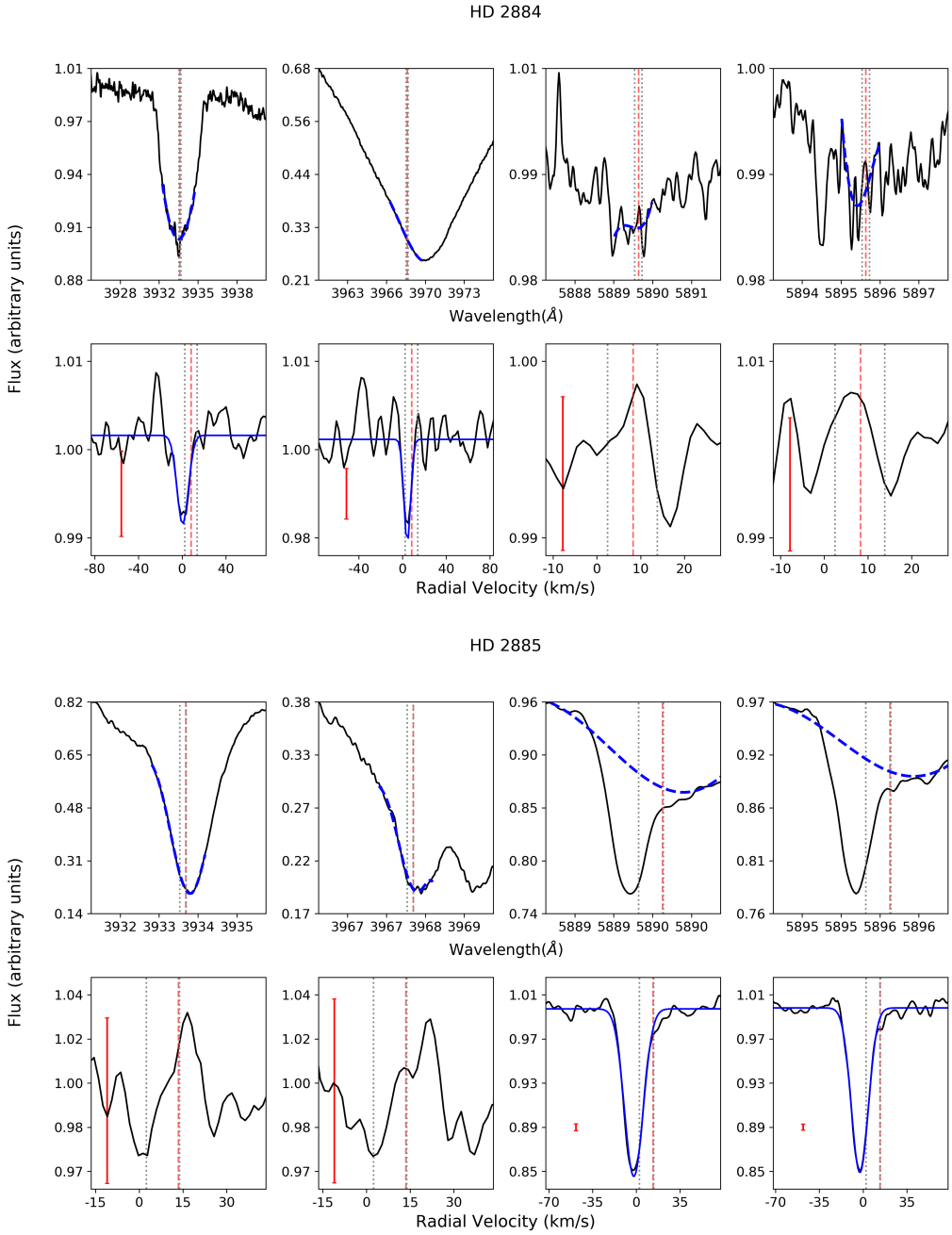

Figure 1 (Cont.): Stars showing narrow non-photospheric absorptions. Top panels: Photospheric Ca II H & K and Na I D lines with fitted modeling dashed blue line, x-axis shows the wavelength. Bottom panels: Residuals once the spectrum is divided by the photosphere, x-axis in velocity. Blue lines mark the fits to the non-photospheric absorptions. Vertical red dashed and grey dotted lines represent the stellar radial velocity and the ISM velocities respectively. Red error bars show three sigma value measured in the continuum adjacent to the photospheric line.

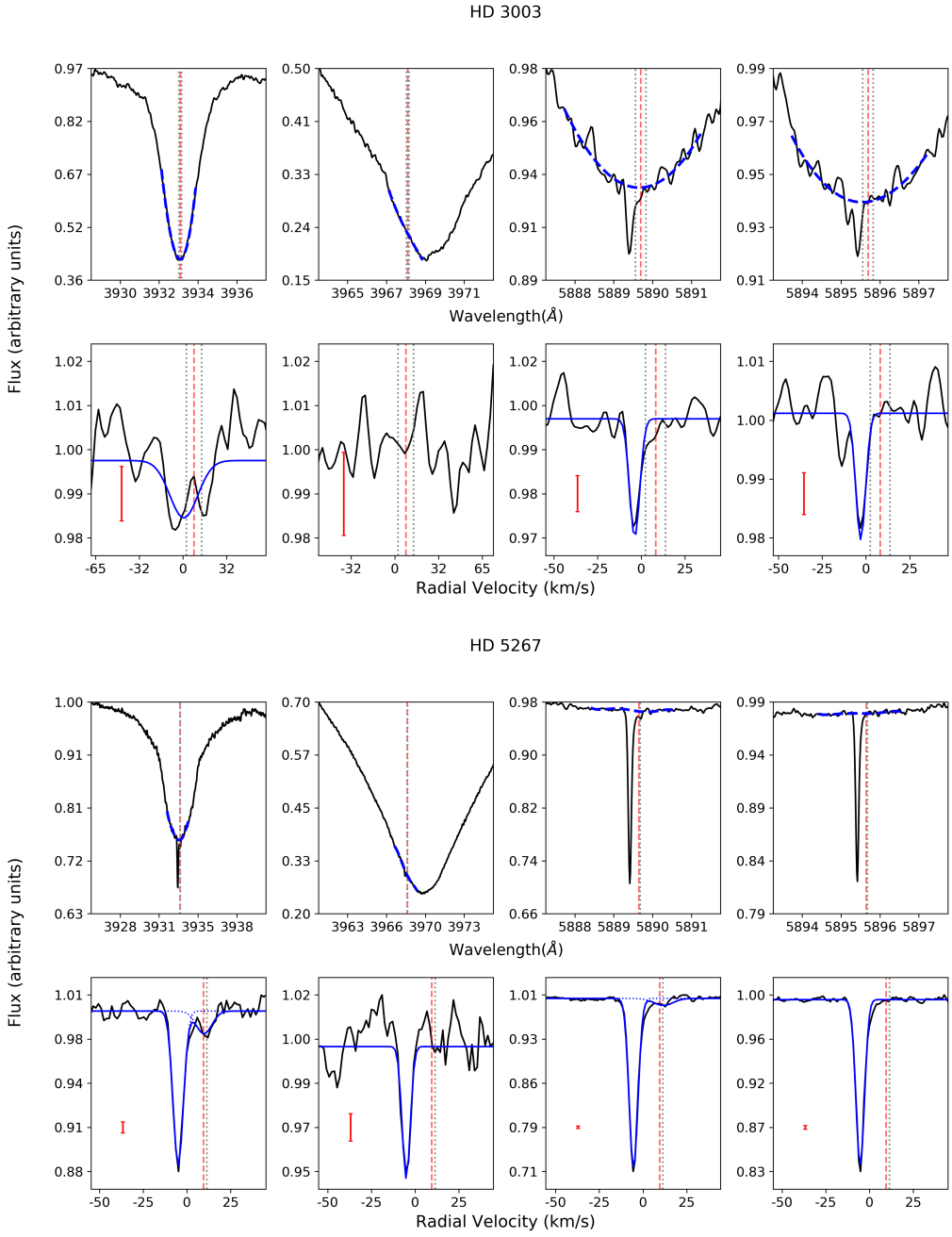

Figure 1 (Cont.): Stars showing narrow non-photospheric absorptions. Top panels: Photospheric Ca II H & K and Na I D lines with fitted modelin dashed blue line, x-axis shows the wavelength. Bottom panels: Residuals once the spectrum is divided by the photosphere, x-axis in velocity. Blue lines mark the fits to the non-photospheric absorptions. Vertical red dashed and grey dotted lines represent the stellar radial velocity and the ISM velocities respectively. Red error bars show three sigma value measured in the continuum adjacent to the photospheric line.

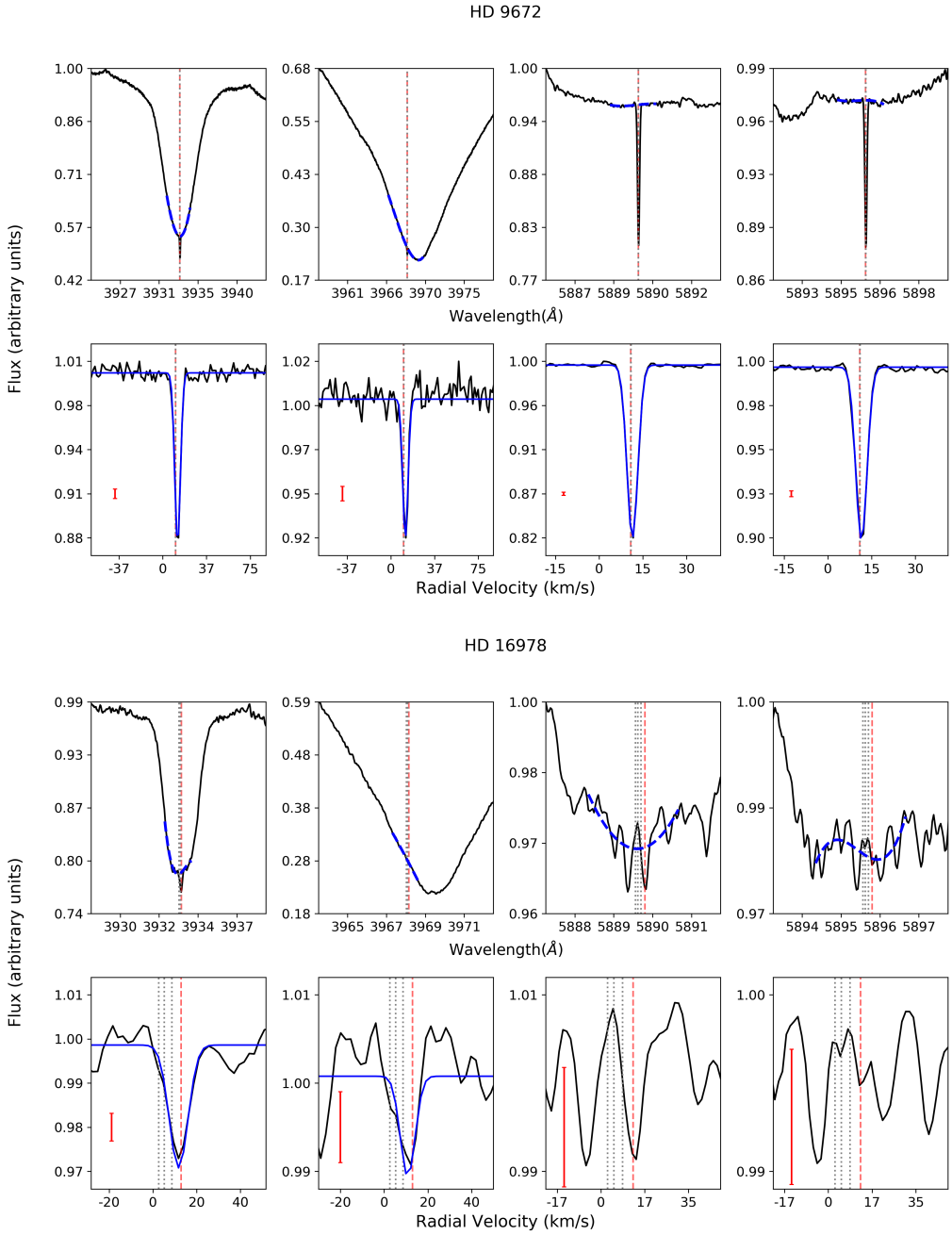

Figure 1 (Cont.): Stars showing narrow non-photospheric absorptions. Top panels: Photospheric Ca II H & K and Na I D lines with fitted modelin dashed blue line, x-axis shows the wavelength. Bottom panels: Residuals once the spectrum is divided by the photosphere, x-axis in velocity. Blue lines mark the fits to the non-photospheric absorptions. Vertical red dashed and grey dotted lines represent the stellar radial velocity and the ISM velocities respectively. Red error bars show three sigma value measured in the continuum adjacent to the photospheric line.

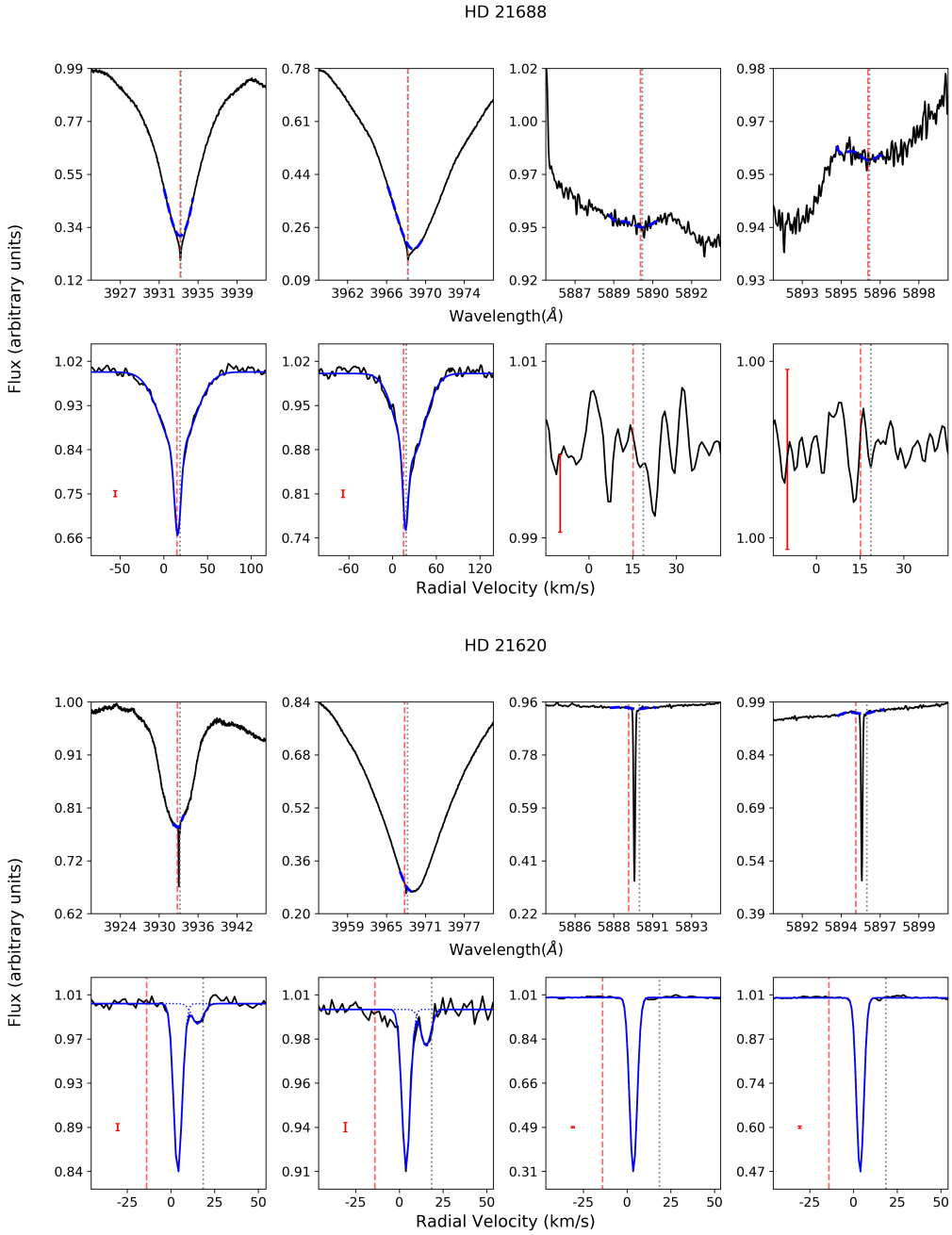

Figure 1 (Cont.): Stars showing narrow non-photospheric absorptions. Top panels: Photospheric Ca II H & K and Na I D lines with fitted modelin dashed blue line, x-axis shows the wavelength. Bottom panels: Residuals once the spectrum is divided by the photosphere, x-axis in velocity. Blue lines mark the fits to the non-photospheric absorptions. Vertical red dashed and grey dotted lines represent the stellar radial velocity and the ISM velocities respectively. Red error bars show three sigma value measured in the continuum adjacent to the photospheric line.

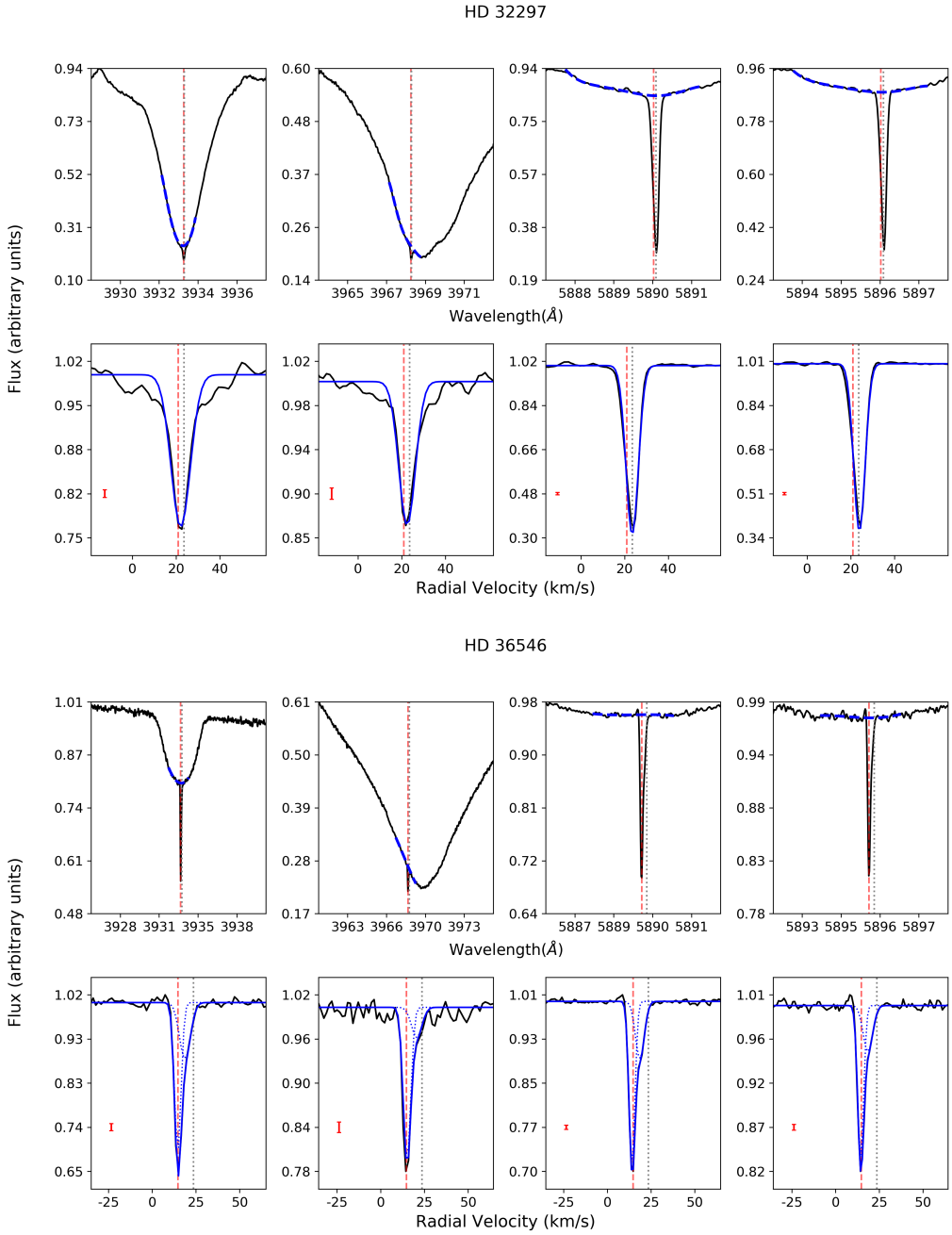

Figure 1 (Cont.): Stars showing narrow non-photospheric absorptions. Top panels: Photospheric Ca II H & K and Na I D lines with fitted modelin dashed blue line, x-axis shows the wavelength. Bottom panels: Residuals once the spectrum is divided by the photosphere, x-axis in velocity. Blue lines mark the fits to the non-photospheric absorptions. Vertical red dashed and grey dotted lines represent the stellar radial velocity and the ISM velocities respectively. Red error bars show three sigma value measured in the continuum adjacent to the photospheric line.

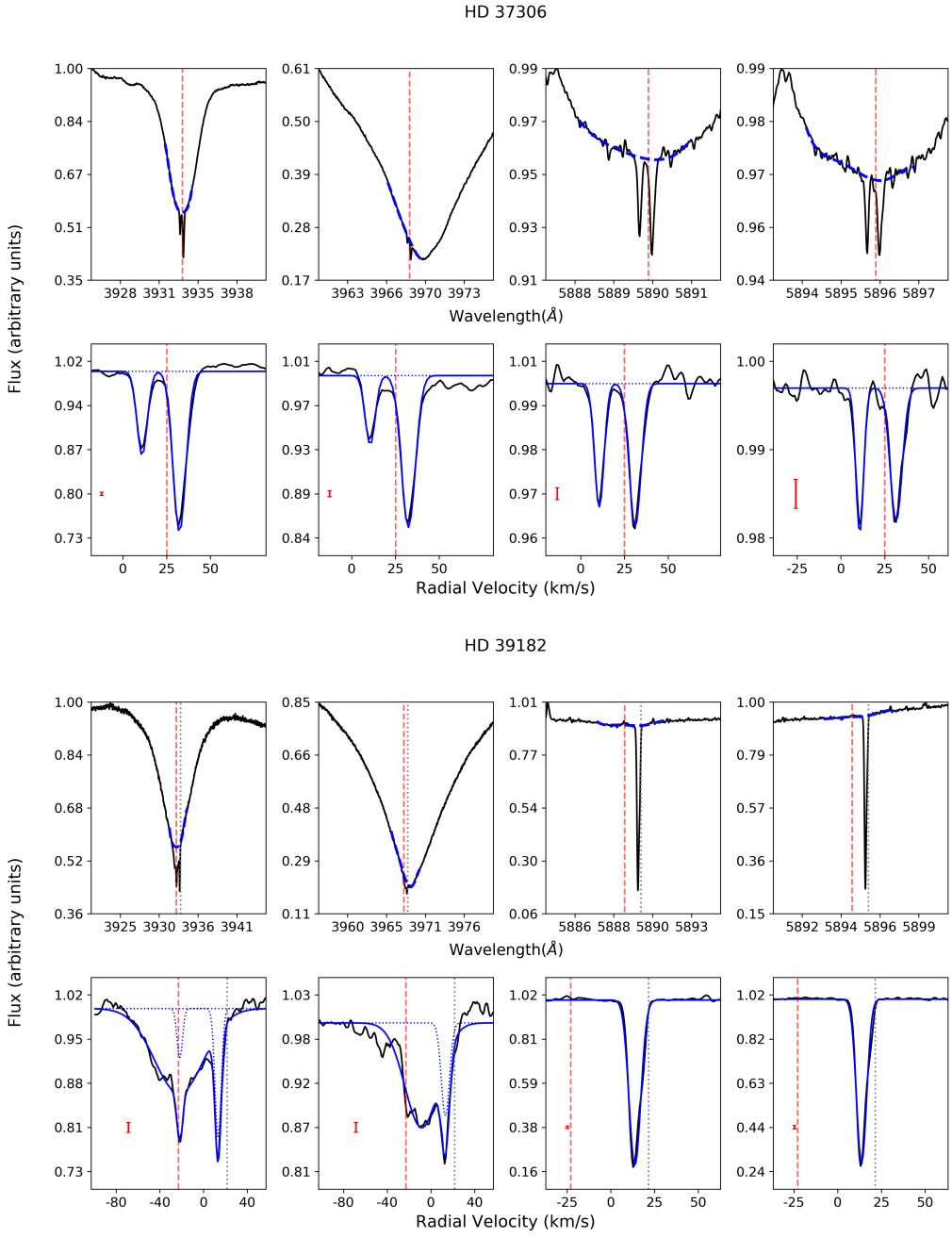

Figure 1 (Cont.): Stars showing narrow non-photospheric absorptions. Top panels: Photospheric Ca II H & K and Na I D lines with fitted modelin dashed blue line, x-axis shows the wavelength. Bottom panels: Residuals once the spectrum is divided by the photosphere, x-axis in velocity. Blue lines mark the fits to the non-photospheric absorptions. Vertical red dashed and grey dotted lines represent the stellar radial velocity and the ISM velocities respectively. Red error bars show three sigma value measured in the continuum adjacent to the photospheric line.

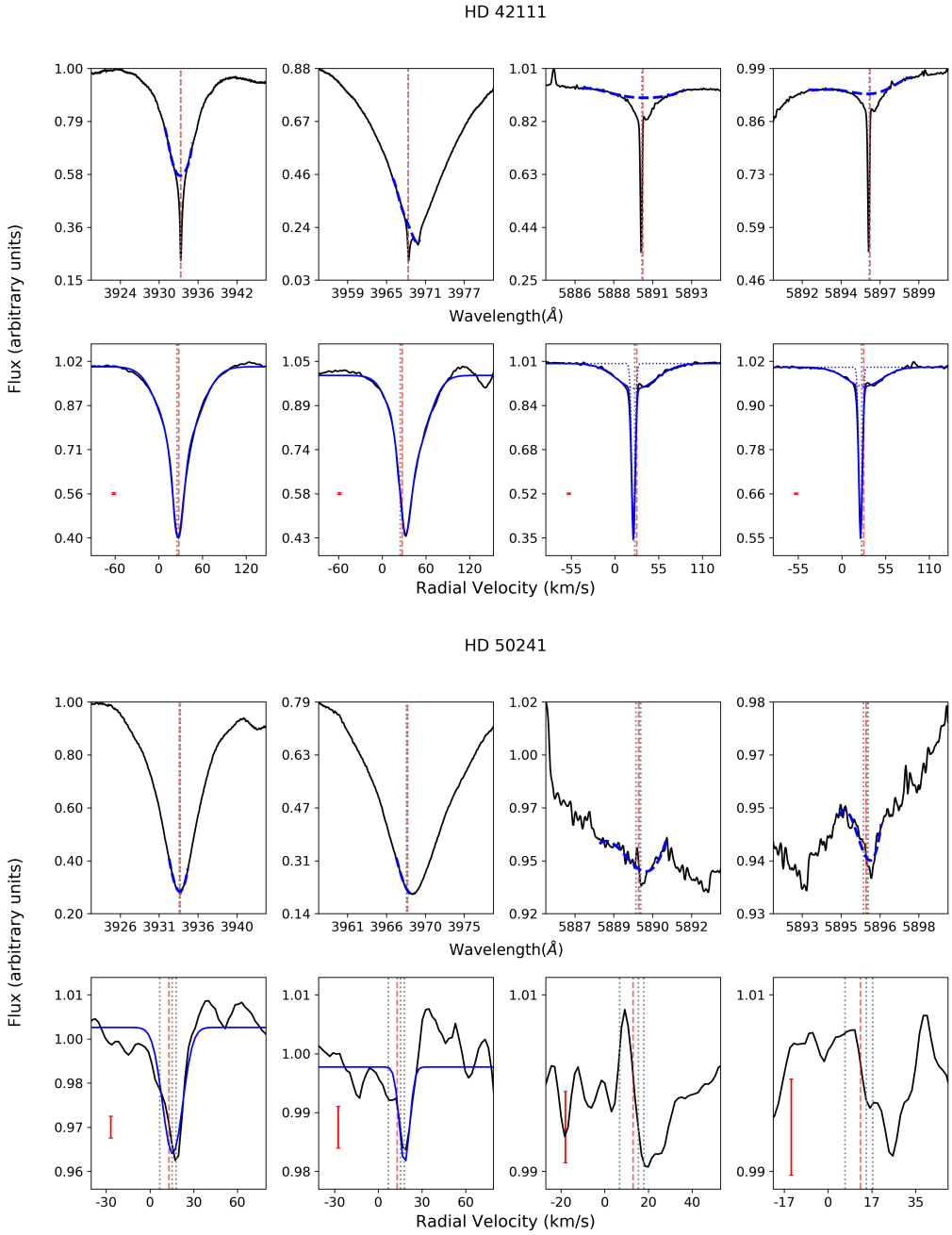

Figure 1 (Cont.): Stars showing narrow non-photospheric absorptions. Top panels: Photospheric Ca II H & K and Na I D lines with fitted modelin dashed blue line, x-axis shows the wavelength. Bottom panels: Residuals once the spectrum is divided by the photosphere, x-axis in velocity. Blue lines mark the fits to the non-photospheric absorptions. Vertical red dashed and grey dotted lines represent the stellar radial velocity and the ISM velocities respectively. Red error bars show three sigma value measured in the continuum adjacent to the photospheric line.

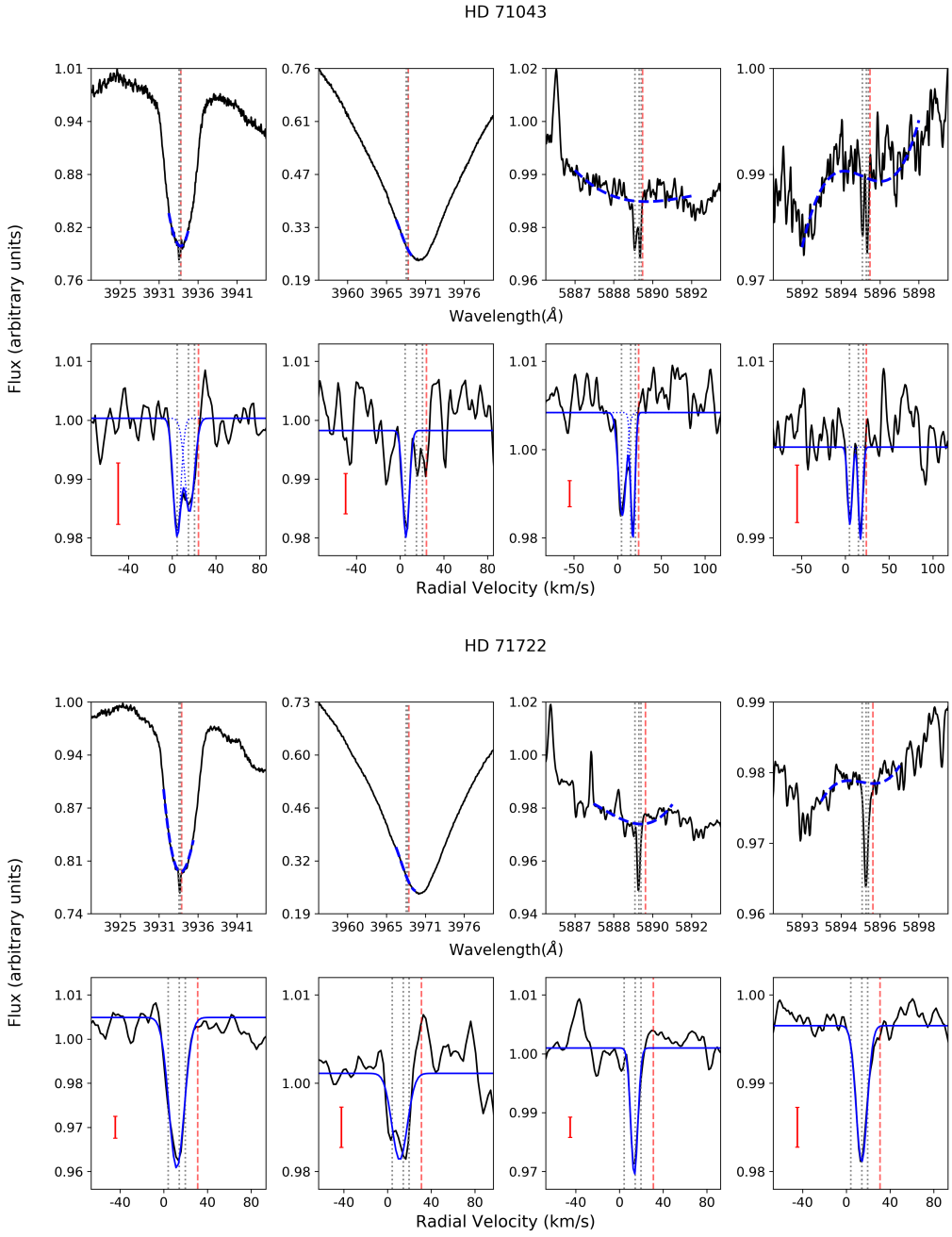

Figure 1 (Cont.): Stars showing narrow non-photospheric absorptions. Top panels: Photospheric Ca II H & K and Na I D lines with fitted modelin dashed blue line, x-axis shows the wavelength. Bottom panels: Residuals once the spectrum is divided by the photosphere, x-axis in velocity. Blue lines mark the fits to the non-photospheric absorptions. Vertical red dashed and grey dotted lines represent the stellar radial velocity and the ISM velocities respectively. Red error bars show three sigma value measured in the continuum adjacent to the photospheric line.

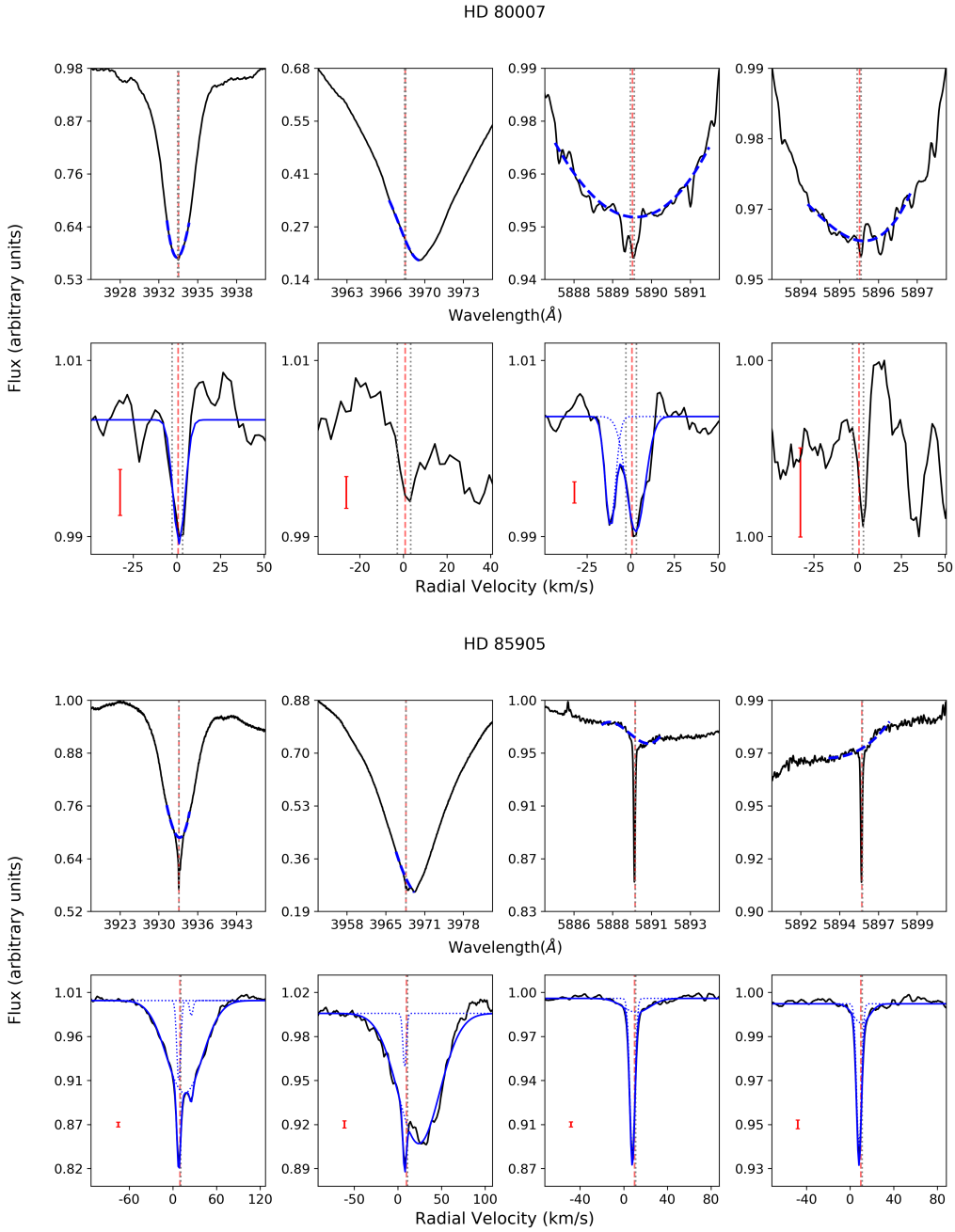

Figure 1 (Cont.): Stars showing narrow non-photospheric absorptions. Top panels: Photospheric Ca II H & K and Na I D lines with fitted modelin dashed blue line, x-axis shows the wavelength. Bottom panels: Residuals once the spectrum is divided by the photosphere, x-axis in velocity. Blue lines mark the fits to the non-photospheric absorptions. Vertical red dashed and grey dotted lines represent the stellar radial velocity and the ISM velocities respectively. Red error bars show three sigma value measured in the continuum adjacent to the photospheric line.

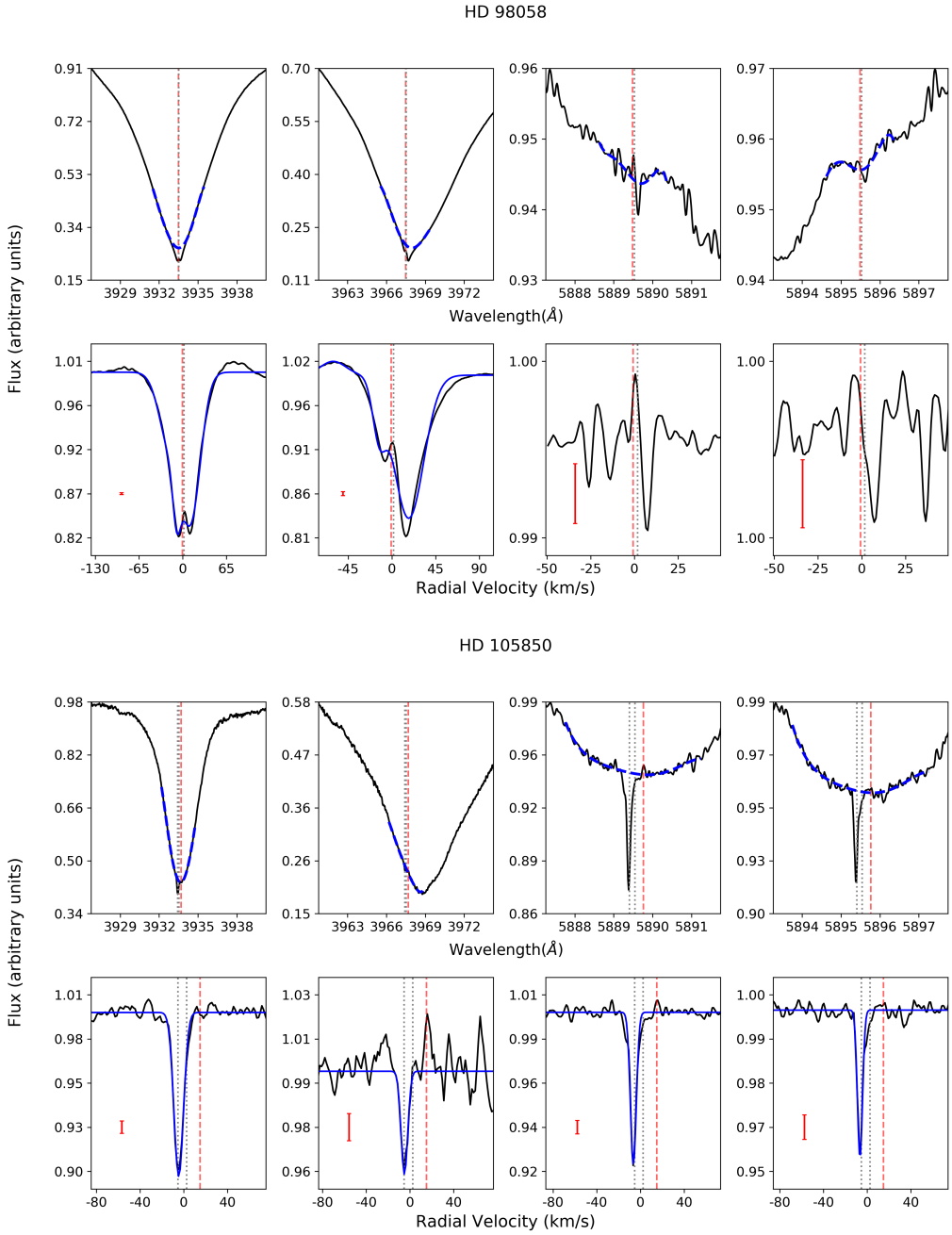

Figure 1 (Cont.): Stars showing narrow non-photospheric absorptions. Top panels: Photospheric Ca II H & K and Na I D lines with fitted modelin dashed blue line, x-axis shows the wavelength. Bottom panels: Residuals once the spectrum is divided by the photosphere, x-axis in velocity. Blue lines mark the fits to the non-photospheric absorptions. Vertical red dashed and grey dotted lines represent the stellar radial velocity and the ISM velocities respectively. Red error bars show three sigma value measured in the continuum adjacent to the photospheric line.

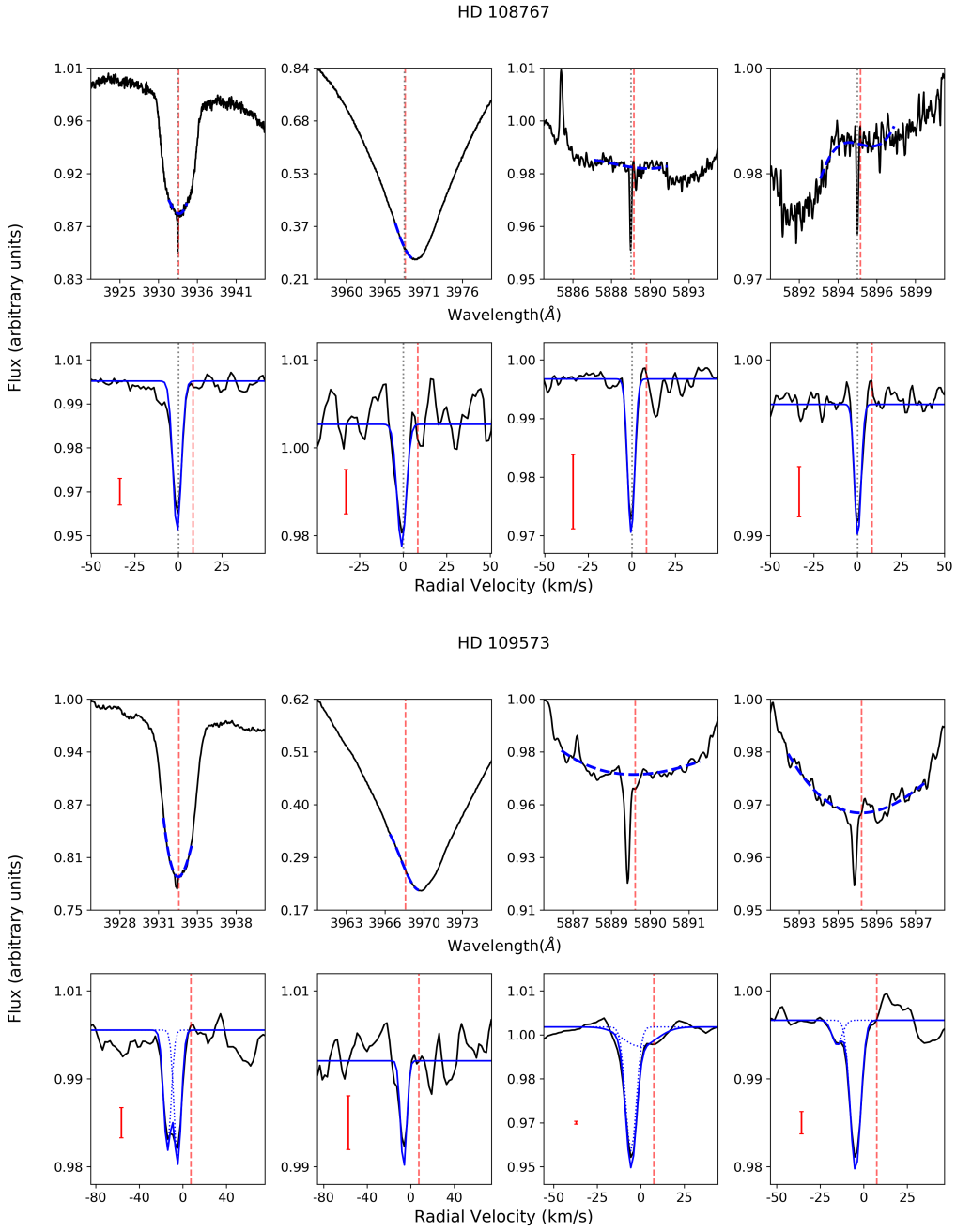

Figure 1 (Cont.): Stars showing narrow non-photospheric absorptions. Top panels: Photospheric Ca II H & K and Na I D lines with fitted modelin dashed blue line, x-axis shows the wavelength. Bottom panels: Residuals once the spectrum is divided by the photosphere, x-axis in velocity. Blue lines mark the fits to the non-photospheric absorptions. Vertical red dashed and grey dotted lines represent the stellar radial velocity and the ISM velocities respectively. Red error bars show three sigma value measured in the continuum adjacent to the photospheric line.

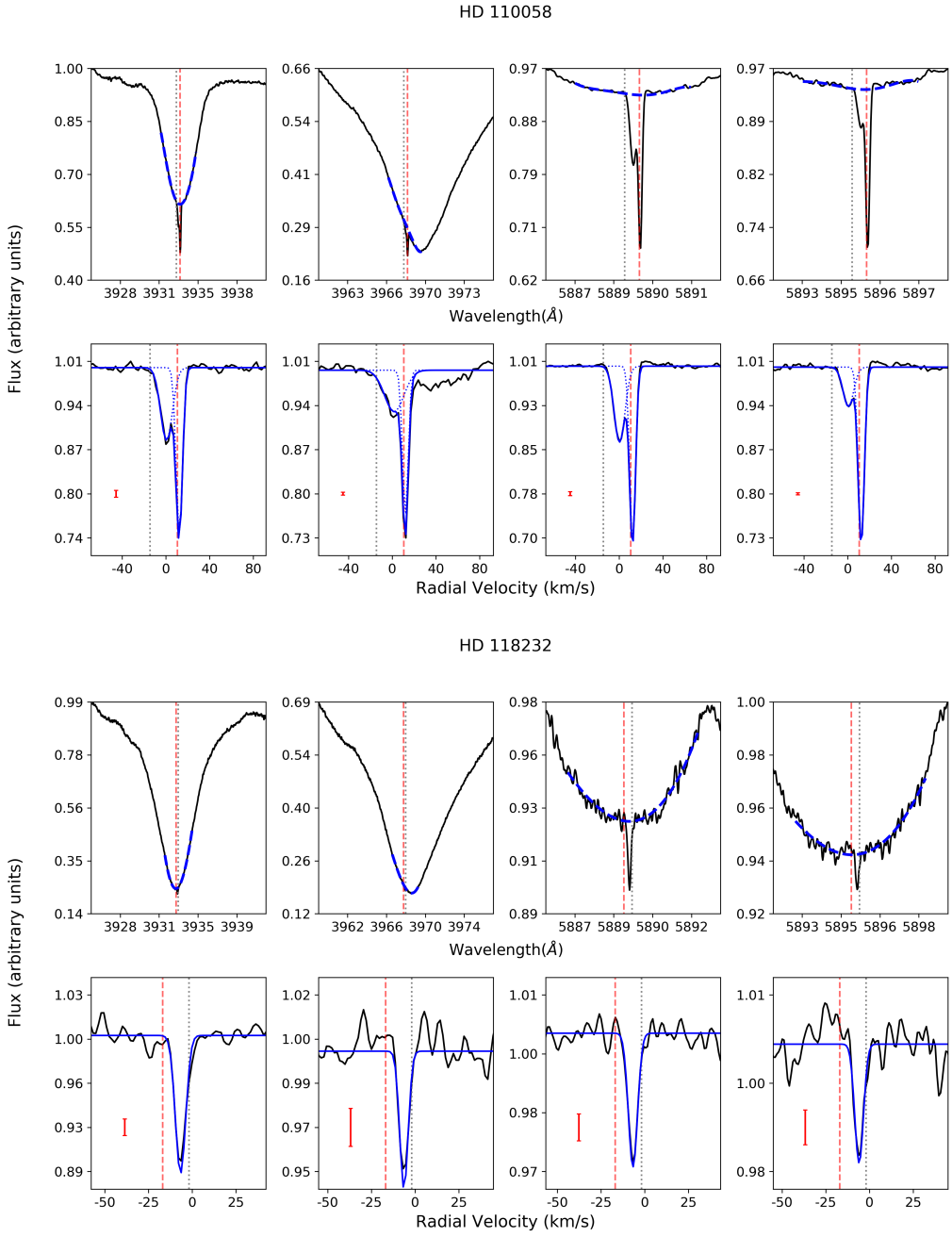

Figure 1 (Cont.): Stars showing narrow non-photospheric absorptions. Top panels: Photospheric Ca II H & K and Na I D lines with fitted modelin dashed blue line, x-axis shows the wavelength. Bottom panels: Residuals once the spectrum is divided by the photosphere, x-axis in velocity. Blue lines mark the fits to the non-photospheric absorptions. Vertical red dashed and grey dotted lines represent the stellar radial velocity and the ISM velocities respectively. Red error bars show three sigma value measured in the continuum adjacent to the photospheric line.

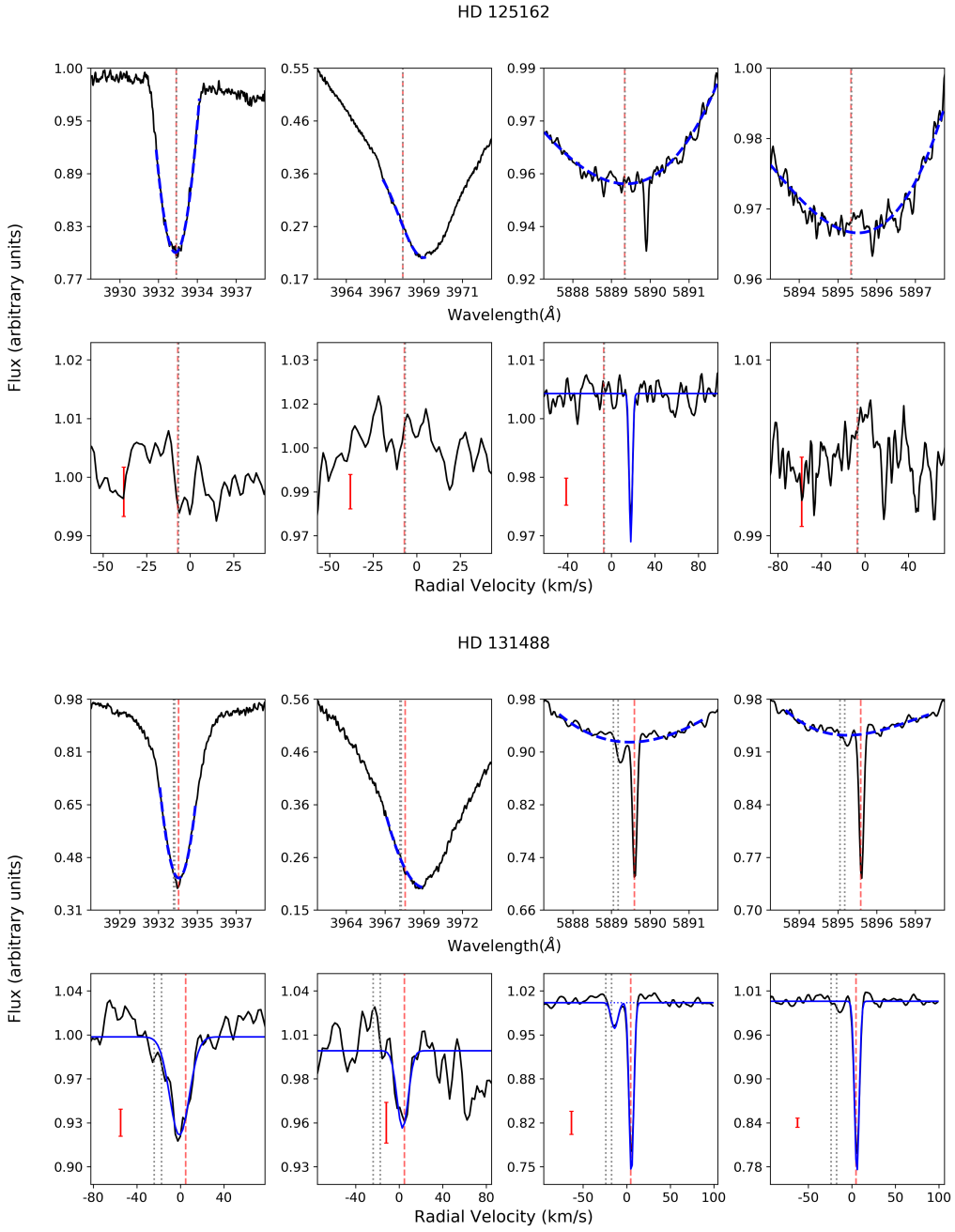

Figure 1 (Cont.): Stars showing narrow non-photospheric absorptions. Top panels: Photospheric Ca II H & K and Na I D lines with fitted modelin dashed blue line, x-axis shows the wavelength. Bottom panels: Residuals once the spectrum is divided by the photosphere, x-axis in velocity. Blue lines mark the fits to the non-photospheric absorptions. Vertical red dashed and grey dotted lines represent the stellar radial velocity and the ISM velocities respectively. Red error bars show three sigma value measured in the continuum adjacent to the photospheric line.

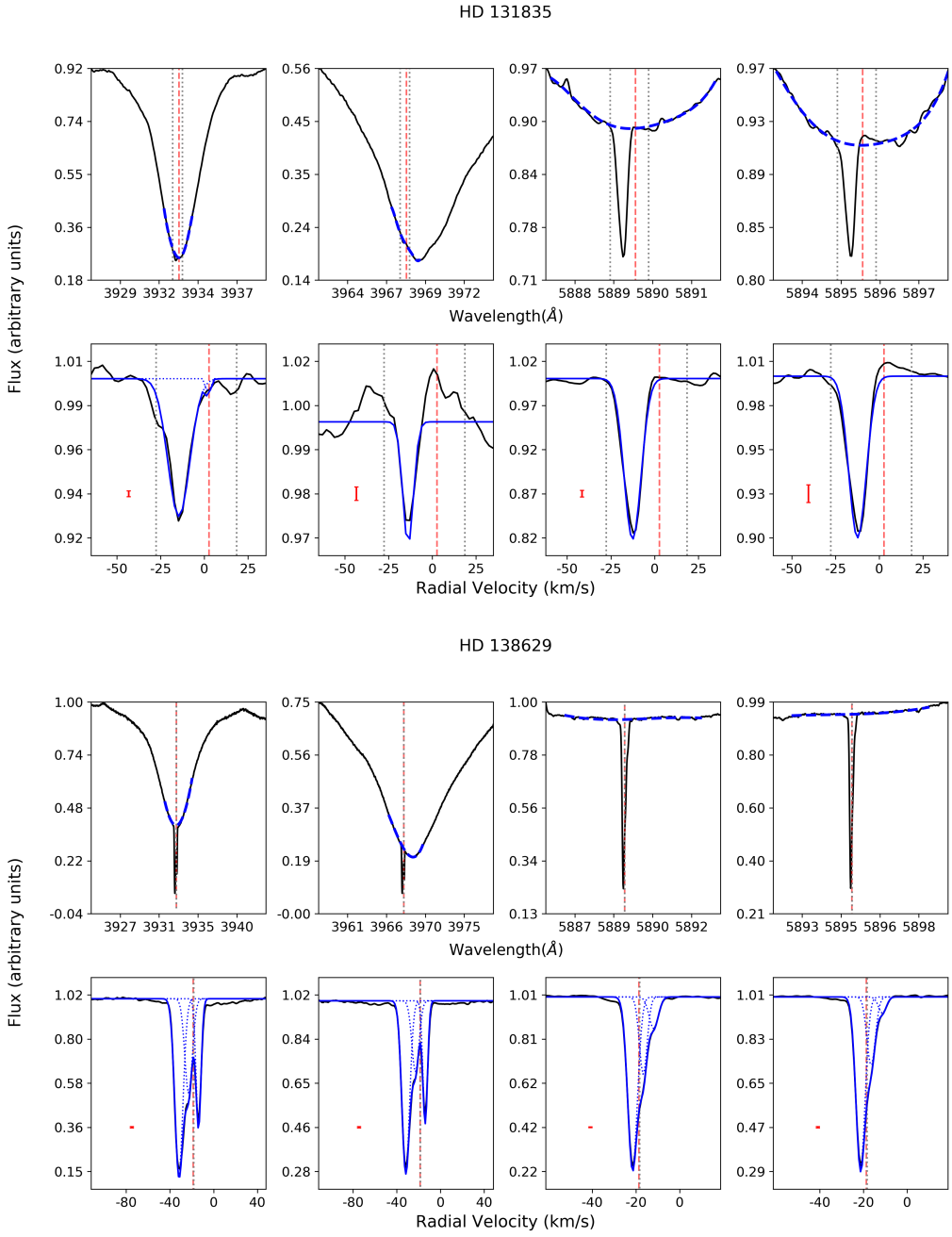

Figure 1 (Cont.): Stars showing narrow non-photospheric absorptions. Top panels: Photospheric Ca II H & K and Na I D lines with fitted modelin dashed blue line, x-axis shows the wavelength. Bottom panels: Residuals once the spectrum is divided by the photosphere, x-axis in velocity. Blue lines mark the fits to the non-photospheric absorptions. Vertical red dashed and grey dotted lines represent the stellar radial velocity and the ISM velocities respectively. Red error bars show three sigma value measured in the continuum adjacent to the photospheric line.

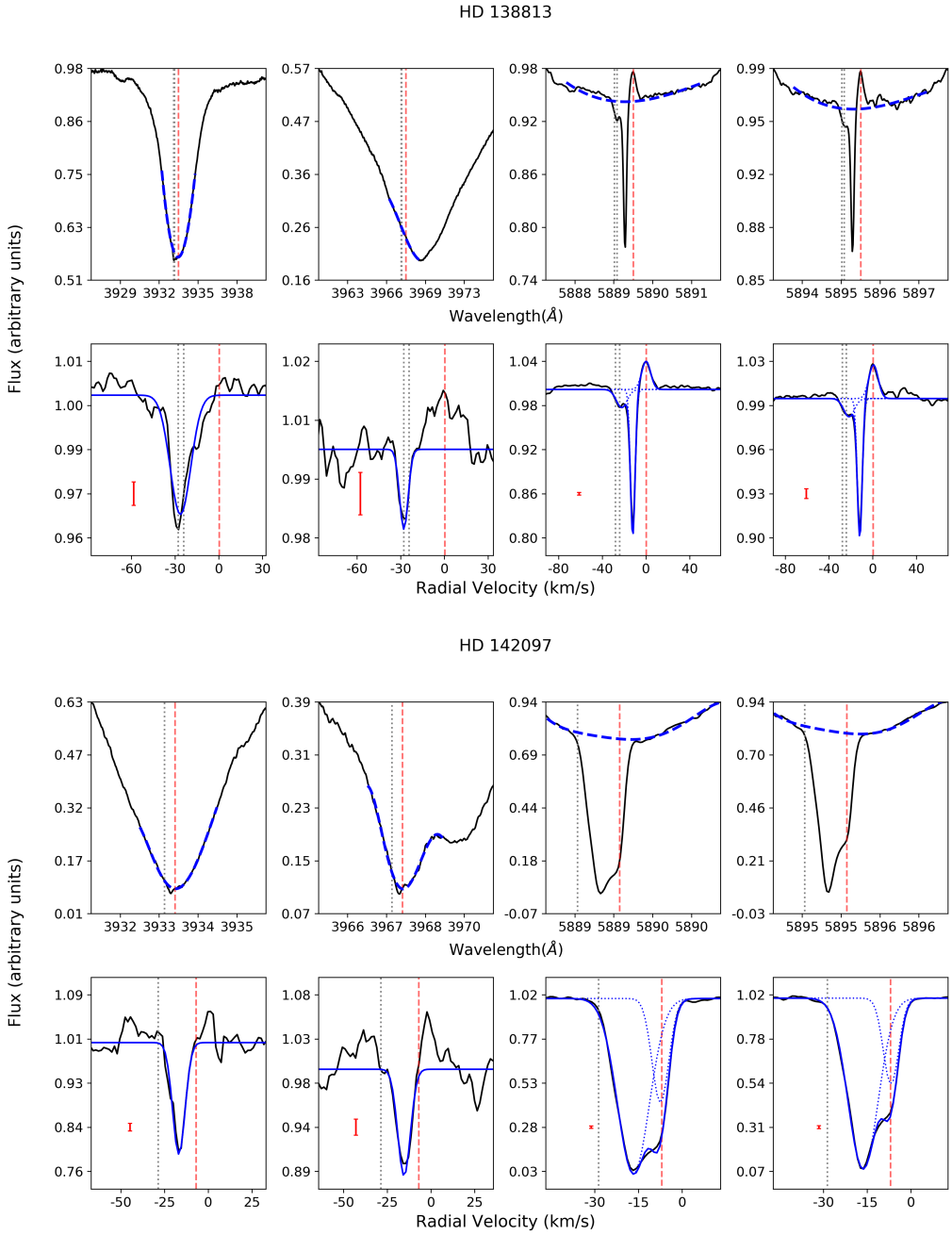

Figure 1 (Cont.): Stars showing narrow non-photospheric absorptions. Top panels: Photospheric Ca II H & K and Na I D lines with fitted modelin dashed blue line, x-axis shows the wavelength. Bottom panels: Residuals once the spectrum is divided by the photosphere, x-axis in velocity. Blue lines mark the fits to the non-photospheric absorptions. Vertical red dashed and grey dotted lines represent the stellar radial velocity and the ISM velocities respectively. Red error bars show three sigma value measured in the continuum adjacent to the photospheric line.

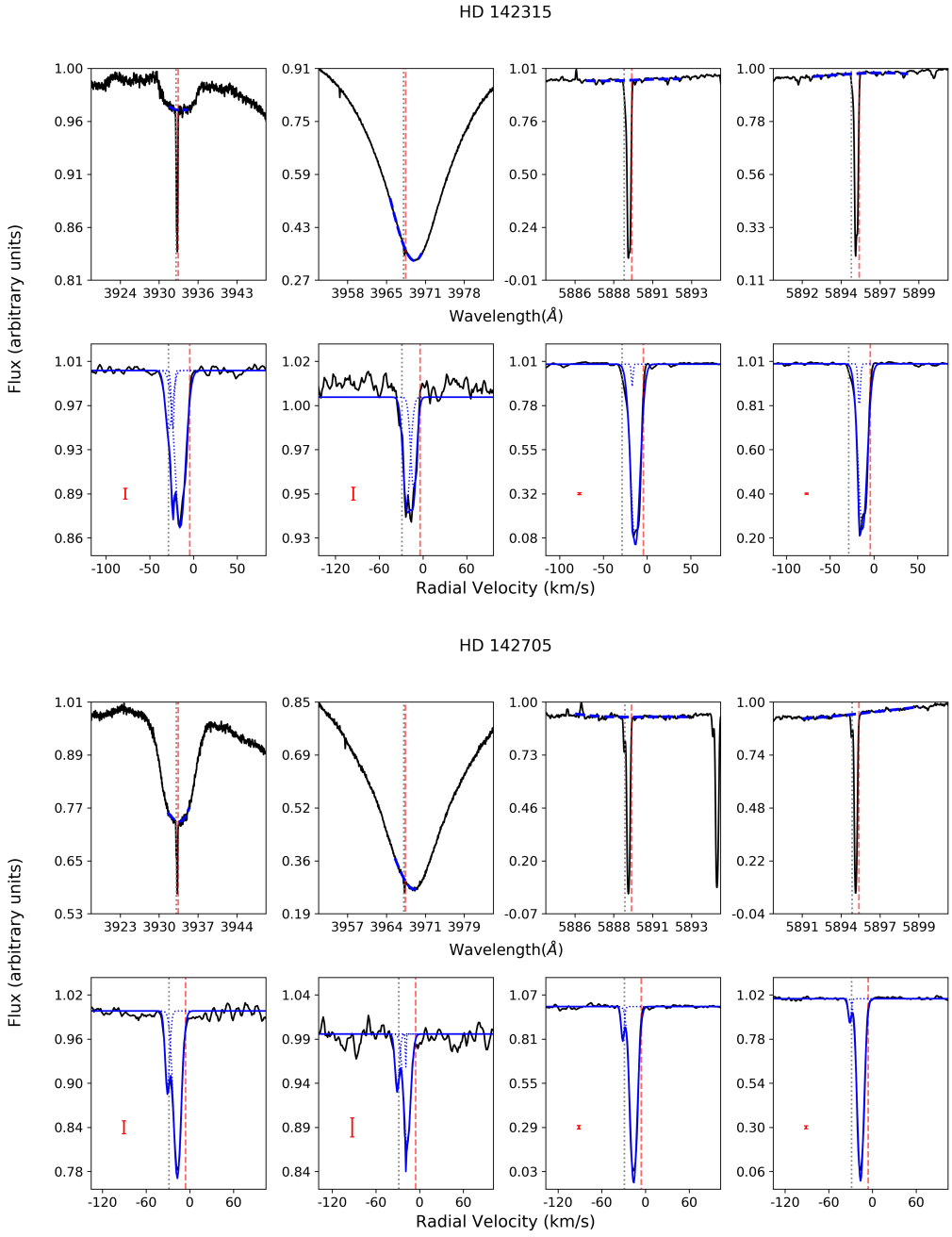

Figure 1 (Cont.): Stars showing narrow non-photospheric absorptions. Top panels: Photospheric Ca II H & K and Na I D lines with fitted modelin dashed blue line, x-axis shows the wavelength. Bottom panels: Residuals once the spectrum is divided by the photosphere, x-axis in velocity. Blue lines mark the fits to the non-photospheric absorptions. Vertical red dashed and grey dotted lines represent the stellar radial velocity and the ISM velocities respectively. Red error bars show three sigma value measured in the continuum adjacent to the photospheric line.

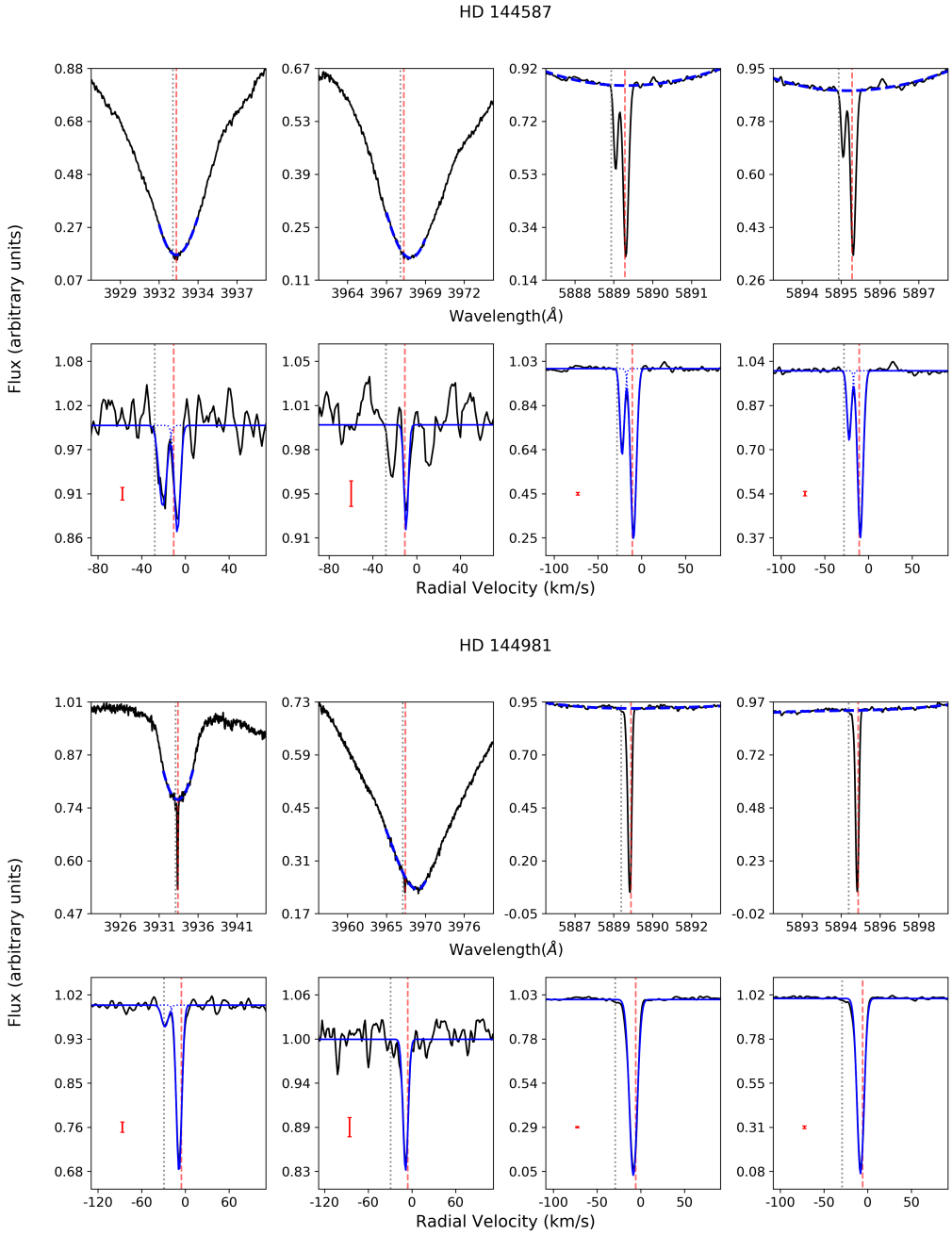

Figure 1 (Cont.): Stars showing narrow non-photospheric absorptions. Top panels: Photospheric Ca II H & K and Na I D lines with fitted modelin dashed blue line, x-axis shows the wavelength. Bottom panels: Residuals once the spectrum is divided by the photosphere, x-axis in velocity. Blue lines mark the fits to the non-photospheric absorptions. Vertical red dashed and grey dotted lines represent the stellar radial velocity and the ISM velocities respectively. Red error bars show three sigma value measured in the continuum adjacent to the photospheric line.

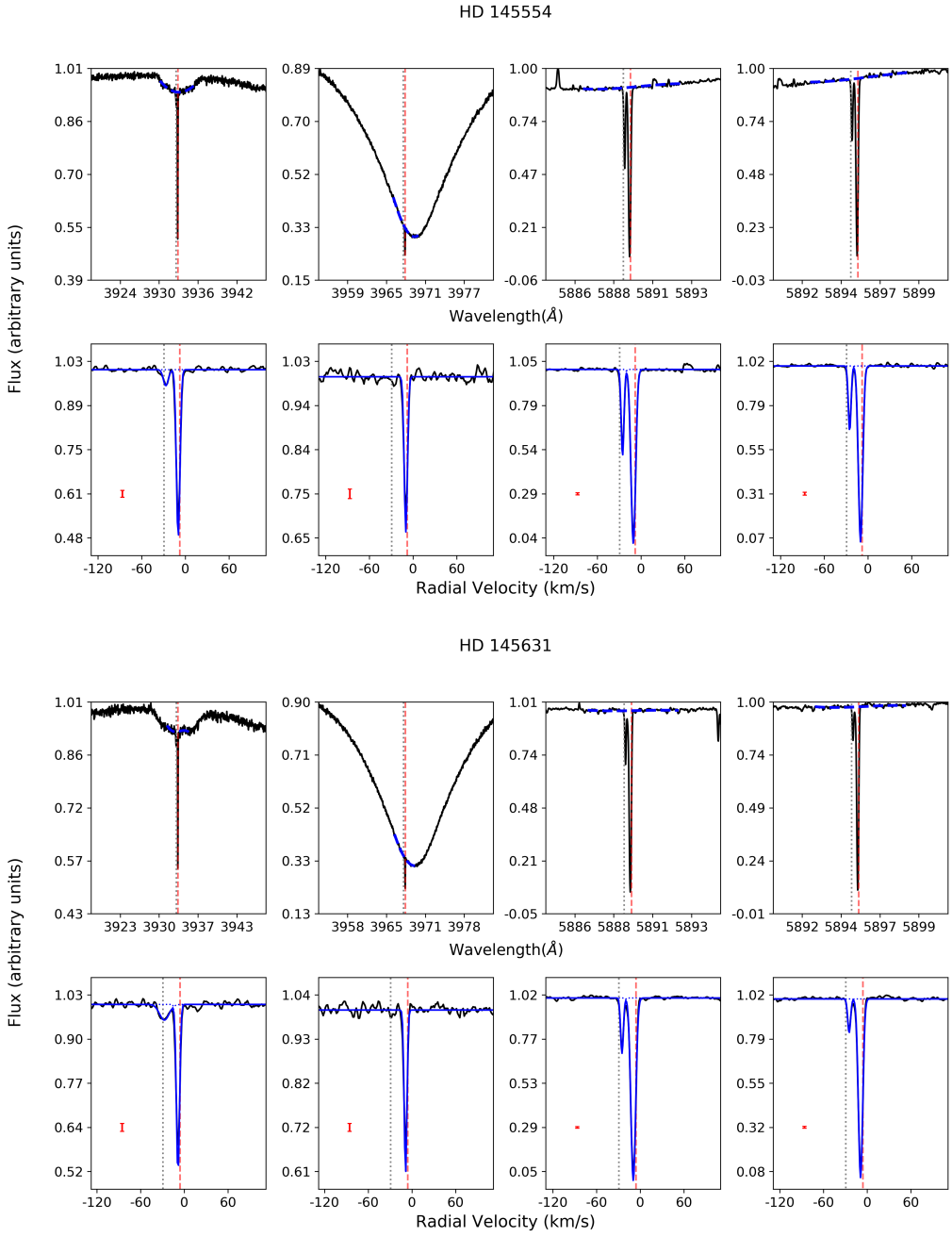

Figure 1 (Cont.): Stars showing narrow non-photospheric absorptions. Top panels: Photospheric Ca II H & K and Na I D lines with fitted modelin dashed blue line, x-axis shows the wavelength. Bottom panels: Residuals once the spectrum is divided by the photosphere, x-axis in velocity. Blue lines mark the fits to the non-photospheric absorptions. Vertical red dashed and grey dotted lines represent the stellar radial velocity and the ISM velocities respectively. Red error bars show three sigma value measured in the continuum adjacent to the photospheric line.

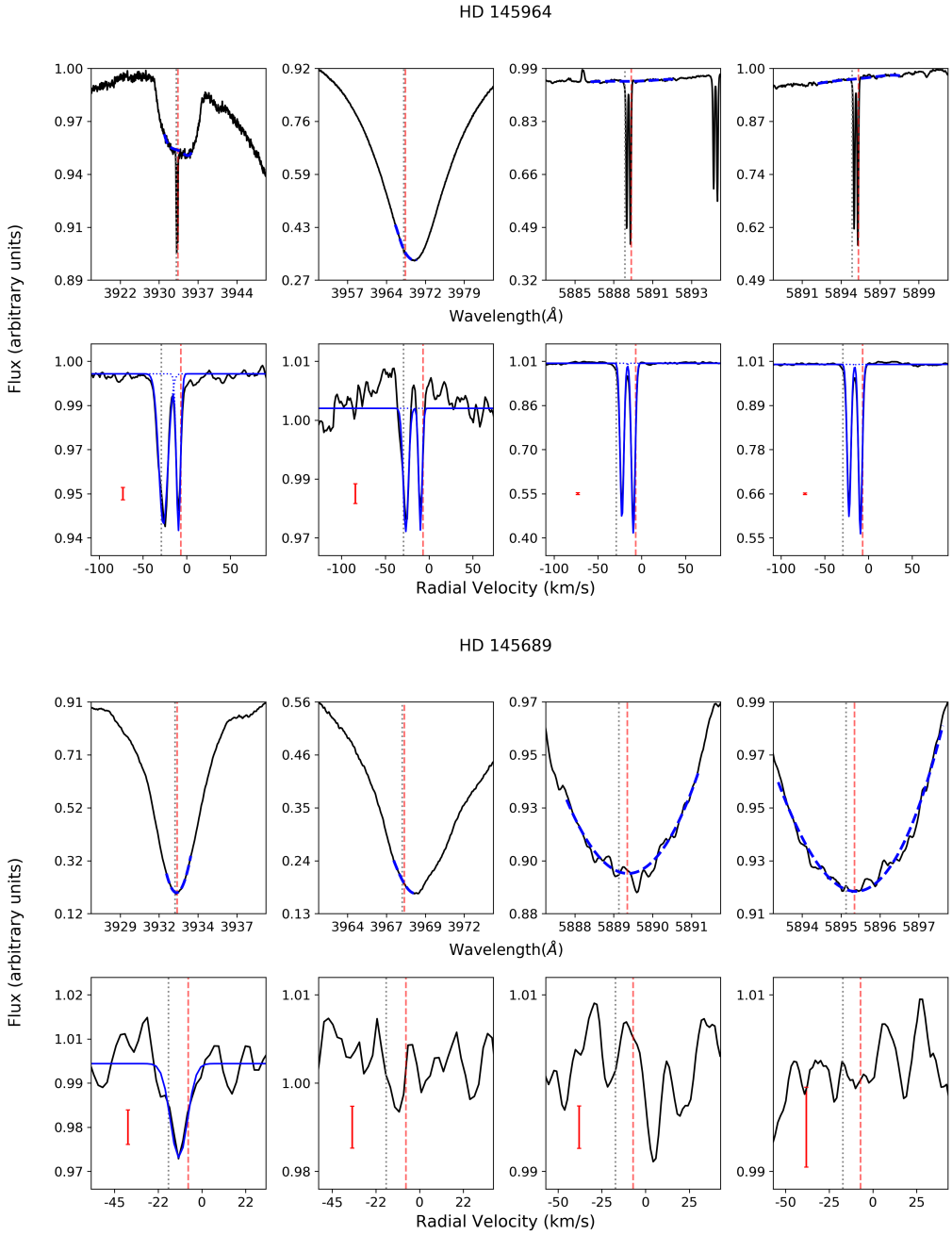

Figure 1 (Cont.): Stars showing narrow non-photospheric absorptions. Top panels: Photospheric Ca II H & K and Na I D lines with fitted modelin dashed blue line, x-axis shows the wavelength. Bottom panels: Residuals once the spectrum is divided by the photosphere, x-axis in velocity. Blue lines mark the fits to the non-photospheric absorptions. Vertical red dashed and grey dotted lines represent the stellar radial velocity and the ISM velocities respectively. Red error bars show three sigma value measured in the continuum adjacent to the photospheric line.

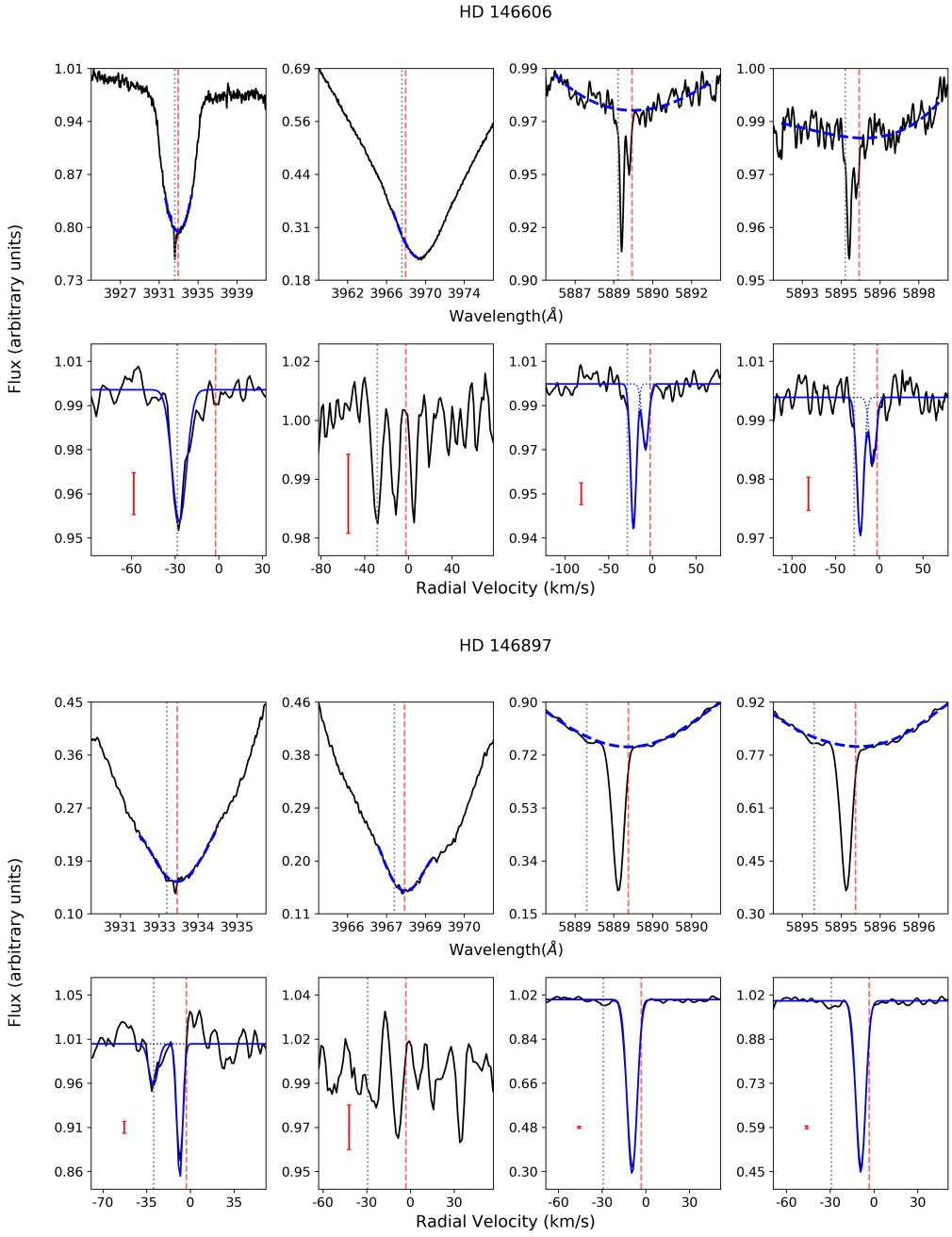

Figure 1 (Cont.): Stars showing narrow non-photospheric absorptions. Top panels: Photospheric Ca II H & K and Na I D lines with fitted modelin dashed blue line, x-axis shows the wavelength. Bottom panels: Residuals once the spectrum is divided by the photosphere, x-axis in velocity. Blue lines mark the fits to the non-photospheric absorptions. Vertical red dashed and grey dotted lines represent the stellar radial velocity and the ISM velocities respectively. Red error bars show three sigma value measured in the continuum adjacent to the photospheric line.

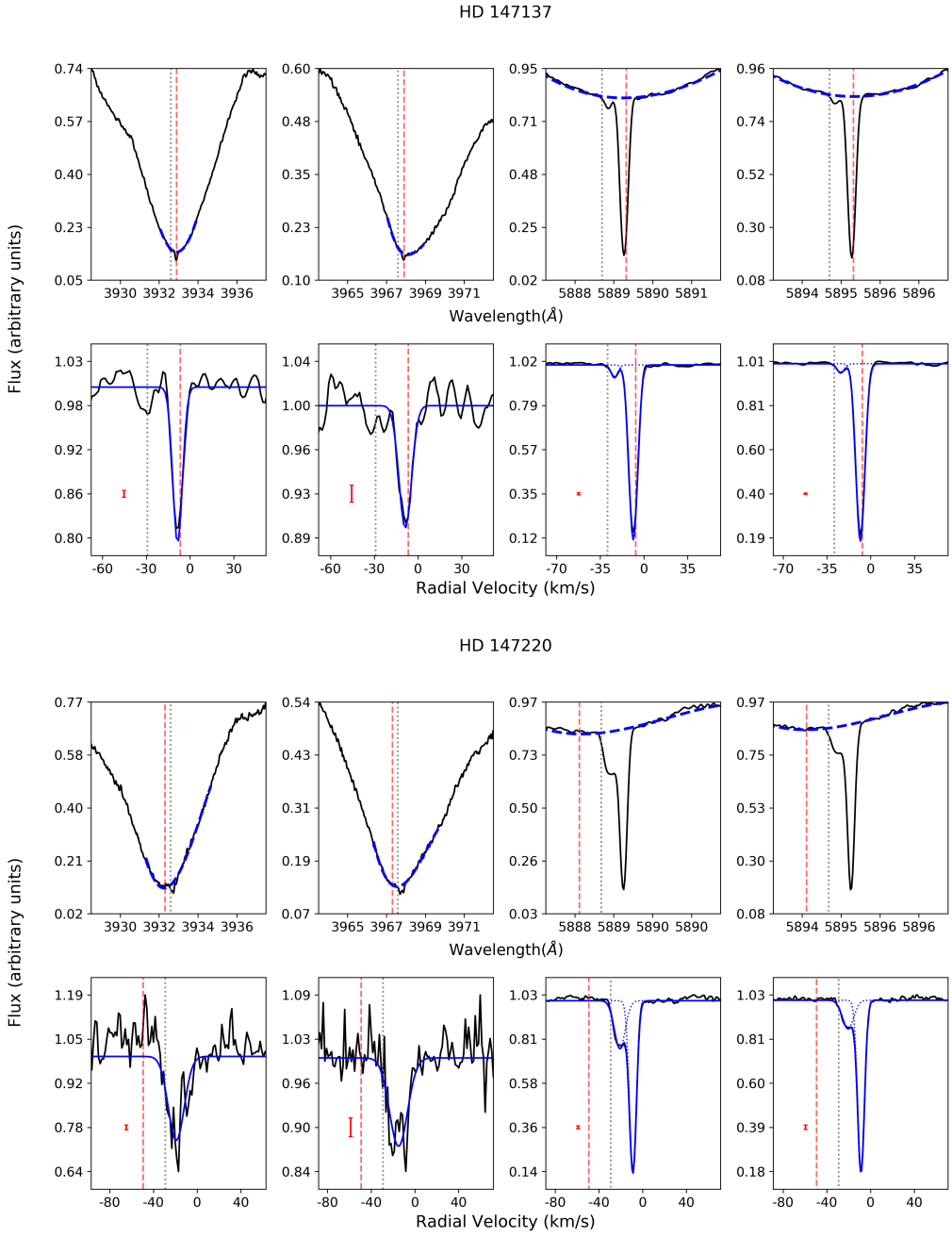

Figure 1 (Cont.): Stars showing narrow non-photospheric absorptions. Top panels: Photospheric Ca II H & K and Na I D lines with fitted modelin dashed blue line, x-axis shows the wavelength. Bottom panels: Residuals once the spectrum is divided by the photosphere, x-axis in velocity. Blue lines mark the fits to the non-photospheric absorptions. Vertical red dashed and grey dotted lines represent the stellar radial velocity and the ISM velocities respectively. Red error bars show three sigma value measured in the continuum adjacent to the photospheric line.

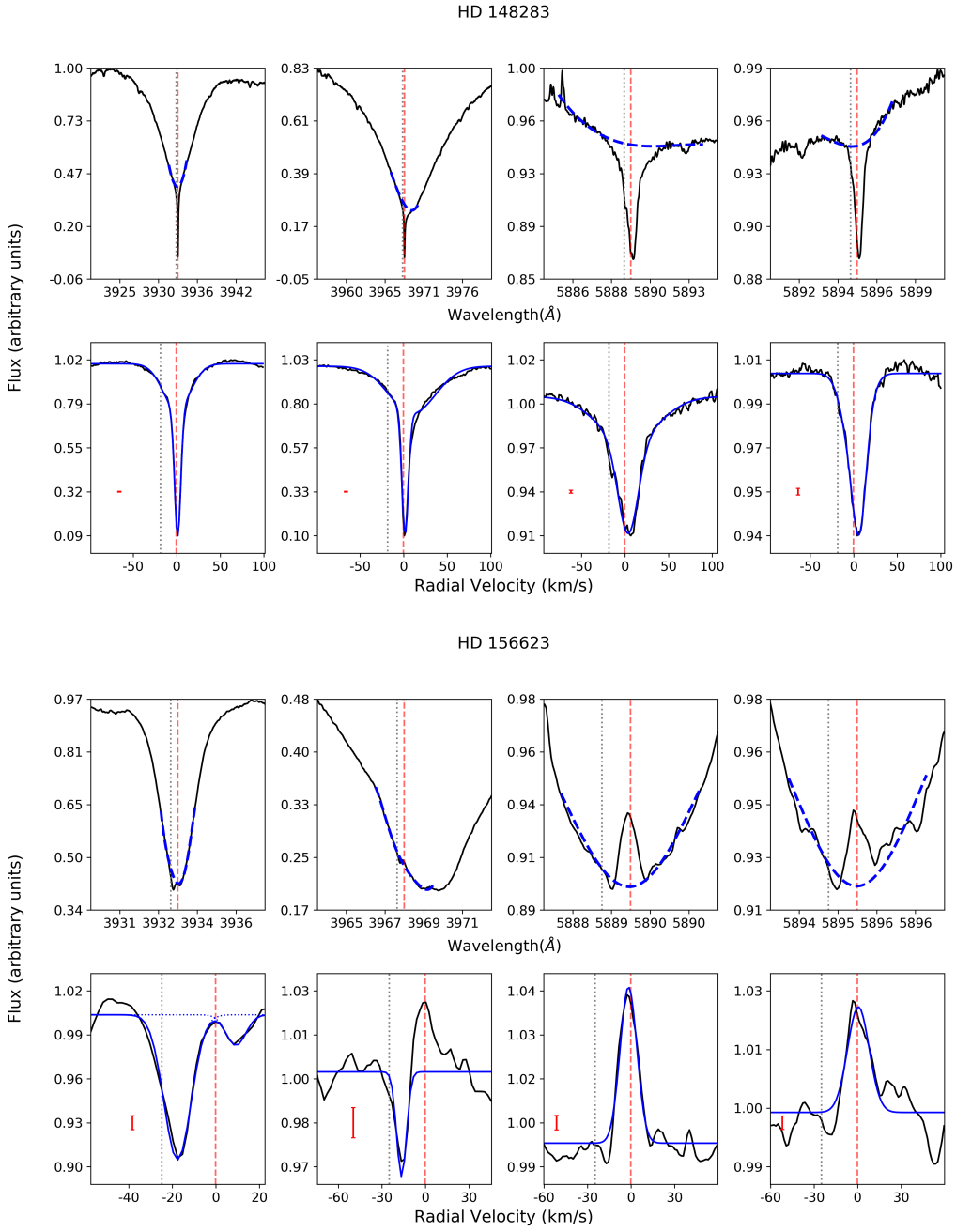

Figure 1 (Cont.): Stars showing narrow non-photospheric absorptions. Top panels: Photospheric Ca II H & K and Na I D lines with fitted modelin dashed blue line, x-axis shows the wavelength. Bottom panels: Residuals once the spectrum is divided by the photosphere, x-axis in velocity. Blue lines mark the fits to the non-photospheric absorptions. Vertical red dashed and grey dotted lines represent the stellar radial velocity and the ISM velocities respectively. Red error bars show three sigma value measured in the continuum adjacent to the photospheric line.

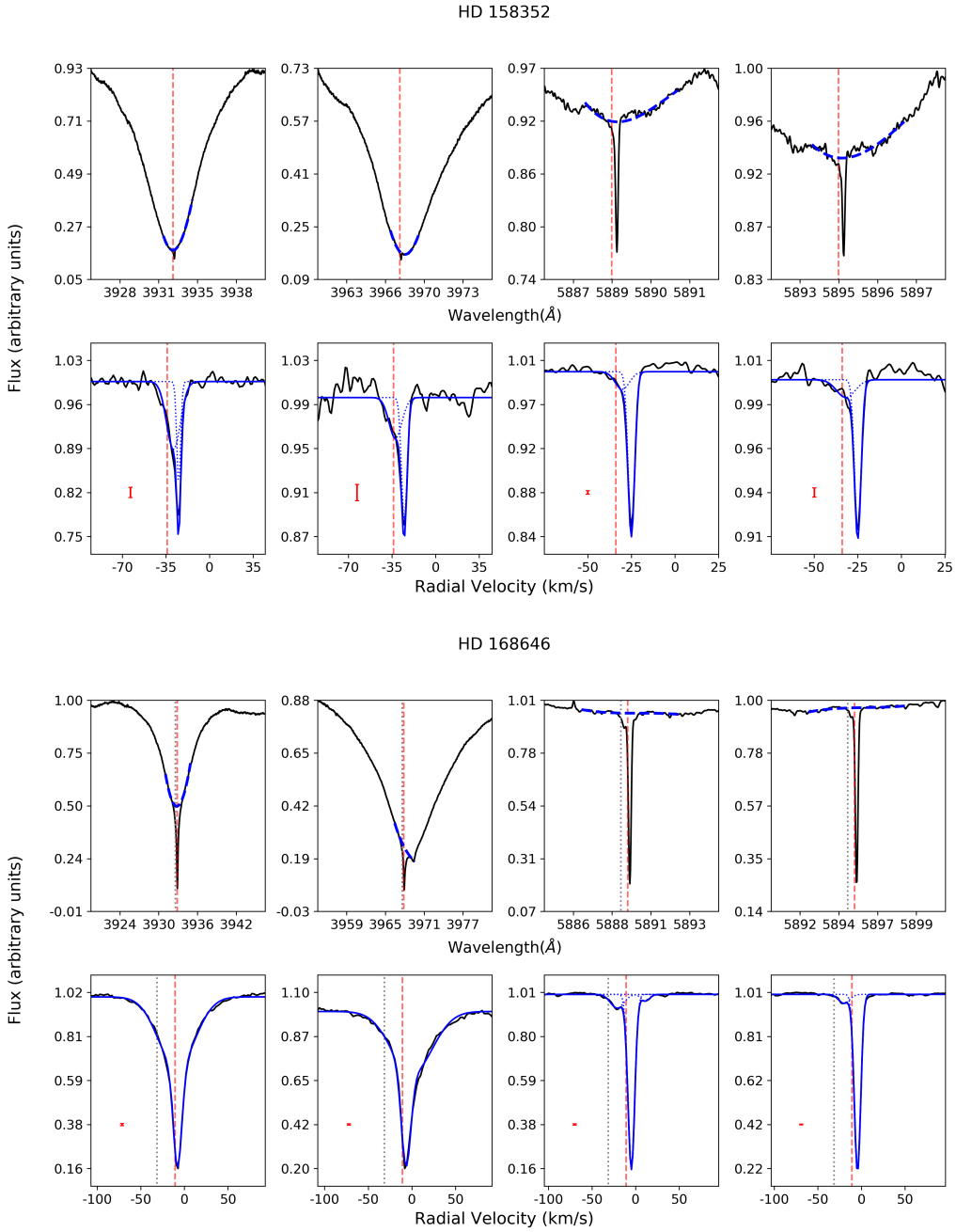

Figure 1 (Cont.): Stars showing narrow non-photospheric absorptions. Top panels: Photospheric Ca II H & K and Na I D lines with fitted modelin dashed blue line, x-axis shows the wavelength. Bottom panels: Residuals once the spectrum is divided by the photosphere, x-axis in velocity. Blue lines mark the fits to the non-photospheric absorptions. Vertical red dashed and grey dotted lines represent the stellar radial velocity and the ISM velocities respectively. Red error bars show three sigma value measured in the continuum adjacent to the photospheric line.

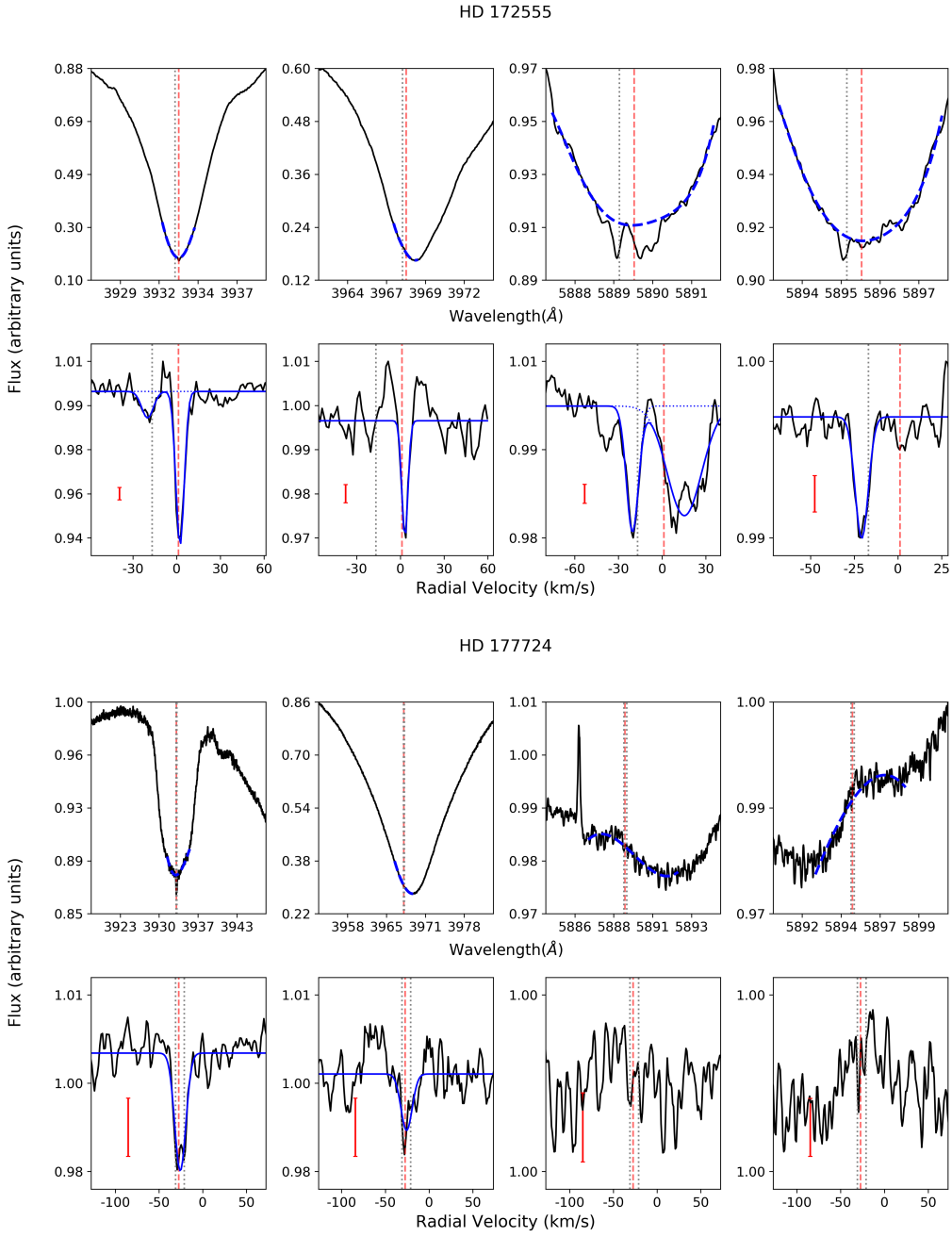

Figure 1 (Cont.): Stars showing narrow non-photospheric absorptions. Top panels: Photospheric Ca II H & K and Na I D lines with fitted modelin dashed blue line, x-axis shows the wavelength. Bottom panels: Residuals once the spectrum is divided by the photosphere, x-axis in velocity. Blue lines mark the fits to the non-photospheric absorptions. Vertical red dashed and grey dotted lines represent the stellar radial velocity and the ISM velocities respectively. Red error bars show three sigma value measured in the continuum adjacent to the photospheric line.

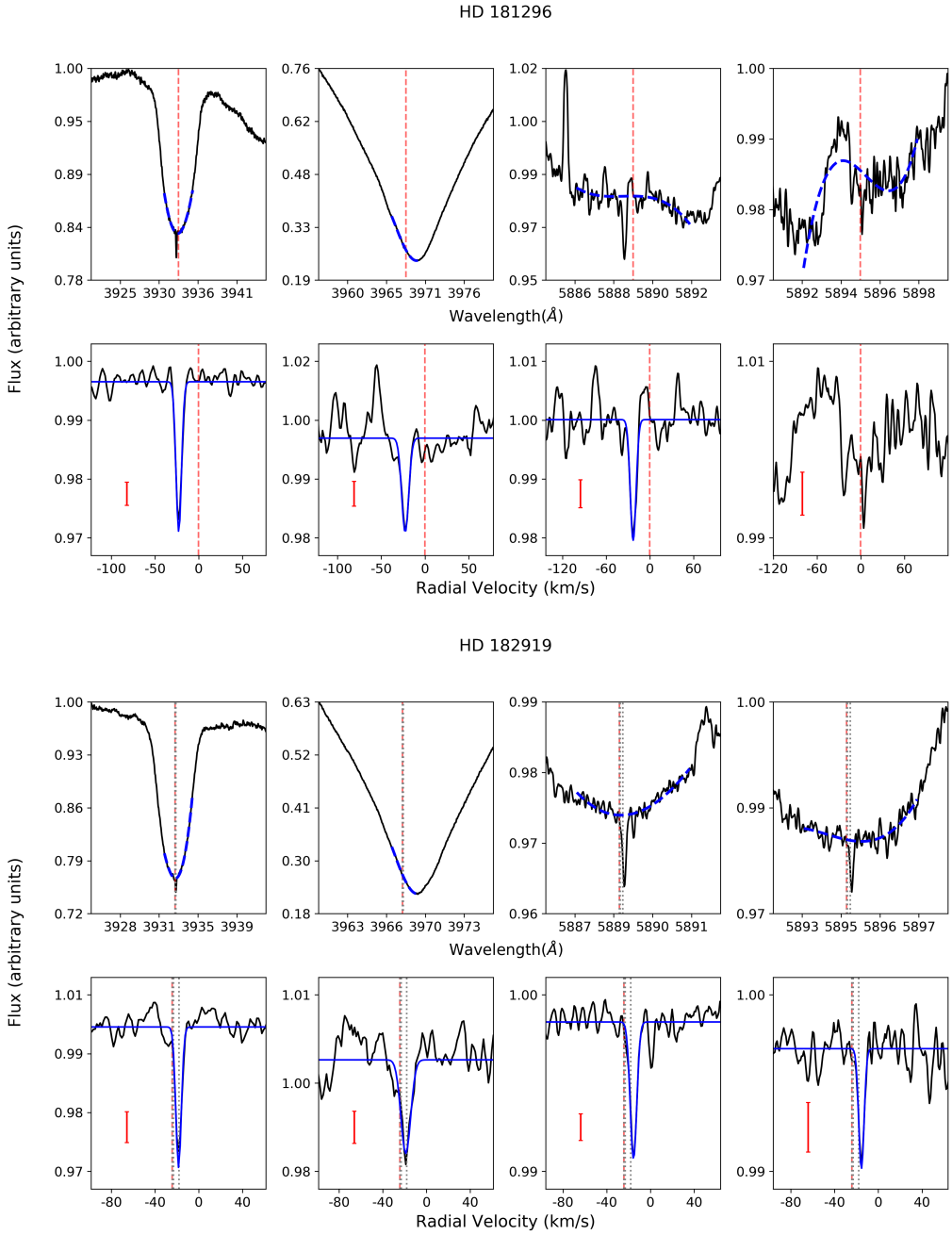

Figure 1 (Cont.): Stars showing narrow non-photospheric absorptions. Top panels: Photospheric Ca II H & K and Na I D lines with fitted modelin dashed blue line, x-axis shows the wavelength. Bottom panels: Residuals once the spectrum is divided by the photosphere, x-axis in velocity. Blue lines mark the fits to the non-photospheric absorptions. Vertical red dashed and grey dotted lines represent the stellar radial velocity and the ISM velocities respectively. Red error bars show three sigma value measured in the continuum adjacent to the photospheric line.

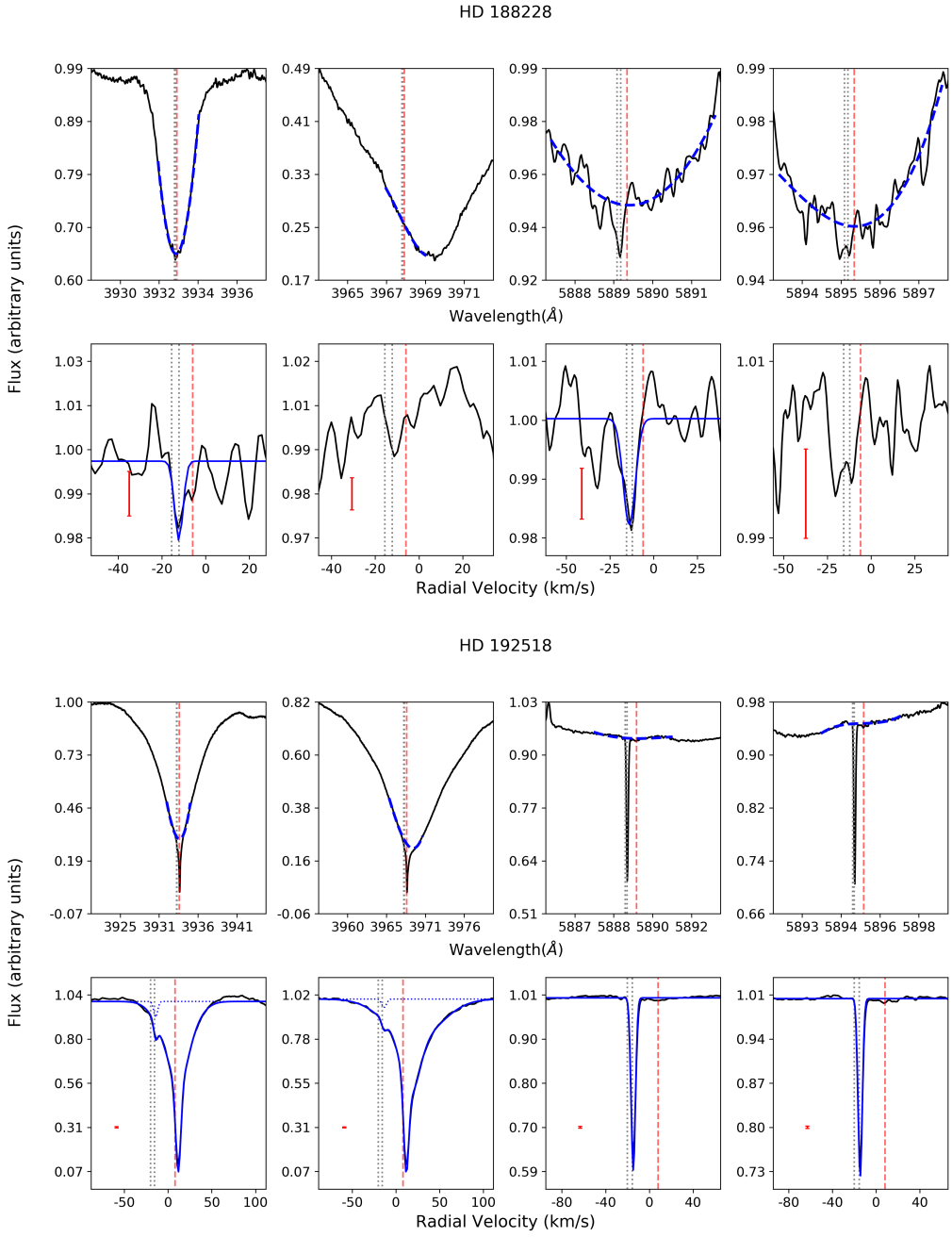

Figure 1 (Cont.): Stars showing narrow non-photospheric absorptions. Top panels: Photospheric Ca II H & K and Na I D lines with fitted modelin dashed blue line, x-axis shows the wavelength. Bottom panels: Residuals once the spectrum is divided by the photosphere, x-axis in velocity. Blue lines mark the fits to the non-photospheric absorptions. Vertical red dashed and grey dotted lines represent the stellar radial velocity and the ISM velocities respectively. Red error bars show three sigma value measured in the continuum adjacent to the photospheric line.

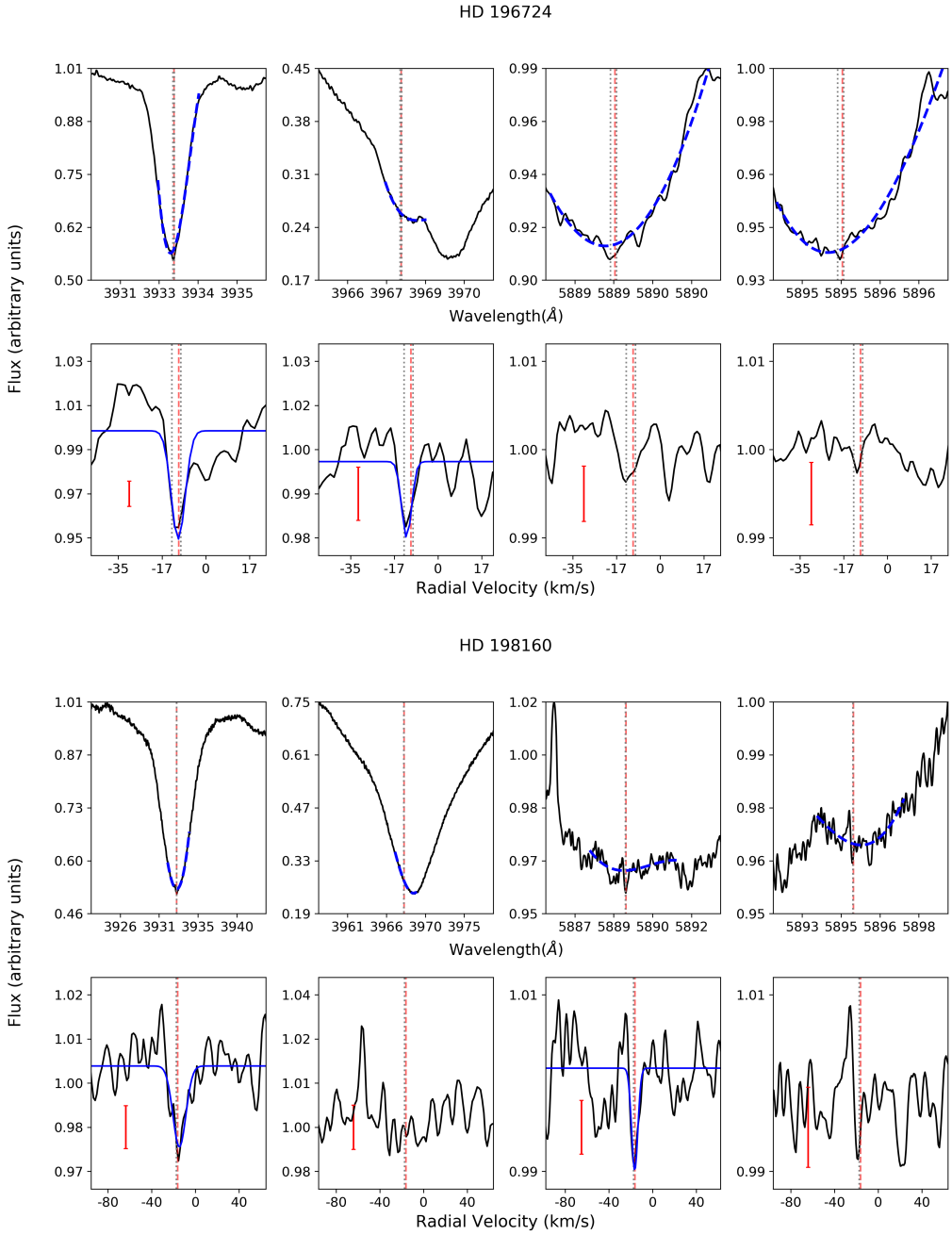

Figure 1 (Cont.): Stars showing narrow non-photospheric absorptions. Top panels: Photospheric Ca II H & K and Na I D lines with fitted modelin dashed blue line, x-axis shows the wavelength. Bottom panels: Residuals once the spectrum is divided by the photosphere, x-axis in velocity. Blue lines mark the fits to the non-photospheric absorptions. Vertical red dashed and grey dotted lines represent the stellar radial velocity and the ISM velocities respectively. Red error bars show three sigma value measured in the continuum adjacent to the photospheric line.

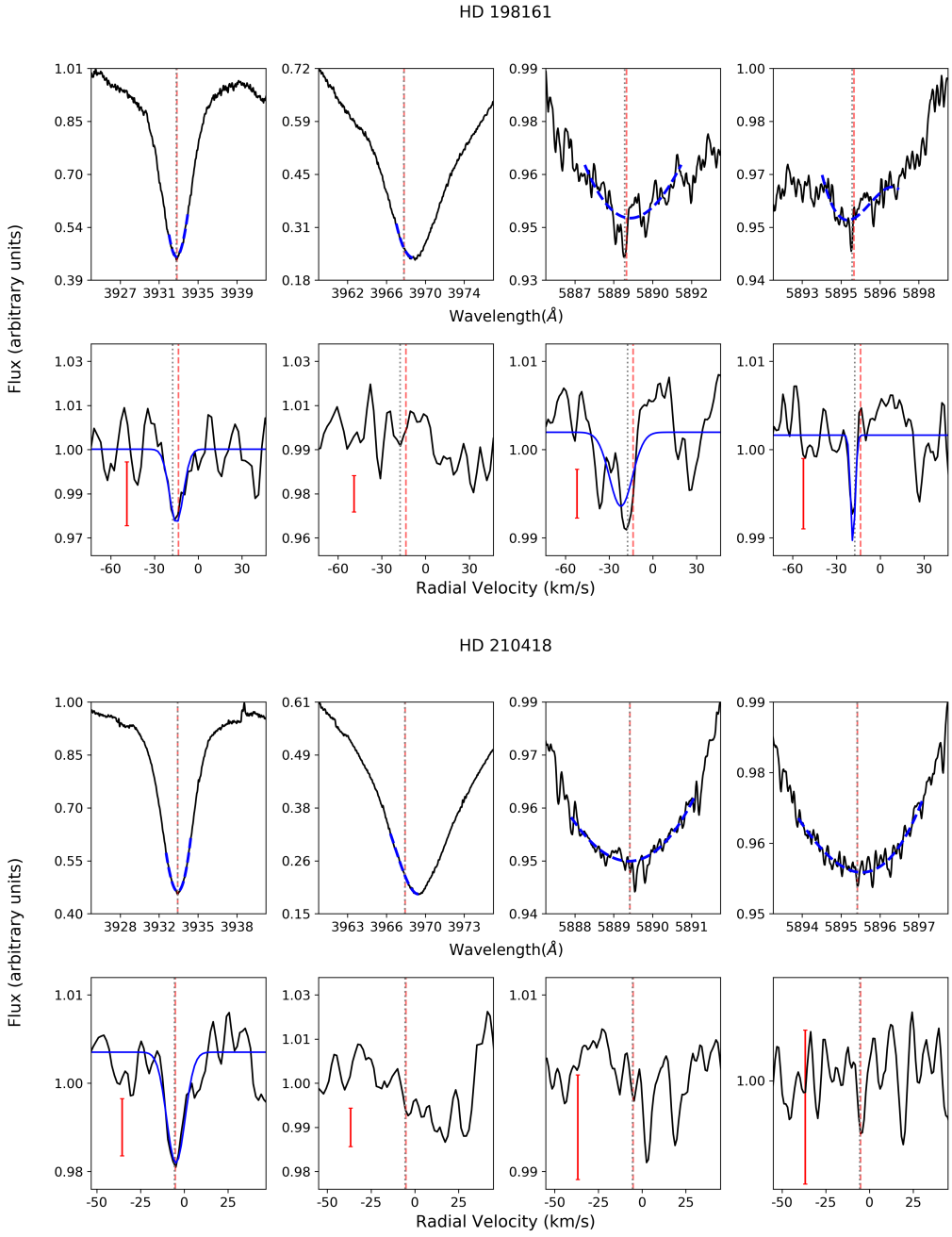

Figure 1 (Cont.): Stars showing narrow non-photospheric absorptions. Top panels: Photospheric Ca II H & K and Na I D lines with fitted modelin dashed blue line, x-axis shows the wavelength. Bottom panels: Residuals once the spectrum is divided by the photosphere, x-axis in velocity. Blue lines mark the fits to the non-photospheric absorptions. Vertical red dashed and grey dotted lines represent the stellar radial velocity and the ISM velocities respectively. Red error bars show three sigma value measured in the continuum adjacent to the photospheric line.

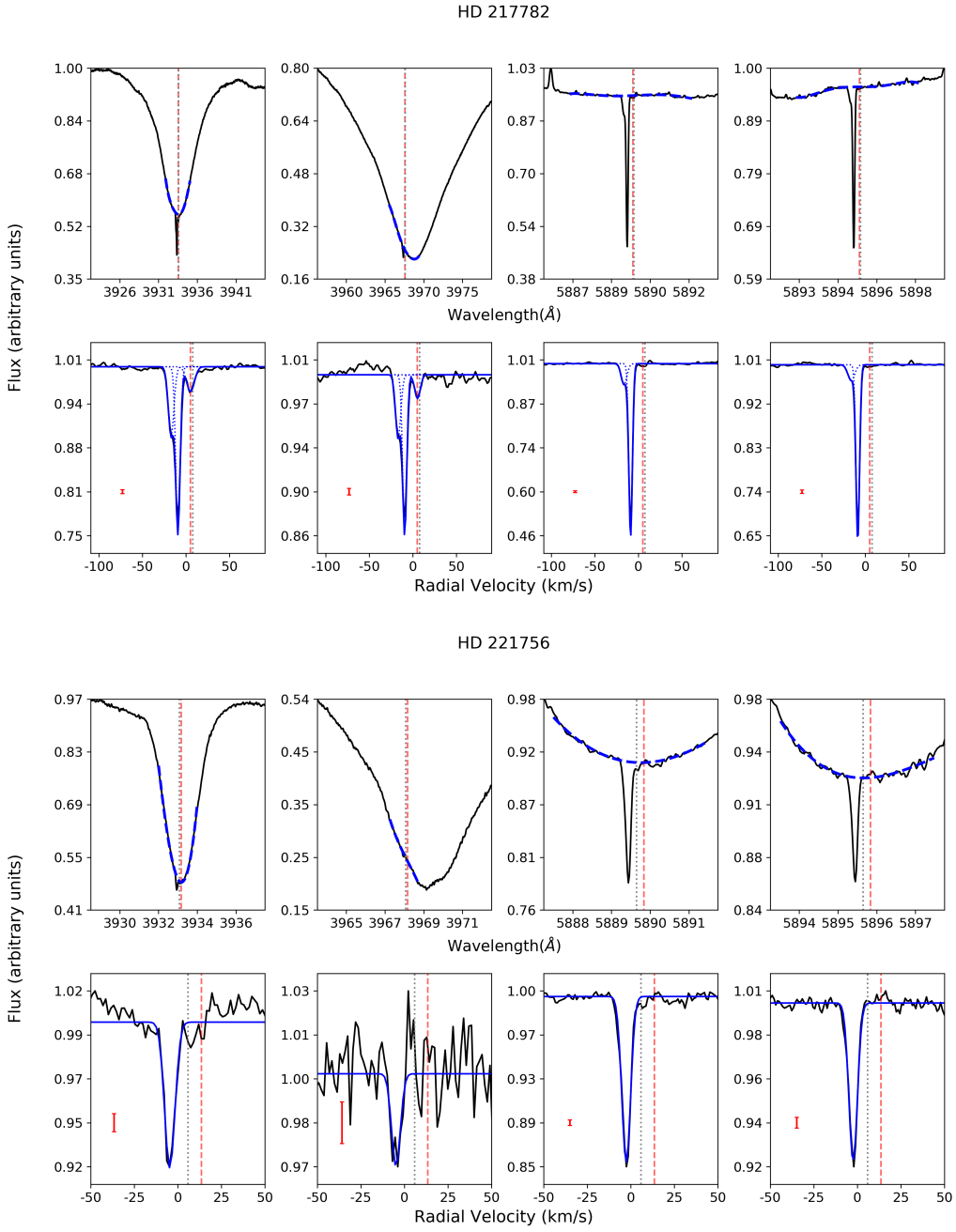

Figure 1 (Cont.): Stars showing narrow non-photospheric absorptions. Top panels: Photospheric Ca II H & K and Na I D lines with fitted modelin dashed blue line, x-axis shows the wavelength. Bottom panels: Residuals once the spectrum is divided by the photosphere, x-axis in velocity. Blue lines mark the fits to the non-photospheric absorptions. Vertical red dashed and grey dotted lines represent the stellar radial velocity and the ISM velocities respectively. Red error bars show three sigma value measured in the continuum adjacent to the photospheric line.

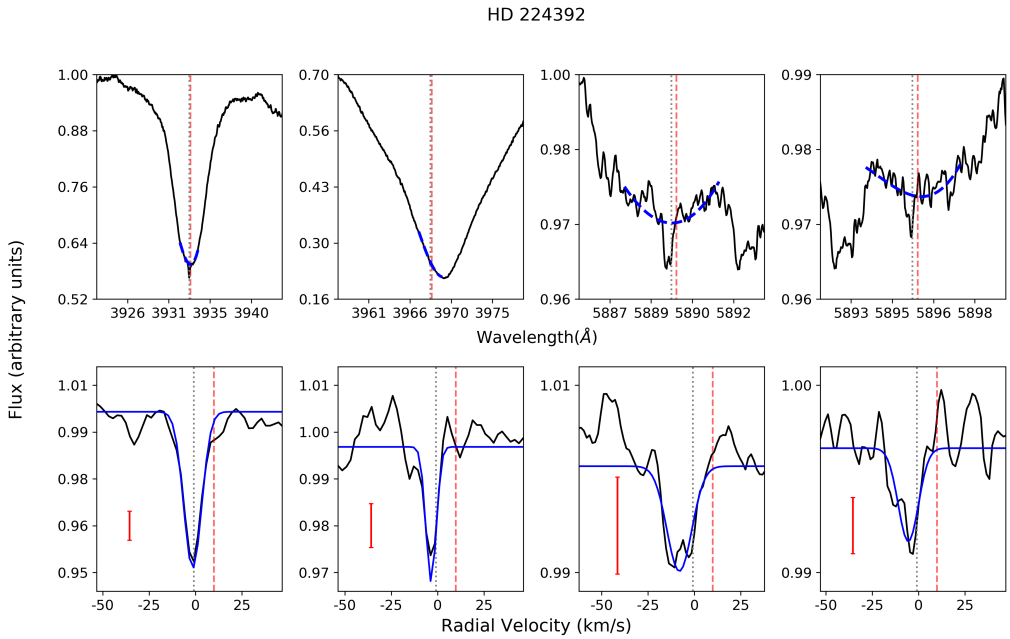

Figure 2 (Cont.): Stars showing narrow non-photospheric absorptions. Top panels: Photospheric Ca II H & K and Na I D lines with fitted modelin dashed blue line, x-axis shows the wavelength. Bottom panels: Residuals once the spectrum is divided by the photosphere, x-axis in velocity. Blue lines mark the fits to the non-photospheric absorptions. Vertical red dashed and grey dotted lines represent the stellar radial velocity and the ISM velocities respectively. Red error bars show three sigma value measured in the continuum adjacent to the photospheric line.

A.2 Tables

Table A.1: Stellar Parameters estimated according to Sect. 3.2.

HD	RA(2000.0)	Dec(2000.0)	Sp. Type	$v_{\rm rad}$ (km/s)	$T_{\rm eff}$ (K)	$\log g$ [cgs]	[M/H]	$v \sin i$ (km/s)
105	00 : 05 : 52.54	−41 : 45 : 11.0	G0V	+1.6 ± 0.4	6000±60	4.38±0.14	−0.03	14.6
203	00 : 06 : 50.09	−23 : 06 : 27.1	F3V	+7.1 ± 1.7	6850±200	4.25±0.30	0.00	170
256	00 : 07 : 18.27	−17 : 23 : 13.2	A2IV/V	−2.2 ± 0.3	8690±50	3.48±0.20	0.00	270
1466	00 : 18 : 26.12	−63 : 28 : 39.0	F8V	+6.4 ± 0.4	6270±60	4.45±0.15	−0.01	18
2262	00 : 26 : 12.20	−43 : 40 : 47.4	A5IV	+11.3 ± 3.7	8110±30	4.01±0.13	0.00	200
2884	00 : 31 : 32.67	−62 : 57 : 29.6	B9V	+8.3 ± 1.6	11620±30	4.45±0.10	−0.05	135
2885	00 : 31 : 33.48	−62 : 57 : 56.0	A2V	+13.5 ± 3.9	9630±30	4.27±0.10	+0.20	40
3003	00 : 32 : 43.91	−63 : 01 : 53.4	A0V	+8.2 ± 2.3	9490±50	4.35±0.14	0.00	95
5267	00 : 54 : 35.23	+19 : 11 : 18.3	A1V	+9.5 ± 1.8	10450±50	4.16±0.10	0.00	144
5448	00 : 56 : 45.21	+38 : 29 : 57.6	A5V	+6.4 ± 0.6	8590±70	3.18±0.10	+0.20	65
7788	01 : 15 : 46.16	−68 : 52 : 33.3	F6V+K1V	+12.4 ± 3.3	6550±200	4.30±0.10	0.00	70
9672	01 : 34 : 37.78	−15 : 40 : 34.9	A1V	+10.9 ± 2.5	9120±50	4.32±0.16	0.00	186
10700	01 : 44 : 04.08	−15 : 56 : 14.9	G8.5V	−16.8 ± 0.1	5330±10	4.55±0.10	−0.51	1.6
12039	01 : 57 : 48.98	−21 : 54 : 05.3	G4V	+5.8 ± 0.4	5700±40	4.31±0.10	−0.06	15.9
14055	02 : 17 : 18.87	+33 : 50 : 49.9	A1V	+7.3 ± 0.2	10040±50	4.34±0.10	0.00	254
14412	02 : 18 : 58.50	−25 : 56 : 44.5	G8V	+7.3 ± 0.2	5310±20	4.55±0.10	−0.53	0.90
15115	02 : 26 : 16.24	+06 : 17 : 33.2	F2V	+6.0 ± 2.7	6750±200	4.25±0.30	0.00	89.8
15257	02 : 28 : 09.98	+29 : 40 : 09.6	F0III	−20.6 ± 0.2	7100±200	3.50±0.30	0.00	65
16978	02 : 39 : 35.36	−68 : 16 : 01.0	B9III	−24.8 ± 0.8	11330±100	4.43±0.11	0.00	96
21688	03 : 29 : 36.03	−12 : 40 : 29.1	A5III/IV	+15.2 ± 0.1	7880±90	4.52±0.30	0.00	180
21620	03 : 31 : 29.34	+49 : 12 : 35.2	A0V	−13.9 ± 0.3	9650±50	3.90±0.10	0.00	260
21997	03 : 31 : 53.65	−25 : 36 : 50.9	A3IV/V	+19.0 ± 1.5	8520±140	4.27±0.31	0.00	60
22484	03 : 36 : 52.38	+00 : 24 : 06.0	F8V	+27.9 ± 0.1	5960±30	3.93±0.10	−0.09	4
27290	04 : 16 : 01.59	−51 : 29 : 11.9	F1V	+26.7 ± 1.6	7300±200	4.25±0.25	0.00	60
28355	04 : 28 : 50.16	+13 : 02 : 51.4	A7V	+39.8 ± 0.3	8730±50	3.53±0.30	+0.50	105
29391	04 : 37 : 36.13	−02 : 28 : 24.8	F0IV	+20.4 ± 3.8	7200±100	4.25±0.25	0.00	84
30051	04 : 43 : 17.20	−23 : 37 : 42.0	F2V	+15.9 ± 5.6	6900±200	4.25±0.25	0.00	50
31295	04 : 54 : 53.73	+10 : 09 : 03.0	A3V	+16.0 ± 0.2	9130±80	4.25±0.26	−1.00	120
32297	05 : 02 : 27.44	+07 : 27 : 39.7	A0V	+21.0 ± 0.9	7980±100	3.77±0.30	−0.50	90
35850	05 : 27 : 04.76	−11 : 54 : 03.5	F8V	+21.1 ± 3.3	6400±200	4.25±0.25	0.00	50
36546	05 : 33 : 30.76	+24 : 37 : 43.7	B8V	+14.7 ± 0.6	9510±50	4.44±0.10	−1.00	150
37286	05 : 36 : 10.30	−28 : 42 : 28.8	A2IV	+24.9 ± 2.9	8640±50	4.11±0.12	0.00	70
37306	05 : 37 : 08.77	−11 : 46 : 31.9	A2V	+25.1 ± 1.3	9600±50	4.48±0.10	0.00	144
38206	05 : 43 : 21.67	−18 : 33 : 26.9	A0V	+26.6 ± 2.3	10480±100	4.50±0.10	0.00	35
39182	05 : 52 : 39.67	+39 : 34 : 28.9	A2V	−22.9 ± 1.0	9020±80	3.42±0.30	+0.20	238
39283	05 : 54 : 50.78	+55 : 42 : 25.0	A2V	−18.3 ± 0.6	9140±40	3.91±0.15	−0.25	68
40136	05 : 56 : 24.29	−14 : 10 : 03.7	F2V	+1.6 ± 0.8	7150±200	4.25±0.25	0.00	18
42111	06 : 08 : 57.90	+02 : 29 : 58.9	A3V	+27.5 ± 1.9	9380±40	3.48±0.10	0.00	252
53842	06 : 46 : 13.54	−83 : 59 : 29.5	F5V	+17.0 ± 0.5	6500±200	4.25±0.25	0.00	50
50241	06 : 48 : 11.46	−61 : 56 : 29.0	A8V	+13.0 ± 2.9	7580±90	3.52±0.30	−0.25	206
50571	06 : 50 : 01.01	−60 : 14 : 56.9	F5V	+26.2 ± 3.1	6450±100	4.25±0.25	0.00	50
56537	07 : 18 : 05.58	+16 : 32 : 25.4	A4IV	−9.6 ± 2.7	8190±100	4.10±0.39	0.00	154
64145	07 : 53 : 29.81	+26 : 45 : 56.8	A5IV	+4.2 ± 3.2	8320±50	3.48±0.10	0.00	165
71043	08 : 22 : 55.16	−52 : 07 : 25.4	A0V	+24.1 ± 2.2	10280±50	4.51±0.10	0.00	224
71722	08 : 26 : 25.21	−52 : 48 : 27.0	A0V	+31.0 ± 2.6	8870±50	4.19±0.12	−1.00	220
74873	08 : 46 : 56.02	+12 : 06 : 35.8	A1VP	+23.0 ± 0.2	8800±70	4.02±0.37	−1.00	115
77190	09 : 01 : 48.84	+27 : 54 : 09.3	A8Vn	+14.5 ± 3.1	8010±120	3.41±0.30	0.00	185
80007	09 : 13 : 11.98	−69 : 43 : 01.9	A1III	+0.8 ± 1.8	9350±40	3.47±0.10	0.00	135
85905	09 : 54 : 31.82	−22 : 29 : 14.9	A1IV	+9.9 ± 2.5	9040±40	3.50±0.10	0.00	285
95418	11 : 01 : 50.48	+56 : 22 : 56.7	A1IV	−12.2 ± 0.6	9700±40	4.01±0.19	0.00	46
98058	11 : 16 : 39.70	−03 : 39 : 05.8	A7IV	−0.3 ± 0.8	7500±50	3.75±0.32	0.00	230

Continued on next page

Table A.1 – continued from previous page

HD	RA(2000.0)	Dec(2000.0)	Sp. Type	$v_{\rm rad}$ (km/s)	$T_{\rm eff}$ (K)	$\log g$ [cgs]	[M/H]	$v \sin i$ (km/s)
102647	11 : 49 : 03.58	+14 : 34 : 19.4	A3Va	−0.4 ± 3.5	8580±50	4.14±0.32	0.00	128
104731	12 : 03 : 39.57	−42 : 26 : 02.6	F5V	+38.5 ± 0.4	6510±70	3.87±0.10	−0.25	7
104860	12 : 04 : 33.73	+66 : 20 : 11.7	F8	−11.9 ± 0.4	6060±70	4.48±0.14	−0.01	15
105234	12 : 07 : 05.52	−78 : 44 : 28.0	A9III/4	+15.3 ± 1.9	8590±50	4.40±0.10	+0.50	85
105850	12 : 11 : 03.84	−23 : 36 : 08.7	A1V	+15.0 ± 3.6	9160±50	4.21±0.13	0.00	128
108767	12 : 29 : 51.86	−16 : 30 : 55.6	A0IV	+8.5 ± 1.1	10850±50	4.35±0.10	0.00	236
109085	12 : 32 : 04.23	−16 : 11 : 45.6	F2V	+0.0 ± 0.5	6950±100	4.20±0.25	0.00	60
109573	12 : 36 : 01.03	−39 : 52 : 10.2	A0V	+7.5 ± 2.0	10060±50	4.44±0.10	−0.50	150
110058	12 : 39 : 46.20	−49 : 11 : 55.5	A0V	10.6 ± 2.6	9000±50	4.13±0.15	−0.50	150
110411	12 : 41 : 53.06	+10 : 14 : 08.3	A3V	−7.9 ± 1.1	9240±50	4.29±0.10	−1.00	154
118232	13 : 34 : 27.26	+49 : 00 : 57.5	A4V	−16.9 ± 0.4	8130±40	3.49±0.10	0.00	160
121191	13 : 55 : 18.86	−53 : 31 : 43.0	A5IV/V	21.5 ± 1.0	7970±90	4.38±0.10	0.00	65
121617	13 : 57 : 41.13	−47 : 00 : 34.2	A1V	+7.0 ± 3.7	9160±70	4.13±0.36	0.00	90
125162	14 : 16 : 23.02	+46 : 05 : 17.9	A3	−10.1 ± 1.5	8660±50	3.96±0.23	−2.00	100
131488	14 : 55 : 08.03	−41 : 07 : 13.4	A1V	+4.8 ± 0.2	9130±60	4.18±0.22	0.00	120
131835	14 : 56 : 54.47	−35 : 41 : 43.7	A2IV	+2.7 ± 2.5	8610±40	4.24±0.18	0.00	105
138629	15 : 31 : 46.98	+40 : 53 : 57.6	A5V	−18.7 ± 1.1	8680±40	3.54±0.10	+0.20	190
139006	15 : 34 : 41.27	+26 : 42 : 52.9	A0V	+9.9 ± 01	9780±40	3.91±0.10	0.00	130
138813	15 : 35 : 16.11	−25 : 44 : 03.0	A0V	+0.3 ± 2.1	9620±50	4.30±0.11	0.00	130
142097	15 : 53 : 21.93	−21 : 58 : 16.7	A5V	−7.0 ± 2.0	8290±70	3.67±0.10	+0.20	45
142315	15 : 54 : 41.60	−22 : 45 : 58.5	B9V	−4.0 ± 2.4	12500±250	4.50±0.25	0.00	275
142705	15 : 56 : 47.85	−23 : 11 : 02.7	A0V	−5.6 ± 3.0	9300±50	3.97±0.11	0.00	300
144587	16 : 07 : 29.93	−23 : 57 : 02.4	A9V	−10.7 ± 4.7	7390±250	4.50±0.30	0.00	112
144981	16 : 09 : 20.89	−19 : 27 : 25.9	A0V	−5.6 ± 4.3	9950±100	4.32±0.22	0.00	215
145554	16 : 12 : 21.83	−19 : 34 : 44.6	B9V	−7.8 ± 3.9	12030±40	4.44±0.10	0.00	260
145631	16 : 12 : 44.10	−19 : 30 : 10.3	B9V	−5.7 ± 2.3	11410±80	4.36±0.10	0.00	287
145964	16 : 14 : 28.88	−21 : 06 : 27.5	B9V	−6.8 ± 3.1	12080±90	4.47±0.13	0.00	306
145689	16 : 17 : 05.41	−67 : 56 : 28.6	A6V	−7.1 ± 1.7	8340±50	4.04±0.10	0.00	105
146606	16 : 18 : 16.16	−28 : 02 : 30.2	A0V	−2.3 ± 1.3	10540±50	4.39±0.10	0.00	165
146624	16 : 18 : 17.90	−28 : 36 : 50.5	A0V	−14.0 ± 1.9	9880±40	4.50±0.10	0.00	34
146897	16 : 19 : 29.24	−21 : 24 : 13.3	F2/3V	−3.1 ± 0.9	6700±200	4.30±0.30	0.00	55
147137	16 : 20 : 50.23	−22 : 35 : 38.8	A9V	−6.6 ± 1.9	7670±40	4.49±0.10	0.00	82
147220	16 : 21 : 21.15	−22 : 06 : 32.3	A9V	−49.3 ± 2.0	7560±80	4.12±0.10	0.00	80
148283	16 : 25 : 24.17	+37 : 23 : 38.7	A5V	−0.5 ± 0.2	8380±40	4.46±0.30	0.00	240
156623	17 : 20 : 50.62	−45 : 25 : 15.0	A0V	−0.2 ± 2.1	9430±80	4.48±0.20	−0.30	75
157728	17 : 24 : 06.59	+22 : 57 : 37.0	A7V	−21.2 ± 0.3	7690±46	3.98±0.10	0.00	60
158352	17 : 28 : 49.66	+00 : 19 : 50.3	A8Vp	−33.9 ± 0.6	7470±140	3.98±0.21	0.00	150
162003	17 : 41 : 56.35	+72 : 08 : 55.8	F5IV/V	−13.3 ± 0.2	6370±50	3.62±0.10	−0.15	13
162917	17 : 53 : 14.19	+06 : 06 : 05.1	F4IV/V	−29.1 ± 0.9	6620±220	4.28±0.14	0.00	28.4
164249	18 : 03 : 03.41	−51 : 38 : 56.4	F6V+M2V	−0.4 ± 0.5	6570±90	4.03±0.13	+0.02	21
168646	18 : 22 : 00.14	−28 : 25 : 47.9	A3III	−10.8 ± 2.6	8750±100	3.00±0.30	0.00	260
172555	18 : 45 : 26.90	−64 : 52 : 16.5	A7V	+1.2 ± 2.9	7994±60	4.23±0.10	0.00	107
173667	18 : 45 : 39.73	+20 : 32 : 46.7	F6V	22.7 ± 0.1	6380±80	3.67±0.12	−0.10	18
177724	19 : 05 : 24.61	+13 : 51 : 48.5	A0IV/Vn	−27.3 ± 2.5	10260±50	4.26±0.10	−0.15	290
181296	19 : 22 : 51.21	−54 : 25 : 26.1	A0V+M7V	−0.3 ± 1.9	10500±170	4.57±0.30	0.00	230
181327	19 : 22 : 58.94	−54 : 32 : 17.0	F5/F6V	+0.1 ± 0.4	6360±60	4.09±0.10	−0.05	28
182640	19 : 25 : 29.90	+03 : 06 : 53.2	F1IV	−37.2 ± 1.8	7000±200	4.25±0.30	0.00	91
182919	19 : 26 : 13.25	+20 : 05 : 51.8	A0V	−24.3 ± 1.4	10460±80	4.47±0.10	0.00	154
183324	19 : 29 : 00.99	+01 : 57 : 01.6	A0IV	17.4 ± 0.4	9830±40	4.50±0.10	−1.00	100
187642	19 : 50 : 47.00	+08 : 52 : 06.0	A7V	−27.2 ± 0.4	7930±40	4.21±0.10	0.00	205
188228	20 : 00 : 35.56	−72 : 54 : 37.8	A0V	−6.0 ± 3.5	10620±50	4.47±0.10	0.00	85
192518	20 : 14 : 14.53	+28 : 41 : 41.3	A5IV	+8.1 ± 0.3	8020±40	4.61±0.10	0.00	220
196724	20 : 38 : 31.34	+21 : 12 : 04.3	A0	−10.8 ± 2.4	10820±80	4.35±0.12	0.00	52
198160	20 : 51 : 38.47	−62 : 25 : 45.6	A2III	−16.2 ± 1.9	8300±40	4.15±0.30	−0.50	200
198161	20 : 51 : 38.76	−62 : 25 : 44.9	A3III	−13.5 ± 3.6	8160±40	3.79±0.30	−0.50	180
199143	20 : 55 : 47.67	−17 : 06 : 51.0	F8V	−4.5 ± 2.1	6200±150	4.25±0.30	0.00	155

Continued on next page

Table A.1 – continued from previous page

HD	RA(2000.0)	Dec(2000.0)	Sp. Type	$v_{\rm rad}$ (km/s)	$T_{\rm eff}$ (K)	$\log g$ [cgs]	[M/H]	$v \sin i$ (km/s)
203280	21 : 18 : 34.77	+62 : 35 : 08.1	A8V	-11.8 ± 1.1	7800±100	3.72±0.26	0.00	210
202917	21 : 20 : 49.96	−53 : 02 : 03.1	G7V	$+0.1 \pm 0.2$	5520±60	4.42±0.14	−0.04	14
210302	22 : 10 : 08.78	−32 : 32 : 54.3	F6V	-16.4 ± 0.2	6460±100	4.17±0.17	+0.18	13.6
210418	22 : 10 : 11.99	+06 : 11 : 52.3	A1V	-5.1 ± 0.8	8820±60	4.18±0.18	−0.25	140
211336	22 : 15 : 02.20	+57 : 02 : 36.9	F0IV	-5.5 ± 0.5	7400±200	4.25±0.30	0.20	91
213617	22 : 32 : 35.48	+20 : 13 : 48.1	F1V	-13.1 ± 0.7	7200±200	4.25±0.30	0.00	94
217782	23 : 02 : 36.38	+42 : 45 : 28.1	A3V	$+5.1 \pm 1.1$	8830±40	3.45±0.10	0.00	212
221756	23 : 34 : 37.54	+40 : 14 : 11.2	A1V	13.5 ± 0.3	9050±60	4.11±0.20	−0.50	100
222368	23 : 39 : 57.04	+05 : 37 : 34.6	F7V	$+5.6 \pm 0.1$	6130±40	3.90±0.10	−0.16	6.8
224392	23 : 57 : 35.08	−64 : 17 : 53.6	A1V	$+9.9 \pm 2.3$	9400±40	4.25±0.10	+0.10	195

Table A.2: Sample of observed stars. Columns are self-explanatory. Numbers within parenthesis in columns 10 to 13 denote the corresponding references. Column 13 specifies the primary selection criteria as described in the text: 1. Previously detected exocomets; 2. Debris Discs; 3. Debris discs with cold gas; 4. Near-Infrared excesses; 5. Young discs; 6. Shell Stars; 7. λ Boo stars.

HD	Other Name	RA(2000.0)	Dec(2000.0)	Sp. Type	Distance (pc)	V (mag)	B-V (mag)	V_{rad} (km/s)	Age (Myr)	L_{IR} / L_*	Assoc.	Sel.Crit
105	HIP 490	00 : 05 : 52.54	−41 : 45 : 11.0	G0V	38.85	7.53	0.6	1.7	45 (9)	$2.4\cdot 10^{-4}$ (1)	Tuc-Hor (4)	5 (1)
203	HR 9	00 : 06 : 50.09	−23 : 06 : 27.1	F3V	39.96	6.19	0.344	6.5	23 (2)	$1.6\cdot 10^{-4}$ (2)	BPMG (3)	5 (2)
256	HR 10	00 : 07 : 18.27	−17 : 23 : 13.2	A2IV/V	145.18	6.23	0.1	-10.2	549 (3)	$<6.1\cdot 10^{-6}$ (3)		1 (3)
1466	HIP 1481	00 : 18 : 26.12	−63 : 28 : 39.0	F8V	42.97	7.46	0.54	6.4	45 (9)	$6.3\cdot 10^{-5}$ (1)	Tuc-Hor (4)	5 (1)
2262	κ Phe	00 : 26 : 12.20	−43 : 40 : 47.4	A5IV	23.81	3.94	0.17	11.3	200 (1)	$7.4\cdot 10^{-6}$ (4)	Castor (1)	4 (4)
2884	β 1 Tuc	00 : 31 : 32.67	−62 : 57 : 29.6	B9V	41.41	4.33	-0.045	14.0	45 (9)	$<6.7\cdot 10^{-6}$ (1)	Tuc-Hor (4)	5 (1)
2885	β 2 Tuc	00 : 31 : 33.48	−62 : 57 : 56.0	A2V	51.04	4.51	0.135	9.8	45 (9)	$<1.8\cdot 10^{-5}$ (1)	Tuc-Hor (4)	5 (1)
3003	β 3 Tuc	00 : 32 : 43.91	−63 : 01 : 53.4	A0V	45.90	5.09	0.04	7.7	45 (9)	$1.1\cdot 10^{-4}$ (1)	Tuc-Hor (4)	5 (1)
5267	66 Psc	00 : 54 : 35.23	+19 : 11 : 18.3	A1V	108.11	5.79	-0.03	8.5	200 (1)	$3.9\cdot 10^{-5}$ (6)		2 (5)
5448	μ And	00 : 56 : 45.21	+38 : 29 : 57.6	A5V	41.26	3.87	0.12	7.2	687 (3)	$<4.4\cdot 10^{-6}$(4)		4 (6)
7788	κ Tuc	01 : 15 : 46.16	−68 : 52 : 33.3	F6V+K1V	20.96	4.25	0.48	7.7	700 (4)	$<4.4\cdot 10^{-6}$ (8)		4 (4)
9672	49 Cet	01 : 34 : 37.78	−15 : 40 : 34.9	A1V	57.07	5.62	0.062	10.3	40 (5)	$1.1\cdot 10^{-3}$ (7)	Argus (7)	1 (7)
10700	τ Cet	01 : 44 : 04.08	−15 : 56 : 14.9	G8.5V	3.65	3.5	0.72	-16.62	5800 (6)	$6.1\cdot 10^{-6}$ (8)		4 (8)
12039	DK Cet	01 : 57 : 48.98	−21 : 54 : 05.3	G4V	41.41	8.06	0.673	6.12	45 (9)	$6.3\cdot 10^{-5}$ (1)	Tuc-Hor (4)	5 (1)
14055	γ Tri	02 : 17 : 18.87	+33 : 50 : 49.9	A1V	34.44	4.0	0.03	9.9	300 (1)	$7.4\cdot 10^{-5}$ (4)		2 (9)
14412	HR 683	02 : 18 : 58.50	−25 : 56 : 44.5	G8V	12.83	6.34	0.73	7.36	6540 (7)	$<2.0\cdot 10^{-6}$ (9)		4 (4)
15115	HIP 11360	02 : 26 : 16.24	+06 : 17 : 33.2	F2V	49.00	6.8	0.35	0.81	45 (9)	$4.8\cdot 10^{-4}$ (10)	Tuc-Hor (8)	2 (10)
15257	HR 717	02 : 28 : 09.98	+29 : 40 : 09.6	F0III	49.93	5.29	0.29	-24.8	1000 (1)	$8.6\cdot 10^{-5}$ (6)		2 (5)
16978	HR 806	02 : 39 : 35.36	−68 : 16 : 01.0	B9III	46.55	4.11	-0.046	13.6	45 (9)	$<8.6\cdot 10^{-7}$(1)	Tuc-Hor (4)	5 (1)
21688	HR 1062	03 : 29 : 36.03	−12 : 40 : 29.1	A5III/IV	143.21	5.58	0.152	15.1	625 (3)			6 (11)
21620	HR 1056	03 : 31 : 29.34	+49 : 12 : 35.2	A0V	135.00	6.28	0.07	-21.4	80 (17)	$2.5\cdot 10^{-5}$ (11)		1 (7)
21997	HR 1082	03 : 31 : 53.65	−25 : 36 : 50.9	A3IV/V	69.64	6.37	0.13	17.3	42 (9)	$5.7\cdot 10^{-4}$ (7)	Columba (1)	3 (10)
22484	10 Tau	03 : 36 : 52.38	+00 : 24 : 06.0	F8V	13.96	4.3	0.85	28.07	7500 (6)	$1.1\cdot 10^{-5}$ (8)		4 (8)
27290	HR 1338	04 : 16 : 01.59	−51 : 29 : 11.9	F1V	20.45	4.2	0.35	25.2	45 (1)	$1.9\cdot 10^{-5}$ (8)	IC 2391 (1)	2 (9)
28355	b Tau	04 : 28 : 50.16	+13 : 02 : 51.4	A7V	48.57	5.01	0.212	37.3	600 (1)	$4.7\cdot 10^{-5}$ (6)	Hyades (1)	4 (4)
29391	HR 1474	04 : 37 : 36.13	−02 : 28 : 24.8	F0IV	29.78	5.22	0.262	12.6	23 (2)	$2.3\cdot 10^{-6}$ (2)	BPMG (3)	5 (2)
30051	HIP 21965	04 : 43 : 17.20	−23 : 37 : 42.0	F2V	63.59	7.11	0.4	19.3	45 (9)	$2.8\cdot 10^{-5}$ (1)	Tuc-Hor (4)	5 (2)
31295	π 1 Ori	04 : 54 : 53.73	+10 : 09 : 03.0	A3V	35.66	4.66	0.081	11.1	123 (1)	$7.6\cdot 10^{-5}$ (5)		7 (12)
32297	HIP 23451	05 : 02 : 27.44	+07 : 27 : 39.7	A0V	132.79	8.14	0.18	23.0	30 (10)	$4.4\cdot 10^{-3}$ (6)		1 (13)
35850	AF Lep	05 : 27 : 04.76	−11 : 54 : 03.5	F8V	26.88	6.31	0.503	17.0	23 (2)	$3.7\cdot 10^{-5}$ (2)	BPMG (3)	5 (2)
36546	HIP 26062	05 : 33 : 30.76	+24 : 37 : 43.7	B8V	101.35	6.95	0.07	20.4	10 (11)	$4.0\cdot 10^{-3}$ (12)		2 (14)
37286	HR 1915	05 : 36 : 10.30	−28 : 42 : 28.8	A2IV	58.89	6.27	0.149	22.4	45 (9)	$1.0\cdot 10^{-4}$ (6)	Tuc-Hor (1)	2 (5)
37306	HR 1919	05 : 37 : 08.77	−11 : 46 : 31.9	A2V	70.46	6.09	0.056	23.0	42 (9)	$1.2\cdot 10^{-4}$ (6)	Columba (2)	2 (5)
38206	HR 1975	05 : 43 : 21.67	−18 : 33 : 26.9	A0V	71.41	5.73	-0.011	25.3	42 (9)	$1.4\cdot 10^{-4}$ (6)	Columba (1)	2 (5)
39182	HR 2025	05 : 52 : 39.67	+39 : 34 : 28.9	A2V	202.46	6.39	0.09	-14.5	407 (3)			6 (11)
39283	ξ Aur	05 : 54 : 50.78	+55 : 42 : 25.0	A2V	72.51	4.96	0.045	-11.8	540 (8)	$<3.1\cdot 10^{-6}$ (11)		6 (15)

Continued on next page

Table A.2 – continued from previous page

HD	Other Name	RA(2000.0)	Dec(2000.0)	Sp. Type	Distance (pc)	V (mag)	B-V (mag)	v_{rad} (km/s)	Age (Myr)	L_{IR} / $L_\star$	Assoc.	Sel.Crit
40136	η Lep	05 : 56 : 24.29	−14 : 10 : 03.7	F2V	14.88	3.72	0.33	-2.14	1390 (1)	$2.6\cdot 10^{-5}$ (6)		4 (8)
42111	HR 2174	06 : 08 : 57.90	+02 : 29 : 58.9	A3V	178.42	5.73	0.07	25.3	319 (3)	$<1.0\cdot 10^{-5}$ (11)		1 (7)
53842	HIP 32435	06 : 46 : 13.54	−83 : 59 : 29.5	F5V	58.87	8.62	0.258	12.2	45 (9)	$<2.1\cdot 10^{-4}$ (6)	Tuc-Hor (4)	5 (1)
50241	α Pic	06 : 48 : 11.46	−61 : 56 : 29.0	A8V	29.60	3.3	0.18	15.3	885 (8)	$<4.4\cdot 10^{-6}$ (4)		1 (15)
50571	HR 2562	06 : 50 : 01.01	−60 : 14 : 56.9	F5V	33.64	6.1	0.45	22.1	300 (1)	$1.5\cdot 10^{-4}$ (10)	B3 (1)	2 (9)
56537	λ Gem	07 : 18 : 05.58	+16 : 32 : 25.4	A4IV	30.93	3.58	0.111	-7.4	314 (1)	$<4.4\cdot 10^{-6}$ (4)	UMA (1)	4 (8)
64145	ϕ Gem	07 : 53 : 29.81	+26 : 45 : 56.8	A5IV	76.31	4.96	0.097	8.0	714 (8)			1 (16)
71043	HR 3300	08 : 22 : 55.16	−52 : 07 : 25.4	A0V	73.25	5.89	0.016	22.5	45 (9)	$6.7\cdot 10^{-5}$ (6)	Tuc-Hor (2)	2 (15)
71722	HR 3341	08 : 26 : 25.21	−52 : 48 : 27.0	A0V	69.33	6.05	0.057	30.2	324 (1)	$8.4\cdot 10^{-5}$ (6)		2 (9)
74873	HR 3481	08 : 46 : 56.02	+12 : 06 : 35.8	A1VP	56.19	5.88	0.107	23.3	539 (1)	$4.8\cdot 10^{-5}$ (5)		7 (12)
77190	67 Cnc	09 : 01 : 48.84	+27 : 54 : 09.3	A8Vn	59.65	6.07	0.22	12.0	19 (8)	$<1.3\cdot 10^{-5}$ (11)		6 (15)
80007	HR 3685	09 : 13 : 11.98	−69 : 43 : 01.9	A1III	34.70	1.69	0.0	-5.1	260 (12)	$<1.7\cdot 10^{-6}$ (3)		1 (3)
85905	HR 3921	09 : 54 : 31.82	−22 : 29 : 14.9	A1IV	176.03	6.23	0.044	9.2	481 (3)	$<4.8\cdot 10^{-6}$ (3)		1 (3)
95418	β UMa	11 : 01 : 50.48	+56 : 22 : 56.7	A1IV	24.45	2.37	-0.02	-13.1	320 (1)	$1.4\cdot 10^{-5}$ (4)	UMA (1)	2 (9)
98058	ϕ Leo	11 : 16 : 39.70	−03 : 39 : 05.8	A7IV	56.47	4.47	0.198	-3.0	921 (8)	$<7.4\cdot 10^{-5}$ (23)		6 (11)
102647	β Leo	11 : 49 : 03.58	+14 : 34 : 19.4	A3Va	11.00	2.13	0.09	-0.2	45 (1)	$2.2\cdot 10^{-5}$ (4)	IC 2391 (1)	4 (8)
104731	HR 4600	12 : 03 : 39.57	−42 : 26 : 02.6	F5V	24.73	5.15	0.41	38.5	360 (6)		CANE (1)	4 (4)
104860	HIP 58876	12 : 04 : 33.73	+66 : 20 : 11.7	F8	45.20	7.91	0.59	-11.73	3140 (1)	$3.0\cdot 10^{-4}$ (6)		2 (9)
105234	EF Cha	12 : 07 : 05.52	−78 : 44 : 28.0	A9III/4	104.54	7.46	0.28	0.0	10 (1)	$1.0\cdot 10^{-3}$ (13)		2 (5)
105850	HR 4635	12 : 11 : 03.84	−23 : 36 : 08.7	A1V	58.81	5.47	0.05	11.0	45 (9)	$6.2\cdot 10^{-5}$ (6)	Tuc-Hor (2)	2 (5)
108767	δ Crv	12 : 29 : 51.86	−16 : 30 : 55.6	A0IV	26.63	2.94	-0.05	13.9	216 (8)	$<4.4\cdot 10^{-6}$ (4)		4 (4)
109085	η Crv	12 : 32 : 04.23	−16 : 11 : 45.6	F2V	18.28	4.31	0.38	-2.8	1400 (13)	$3.4\cdot 10^{-4}$ (14)		3 (17)
109573	HR 4796	12 : 36 : 01.03	−39 : 52 : 10.2	A0V	71.91	5.78	0.009	7.1	8 (1)	$4.6\cdot 10^{-3}$ (15)	TWA (1)	2 (5)
110058	HIP 61782	12 : 39 : 46.20	−49 : 11 : 55.5	A0V	129.98	7.97	0.15	5.0	15 (14)	$1.4\cdot 10^{-3}$ (6)	LCC (5)	3 (18)
110411	ρ Vir	12 : 41 : 53.06	+10 : 14 : 08.3	A3V	38.16	4.88	0.09	-0.7	86 (1)	$6.4\cdot 10^{-5}$ (4)		1 (7)
118232	24 CVn	13 : 34 : 27.26	+49 : 00 : 57.5	A4V	55.28	4.7	0.12	-18.3	612 (1)	$2.6\cdot 10^{-5}$ (11)		6 (15)
121191	SAO 241295	13 : 55 : 18.86	−53 : 31 : 43.0	A5IV/V	132.11	8.16	0.24	12.0	16 (14)	$4.7\cdot 10^{-3}$ (16)	LCC/UCL (8)	3 (18)
121617	SAO 224570	13 : 57 : 41.13	−47 : 00 : 34.2	A1V	116.87	7.29	0.07	7.8	16 (14)	$4.8\cdot 10^{-3}$ (17)	UCL (9)	3 (18)
125162	λ *Böo*	14 : 16 : 23.02	+46 : 05 : 17.9	A3	30.36	4.18	0.08	7.9	313 (1)	$4.4\cdot 10^{-5}$ (4)		7 (12)
131488	SAO 225290	14 : 55 : 08.03	−41 : 07 : 13.4	A1V	154.62	8.0	0.09	5.8	16 (14)	$5.5\cdot 10^{-3}$ (16)	UCL (8)	3 (18)
131835	HIP 73145	14 : 56 : 54.47	−35 : 41 : 43.7	A2IV	133.65	7.86	0.19	0.5	16 (14)	$3.0\cdot 10^{-3}$ (18)	UCL (5)	3 (18)
138629	HR 5774	15 : 31 : 46.98	+40 : 53 : 57.6	A5V	127.20	4.98	0.96	-16.0	–			1 (19)
139006	α CrB	15 : 34 : 41.27	+26 : 42 : 52.9	A0V	23.01	2.24	-0.02	1.4	314 (1)	$1.5\cdot 10^{-5}$ (4)	UMA (1)	2 (9)
138813	HIP 76310	15 : 35 : 16.11	−25 : 44 : 03.0	A0V	137.41	7.3	0.07	4.4	10 (14)	$9.0\cdot 10^{-4}$ (6)	US (6)	3 (18)
142097	HIP 77815	15 : 53 : 21.93	−21 : 58 : 16.7	A5V	140.92	8.39	0.41	-0.1	11 (16)	$<3.0\cdot 10^{-4}$ (19)	US (6)	5 (20)
142315	HIP 77911	15 : 54 : 41.60	−22 : 45 : 58.5	B9V	145.34	6.87	0.034	-7.4	11 (1)	$3.8\cdot 10^{-4}$ (19)	US (6)	5 (20)
142705	HIP 78099	15 : 56 : 47.85	−23 : 11 : 02.7	A0V	144.33	7.74	0.18	-6.5	11 (16)	$<1.7\cdot 10^{-4}$ (19)	US (6)	5 (20)
144587	HIP 78996	16 : 07 : 29.93	−23 : 57 : 02.4	A9V	144.01	8.31	0.42	0.0	11 (1)	$3.2\cdot 10^{-4}$ (19)	US (6)	5 (20)
144981	HIP 79156	16 : 09 : 20.89	−19 : 27 : 25.9	A0V	150.59	8.04	0.18	-1.3	11 (1)	$1.2\cdot 10^{-4}$(19)	US (6)	5 (20)
145554	HIP 79410	16 : 12 : 21.83	−19 : 34 : 44.6	B9V	136.83	7.64	0.13	-9.4	11 (1)	$1.4\cdot 10^{-4}$ (19)	US (6)	5 (20)

Continued on next page

Table A.2 – continued from previous page

HD	Other Name	RA(2000.0)	Dec(2000.0)	Sp. Type	Distance (pc)	V (mag)	B-V (mag)	v_{rad} (km/s)	Age (Myr)	L_{IR} / $L_\star$	Assoc.	Sel.Crit
145631	HIP 79439	16 : 12 : 44.10	−19 : 30 : 10.3	B9V	140.72	7.6	0.13	-9.5	11 (1)	$6.3\cdot 10^{-5}$ (19)	US (6)	5 (20)
145964	HR 6051	16 : 14 : 28.88	−21 : 06 : 27.5	B9V	112.18	6.41	0.001	-7.8	11 (1)	$1.5\cdot 10^{-5}$ (6)	US (6)	1 (7)
145689	HIP 79797	16 : 17 : 05.41	−67 : 56 : 28.6	A6V	55.55	5.95	0.148	-9.0	40 (1)	$4.9\cdot 10^{-5}$ (6)	Argus (1)	5 (21)
146606	HIP 79878	16 : 18 : 16.16	−28 : 02 : 30.2	A0V	137.27	7.06	-0.01	0.8	11 (1)	$9.5\cdot 10^{-5}$ (19)	US (6)	5 (20)
146624	d Sco	16 : 18 : 17.90	−28 : 36 : 50.5	A0V	41.29	4.79	0.03	-13.0	23 (2)	$<5.0\cdot 10^{-7}$ (2)	BPMG (3)	5 (2)
146897	HIP 79977	16 : 19 : 29.24	−21 : 24 : 13.3	F2/3V	131.50	9.11	0.47	-1.1	15 (16)	$5.6\cdot 10^{-3}$ (6)	US (6)	3 (21)
147137	HIP 80088	16 : 20 : 50.23	−22 : 35 : 38.8	A9V	143.92	9.03	0.39	-0.8	11 (1)	$5.7\cdot 10^{-4}$ (19)	US (6)	5 (20)
147220	HIP 80130	16 : 21 : 21.15	−22 : 06 : 32.3	A9V	158.88	8.59	0.45	-1.0	–	$<3.3\cdot 10^{-4}$ (19)	US (6)	5 (20)
148283	HR 6123	16 : 25 : 24.17	+37 : 23 : 38.7	A5V	77.45	5.54	0.17	-1.3	854 (8)	$<8.4\cdot 10^{-6}$ (11)		6 (11)
156623	HIP 84881	17 : 20 : 50.62	−45 : 25 : 15.0	A0V	111.75	7.26	0.09	-0.2	16 (14)	$7.8\cdot 10^{-3}$ (20)	UCL (5)	3 (21)
157728	73 Her	17 : 24 : 06.59	+22 : 57 : 37.0	A7V	42.75	5.72	0.21	-19.7	534 (1)	$2.9\cdot 10^{-4}$ (6)		2 (5)
158352	HR 6507	17 : 28 : 49.66	+00 : 19 : 50.3	A8Vp	63.46	5.41	0.23	-36.1	890 (1)	$9.3\cdot 10^{-5}$ (11)		2 (5)
162003	ψ 1 Dra A	17 : 41 : 56.35	+72 : 08 : 55.8	F5IV/V	21.42	4.56	0.44	-13.3	2326 (8)	$<4.4\cdot 10^{-6}$ (8)		4 (6)
162917	HR 6670	17 : 53 : 14.19	+06 : 06 : 05.1	F4IV/V	30.80	5.77	0.4	-29.1	1210 (1)	$6.5\cdot 10^{-5}$ (6)		2 (5)
164249	HIP 88399	18 : 03 : 03.41	−51 : 38 : 56.4	F6V+M2V	49.61	7.01	0.456	-0.4	23 (2)	$8.4\cdot 10^{-4}$ (2)	BPMG (3)	5 (2)
168646	HR 6864	18 : 22 : 00.14	−28 : 25 : 47.9	A3III	191.33	6.15	0.242	-11.5	662 (3)			6 (11)
172555	HR 7012	18 : 45 : 26.90	−64 : 52 : 16.5	A7V	28.55	4.78	0.191	2.0	23 (2)	$7.1\cdot 10^{-4}$ (4)	BPMG (3)	1 (22)
173667	110 Her	18 : 45 : 39.73	+20 : 32 : 46.7	F6V	19.21	4.19	0.46	23.05	2687 (8)	$7.0\cdot 10^{-7}$ (9)		4 (8)
177724	ζ Aql	19 : 05 : 24.61	+13 : 51 : 48.5	A0IV/Vn	25.46	2.99	0.01	-25.0	356 (1)	$<1.6\cdot 10^{-6}$		4 (8)
181296	η Tel	19 : 22 : 51.21	−54 : 25 : 26.1	A0V+M7V	48.22	5.02	0.015	13.0	23 (2)	$2.4\cdot 10^{-4}$ (6)	BPMG (3)	3 (2)
181327	HIP 95270	19 : 22 : 58.94	−54 : 32 : 17.0	F5/F6V	48.21	7.04	0.46	0.2	23 (2)	$2.0\cdot 10^{-3}$ (6)	BPMG (3)	3 (23)
182640	δ Aql	19 : 25 : 29.90	+03 : 06 : 53.2	F1IV	15.53	3.36	0.32	-34.0	1385 (8)			4 (6)
182919	5 Vul	19 : 26 : 13.25	+20 : 05 : 51.8	A0V	71.98	5.59	0.002	-20.9	198 (1)	$3.4\cdot 10^{-5}$ (6)		1 (7)
183324	c Aql	19 : 29 : 00.99	+01 : 57 : 01.6	A0IV	60.68	5.79	0.083	12.0	140 (1)	$1.8\cdot 10^{-5}$ (5)		1 (7)
187642	α Aql	19 : 50 : 47.00	+08 : 52 : 06.0	A7V	5.13	0.76	0.22	-26.6	991 (8)	$<4.4\cdot 10^{-6}$ (4)		4 (8)
188228	ϵ Pav	20 : 00 : 35.56	−72 : 54 : 37.8	A0V	32.22	3.95	-0.006	-6.7	40 (1)	$4.4\cdot 10^{-6}$ (4)	Argus (7)	2 (9)
192518	HR 7731	20 : 14 : 14.53	+28 : 41 : 41.3	A5IV	93.37	5.2	0.17	7.0	607 (8)			6 (11)
196724	29 Vul	20 : 38 : 31.34	+21 : 12 : 04.3	A0	64.00	4.82	-0.02	-17.1	224 (8)	$<2.4\cdot 10^{-6}$ (11)		6 (15)
198160	HR 7959	20 : 51 : 38.47	−62 : 25 : 45.6	A2III	74.00	6.21	0.14	-16.0	735 (8)	$2.0\cdot 10^{-5}$ (5)		7 (12)
198161	HR 7960	20 : 51 : 38.76	−62 : 25 : 44.9	A3III	73.90	6.56	0.18	-10.0	735 (8)			7 (12)
199143	HIP 103311	20 : 55 : 47.67	−17 : 06 : 51.0	F8V	45.66	7.32	0.52	-4.5	23 (2)	$<2.6\cdot 10^{-6}$ (2)	BPMG	5 (2)
203280	α Cep	21 : 18 : 34.77	+62 : 35 : 08.1	A8V	15.04	2.46	0.22	-15.8	987 (8)	$<2.1\cdot 10^{-6}$ (24)		4 (8)
202917	HIP 105388	21 : 20 : 49.96	−53 : 02 : 03.1	G7V	46.85	8.67	0.65	-0.9	45 (9)	$2.5\cdot 10^{-4}$ (1)	Tuc-Hor (4)	5 (1)
210302	τ PsA	22 : 10 : 08.78	−32 : 32 : 54.3	F6V	18.35	4.92	0.48	-16.25	3530 (7)	$<4.4\cdot 10^{-6}$ (8)		4 (4)
210418	θ Peg	22 : 10 : 11.99	+06 : 11 : 52.3	A1V	28.30	3.55	0.07	-7.9	545 (8)	$<4.4\cdot 10^{-6}$ (4)		4 (6)
211336	ϵ Cep	22 : 15 : 02.20	+57 : 02 : 36.9	F0IV	26.30	4.19	0.28	-4.7	1063 (1)	$1.9\cdot 10^{-5}$ (6)		4 (8)
213617	39 Peg	22 : 32 : 35.48	+20 : 13 : 48.1	F1V	53.58	6.44	0.33	-18.9	930 (1)	$6.5\cdot 10^{-5}$ (6)		2 (5)
217782	2 And	23 : 02 : 36.38	+42 : 45 : 28.1	A3V	129.20	5.1	0.08	2.1	478 (3)	$<9.6\cdot 10^{-6}$ (11)		1 (7)
221756	15 And	23 : 34 : 37.54	+40 : 14 : 11.2	A1V	77.28	5.56	0.089	13.1	613 (8)	$1.5\cdot 10^{-5}$ (5)		7 (12)
222368	ι Psc	23 : 39 : 57.04	+05 : 37 : 34.6	F7V	13.71	4.12	0.5	5.67	3287 (3)	$1.1\cdot 10^{-6}$ (8)		4 (6)

Continued on next page

Table A.2 – continued from previous page

HD	Other Name	RA(2000.0)	Dec(2000.0)	Sp. Type	Distance (pc)	V (mag)	B-V (mag)	v_{rad} (km/s)	Age (Myr)	L_{IR} / $L_\star$	Assoc.	Sel.Crit
224392	η Tuc	23 : 57 : 35.08	−64 : 17 : 53.6	A1V	47.07	5.0	0.056	32.5	45 (9)	$<1.6\cdot 10^{-5}$ (1)	Tuc-Hor (4)	5 (1)

References for age: (1) Chen et al. (2014); (2) Mamajek & Bell (2014); (3) Gontcharov (2012); (4) Gáspár et al. (2013); (5) Torres et al. (2008); (6) Maldonado et al. (2012); (7) Eiroa et al. (2013); (8) David & Hillenbrand (2015); (9) Bell et al. (2015a); (10) Kalas (2005); (11) Lisse et al. (2017); (12) Su et al. (2006); (13) Marino et al. (2017); (14) Pecaut & Mamajek (2016); (15) Bochanski et al. (2018); (16) Pecaut et al. (2012); (17) Roberge & Weinberger (2008);

References for $L_{IR}/L_\star$ (1) Donaldson et al. (2012); (2) Riviere-Marichalar et al. (2014); (3) Redfield et al. (2007) ; (4) Thureau et al. (2014); (5) Draper et al. (2016); (6) Chen et al. (2014); (7) Moór et al. (2015b); (8) Sibthorpe et al. (2018); (9) Eiroa et al. (2013); (10) Moór et al. (2011c); (11) Roberge & Weinberger (2008); (12) Lisse et al. (2017); (13) Currie et al. (2011)5; (14) Duchêne et al. (2014); (15) Riviere-Marichalar et al. (2013); (16) Vican et al. (2016); (17) Moór et al. (2011b); (18) Moór et al. (2015a); (19) Donaldson et al., private communication; (20) Cotten & Song (2016); (21) Plavchan et al. (2009) (22) Cataldi et al. (2019)

References for associations: (1) Chen et al. (2014); (2) Zuckerman & Song (2012); (3) Riviere-Marichalar et al. (2013); (4) Donaldson et al. (2012); (5) Lieman-Sifry et al. (2016); (6) de Zeeuw et al. (1999);(7) Zuckerman (2019); (8) Desidera et al. (2015)

References for selection criteria: (1) Donaldson et al. (2012); (2) Riviere-Marichalar et al. (2014); (3) Redfield et al. (2007) ; (4) Ertel et al. (2014); (5) Chen et al. (2014); (6) Nuñez et al. (2017); (7) Welsh & Montgomery (2013); (8) Absil et al. (2013); (9) Pawellek et al. (2014); (10) Moór et al. (2011b); (11) Abt (2008); (12) Draper et al. (2016); (13) Redfield (2007); (14) Currie et al. (2017); (15) Roberge & Weinberger (2008); (16) Welsh & Montgomery (2015); (17) Marino et al. (2017); (18) Moór et al. (2017); (19) Lagrange-Henri et al. (1990c); (20) Donaldson et al., private communication; (21) Lieman-Sifry et al. (2016); (22) Kiefer et al. (2014a); (23) Marino et al. (2016); (24) Chen et al. (2005)

Table A.3: Plausible origin of the observed narrow non-photospheric absorptions for each star. Equivalent widths (EW), radial velocities (RV), full width half maximum (FWHM), and column densities (N) are given for each absorption as estimated from the median spectra. Radial velocities of the stars (v_{rad}) and the radial velocity of the interstellar clouds (v_{ISM}), if present, are also given. The convention for the plausible origin is the following. CS: circumstellar; ISM: interstellar medium; CS+ISM: both types origins are plausible. A question mark indicates that the origin is ambiguous. Absorptions marked with an asterisk (*) in the EW are triangular shell-like absorptions.

Star	V_{rad}	V_{ISM}	Ca II K/H				Na I D2/D1				Origin
			EW	RV	FWHM	N	EW	RV	FWHM	N	
	(km/s)	(km/s)	(*m*Å)	(km/s)	(km/s)	(cm^{-2})	(*m*Å)	(km/s)	(km/s)	(cm^{-2})	
HD 256	-2.2±0.3	3.16 (LIC)	190.9*/180.3*	-1.8/-0.82	10.67/11.05	$4.88\cdot 10^{12}$	1.2/0.4	3.2/3.3	4.17/1.80	$5.91\cdot 10^{9}$	CS
		-2.73 (Mic)									
		1.01 (Cet)									
HD 2884	8.3±1.6	13.85 (Dor)	2.1/1.66	0.5/4.3	12.13/7.1	$4.28\cdot 10^{10}$					?
		2.46 (Vel)									
HD 2885	13.5±3.9	13.84 (Dor)					56.8/52.3	-2.0/-2.5	17.68/16.1	$1.85\cdot 10^{12}$	?
		2.46 (Vel)									
HD 3003	8.2±2.3	13.84 (Dor)	4.5/¡1.5	0.6/-	24.55/-	$4.82\cdot 10^{10}$	4.8/2.9	-3.7/-3.0	6.84/6.57	$4.61\cdot 10^{10}$	?
		2.46 (Vel)									
HD 5267	9.5±1.8	11.44 (LIC)	11.4/4.0	-5.0/-5.1	6.86/5.47	$1.22\cdot 10^{11}$	34.8/20.0	-5.4/-5.3	6.00/5.80	$3.79\cdot 10^{11}$	CS?+ISM
			2.6/¡1.0	9.7/-	10.64/-	$2.78\cdot 10^{10}$	3.1/¡1.0	11.7/-	12.8/-	$1.53\cdot 10^{10}$	
HD 9672	10.9±2.5	11.01 (LIC)	10.6/6.0	13.5/12.9	7.4/7.1	$1.83\cdot 10^{11}$	16.4/9.3	11.5/10.6	4.4/4.0	$3.21\cdot 10^{11}$	CS+ISM
HD 16978	12.9±1.8	2.65 (G)	4.9/1.6	11.6/10.8	10.57/7.98	$5.24\cdot 10^{10}$					CS
		5.19 (Cet)									
		8.66 (Vel)									
HD 21688	15.2±0.1	18.71 (LIC)	123.9*/99.84	15.7/17.9	13.92/13.45	$2.61\cdot 10^{12}$					CS
HD 21620	-13.9±0.3	18.52 (LIC)	12.4/6.7	4.0/3.9	5.67/5.50	$3.65\cdot 10^{11}$	73.5/54.9	3.7/3.8	5.11/4.87	$6.55\cdot 10^{11}$	CS+ISM
			2.0/1.9	15.3/15.3	7.60/6.63	$2.12\cdot 10^{11}$					
HD 32297	21.0±0.9	23.59 (LIC)	19.4/9.8	22.7/21.9	9.7/6.9	$2.08\cdot 10^{11}$	93.0/84.0	19.7/20.8	6.69/6.23	$1.05\cdot 10^{12}$	CS
HD 36546	14.7±0.6	23.53 (LIC)	18.7/14.5	14.6/15.0	4.43/5.04	$3.74\cdot 10^{11}$	24.3/13.9	14.1/14.33	4.01/4.02	$2.56\cdot 10^{11}$	CS
			10.9/4.0	18.7/20.8	7.40/8.67	$1.28\cdot 10^{11}$	12.9/6.8	18.6/18.5	6.04/6.49	$2.05\cdot 10^{10}$	
HD 37306	25.1±1.3		13.1/6.3	11.0/10.6	6.91/6.75	$1.40\cdot 10^{11}$	4.6/2.23	10.6/10.7	6.41/5.22	$2.27\cdot 10^{10}$	CS+ISM
			31.6/19.3	32.3/32.5	8.71/9.39	$3.38\cdot 10^{11}$	6.7/3.17	31.2/31.6	7.95/8.08	$3.30\cdot 10^{10}$	
HD 39182	-22.9±1.0	21.62 (LIC)	19.6/14.5	13.3/13.3	6.70/8.81	$3.81\cdot 10^{11}$	131.8/102.5	13.8/13.7	7.83/6.8	$1.21\cdot 10^{12}$	CS
			6.9/¡3.0	-21.8/-	5.92/-	$7.28\cdot 10^{10}$					
			103.1*/67.1	-22.6/-18.3	55.43/36.49	$1.92\cdot 10^{12}$					
HD 42111	27.5±1.9	24.83 (Aur)	318.3*/285.9	27.2/29.3	25.93/26.86	$9.66\cdot 10^{12}$	113.7/55.9	27.0/27.8	58.67/52.84	$5.60\cdot 10^{11}$	CS+ISM
							61.8/43.5	23.2/23.5	5.23/5.14	$5.40\cdot 10^{11}$	
HD 50241	13.0±2.9	6.81 (Blue)	8.4/4.0	15.6/16.8	16.25/8.92	$9.35\cdot 10^{10}$					CS
		17.9 (Cet)									
		15.34 (Vel)									
HD 71043	24.1±2.2	4.62 (G)	2.5/¡1.5	16.0/-	10.35/-	$2.68\cdot 10^{10}$	1.9/0.99	17.5/17.3	5.66/5.47	$4.33\cdot 10^{10}$	ISM

Continued on next page

Table A.3 – continued from previous page

Star	V_{rad}	V_{ISM}	Ca II K/H				Na I D2/D1				Origin
			EW	RV	FWHM	N	EW	RV	FWHM	N	
	(km/s)	(km/s)	(*m*Å)	(km/s)	(km/s)	(cm^{-2})	(*m*Å)	(km/s)	(km/s)	(cm^{-2})	
		20.5 (Cet)	2.5/1.9	4.5/5.4	8.28/7.10	$5.01\cdot 10^{10}$	2.9/0.88	5.3/5.1	10.47/5.88	$1.43\cdot 10^{10}$	
		15.0 (Vel)									
HD 71722	31.0±2.6	4.19 (G)	7.9/3.2	11.8/11.0	16.49/16.45	$8.46\cdot 10^{10}$	4.5/4.1	13.6/14.1	7.55/12.01	$9.56\cdot 10^{10}$	ISM
		19.65 (Cet)									
		14.33 (Vel)									
HD 80007	0.8±1.8	-2.75 (G)	1.5/¡1.0	1.3/-	8.2/-	$1.51\cdot 10^{10}$	2.7/¡1.0	3.0/-	12.57/-	$1.33\cdot 10^{10}$	CS
		3.35 (Blue)					1.4/¡1.0	-11.6/-	7.04/-	$6.90\cdot 10^{9}$	
HD 85905	9.9±2.5	11.01 (G)	80.5*/75.3	16.2/18.5	58.25/56.35	$4.29\cdot 10^{12}$	6.3/2.9	11.6/10.3	29.08/17.56	$3.10\cdot 10^{10}$	CS+ISM
			7.6/3.56	8.1/7.7	6.22/4.49	$8.13\cdot 10^{10}$	13.4/6.5	7.9/8.1	5.52/5.23	$6.60\cdot 10^{10}$	
			1.2/¡1.0	25.5/-	5.20/-	$1.28\cdot 10^{10}$					
HD 98058	0.7±1.5	1.75 (Leo)	124.9*/94.4	-7.8/8.9	48.81/50.29	$2.44\cdot 10^{12}$					CS
HD 105850	15.0±3.6	2.54 (Gem)	15.3/4.6	-4.6/-5.1	10.35/7.19	$1.64\cdot 10^{11}$	10.4/4.8	-6.5/-6.6	6.41/5.52	$5.12\cdot 10^{10}$	ISM
		-5.36 (Leo)									
HD 108767	8.5±1.1	0.21 (Gem)	3.4/1.6	-0.6/-0.8	5.59/6.19	$3.64\cdot 10^{10}$	2.9/1.2	-0.3/0.2	4.80/4-48	$1.43\cdot 10^{10}$	ISM
HD 109573	7.5±2.0		2.1/¡1.0	-14.2/-	8.05/-	$2.25\cdot 10^{10}$	3.2/0.5	-0.5/-15.3	22.7/6.88	$1.58\cdot 10^{10}$	CS
			2.3/1.1	-4.7/-6.0	7.80/-6.62	$2.46\cdot 10^{10}$	6.4/2.8	-5.6/-4.7	7.19/7.01	$3.15\cdot 10^{10}$	
HD 110058	10.6±2.6	-14.46 (G)	27.0/24.1	12.7/12.0	6.8/6.22	$5.41\cdot 10^{11}$	46.0/39.1	12.5/12.4	6.31/6.57	$1.98\cdot 10^{12}$	CS
			19.9/10.0	1.2/1.8	12.6/13.4	$1.21\cdot 10^{14}$	34.0/18.9	0.9/0.6	11.71/11.5	$1.67\cdot 10^{11}$	
HD 118232	-16.9±0.4	-1.87 (NGP)	10.6/4.3	-6.7/-6.4	6.92/5.64	$1.13\cdot 10^{11}$	3.9/1.9	-6.7/-5.9	6.19/584	$1.92\cdot 10^{10}$	ISM
HD 125162	-10.1±1.5	-6.64 (NGP)					1.9/¡1.0	17.8/-	3.41/-	$9.36\cdot 10^{9}$	ISM
HD 131488	4.8±0.2	-23.91 (G)	23.0/8.7	-0.8/2.5	21.09/12.1	$2.46\cdot 10^{11}$	33.5/30.1	5.4/5.7	6.18/6.03	$4.83\cdot 10^{11}$	CS
							7.3/¡5.0	-13.8/-	8.94/-	$8.23\cdot 10^{10}$	
HD 131835	2.7±2.5	18.56 (Gem)	8.3/4.1	-14.5/-13.8	7.40/7.50	$8.88\cdot 10^{10}$	41.0/32.0	-11.8/-12.4	11.52/11.73	$4.34\cdot 10^{11}$	?
		-27.63 (NGP)	2.1/1.4	-5.9/-4.8	7.91/7.68	$2.25\cdot 10^{10}$					
			0.7/¡0.1	2.2/-	2.3/-	$7.49\cdot 10^{9}$					
HD 138629	-18.7±1.1	-18.29 (NGP)	47.5/36.5	-13.8/-13.9	5.41/5.05	$9.39\cdot 10^{11}$	14.7/5.8	-11.9/-11.3	4.95/4.22	$7.24\cdot 10^{10}$	CS+ISM
			53.4/32.8	-22.9/-22.8	8.20/7.77	$1.07\cdot 10^{12}$	83.7/72.0	-21.6/-21.3	5.21/4.94	$9.16\cdot 10^{11}$	
			105.8/84.8	-31.8/-31.8	8.71/8.29	$2.18\cdot 10^{12}$	30.2/26.5	-16.7/-16.5	4.18/4.54	$3.25\cdot 10^{11}$	
HD 138813	0.3±2.1	-27.82 (G)	5.6/1.4	-27.5/-27.8	18.70/6.87	$5.99\cdot 10^{10}$	5.9/3.2	-22.2/-21.7	11.62	$6.92\cdot 10^{10}$	ISM
		-24.16 (Gem)					20.1/11.1	-12.1/-11.8	5.28	$2.36\cdot 10^{11}$	
							-7.55/-5.2	0.2/0.6	10.04	$6.59\cdot 10^{10}$	
HD 142097	-7.0±2.0	-28.67 (G)	24.2/14.0	-16.8/-15.4	8.41/8.50	$5.32\cdot 10^{11}$	263.9/231.9	-16.7/-16.4	12.83/12.11	$3.11\cdot 10^{12}$	ISM
							82.9/59.8	-7.5/-6.8	6.78/6.20	$7.32\cdot 10^{11}$	
HD 142315	-4.0±2.4	-28.64 (G)	26.5/6.3	-15.0/-12.7	14.05/9.79	$2.99\cdot 10^{11}$	255.1/194.9	-13.2/-12.8	12.78/12.22	$2.30\cdot 10^{12}$	ISM
			2.6/¡1.5	-23.6/-	3.45/-	$2.93\cdot 10^{10}$	5.5/5.3	-16.9/-16.7	2.21/2.06	$1.48\cdot 10^{11}$	
			6.8/7.0	-28.0/-22.9	9.55/9.00	$7.67\cdot 10^{10}$					
HD 142705	-5.6±3.0	-28.66 (G)	11.1/6.1	-30.8/-30.8	7.39/6.78	$2.84\cdot 10^{11}$	19.7/12.6	-31.3/-31.1	4.9/4.71	$1.77\cdot 10^{11}$	ISM
			40.5/19.9	-17.1/17.2	12.45/11.15	$4.33\cdot 10^{11}$	256.4/225.6	-16.2/-16.2	11.8/10.89	$3.02\cdot 10^{12}$	
HD 144587	-10.7±4.7	-28.81 (G)	11.6/5.1	-7.4/-9.6	6.2/4.52	$1.24\cdot 10^{11}$	122.4/97.7	-9.3/-9.4	7.75/7.43	$1.16\cdot 10^{12}$	ISM

Continued on next page

Table A.3 – continued from previous page

Star	V_{rad}	V_{ISM}	Ca II K/H				Na I D2/D1				Origin
			EW	RV	FWHM	N	EW	RV	FWHM	N	
	(km/s)	(km/s)	(*m*Å)	(km/s)	(km/s)	(cm^{-2})	(*m*Å)	(km/s)	(km/s)	(cm^{-2})	
			12.0/¡6.0	-20.7/-	8.5/-	$1.28\cdot 10^{11}$	46.1/30.5	-22.3/-22.1	5.77/5.58	$4.06\cdot 10^{11}$	
HD 144981	-5.6±4.3	-29.16 (G)	39.9/19.5	-8.7/-8.7	8.90/8.33	$4.27\cdot 10^{11}$	215.7/184.6	-8.5/-8.1	10.59/9.45	$2.31\cdot 10^{12}$	ISM
			6.2/¡3.0	-27.9/-	10.68/-	$6.64\cdot 10^{10}$					
HD 145554	-7.8±3.9	-29.2 (G)	5.6/¡3.0	-26.8/-	7.95/-	$5.99\cdot 10^{10}$	46.2/32.9	-25.2/-25.0	4.50/4.5	$4.04\cdot 10^{11}$	ISM
			42.3/24.7	-9.8/-9.8	5.79/5.25	$9.16\cdot 10^{11}$	154.3/138.3	-10.5/-10.1	7.45/6.94	$2.02\cdot 10^{12}$	
HD 145631	-5.7±2.3	-29.21 (G)	35.1/24.9	-8.6/-8.7	5.14/4.46	$6.68\cdot 10^{11}$	162.7/139.9	-9.5/-9.1	7.75/7.03	$1.78\cdot 10^{12}$	ISM
			9.8/¡1.8	-27.3/-	15.44/-	$1.05\cdot 10^{11}$	28.7/17.6	-25.0/-24.7	4.51/4.66	$2.70\cdot 10^{11}$	
HD 145964	-6.8±3.1	-29.14 (G)	9.9/2.5	-26.7/-26.5	12.38/7.00	$1.06\cdot 10^{11}$	55.5/41.5	-22.5/-22.2	4.98/5.03	$4.97\cdot 10^{11}$	CS
			4.6/1.6	-9.4/-9.8	5.55/5.46	$4.92\cdot 10^{10}$	60.6/86.8	-9.5/-9.3	4.98/4.92	$5.42\cdot 10^{11}$	
HD 145689	-7.1±1.7	-17.21 (G)	4.1/¡0.5	-11.9/-	10.3/-	$4.39\cdot 10^{10}$					CS
HD 146606	-2.3±1.3	-28.52 (G)	7.5/¡2.5	-27.1/-	11.5/-	$8.03\cdot 10^{10}$	9.8/5.9	-21.6/-21.7	7.82/9.23	$1.57\cdot 10^{11}$	ISM
							4.8/2.8	-7.8/-7.3	8.56/9.18	$8.36\cdot 10^{10}$	
HD 146897	-3.1±0.9	-29.19 (G)	11.2/¡0.9	-8.3/-	5.36/-	$1.20\cdot 10^{11}$	118.2/80.0	-9.4/-9.0	7.93/7.72	$1.06\cdot 10^{12}$	ISM
			5.5/¡0.9	-29.5/-	8.58/-	$5.89\cdot 10^{10}$					
HD 147137	-6.6±-1.9	-29.12 (G)	22.6/14.1	-8.5/-8.7	7.78/10.1	$4.47\cdot 10^{11}$	154.4/145.1	-8.6/-8.3	8.34/8.42	$5.00\cdot 10^{12}$	ISM
							8.5/6.2	-23.7/-23.9	6.24/6.85	$7.53\cdot 10^{10}$	
HD 147220	-49.3±2.0	-29.16 (G)	62.3/34.5	-19.1/-15.0	17.21/19.49	$1.56\cdot 10^{12}$	59.5/34.8	-20.9/-20.6	11.76/12.1	$5.93\cdot 10^{11}$	ISM
							135.2/126.3	-8.9/-8.7	7.50/7.4	$3.31\cdot 10^{12}$	
HD 148283	-0.5±0.2	-18.54 (NGP)	203.1*/198.2*	1.3/1.6	91.50/90.12	$1.47\cdot 10^{13}$	84.0/33.5	3.6/3.4	34.63/23.51	$4.14\cdot 10^{11}$	CS
HD 156623	-0.2±2.1	-24.89 (G)	9.0/3.7	-15.0/-16.4	18.72/8.79	$9.63\cdot 10^{10}$	-10.6/-8.5	-1.8/0.5	13.66/17.66	$1.01\cdot 10^{11}$	CS+ISM
			4.3/¿2.0	8.1/-	6.00	$4.60\cdot 10^{10}$					
HD 158352	-33.9±0.6		8.6/8.3	-24.7/-25.2	3.56/5.1	$5.26\cdot 10^{12}$	14.5/7.8	-25.0/-24.9	4.43/4.37	$1.96\cdot 10^{11}$	CS+ISM?
			20.5/6.5	-28.9/-32.2	13.17/12.30	$2.19\cdot 10^{11}$	3.5/2.6	-30.2/-31.7	9.58/12.62	$3.14\cdot 10^{10}$	
HD 168646	-10.8±2.6	-31.44 (Aql)	315.4*/252.9	-7.3/-6.6	16.07/17.00	$6.51\cdot 10^{12}$	156.6/154.5	-4.8/-4.5	8.98/8.59	$2.40\cdot 10^{12}$	CS
							7.7/¡3.0	11.1/-	11.51/-	$3.79\cdot 10^{10}$	
							24.7/12.4	-21.1/-19.9	17.84/-14.77	$1.36\cdot 10^{12}$	
HD 172555	1.2±2.9	-16.84 (G)	6.1/3.0	2.3/3.1	6.8/4.94	$6.53\cdot 10^{10}$	8.0/¡1.0	15.4/-	28.03/-	$3.94\cdot 10^{10}$	CS+ISM
			1.5/¡1.0	-19.9/-	9.5/-	$1.61\cdot 10^{10}$	3.2/1.78	-20.4/-20.3	9.78/8.88	$3.60\cdot 10^{10}$	
HD 177724	-27.3±2.5	-21.03 (G)	3.4/1.9	-25.7/-25.6	15.02/15.2	$8.25\cdot 10^{10}$					?
		-30.96 (Aql)									
HD 181296	-0.3±1.9		3.9/2.2	-22.8/-22.7	8.40/9.45	$1.06\cdot 10^{11}$	4.0/¡0.4	-22.9/-	9.34/-	$1.97\cdot 10^{10}$	CS
HD 182919	-24.3±1.4	-18.05 (G)	2.8/2.6	-18.5/-18.9	5.98/10.5	$1.22\cdot 10^{11}$	1.8/0.7	-15.5/-15.5	7.13/5.81	$8.87\cdot 10^{9}$	CS+ISM
		-24.21 (Mic)									
		-26.30 (Aql)									
HD 188228	-6.0±3.5	-12.18 (G)	1.3/¡0.5	-13.9/-	8.24/-	$3.43\cdot 10^{10}$	3.2/¡1.5	-13.9/-	8.26/-	$1.58\cdot 10^{10}$	ISM
		-15.57 (Vel)									
HD 192518	8.1±0.3	-20.08 (Mic)	6.2/4.1	-14.1/-13.5	5.20/6.37	$6.64\cdot 10^{10}$	39.3/26.8	-14.6/-14.5	4.64/4.54	$3.44\cdot 10^{11}$	CS+ISM
		-15.53 (Aql)	267.0*/363.7	12.0/11.7	10.68/20.87	$9.69\cdot 10^{12}$					
HD 196724	-10.8±2.3	-13.52 (Eri)	4.3/1.4	-11.7/-12.5	5.03/4.62	$3.10\cdot 10^{10}$					?

Continued on next page

Table A.3 – continued from previous page

Star	V_{rad}	V_{ISM}	Ca II K/H				Na I D2/D1				Origin
			EW	RV	FWHM	N	EW	RV	FWHM	N	
	(km/s)	(km/s)	(mÅ)	(km/s)	(km/s)	(cm^{-2})	(mÅ)	(km/s)	(km/s)	(cm^{-2})	
		-9.93 (Aql)									
HD 198160	-16.2±1.9	-17.42 (Vel)	3.9/¡1.5	-14.7/-	13.96/-	$4.17\cdot 10^{10}$	1.2/¡0.5	-16.4/-	6.78/-	$5.70\cdot 10^{9}$	ISM
HD 198161	-13.5±3.6	-17.41 (Vel)	3.8/¡1.5	-14.9/-	11.24/-	$4.07\cdot 10^{10}$	3.4/1.0	-21.9/-18.7	18.48/3.8	$1.67\cdot 10^{10}$	ISM
HD 210418	-5.1±0.8	-5.49 (LIC)	3.0/¡1.5	-4.8/-	12.29/-	$3.21\cdot 10^{10}$					?
HD 217782	5.1±1.1	7.63 (Hyades)	20.4/10.7	-9.2/-9.4	5.92/5.51	$7.05\cdot 10^{11}$	53.9/36.1	-8.9/-8.6	4.80/4.64	$4.75\cdot 10^{11}$	CS
			11.0/5.5	-17.1/-17.0	7.58/7.04	$1.18\cdot 10^{11}$	10.6/6.2	-16.4/-16.1	7.71/9.18	$1.08\cdot 10^{11}$	
			5.5/2.2	5.2/5.3	10.55/7.6	$5.89\cdot 10^{10}$					
HD 221756	13.5±0.3	5.88 (LIC)	6.3/2.63	-4.7/-4.8	6.12/5.92	$6.74\cdot 10^{10}$	17.9/9.21	-2.6/-2.4	5.96/5.78	$3.70\cdot 10^{12}$	ISM
		9.00 (Hyades)									
HD 224392	9.9±2.3	-0.86 (Vel)	8.2/3.9	-1.5/-3.5	11.37/6.56	$8.78\cdot 10^{10}$	2.9/1.6	-8.1/5.59	15.80/12.81	$3.23\cdot 10^{10}$	?

Appendix B

Field Stars

This section provides information on non-photospheric absorption features of field stars around HD 131488, HD 131835, HD 138813, and HD 146897. These four stars were selected due to the ambiguous origin of their non-photospheric absorptions. The data are based on a search of stars in a field of 5deg in radius around each of the four stars, and parallaxes between 6 and 10 mas, so that the field stars are located at comparable distances of the cold-gas-bearing debris-disc stars. We recall that they are members of the Scorpius-Centaurus OB association. Spectra of the field stars have been retrieved from the ESO archive of FEROS[1], HARPS[2] and UVES[3], as well as our own observations in the case of HD 146897. Field stars around each debris-disc star, their angular distances, stellar radial velocities, and velocities of non-photospheric features are given in Tables A.1 to A.4.

HD 131488. The field stars HD 132058, HD 133937, and HD 135454 have features at $\sim$ –20 km/s (Table A.1), relatively close in velocity to the velocity vectors of the G and Mic clouds in the Colorado model. HD 128207, HD 131120, HD 132094, and HD 133880 have a common feature at $\sim$ –13 km/s, suggesting it is an interstellar absorption not traced in the Colorado model. The star HD 132200 presents two features at –6.9 km/s and 4.6 km/s, which are close to the ones observed in HD 131488 at –3.2 km/s and 4.0 km/s. The HD 132200 feature at -6.9 km/s remains practically constant. This absorption, and the -3.2 km/s of our debris-disc star, are close to the mean velocity of $\sim$ – 6.6 km/s that characterise the approaching face of the bubble around the OB association (Pöppel et al., 2010). Thus, they could have an ISM origin. At the same time, the HD 132200 4.6 km/s feature varies significantly (Fig. A.1), which suggests it is related to the star. This fact also suggests that the 4.0 km/s absorption in HD 131488, which coincides with the stellar radial velocity, is likely circumstellar.

HD 131835. All field stars, as well as HD 131835, share the $\sim$ –13.0 km/s feature mentioned above (Table A.2), which likely has an ISM origin. One of the field stars, HD 132955, presents a second, strong feature at $\sim$ 3.8 km/s. Our star, HD 131835, also has a very weak (requiring confirmation) 2.2 km/s feature at the stellar radial velocity. If real, its CS or ISM origin is ambiguous. None of the field stars have a feature close to the one at -5.9 km/s of HD 131835. This absorption might correspond to

[1] http://archive.eso.org/wdb/wdb/adp/phase3_spectral/ form?collection_name=FEROS
[2] http://archive.eso.org/wdb/wdb/eso/repro/form
[3] http://archive.eso.org/wdb/wdb/eso/uves/form

Table B.1: HD 131488: field stars

Star	r (deg.)	v_{rad} (km/s)	v_{CaIIK} (km/s)
HD 131488		5.8	–3.2/4.0
HD 128207	3.60	2.0	–13.0
HD 131120	3.35	6.1	–16.0
HD 132058	2.11	0.2	–19.1
HD 132094	3.81	0.9	–11.4
HD 132200	1.24	8.0	–6.9/4.6
HD 133880	2.53	2.8	–13.0
HD 133937	3.06	2.0	–21.4
HD 135454	4.20	1.4	–24.4

the one at –6.6 km/s which characterises the mentioned bubble of the OB association.

Table B.2: HD 131835: field stars.

Star	r (deg.)	v_{rad} (km/s)	v_{CaIIK} (km/s)
HD 131835		2.6	-13.8/-5.9/2.2
HD 131120	2.26	6.1	–16.0
HD 132094	1.69	0.9	–11.4
HD 132955	3.30	9.5	–13.7/3.8

HD 138813. Like HD 138813, all field stars show a non-photospheric absorption Na I D2 at ~ -13 km/s (Table A.3), strongly suggesting an ISM origin.

HD 146897. Absorption features at velocities close to the ones of HD 146897 are detected in the Ca II and/or Na I lines of the field stars (Table A.4). This suggests an ISM origin for the HD 146897 non-photospheric absorptions.

Table B.3: HD 138813: field stars.

Star	r (deg.)	v_{rad} (km/s)	v_{NaID2} (km/s)
HD 138813		–0.4	-12.0
HD 141637	3.54	–3.0	–13.3/-8.7
HD 136246	4.16	-2.7	–16.0
HD 142301	4.40	-8.7	–14.3
HD 142184	4.58	-9.2	–13.3
HD 142250	4.59	–1.3	–12.8

Table B.4: HD 146897: field stars.

Star	r (deg.)	v_{rad} (km/s)	v_{CaIIK} (km/s)	v_{NaID2} (km/s)
HD 146897		–4.0	–30.0,–8.0	-8.8
HD 144587	3.76	0.0	–	–22.5,–9.2
HD 145554	2.47	–6.1	–25.9,–9.2	–25.5,–10.2
HD 145631	2.47	–5.6	–27.5,–9.2	–25.5,–10.2
HD 145964	1.20	–7.8	–25.2,-9.2	–22.5,–9.2
HD 147137	1.23	–0.8	–9.2	–8.7
HD 147932	2.45		–8.4	–9.5

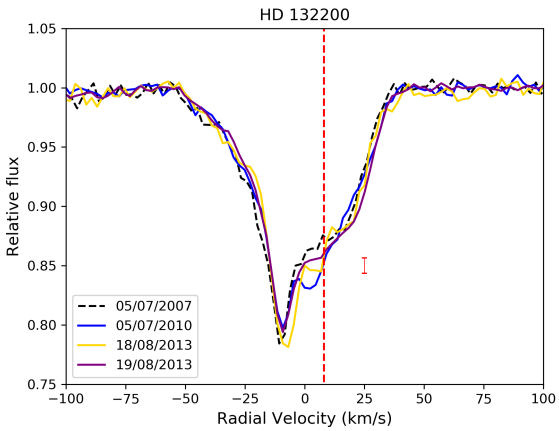

Figure 1: Ca II K line profiles of HD 132200. Solid lines are for FEROS spectra and the dashed line is for a HARPS spectrum. Observing dates are indicated. Vertical red dashed line indicates the radial velocity of the star. A 3-σ error bar is plotted in red.

Appendix C

Binary nature of HR 10:Tables

Table C.1: Spectroscopic observations of HR 10.

Dedicated spectroscopic campaigns.

Dates	N	Resolution	Spectral range (nm)	Telescope / Observatory Spectrograph
2015-09 04-07 2015-12 20-23 2016-07 12	17 8 1	85 000	377 – 900	1.2-m Mercator Telescope / La Palma High Efficiency & Resolution Mercator Echelle Spectrograph (HERMES)
2015-10 22-23	3	48 000	350 – 920	2.2-m ESO-MPIA Telescope / La Silla Fibre-fed Extended Range Optical Echelle Spectrograph (FEROS)
2017-10-05 to 2018-01-03	10	67 000	370 – 910	2.5-m Nordic Optical Telescope (NOT) / La Palma FIbre-fed Echelle Spectrograph (FIES)
2018-11-23 to 2019-01-08	12			
2017-10-06 to 2018-01-02	21	115 000	383 – 693	3.6-m Telescopio Nazionale Galileo (TNG) / La Palma High Accuracy Radial velocity Planet Searcher North (HARPS-N)
2017-07-21 to 2017-12-30	21	94 600 (VIS) 80 400 (NIR)	520- 960 960–1710	3.5-m CAHA Telescope/Calar Alto Calar Alto high-Resolution search for M dwarfs with Exoearths with Near-infrared and optical Echelle Spectrographs (CARMENES)

Note: Dates of the specific nights of the campaigns are given in Table C.2. Data from CARMENES will be used in a forthcoming paper.

Observations extracted from publications or archives.

Dates	N	Resolution	Spectral range (line or nm)	Telescope / Observatory Spectrograph	Ref.
1986-08-15	1	60 000	Ca II K	1.4-m Coudé Auxiliary Telescope (CAT) / La Silla	1
1998-10-15	1	100 000		ESO Coudé Echelle Spectrometer (CES)	
1996-11-30	1	1 000 000	Ca II K	3.6-m Telescope / Anglo Australian Observatory	2
1997-06-20	1			Ultra High Resolution Facility (UHRF)	2
2005-06-15	1				3
1998-10-25	1	49 000	380 – 590	4.2-m William Herschel Telescope / La Palma	4
1999-01-28	1			Utrech Echelle Spectrograph (UES)	
2004-08-28	1	240 000	Ca II K	2.7-m Harlan J. Smith Telescope / McDonald Observatory	3
2004-08-29	1			Cross-Dispersed Echelle Spectrometer (CS21)	
2005-09-15	1				
2007-06-28	14	60 000	360 – 450 460 – 670	8-m ESO–Very Large Telescope / Paranal	ESO
2007-07-11	6				
2007-07-15	14			Ultraviolet and Visual Echelle Spectrograph (UVES)	Archive
2007-07-26	34				
2007-07-27	6				
2010-09-01	3		336 – 810	10-m Keck I Telescope/ Hawaii	Keck
2011-12-08	3			High Resolution Echelle Spectrometer (HIRES)	Archive
2015-01-18	1	120 000	378 – 691	3.6-m ESO Telescope / La Silla	ESO
2015-01-19	2				
2015-01-20	1			High Accuracy Radial velocity Planet Searcher (HARPS)	Archive
2015-01-21	2				

Notes: "N" is the number of spectra. References: (1) Lagrange-Henri et al. (1990a), (2) Welsh et al. (1998), (3) Redfield et al. (2007), (4) EXPORT La Palma International Time campaigns, Mora et al. (2001).

Table C.2: Radial velocities (RV) and velocity dispersions (b) of the deep 'D' and shallow 'S' components of the CS Ca II K absorptions. For those cases when a four-Gaussian fit was feasible, the parameters of the weak 'd' and 's' components that appear redshifted with respect to D and S, respectively, are also given.

Date	N	BJD (TDB) (days)	Component								Instrument
			D		S		d		s		
			RV (km/s)	b (km/s)	RV (km/s)	b (km/s)	RV (km/s)	b (km/s)	RV (km/s)	b (km/s)	
1986-08-15	1	2446657.5000	-8.66 ± 2.00	10.1	$+9.38 \pm 2.00$	9.0					CES
1988-10-15	1	2447449.5000	-4.49 ± 2.00	9.8	$+5.83 \pm 2.00$	10.3					CES
1996-11-30(†)	1	2450417.5022	-10.40 ± 2.00	2.1	$+7.40 \pm 2.00$	3.8					UHRF
1997-06-20(†)	1	2450619.5011	$+9.20 \pm 2.00$	3.0	-16.60 ± 2.00	2.6	$+16.20 \pm 2.00$	4.5			UHRF
1998-10-25	1	2451112.4652	-16.03 ± 2.00	10.0	$+10.00 \pm 2.00$	10.0	-6.51 ± 3.00	13.7	$+20.01 \pm 3.00$	9.8	UES
1999-01-28	1	2451207.3363	-8.78 ± 2.00	10.0							UES
2004-08-28 2004-08-29	2	2453246.3741	-17.33 ± 2.00	8.5:	$+13.80 \pm 2.00$	7.9:					CS21
2004-10-19	1	2453297.7801	-14.77 ± 2.00								CS21
2005-06-15	1	2453537.3058	-2.10 ± 2.00	12.3:							UHRF
2005-09-15	1	2453628.8717	$+9.32 \pm 2.00$	14.7	-17.38 ± 2.00	16.3:			-4.43 ± 2.00	7.4	CS21
2007-06-28	14	2454279.8221	-0.59 ± 1.50	7.8	-4.40 ± 1.50	7.0					UVES
2007-07-11	6	2454292.8971	$+0.31 \pm 1.50$	6.2	-6.04 ± 1.50	4.6					UVES
2007-07-15	14	2454296.9144	$+0.91 \pm 1.50$	6.4	-6.07 ± 1.50	6.0					UVES
2007-07-26	34	2454307.7830	$+1.27 \pm 1.50$	7.5	-8.96 ± 1.50	8.0					UVES
2007-07-27	6	2454308.7539	$+2.18 \pm 1.50$	8.0	-7.82 ± 1.50	8.0					UVES
2010-09-01	1	2455441.1252	-14.33 ± 1.50	10.5	$+14.05 \pm 1.50$	9.8	-4.01 ± 2.00	8.4	$+18.73 \pm 2.00$	10.4	HIRES
2011-12-08	1	2455903.7969	$+15.17 \pm 1.50$	8.0	-24.10 ± 1.50	10.4	$+23.67 \pm 2.00$	10.2	-4.97 ± 2.00	8.0	HIRES
2015-01-18	1	2457041.4530	-14.41 ± 1.50	8.2	$+14.05 \pm 1.50$	11.0	-4.00 ± 2.00	9.4	$+24.10 \pm 2.00$	9.8	HARPS
2015-01-19	2	2457042.4529	-14.45 ± 1.50	8.0	$+14.15 \pm 1.50$	11.4	-6.24 ± 2.00	10.2	$+23.30 \pm 2.00$	10.0	HARPS
2015-01-20	1	2457043.4527	-14.41 ± 1.50	8.8	$+13.65 \pm 1.50$	11.0	-1.99 ± 2.00	11.0	$+23.28 \pm 2.00$	9.7	HARPS
2015-01-21	2	2457044.4527	-14.58 ± 1.50	8.4	$+14.22 \pm 1.50$	11.0	-3.99 ± 2.00	10.3	$+23.03 \pm 2.00$	11.0	HARPS
2015-09-04 2015-09-07	17	2457271.0769	$+0.08 \pm 1.50$	9.4	-7.36 ± 1.50	13.1	$+10.31 \pm 2.00$	15.8	$+5.95 \pm 2.00$	11.1	HERMES
2015-10-22 2015-10-23	3	2457318.1488	$+5.41 \pm 1.50$	9.2	-14.88 ± 1.50	9.4	$+14.78 \pm 2.00$	19.9:	-3.22 ± 2.00	19.7:	FEROS
2015-12-20	3	2457377.3295	$+12.22 \pm 1.50$	10.5	-19.22 ± 1.50	11.9	$+24.37 \pm 2.00$	10.2	-3.02 ± 2.00	13.0	HERMES
2015-12-22	2	2457379.3572	$+13.03 \pm 1.50$	9.5	-22.19 ± 1.50	13.6	$+25.85 \pm 2.00$	11.0	-4.11 ± 2.00	8.8	HERMES
2015-12-23	3	2457380.3501	$+13.12 \pm 1.50$	9.6	-21.28 ± 1.50	10.0	$+27.98 \pm 2.00$	11.0	-5.80 ± 2.00	14.0	HERMES
2016-07-12	1	2457581.7080	-0.63 ± 1.50	7.1	-5.95 ± 1.50	6.1					HERMES
2017-10-05	1	2458031.5276	$+1.84 \pm 1.50$	9.0	-6.05 ± 1.50	19.4					FIES
2017-10-06	1	2458032.5772	$+1.80 \pm 1.50$	7.7	-6.36 ± 1.50	13.3					HARPS-N
2017-10-12	2	2458038.5469	$+2.07 \pm 1.50$	7.9	-7.69 ± 1.50	11.5					HARPS-N

Table C.2 – continued from previous page

Date	N	BJD (TDB) (days)	Component								Instrument
			D		S		d		s		
			RV (km/s)	b (km/s)	RV (km/s)	b (km/s)	RV (km/s)	b (km/s)	RV (km/s)	b (km/s)	
2017-10-17	1	2458043.5495	$+3.00 \pm 1.50$	9.9	-9.46 ± 1.50	14.5					FIES
2017-10-23 2017-10-24	2	2458050.4980	$+3.18 \pm 1.50$	4.8	-9.12 ± 1.50	13.2	$+15.99 \pm 2.00$	15.7	$+4.14 \pm 2.00$	12.1	HARPS-N
2017-10-29	1	2458056.3919	$+4.40 \pm 1.50$	9.5	-9.74 ± 1.50	15.5					FIES
2017-10-29	2	2458056.4748	$+4.26 \pm 1.50$	5.4	-9.57 ± 1.50	17.0:	$+16.02 \pm 2.00$	20.5:	$+4.47 \pm 2.00$	16.1:	HARPS-N
2017-11-09	1	2458067.4778	$+5.15 \pm 1.50$	11.9	-11.31 ± 1.50	13.9					FIES
2017-11-18	2	2458076.3180	$+6.38 \pm 1.50$	9.6	-15.05 ± 1.50	13.2	$+20.01 \pm 2.00$	14.1	-5.61 ± 2.00	10.0	HARPS-N
2017-11-28	1	2458086.4462	$+8.32 \pm 1.50$	10.4	-14.88 ± 1.50	11.4	$+20.62 \pm 2.00$	10.0	-2.61 ± 2.00	12.1	FIES
2017-12-01	1	2458089.4417	$+8.48 \pm 1.50$	9.2	-15.91 ± 1.50	10.5	$+18.97 \pm 2.00$	13.2	-2.84 ± 2.00	13.8	FIES
2017-12-03	2	2458091.3887	$+8.71 \pm 1.50$	9.1	-15.84 ± 1.50	11.0	$+20.45 \pm 2.00$	11.3	-3.97 ± 2.00	9.6	HARPS-N
2017-12-06	1	2458094.4387	$+9.46 \pm 1.50$	10.9	-15.10 ± 1.50	12.2	$+23.01 \pm 2.00$	10.0	-3.00 ± 2.00	10.9	FIES
2017-12-09	2	2458097.3047	$+8.99 \pm 1.50$	7.9	-16.55 ± 1.50	13.6	$+19.03 \pm 2.00$	10.4	-1.95 ± 2.00	11.8	HARPS-N
2017-12-15	2	2458103.3163	$+10.29 \pm 1.50$	9.5	-17.72 ± 1.50	10.8	$+22.45 \pm 2.00$	11.0	-3.09 ± 2.00	11.5	HARPS-N
2017-12-18	1	2458106.3321	$+10.02 \pm 1.50$	9.0	-17.03 ± 1.50	12.9	$+18.61 \pm 2.00$	13.1	-1.62 ± 2.00	11.4	FIES
2017-12-21	2	2458109.3041	$+10.67 \pm 1.50$	9.0	-19.01 ± 1.50	11.6	$+21.65 \pm 2.00$	7.0	-4.00 ± 2.00	8.5	HARPS-N
2017-12-22	1	2458110.3674	$+11.18 \pm 1.50$	9.8	-16.14 ± 1.50	15.8	$+20.87 \pm 2.00$	9.8	-0.36 ± 2.00	12.3	FIES
2017-12-27	2	2458115.3078	$+11.39 \pm 1.50$	7.2	-19.69 ± 1.50	11.2	$+20.05 \pm 2.00$	12.2	-6.82 ± 2.00	7.0	HARPS-N
2018-01-02	2	2458121.3055	$+12.71 \pm 1.50$	7.3	-21.15 ± 1.50	12.1	$+21.05 \pm 2.00$	10.1	-2.91 ± 2.00	9.0	HARPS-N
2018-01-03	1	2458122.3461	$+12.85 \pm 1.50$	9.6	-18.89 ± 1.50	10.5	$+22.02 \pm 2.00$	10.0	-7.52 ± 2.00	10.0	FIES
2018-11-23	1	2458446.4436	-15.08 ± 1.50	10.0	$+12.90 \pm 1.50$	12.5	-3.00 ± 2.00	10.1	$+20.49 \pm 2.00$	10.0	FIES
2018-11-26	1	2458449.3208	-14.90 ± 1.50	10.0	$+14.01 \pm 1.50$	8.0	-5.88 ± 2.00	10.0	$+24.75 \pm 2.00$	7.8	FIES
2018-12-01	1	2458454.3734	-14.82 ± 1.50	9.8	$+13.23 \pm 1.50$	14.5	-6.21 ± 2.00	10.2	$+21.79 \pm 2.00$	8.7	FIES
2018-12-07	1	2458460.3696	-15.12 ± 2.00	10.3:	$+12.52 \pm 2.00$	17.3:			$+21.66 \pm 3.00$	21.7:	FIES
2018-12-10	1	2458463.4205	-15.29 ± 1.50	10.0	$+14.43 \pm 1.50$	8.0	-4.01 ± 2.00	10.0	$+22.01 \pm 2.00$	10.0	FIES
2018-12-22	1	2458475.3701	-15.09 ± 1.50	10.7	$+14.35 \pm 1.50$	8.1			$+22.37 \pm 2.00$	10.6	FIES
2018-12-24	1	2458477.3687	-14.26 ± 1.50	10.7:							FIES
2018-12-26	1	2458479.3677	-14.69 ± 1.50	10.1	$+14.39 \pm 1.50$	8.0	-2.37 ± 2.00	10.9	$+22.01 \pm 2.00$	9.0	FIES
2018-12-27	1	2458480.3449	-15.53 ± 1.50	10.0	$+15.27 \pm 1.50$	9.3	-5.03 ± 2.00	10.5	$+22.25 \pm 2.00$	8.9	FIES
2019-01-02	1	2458486.3505	-14.80 ± 1.50	9.6	$+16.06 \pm 1.50$	8.2	-5.28 ± 2.00	10.0	$+24.16 \pm 2.00$	8.0	FIES
2019-01-06	1	2458490.3547	-14.84 ± 1.50	9.8	$+17.04 \pm 1.50$	8.5	-5.48 ± 2.00	12.4	$+22.01 \pm 2.00$	8.1	FIES
2019-01-08	1	2458492.3427	-14.15 ± 1.50	9.6	$+13.04 \pm 1.50$	7.9	-4.20 ± 2.00	9.9	$+22.95 \pm 2.00$	8.0	FIES

Notes: 'N' is the number of spectra. (†): Radial velocities and velocity dispersions for these two dates have been taken from Welsh et al. (1998), since the observations were not available for direct measurements following the same method used in this work. (:) Noisy spectra.

Appendix D

Observing Log

Star	Date (UT)	Instrument	Date (UT)	Instrument	Date (UT)	Instrument
HD 105 (108)	20151022T0403	FEROS	20151023T0354	FEROS	20151024T0421	FEROS
HD 203 (212)	20150803T0314	HEROS	20150803T0400	HEROS	20150804T0427	HEROS
	20150805T0311	HEROS	20150806T0230	HEROS	20150919T2344	HEROS
	20150920T2324	HEROS	20150923T2307	HEROS	20150924T2300	HEROS
	20151022T0401	FEROS	20151023T0338	FEROS	20151024T0428	FEROS
HR 10 (287)	20150904T0007	HERMES	20150904T0020	HERMES	20150904T0051	HERMES
	20150904T0217	HERMES	20150904T0336	HERMES	20150905T0012	HERMES
	20150905T0033	HERMES	20150905T0054	HERMES	20150905T0314	HERMES
	20150906T0024	HERMES	20150906T0045	HERMES	20150906T0353	HERMES
	20150906T0414	HERMES	20150907T0016	HERMES	20150907T0036	HERMES
	20150907T0257	HERMES	20150907T0317	HERMES	20151022T0402	FEROS
	20151023T0102	FEROS	20151023T0439	FEROS	20151220T1943	HERMES
	20151220T2004	HERMES	20151220T2025	HERMES	20151222T2034	HERMES
	20151222T2100	HERMES	20151223T1951	HERMES	20151223T2017	HERMES
	20151223T2145	HERMES	20160712T0447	HERMES		
HD 1466 (316)	20151023T0126	FEROS	20151023T0521	FEROS	20151024T0456	FEROS
κ Phe (247)	20151023T0112	FEROS	20151024T0517	FEROS		
HD 2884 (251)	20151023T0134	FEROS	20151023T0457	FEROS	20151024T0505	FEROS
	20170924T0543	FEROS				
HD 2885 (141)	20151023T0138	FEROS	20151023T0501	FEROS	20151024T0508	FEROS
HD 3003 (160)	20151023T0141	FEROS	20151024T0513	FEROS		
HD 5267 (419)	20160126T2012	FIES	20160127T1958	FIES	20160712T0427	HERMES
	20160713T0301	HERMES	20160714T0300	HERMES	20160715T0315	HERMES

Star	Date (UT)	Instrument	Date (UT)	Instrument	Date (UT)	Instrument
	20160717T0301	FIES	20160717T0516	FIES	20160718T0259	FIES
	20160718T0449	FIES	20160719T0258	FIES	20160719T0501	FIES
	20160720T0316	FIES	20170924T0513	FEROS	20170924T0701	FEROS
	20170926T0639	FEROS	20170927T0619	FEROS	20170930T0457	FEROS
	20171001T0435	FEROS				
HD 5448	20151220T1914	HERMES	20160126T2026	FIES	20160127T2011	FIES
(301)	20160713T0253	HERMES	20160714T0414	HERMES	20160717T0255	FIES
	20160718T0310	FIES	20160718T0509	FIES	20160719T0308	FIES
	20160720T0355	FIES				
κ Tuc	20151023T0146	FEROS	20151023T0704	FEROS	20151024T0501	FEROS
(381)						
49 Cet	20150904T0107	HERMES	20150904T0143	HERMES	20150904T0318	HERMES
(405)	20150904T0539	HERMES	20150905T0117	HERMES	20150905T0133	HERMES
	20150905T0335	HERMES	20150905T0523	HERMES	20150906T0126	HERMES
	20150906T0134	HERMES	20150906T0221	HERMES	20150906T0237	HERMES
	20150906T0529	HERMES	20150907T0113	HERMES	20150907T0129	HERMES
	20150907T0414	HERMES	20150907T0430	HERMES	20151220T2058	HERMES
	20151220T2119	HERMES	20151222T2135	HERMES	20151222T2201	HERMES
	20151222T2227	HERMES	20151223T2113	HERMES	20151223T2246	HERMES
	20160126T1956	FIES	20160126T2041	FIES	20160127T1936	FIES
	20160127T1945	FIES	20160127T1948	HERMES	20160127T2001	HERMES
	20160128T1928	HERMES	20160128T1941	HERMES	20160130T1958	HERMES
	20160130T2011	HERMES	20160714T0500	HERMES	20160715T0449	HERMES
	20160717T0506	FIES	20160718T0458	FIES	20160719T0448	FIES
	20170923T0919	FEROS				
τ Cet	20151023T0152	FEROS	20151023T0540	FEROS		
(481)						
HD 12039	20151023T0604	FEROS				
(453)						
HD 14055	20150831T0123	HEROS	20150831T0533	HEROS	20151024T2225	HEROS
(412)	20151025T2057	HEROS	20151027T2014	HEROS	20151028T0235	HEROS
	20160126T2033	FIES	20160127T2204	FIES	20160127T2207	FIES
	20160303T2020	HERMES	20160303T2024	HERMES	20160304T2018	HERMES
	20160304T2022	HERMES	20160305T2012	HERMES	20160306T2038	HERMES
	20160712T0505	HERMES	20160713T0506	HERMES	20160714T0351	HERMES
	20160715T0403	HERMES	20160717T0349	FIES	20160718T0359	FIES
	20160719T0404	FIES	20160720T0359	FIES		
HD 14412	20151023T0218	FEROS	20151023T0659	FEROS		
(401)						
HD 15115	20160126T2103	FIES	20160127T2134	FIES	20160717T0429	FIES
(166)	20160718T0418	FIES	20160719T0410	FIES		
HD 15257	20160126T2315	FIES	20160127T2217	FIES	20160127T2314	FIES
(149)	20160713T0418	HERMES	20160714T0421	HERMES	20160715T0411	HERMES
	20160717T0340	FIES	20160718T0326	FIES	20160719T0324	FIES
HD 16978	20151023T0229	FEROS	20151024T0534	FEROS	20170923T0845	FEROS
(309)	20170924T0534	FEROS	20170925T0654	FEROS		

Star	Date (UT)	Instrument	Date (UT)	Instrument	Date (UT)	Instrument
HR 1062	20150904T0301	HERMES	20150904T0518	HERMES	20150905T0254	HERMES
(257)	20150905T0504	HERMES	20150906T0317	HERMES	20150906T0332	HERMES
	20150906T0548	HERMES	20150907T0339	HERMES	20150907T0355	HERMES
	20151220T2142	HERMES	20151220T2203	HERMES	20151222T2336	HERMES
	20151224T0030	HERMES	20160127T2131	HERMES	20160128T2134	HERMES
	20160130T2109	HERMES				
HD 21620	20150904T0123	HERMES	20150904T0244	HERMES	20150905T0153	HERMES
(411)	20150905T0209	HERMES	20150905T0400	HERMES	20150906T0257	HERMES
	20150906T0607	HERMES	20150907T0149	HERMES	20150907T0204	HERMES
	20150907T0533	HERMES	20150907T0549	HERMES	20151220T2336	HERMES
	20151221T0002	HERMES	20151221T0253	HERMES	20151223T0005	HERMES
	20151223T0031	HERMES	20151224T0103	HERMES	20151224T0129	HERMES
	20160127T2147	HERMES	20160127T2355	HERMES	20160128T0030	HERMES
	20160128T2105	HERMES	20160128T2319	HERMES	20160130T2130	HERMES
	20160130T2320	HERMES	20160303T2106	HERMES	20160304T2116	HERMES
	20160305T2103	HERMES	20160306T2119	HERMES	20160714T0435	HERMES
	20160715T0425	HERMES	20160717T0442	FIES	20160718T0430	FIES
	20160719T0421	FIES	20160720T0453	FIES	20170306T1957	HERMES
	20170308T2024	HERMES	20170309T2044	HERMES	20170310T2046	HERMES
	20170311T1944	HERMES	20170313T2028	HERMES		
HD 21997	20150904T0503	HERMES	20150905T0422	HERMES	20150905T0443	HERMES
(594)	20150906T0448	HERMES	20150906T0508	HERMES	20150907T0451	HERMES
	20150907T0512	HERMES	20150919T0453	HEROS	20150920T0251	HEROS
	20150924T0340	HEROS	20150925T0311	HEROS	20150926T0440	HEROS
	20151023T0225	FEROS	20151023T0611	FEROS	20151024T0526	FEROS
	20151110T2302	HEROS	20151111T2230	HEROS	20151114T0058	HEROS
	20151114T2216	HEROS	20151220T2236	HERMES	20151220T2307	HERMES
	20151223T2320	HERMES	20160127T2016	HERMES	20160128T1956	HERMES
	20160130T2035	HERMES	20170923T0436	FEROS	20170923T0612	FEROS
	20170923T0859	FEROS	20170924T0522	FEROS	20170924T0810	FEROS
	20170925T0634	FEROS	20170926T0652	FEROS	20170926T0828	FEROS
	20170927T0631	FEROS	20170929T0505	FEROS	20170930T0505	FEROS
	20170930T0927	FEROS	20171001T0426	FEROS		
10 τ	20150919T0519	HEROS	20150920T0148	HEROS	20150924T0133	HEROS
(919)	20150925T0131	HEROS	20151023T0246	FEROS	20151109T2223	HEROS
	20151109T0111	HEROS	20151114T2100	HEROS	20151114T0130	HEROS
	20151221T0017	HERMES				
HD 27290	20151023T0359	FEROS	20151024T0538	FEROS	20160328T0051	FEROS
(199)						
B τ	20150930T0259	HEROS	20151001T0235	HEROS	20151003T0340	HEROS
(148)	20151004T0217	HEROS	20151209T2056	HEROS	20151209T0017	HEROS
	20151221T0035	HERMES				
HD 29391	20151023T0404	FEROS	20160127T0033	FIES		
(191)						
HD 30051	20151023T0416	FEROS	20160126T2240	FIES	20160127T2239	FIES
(291)	20160127T2324	FIES	20160328T0027	FEROS	20160329T0008	FEROS

Star	Date (UT)	Instrument	Date (UT)	Instrument	Date (UT)	Instrument
HD 31295	20151221T0049	HERMES	20151224T0142	HERMES	20160128T2254	HERMES
(209)	20160128T0034	HERMES	20160130T2159	HERMES		
HD 32297	20150904T0405	HERMES	20150904T0436	HERMES	20151221T0122	HERMES
(223)	20151221T0153	HERMES	20151221T0224	HERMES	20151223T0106	HERMES
	20151223T0136	HERMES	20151224T0215	HERMES	20151224T0246	HERMES
	20160126T2133	FIES	20160126T2205	FIES	20160127T2022	FIES
	20160127T2053	FIES	20160127T2216	HERMES	20160127T2246	HERMES
	20160128T2149	HERMES	20160128T2220	HERMES	20160130T2216	HERMES
	20160130T2247	HERMES	20170924T0726	FEROS	20170926T0704	FEROS
	20170926T0847	FEROS	20170927T0703	FEROS	20170927T0847	FEROS
	20170929T0740	FEROS	20170930T0705	FEROS	20170930T0825	FEROS
	20171001T0651	FEROS				
HD 35850	20151015T0217	HEROS	20151016T0230	HEROS	20151017T0545	HEROS
(190)	20151019T0440	HEROS	20151020T0246	HEROS	20151023T0619	FEROS
	20151210T0041	HEROS	20151210T0143	HEROS	20151210T0308	HEROS
	20151213T2132	HEROS	20151217T2152	HEROS	20151218T2157	HEROS
	20160127T0043	FIES	20160128T0054	FIES	20160329T0101	FEROS
HD 36546	20170306T2017	HERMES	20170307T1952	HERMES	20170307T2122	HERMES
(221)	20170308T1951	HERMES	20170309T2056	HERMES	20170310T2013	HERMES
	20170312T2003	HERMES	20170401T2046	HERMES		
HD 37286	20151023T0422	FEROS	20151024T0545	FEROS	20160329T0115	FEROS
(160)						
HD 37306	20151023T0751	FEROS	20151023T0831	FEROS	20160303T2040	HERMES
(441)	20160303T2218	HERMES	20160303T2239	HERMES	20160304T2043	HERMES
	20160304T2230	HERMES	20160304T2251	HERMES	20160305T2031	HERMES
	20160305T2227	HERMES	20160306T2059	HERMES	20160321T2023	FIES
	20160328T0036	FEROS	20160329T0017	FEROS	20170307T2047	HERMES
	20170308T2038	HERMES	20170309T2016	HERMES	20170310T2059	HERMES
	20170311T2053	HERMES	20170312T2128	HERMES	20170313T2051	HERMES
	20170923T0630	FEROS	20170923T0908	FEROS	20170924T0709	FEROS
	20170925T0711	FEROS	20170925T0719	FEROS	20170926T0743	FEROS
	20170927T0655	FEROS	20170930T0914	FEROS		
HD 38206	20151023T0428	FEROS	20151023T0757	FEROS	20160303T1955	HERMES
(353)	20160303T2009	HERMES	20160303T2129	HERMES	20160303T2142	HERMES
	20160304T1949	HERMES	20160304T2005	HERMES	20160304T2141	HERMES
	20160304T2154	HERMES	20160305T1953	HERMES	20160305T2157	HERMES
	20160306T2019	HERMES	20160326T0131	FEROS	20160328T0044	FEROS
	20160328T0128	FEROS	20160329T0026	FEROS	20160329T0124	FEROS
	20161230T0024	FIES	20170307T2103	HERMES	20170308T2100	HERMES
	20170309T2031	HERMES	20170310T2114	HERMES	20170311T2007	HERMES
	20170312T2036	HERMES	20170313T2005	HERMES		
HR 2025	20170307T2024	HERMES	20170307T2155	HERMES	20170308T2113	HERMES
(243)	20170309T2129	HERMES	20170310T2126	HERMES	20170311T2029	HERMES
	20170312T2054	HERMES	20170313T2119	HERMES	20170331T2037	HERMES
	20170403T2029	HERMES				

Star	Date (UT)	Instrument	Date (UT)	Instrument	Date (UT)	Instrument
ξ Aur	20170401T2007	HERMES	20170402T2007	HERMES		
(219)						
η Lep	20151015T0342	HEROS	20151016T0304	HEROS	20151017T0650	HEROS
(212)	20151019T0512	HEROS	20151023T0451	FEROS	20151210T0125	HEROS
	20151213T2157	HEROS	20151217T2217	HEROS	20151218T0306	HEROS
	20151223T0147	HERMES	20160328T0056	FEROS		
HD 42111	20150904T0528	HERMES	20150905T0542	HERMES	20150905T0558	HERMES
(446)	20151221T0321	HERMES	20151223T0215	HERMES	20151224T0314	HERMES
	20160128T2302	HERMES	20160128T0043	HERMES	20160130T2359	HERMES
	20160303T2159	HERMES	20160304T2210	HERMES	20160305T2131	HERMES
	20160305T2329	HERMES	20160306T2246	HERMES	20170308T2136	HERMES
	20170309T2152	HERMES	20170311T2110	HERMES	20170311T2128	HERMES
	20170312T2151	HERMES	20170313T2152	HERMES	20170329T2013	HERMES
	20170330T2009	HERMES	20170402T2017	HERMES	20170403T2012	HERMES
	20170404T0131	FEROS	20170405T0042	FEROS	20170406T0050	FEROS
	20170408T0101	FEROS	20170409T0050	FEROS		
HD 53842	20151023T0633	FEROS	20160328T0232	FEROS		
(102)						
HD 50241	20151023T0526	FEROS	20160326T0144	FEROS	20160326T0304	FEROS
(617)	20160326T0305	FEROS	20160327T0229	FEROS	20160327T0230	FEROS
	20160328T0102	FEROS	20160328T0159	FEROS	20160328T0322	FEROS
	20160329T0031	FEROS	20160329T0153	FEROS	20160329T0314	FEROS
	20170924T0806	FEROS				
HD 50571	20151023T0532	FEROS	20160326T0232	FEROS		
(165)						
λ Gem	20151221T0433	HERMES	20160131T0049	HERMES	20160328T0108	FEROS
(186)						
ϕ Gem	20170328T2002	HERMES	20170331T2012	HERMES	20170402T2028	HERMES
(238)						
HD 71043	20151023T0640	FEROS	20160326T0238	FEROS	20170923T0852	FEROS
(302)	20170924T0923	FEROS	20170925T0704	FEROS	20170927T0829	FEROS
HD 71722	20151023T0648	FEROS	20160326T0151	FEROS	20160326T0326	FEROS
(461)	20160326T0447	FEROS	20160327T0238	FEROS	20160327T0504	FEROS
	20160328T0118	FEROS	20160328T0332	FEROS	20160329T0041	FEROS
	20160329T0203	FEROS	20160329T0324	FEROS	20160329T0440	FEROS
HD 74873	20151221T0450	HERMES	20151221T0506	HERMES	20151224T0516	HERMES
(299)	20160129T0451	HERMES	20160131T0029	HERMES	20160304T0011	HERMES
	20160304T0027	HERMES	20160304T0203	HERMES	20160305T0020	HERMES
	20160305T0203	HERMES	20160305T2352	HERMES	20160306T0211	HERMES
	20160307T0052	HERMES				
67 Cnc	20170401T2020	HERMES	20170402T2041	HERMES		
(194)						
HR 3685	20160326T0156	FEROS	20160326T0157	FEROS	20160326T0331	FEROS
(738)	20160326T0332	FEROS	20160326T0541	FEROS	20160326T0542	FEROS
	20160327T0242	FEROS	20160327T0244	FEROS	20160327T0508	FEROS

Star	Date (UT)	Instrument	Date (UT)	Instrument	Date (UT)	Instrument
	20160327T0510	FEROS	20160328T0133	FEROS	20160328T0134	FEROS
	20160328T0336	FEROS	20160328T0338	FEROS	20160328T0537	FEROS
	20160328T0538	FEROS	20160329T0045	FEROS	20160329T0047	FEROS
	20160329T0208	FEROS	20160329T0209	FEROS	20160329T0330	FEROS
	20160329T0332	FEROS	20160329T0512	FEROS	20160329T0513	FEROS
	20170402T0048	FEROS	20170402T0049	FEROS	20170403T0100	FEROS
	20170403T0101	FEROS	20170405T0057	FEROS	20170405T0058	FEROS
	20170406T0035	FEROS	20170406T0037	FEROS	20170407T0157	FEROS
	20170407T0158	FEROS	20170408T0128	FEROS	20170408T0129	FEROS
HD 85905	20151221T0534	HERMES	20151221T0600	HERMES	20151223T0453	HERMES
(593)	20151223T0606	HERMES	20151223T0654	HERMES	20151224T0453	HERMES
	20151224T0558	HERMES	20151224T0701	HERMES	20160127T0340	FIES
	20160129T0314	HERMES	20160129T0357	HERMES	20160131T0157	HERMES
	20160131T0313	HERMES	20160303T2304	HERMES	20160303T2326	HERMES
	20160304T0050	HERMES	20160304T0116	HERMES	20160304T2315	HERMES
	20160304T2338	HERMES	20160305T0055	HERMES	20160305T0121	HERMES
	20160305T2300	HERMES	20160306T0051	HERMES	20160306T0122	HERMES
	20160306T2317	HERMES	20160306T2348	HERMES	20160307T0127	HERMES
	20170308T2148	HERMES	20170310T2144	HERMES	20170311T2147	HERMES
	20170311T2337	HERMES	20170312T0021	HERMES	20170329T2234	HERMES
	20170331T2231	HERMES	20170401T2225	HERMES	20170402T0029	FEROS
	20170402T0416	FEROS	20170402T2227	HERMES	20170403T0114	FEROS
	20170403T2216	HERMES	20170404T0145	FEROS	20170405T0111	FEROS
	20170406T0104	FEROS	20170407T0209	FEROS	20170408T0113	FEROS
	20170408T0513	FEROS	20170409T0104	FEROS		
HD 95418	20160108T0034	HEROS	20160127T0212	FIES	20160127T0214	FIES
(426)	20160127T0530	FIES	20160127T0531	FIES	20160128T0129	FIES
	20160128T0143	FIES	20160128T0145	FIES	20160303T0228	FIES
	20160303T2356	HERMES	20160303T2358	HERMES	20160304T0215	HERMES
	20160304T0218	HERMES	20160305T0007	HERMES	20160305T0143	HERMES
	20160305T0146	HERMES	20160306T0008	HERMES	20160306T0249	HERMES
	20160307T0107	HERMES	20160711T2057	HERMES	20160718T2134	FIES
	20160719T2137	FIES	20170307T0154	HERMES	20170307T0157	HERMES
	20170307T0202	HERMES	20170307T0317	HERMES	20170307T0318	HERMES
	20170307T0345	HERMES	20170307T0348	HERMES	20170307T0510	HERMES
	20170307T0514	HERMES	20170307T2115	HERMES	20170307T2117	HERMES
	20170308T0410	HERMES	20170308T2212	HERMES	20170308T2214	HERMES
	20170309T2204	HERMES	20170309T2206	HERMES	20170311T0455	HERMES
	20170311T2328	HERMES	20170311T2331	HERMES	20170312T2209	HERMES
ϕ Leo	20151221T0627	HERMES	20151223T0501	HERMES	20151223T0614	HERMES
(1934)	20151223T0706	HERMES	20151223T0715	HERMES	20151224T0524	HERMES
	20160127T0411	FIES	20160127T0536	FIES	20160128T0114	HERMES
	20160128T0126	HERMES	20160129T0339	HERMES	20160129T0510	HERMES
	20160129T0623	HERMES	20160131T0220	HERMES	20160131T0344	HERMES
	20160131T0451	HERMES	20160303T2343	HERMES	20160303T2348	HERMES
	20160304T0300	HERMES	20160304T0306	HERMES	20160304T2354	HERMES

Star	Date (UT)	Instrument	Date (UT)	Instrument	Date (UT)	Instrument
	20160304T2359	HERMES	20160305T0307	HERMES	20160305T0314	HERMES
	20160306T0016	HERMES	20160306T0257	HERMES	20160307T0010	HERMES
	20160307T0213	HERMES	20160307T0224	HERMES	20160326T0138	FEROS
	20160326T0312	FEROS	20160326T0315	FEROS	20160326T0553	FEROS
	20160327T0252	FEROS	20160327T0449	FEROS	20160327T0454	FEROS
	20160327T0601	FEROS	20160328T0153	FEROS	20160328T0346	FEROS
	20160328T0548	FEROS	20160329T0218	FEROS	20160329T0340	FEROS
	20160329T0522	FEROS	20160511T2021	HERMES	20160511T2044	HERMES
	20160511T2054	HERMES	20160511T2105	HERMES	20160511T2116	HERMES
	20160511T2127	HERMES	20160511T2138	HERMES	20160511T2151	HERMES
	20160511T2202	HERMES	20160511T2213	HERMES	20160511T2224	HERMES
	20160511T2234	HERMES	20160511T2245	HERMES	20160511T2317	HERMES
	20160511T2327	HERMES	20160511T2338	HERMES	20160511T2349	HERMES
	20160512T0000	HERMES	20160512T0011	HERMES	20160512T0020	HERMES
β Leo	20151221T0631	HERMES	20160115T0157	HEROS	20160116T0157	HEROS
(326)	20160127T0220	FIES	20160127T0221	FIES	20160127T0640	FIES
	20160127T0642	FIES	20160127T0644	FIES	20160129T0517	HERMES
	20160131T0446	HERMES	20160131T0447	HERMES	20160326T0209	FEROS
	20160326T0211	FEROS	20160329T0130	FEROS	20160329T0131	FEROS
	20160711T2053	HERMES	20160712T2055	HERMES	20160713T2057	HERMES
	20160717T2129	FIES	20160718T2130	FIES	20160719T2133	FIES
HD 104731	20160326T0217	FEROS	20160329T0140	FEROS		
(271)						
hd 104860	20160127T0233	FIES	20160127T0305	FIES		
(154)						
EF Cha	20170402T0343	FEROS	20170403T0155	FEROS	20170404T0206	FEROS
(375)	20170405T0150	FEROS	20170406T0238	FEROS	20170407T0304	FEROS
	20170408T0159	FEROS	20170409T0314	FEROS		
HD 105850	20160326T0222	FEROS	20160329T0147	FEROS	20170309T0219	HERMES
(311)	20170329T0244	HERMES	20170331T0326	HERMES		
δ Crv	20151221T0636	HERMES	20151223T0619	HERMES	20160115T0245	HEROS
(324)	20160116T0513	HEROS	20160127T0407	FIES	20160129T0521	HERMES
	20160131T0253	HERMES	20160304T0149	HERMES	20160304T0151	HERMES
	20160305T0138	HERMES	20160305T0345	HERMES	20160305T0348	HERMES
	20160306T0142	HERMES	20160307T0146	HERMES	20160307T0204	HERMES
	20170307T0311	HERMES	20170329T0259	HERMES		
η crv	20151221T0647	HERMES	20151223T0623	HERMES	20160129T0526	HERMES
(138)	20160131T0302	HERMES				
HR 4796	20160326T0205	FEROS	20160326T0343	FEROS	20160327T0259	FEROS
(714)	20160327T0704	FEROS	20160327T0947	FEROS	20160328T0145	FEROS
	20160328T0356	FEROS	20160328T0734	FEROS	20160328T1012	FEROS
	20160329T0229	FEROS	20160329T0354	FEROS	20160329T0802	FEROS
	20170402T0210	FEROS	20170402T0712	FEROS	20170403T0352	FEROS
	20170404T0346	FEROS	20170405T0449	FEROS	20170405T0621	FEROS
	20170406T0318	FEROS	20170407T0402	FEROS	20170407T0709	FEROS
	20170408T0238	FEROS	20170409T0339	FEROS		

Star	Date (UT)	Instrument	Date (UT)	Instrument	Date (UT)	Instrument
HD 110058	20170402T0440	FEROS	20170403T0414	FEROS	20170404T0402	FEROS
(383)	20170405T0329	FEROS	20170406T0331	FEROS	20170407T0418	FEROS
	20170408T0251	FEROS	20170409T0410	FEROS		
HD 110411	20151221T0615	HERMES	20151221T0702	HERMES	20151221T0715	HERMES
(625)	20151223T0513	HERMES	20151223T0537	HERMES	20151224T0612	HERMES
	20160127T0423	FIES	20160127T0559	FIES	20160115T0201	HEROS
	20160116T0201	HEROS	20160129T0347	HERMES	20160129T0543	HERMES
	20160131T0231	HERMES	20160131T0238	HERMES	20160131T0359	HERMES
	20160131T0405	HERMES	20160131T0512	HERMES	20160131T0519	HERMES
	20160304T0135	HERMES	20160304T0142	HERMES	20160304T0314	HERMES
	20160304T0321	HERMES	20160304T0644	HERMES	20160305T0036	HERMES
	20160305T0325	HERMES	20160305T0336	HERMES	20160305T0626	HERMES
	20160306T0027	HERMES	20160306T0151	HERMES	20160306T0311	HERMES
	20160306T0327	HERMES	20160307T0021	HERMES	20160307T0032	HERMES
	20160307T0155	HERMES	20160711T2100	HERMES	20160712T2206	HERMES
	20160713T2124	HERMES	20160714T2054	HERMES	20160716T2231	FIES
	20160718T2137	FIES	20160719T2147	FIES	20170307T0220	HERMES
	20170307T0231	HERMES	20170307T0242	HERMES	20170307T0602	HERMES
	20170307T0613	HERMES	20170308T0519	HERMES	20170309T0455	HERMES
	20170312T0442	HERMES	20170313T0437	HERMES	20170329T0311	HERMES
	20170331T0341	HERMES	20170401T0312	HERMES	20170402T0151	FEROS
	20170403T0221	FEROS	20170404T0243	FEROS	20170404T0325	HERMES
	20170405T0216	FEROS	20170406T0303	FEROS	20170407T0329	FEROS
	20170408T0224	FEROS	20170409T0354	FEROS		
24 CVn	20170402T0318	HERMES	20170403T0320	HERMES		
(148)						
HD 121191	20170601T0121	FEROS				
(193)						
HD 121617	20170409T0238	FEROS	20170409T0611	FEROS		
(161)						
λ *Boo*	20151223T0524	HERMES	20151224T0627	HERMES	20160127T0435	FIES
(221)	20160127T0724	FIES	20160711T2048	HERMES	20160711T2353	HERMES
HD 131488	20170409T0219	FEROS	20170409T0551	FEROS		
(172)						
HD 131835	20160326T0408	FEROS	20160326T0755	FEROS	20160327T0322	FEROS
(568)	20160327T0544	FEROS	20160327T0754	FEROS	20160328T0315	FEROS
	20160328T0455	FEROS	20160328T0808	FEROS	20160329T0304	FEROS
	20160329T0429	FEROS	20160329T0836	FEROS	20170403T0519	FEROS
	20170407T0456	FEROS	20170408T0322	FEROS		
HR 5774	20170307T0324	HERMES	20170307T0445	HERMES	20170307T0455	HERMES
(427)	20170308T0359	HERMES	20170308T0615	HERMES	20170309T0237	HERMES
	20170310T0508	HERMES	20170311T0502	HERMES	20170312T0505	HERMES
	20170313T0455	HERMES	20170329T0330	HERMES	20170331T0359	HERMES
	20170401T0330	HERMES	20170402T0613	HERMES	20170404T0541	HERMES
α CrB	20160127T0442	FIES	20160127T0444	FIES	20160127T0656	FIES
(326)	20160127T0657	FIES	20160711T2359	HERMES	20160714T0041	HERMES

Star	Date (UT)	Instrument	Date (UT)	Instrument	Date (UT)	Instrument
	20160716T2314	FIES	20160717T2356	FIES	20160718T2220	FIES
	20160719T0055	FIES	20160719T2331	FIES		
HIP 76310	20160304T0412	HERMES	20160304T0443	HERMES	20160305T0407	HERMES
(450)	20160305T0438	HERMES	20160305T0509	HERMES	20160306T0418	HERMES
	20160306T0449	HERMES	20160326T0424	FEROS	20160326T0817	FEROS
	20160327T0336	FEROS	20160327T0626	FEROS	20160327T0828	FEROS
	20160328T0421	FEROS	20160328T0833	FEROS	20160329T0506	FEROS
	20160329T0901	FEROS	20160711T2124	HERMES	20160712T2218	HERMES
	20160712T2249	HERMES	20160713T2133	HERMES	20160713T2204	HERMES
	20160714T2102	HERMES	20160716T2118	FIES	20160717T2133	FIES
	20160718T2147	FIES	20160719T2215	FIES	20170309T0503	HERMES
	20170310T0555	HERMES	20170310T0626	HERMES	20170314T0437	HERMES
	20170314T0508	HERMES	20170314T0539	HERMES	20170403T0452	FEROS
	20170404T0421	HERMES	20170405T0505	FEROS	20170406T0443	FEROS
	20170408T0354	FEROS				
HIP 77815	20160326T0649	FEROS	20160716T2153	FIES	20170308T0415	HERMES
(127)	20170308T0446	HERMES	20170313T0555	HERMES	20170329T0356	HERMES
	20170330T0337	HERMES	20170330T0408	HERMES	20170331T0425	HERMES
	20170401T0452	HERMES	20170402T0636	FEROS	20170405T0401	FEROS
	20170406T0402	FEROS	20170407T0547	FEROS	20170408T0415	FEROS
HIP 77911	20160711T2107	HERMES	20160326T0701	FEROS	20170401T0419	HERMES
(372)	20170401T0557	HERMES	20170402T0342	HERMES	20170402T0412	HERMES
	20170402T0540	FEROS	20170405T0532	FEROS		
HIP 78099	20160326T0719	FEROS	20160327T0354	FEROS	20160714T2145	HERMES
(123)	20160714T2216	HERMES	20170403T0344	HERMES	20170404T0440	FEROS
HIP 78996	20160327T0424	FEROS	20160717T2210	FIES	20170311T0619	HERMES
(167)	20170330T0546	HERMES	20170403T0638	FEROS	20170409T0652	FEROS
HIP 79156	20160328T0724	FEROS	20160717T2255	FIES	20160719T2335	FIES
(168)	20170406T0532	FEROS				
HIP 79410	20160329T0556	FEROS	20160714T2248	HERMES	20160714T2319	HERMES
(150)	20170402T0445	HERMES				
HIP 79439	20160329T0630	FEROS	20160716T2251	FIES	20170309T0553	HERMES
(212)	20170329T0541	HERMES	20170329T0612	HERMES	20170330T0513	HERMES
	20170402T0824	FEROS				
HD 145964	20160304T0514	HERMES	20160304T0540	HERMES	20160305T0542	HERMES
(576)	20160306T0522	HERMES	20160306T0553	HERMES	20160326T0614	FEROS
	20160327T0649	FEROS	20160328T0622	FEROS	20160329T0747	FEROS
	20160711T2330	HERMES	20160713T2101	HERMES	20160713T2340	HERMES
	20160716T2054	FIES	20160717T2056	FIES	20160718T2056	FIES
	20160719T2058	FIES	20170307T0529	HERMES	20170307T0545	HERMES
	20170308T0541	HERMES	20170308T0557	HERMES	20170309T0536	HERMES
	20170310T0516	HERMES	20170311T0514	HERMES	20170312T0524	HERMES
	20170329T0428	HERMES	20170330T0441	HERMES	20170331T0458	HERMES
	20170402T0516	FEROS	20170402T0517	HERMES	20170403T0435	HERMES

Star	Date (UT)	Instrument	Date (UT)	Instrument	Date (UT)	Instrument
	20170403T0614	FEROS	20170404T0349	HERMES	20170404T0453	HERMES
	20170404T0540	FEROS	20170404T0745	FEROS	20170405T0635	FEROS
	20170405T0824	FEROS	20170406T0603	FEROS	20170407T0528	FEROS
	20170408T0602	FEROS	20170409T0627	FEROS		
HIP 79797	20160328T0530	FEROS	20170404T0630	FEROS	20170405T0605	FEROS
(324)	20170407T0716	FEROS	20170408T0544	FEROS		
HIP 79878	20160711T2225	HERMES	20160719T2249	FIES	20170403T0555	FEROS
(150)	20170409T0435	FEROS				
HD 146624	20160328T0650	FEROS	20160716T2141	FIES	20170405T0553	FEROS
(246)						
HIP 79977	20160712T2100	HERMES	20160712T2131	HERMES	20170405T0702	FEROS
(165)	20170405T0733	FEROS	20170407T0726	FEROS	20170407T0756	FEROS
	20170930T0017	FEROS	20170930T0048	FEROS	20171001T0012	FEROS
	20171001T0042	FEROS				
HIP 80088	20160326T0522	FEROS	20160718T2224	FIES	20160718T2256	FIES
(220)	20170406T0709	FEROS	20170406T0735	FEROS	20170408T0730	FEROS
	20170408T0756	FEROS				
HIP 80130	20160713T2236	HERMES	20160713T2307	HERMES	20170401T0525	HERMES
(139)	20170403T0759	FEROS	20170409T0726	FEROS	20170409T0747	FEROS
HR 6123	20150903T2033	HERMES	20150903T2133	HERMES	20150903T2235	HERMES
(642)	20150903T2336	HERMES	20150904T2032	HERMES	20150904T2130	HERMES
	20150904T2222	HERMES	20150904T2230	HERMES	20150905T2036	HERMES
	20150905T2043	HERMES	20150905T2141	HERMES	20150905T2148	HERMES
	20150905T2315	HERMES	20150905T2321	HERMES	20150906T2028	HERMES
	20150906T2034	HERMES	20150906T2145	HERMES	20150906T2152	HERMES
	20150906T2302	HERMES	20150906T2309	HERMES	20160127T0449	FIES
	20160127T0502	FIES	20160127T0611	FIES	20160127T0624	FIES
	20160129T0423	HERMES	20160129T0435	HERMES	20160129T0554	HERMES
	20160129T0606	HERMES	20160131T0417	HERMES	20160131T0430	HERMES
	20160131T0530	HERMES	20160131T0542	HERMES	20160304T0230	HERMES
	20160304T0246	HERMES	20160304T0334	HERMES	20160304T0347	HERMES
	20160304T0631	HERMES	20160305T0229	HERMES	20160305T0250	HERMES
	20160305T0609	HERMES	20160306T0235	HERMES	20160306T0349	HERMES
	20160306T0620	HERMES	20160307T0248	HERMES	20160307T0315	HERMES
	20160712T0003	HERMES	20160712T2322	HERMES	20160713T0218	HERMES
	20160714T0013	HERMES	20160714T2352	HERMES	20160715T0206	HERMES
	20160716T2330	FIES	20160717T2245	FIES	20160718T0226	FIES
	20160718T2329	FIES	20160719T0201	FIES	20160719T2201	FIES
	20160720T0127	FIES	20170308T0527	HERMES	20170308T0644	HERMES
	20170309T0249	HERMES	20170310T0540	HERMES	20170311T0547	HERMES
	20170312T0557	HERMES	20170313T0513	HERMES	20170403T0549	HERMES
HIP 84881	20151022T0514	FEROS	20160326T0438	FEROS	20160326T0838	FEROS
(567)	20160327T0441	FEROS	20160327T0902	FEROS	20160328T0520	FEROS
	20160328T0858	FEROS	20160329T0655	FEROS	20160329T0925	FEROS
	20170402T0931	FEROS	20170405T0839	FEROS	20170406T0619	FEROS

Star	Date (UT)	Instrument	Date (UT)	Instrument	Date (UT)	Instrument
	20170408T0717	FEROS				
HD 157728	20160127T0545	FIES	20160127T0711	FIES	20160712T0146	HERMES
(476)	20160717T0210	FIES	20160718T0235	FIES	20160719T0239	FIES
HR 6507	20170401T0352	HERMES	20170402T0542	HERMES	20170403T0410	HERMES
(190)	20170404T0516	HERMES				
HD 162003	20160127T0519	FIES	20160127T0702	FIES	20160129T0534	HERMES
(365)	20160131T0501	HERMES				
hd 162917	20160712T0111	HERMES	20160713T0317	HERMES	20160717T0219	FIES
(126)	20160718T0247	FIES	20160719T0248	FIES		
HD 164249	20151022T0355	FEROS	20151023T0035	FEROS		
(225)						
HR 6864	20170402T0607	FEROS	20170403T0713	FEROS	20170404T0658	FEROS
(318)	20170405T0650	FEROS	20170405T0832	FEROS	20170406T0654	FEROS
	20170407T0701	FEROS	20170408T0638	FEROS	20170409T0643	FEROS
HD 172555	20151022T0356	FEROS	20151023T0238	FEROS	20160326T0534	FEROS
(468)	20160326T0849	FEROS	20160327T0715	FEROS	20160327T0958	FEROS
	20160328T0638	FEROS	20160328T0943	FEROS	20160329T0706	FEROS
	20160329T0934	FEROS	20170402T0629	FEROS	20170403T0721	FEROS
	20170404T0707	FEROS	20170405T0657	FEROS	20170406T0703	FEROS
	20170407T0656	FEROS	20170408T0647	FEROS	20170924T0127	FEROS
	20170928T0135	FEROS	20170930T0133	FEROS	20171001T0128	FEROS
110 Her	20150903T2053	HERMES	20150903T2141	HERMES	20150903T2145	HERMES
(423)	20150903T2156	HERMES	20150903T2259	HERMES	20150903T2302	HERMES
	20150904T0035	HERMES	20150904T2041	HERMES	20150904T2138	HERMES
	20150904T2239	HERMES	20150904T2243	HERMES	20150904T2337	HERMES
	20150904T2341	HERMES	20150905T2051	HERMES	20150905T2054	HERMES
	20150905T2157	HERMES	20150905T2200	HERMES	20150906T2059	HERMES
	20150906T2102	HERMES	20150906T2217	HERMES	20150906T2220	HERMES
ζ Aql	20160305T0637	HERMES	20160306T0651	HERMES	20160328T1001	FEROS
(467)	20160712T0142	HERMES	20160713T0248	HERMES	20160714T0410	HERMES
	20160717T0242	FIES	20160718T0013	FIES	20160719T0124	FIES
	20160720T0425	FIES	20170307T0650	HERMES	20170308T0639	HERMES
	20170312T0634	HERMES	20170313T0533	HERMES	20170329T0633	HERMES
	20170329T0638	HERMES				
HD 181296	20151022T0357	FEROS	20151023T0041	FEROS	20151024T0309	FEROS
(415)	20160326T0620	FEROS	20160326T0855	FEROS	20160327T0719	FEROS
	20160327T1004	FEROS	20160328T0644	FEROS	20160328T0949	FEROS
	20160329T0712	FEROS	20160329T0942	FEROS	20170403T0726	FEROS
	20170404T0739	FEROS	20170405T0815	FEROS	20170406T0802	FEROS
	20170407T0840	FEROS	20170408T0652	FEROS	20170924T0132	FEROS
	20170928T0143	FEROS	20171001T0122	FEROS		
HD 181327	20170403T0731	FEROS	20170404T0713	FEROS	20170406T0806	FEROS
(221)	20170407T0845	FEROS	20170408T0657	FEROS		
δ Aql	20160328T0957	FEROS	20160711T2303	HERMES		

Star	Date (UT)	Instrument	Date (UT)	Instrument	Date (UT)	Instrument
(206)						
5 Vul	20150905T2209	HERMES	20150905T2216	HERMES	20150905T2331	HERMES
(438)	20150905T2338	HERMES	20150906T2044	HERMES	20150906T2051	HERMES
	20150906T2203	HERMES	20150906T2210	HERMES	20150906T2334	HERMES
	20150906T2341	HERMES	20160304T0602	HERMES	20160304T0614	HERMES
	20160305T0649	HERMES	20160306T0639	HERMES	20160712T0016	HERMES
	20160712T0400	HERMES	20160712T2341	HERMES	20160713T0236	HERMES
	20160714T0027	HERMES	20160714T0246	HERMES	20160715T0005	HERMES
	20160715T0219	HERMES	20160716T2341	FIES	20160717T0231	FIES
	20160717T0417	FIES	20160717T2337	FIES	20160718T0315	FIES
	20160719T0059	FIES	20160719T0314	FIES	20160720T0432	FIES
	20170307T0627	HERMES	20170307T0638	HERMES	20170308T0626	HERMES
	20170309T0626	HERMES	20170311T0604	HERMES	20170312T0617	HERMES
	20170313T0537	HERMES	20170407T0914	FEROS	20170409T0922	FEROS
HD 183324	20160711T2202	HERMES	20160712T0043	HERMES	20160712T0341	HERMES
(337)	20160713T0004	HERMES	20160714T0044	HERMES	20160714T0337	HERMES
	20160715T0018	HERMES	20160715T0301	HERMES	20160716T2241	FIES
	20160717T0130	FIES	20160717T0330	FIES	20160718T0208	FIES
	20160718T0406	FIES	20160718T2339	FIES	20160719T0229	FIES
	20160719T2321	FIES	20160720T0201	FIES	20170329T0514	HERMES
	20170331T0526	HERMES	20170404T0530	HERMES	20170404T0819	FEROS
	20170405T0807	FEROS	20170407T0831	FEROS	20170409T0851	FEROS
α Aql	20150903T2058	HERMES	20150903T2200	HERMES	20150903T2309	HERMES
(329)	20150904T2045	HERMES	20150904T2046	HERMES	20150904T2148	HERMES
	20150904T2150	HERMES	20150905T2058	HERMES	20150905T2059	HERMES
	20150906T2105	HERMES	20150906T2106	HERMES	20150907T0001	HERMES
	20150907T0002	HERMES	20160711T2308	HERMES		
HD 188228	20151022T0359	FEROS	20151023T0252	FEROS	20151024T0328	FEROS
(147)	20160328T1019	FEROS				
HR 7731	20150903T2244	HERMES	20150903T2355	HERMES	20150904T0202	HERMES
(410)	20150904T2250	HERMES	20150904T2256	HERMES	20150904T2348	HERMES
	20150904T2354	HERMES	20150905T0224	HERMES	20150905T0231	HERMES
	20150905T2244	HERMES	20150905T2250	HERMES	20150906T0001	HERMES
	20150906T0006	HERMES	20150906T2234	HERMES	20150906T2239	HERMES
	20150906T2350	HERMES	20150906T2356	HERMES	20150907T0219	HERMES
	20150907T0225	HERMES	20151223T1911	HERMES	20151223T1922	HERMES
	20160711T2317	HERMES	20160713T0022	HERMES	20160715T0031	HERMES
	20160716T2352	FIES	20160718T0001	FIES	20160719T0111	FIES
	20160720T0442	FIES	20170329T0454	HERMES	20170330T0614	HERMES
	20170403T0503	HERMES	20170404T0558	HERMES		
29 Vul	20170402T0559	HERMES	20170403T0526	HERMES	20170404T0550	HERMES
(329)	20170924T0139	FEROS				
HR 7959	20170404T0800	FEROS	20170405T0854	FEROS	20170407T0905	FEROS
(297)	20170924T0158	FEROS				
HR 7960	20170404T0809	FEROS	20170924T0213	FEROS	20170926T0754	FEROS
(190)	20170927T0742	FEROS				

Star	Date (UT)	Instrument	Date (UT)	Instrument	Date (UT)	Instrument
HD 199143	20151022T0358	FEROS	20151023T0054	FEROS	20160326T0917	FEROS
(353)	20160327T0936	FEROS	20160328T0933	FEROS	20160329T1016	FEROS
α Cep	20150903T2103	HERMES	20150903T2150	HERMES	20150903T2251	HERMES
(285)	20150904T2053	HERMES	20150904T2055	HERMES	20150904T2144	HERMES
	20150904T2302	HERMES	20150904T2304	HERMES	20150905T2104	HERMES
	20150905T2105	HERMES	20150905T2224	HERMES	20150905T2225	HERMES
	20150906T2111	HERMES	20150906T2112	HERMES	20150906T2225	HERMES
	20150906T2227	HERMES	20160711T2312	HERMES		
HD 202917	20151022T0359	FEROS	20151023T0325	FEROS	20151024T0402	FEROS
(248)						
τ PsA	20151022T0400	FEROS	20151023T0332	FEROS	20151024T0408	FEROS
(351)						
HD 210418	20160712T0336	HERMES	20160712T0442	HERMES	20160713T0339	HERMES
(558)	20160715T0254	HERMES	20160717T0204	FIES	20160717T0412	FIES
	20160717T0502	FIES	20160718T0202	FIES	20160718T0354	FIES
	20160719T0149	FIES	20160719T0434	FIES	20160720T0343	FIES
ϵ Cep	20150903T2107	HERMES	20150903T2123	HERMES	20150903T2225	HERMES
(363)	20150903T2327	HERMES	20150903T2347	HERMES	20150904T0156	HERMES
	20150904T2100	HERMES	20150904T2104	HERMES	20150904T2157	HERMES
	20150904T2310	HERMES	20150904T2315	HERMES	20150905T0239	HERMES
	20150905T2111	HERMES	20150905T2116	HERMES	20150905T2231	HERMES
	20150905T2236	HERMES	20150905T2347	HERMES	20150905T2352	HERMES
	20150906T2117	HERMES	20150906T2122	HERMES	20150906T2248	HERMES
	20150906T2253	HERMES	20150907T0053	HERMES	20150907T0058	HERMES
	20160712T0134	HERMES				
HD 213617	20160712T0307	HERMES	20160713T0344	HERMES	20160714T0221	HERMES
(177)	20160715T0330	HERMES	20160717T0146	FIES	20160717T0354	FIES
	20160718T0144	FIES	20160719T0211	FIES	20160720T0325	FIES
HD 217782	20150903T2114	HERMES	20150903T2208	HERMES	20150903T2318	HERMES
(526)	20150904T0232	HERMES	20150904T2114	HERMES	20150904T2120	HERMES
	20150904T2205	HERMES	20150904T2212	HERMES	20150904T2323	HERMES
	20150904T2329	HERMES	20150905T2124	HERMES	20150905T2130	HERMES
	20150905T2259	HERMES	20150905T2305	HERMES	20150906T0103	HERMES
	20150906T0108	HERMES	20150906T0431	HERMES	20150906T2130	HERMES
	20150906T2136	HERMES	20150906T2318	HERMES	20150906T2324	HERMES
	20150907T0233	HERMES	20150907T0239	HERMES	20151222T1949	HERMES
	20151222T2005	HERMES	20151223T2044	HERMES	20160712T0030	HERMES
	20160712T0413	HERMES	20160713T0143	HERMES	20160713T0432	HERMES
	20160714T0206	HERMES	20160714T0358	HERMES	20160715T0240	HERMES
	20160717T0108	FIES	20160717T0312	FIES	20160718T0126	FIES
	20160718T0336	FIES	20160719T0129	FIES	20160719T0335	FIES
	20160720T0151	FIES	20160720T0405	FIES		
HD 221756	20151222T2302	HERMES	20151223T2212	HERMES	20151223T2354	HERMES
(326)	20151224T0034	HERMES	20160130T1926	HERMES	20160130T1943	HERMES
	20160712T0057	HERMES	20160713T0158	HERMES	20160713T0445	HERMES
	20160714T0316	HERMES	20160714T0515	HERMES	20160715T0152	HERMES

Star	Date (UT)	Instrument	Date (UT)	Instrument	Date (UT)	Instrument
	20160715T0508	HERMES	20160717T0120	FIES	20160717T0321	FIES
	20160718T0135	FIES	20160718T0345	FIES	20160719T0138	FIES
	20160719T0350	FIES	20160720T0139	FIES	20160720T0414	FIES
HD 222368	20160712T0330	HERMES	20160713T0210	HERMES	20160713T0459	HERMES
(335)	20160714T0330	HERMES	20160715T0232	HERMES	20160717T0247	FIES
	20160717T0455	FIES	20160718T0219	FIES	20160718T0443	FIES
	20160719T0154	FIES	20160719T0439	FIES	20160720T0348	FIES
HD 224392	20151023T0108	FEROS	20151023T0444	FEROS	20151024T0437	FEROS
(280)	20170923T0446	FEROS	20170924T0146	FEROS	20170925T0649	FEROS
	20170925T0658	FEROS				

Bibliography

Absil, O., Defrère, D., Coudé du Foresto, V., et al. 2013, A&A, 555, A104

Absil, O., di Folco, E., Mérand, A., et al. 2006, A&A, 452, 237

Absil, O., Le Bouquin, J. B., Berger, J. P., et al. 2011, A&A, 535, A68

Abt, H. A. 2008, ApJS, 174, 499

Abt, H. A. 2015, PASP, 127, 1218

Abt, H. A. & Morrell, N. I. 1995, The Astrophysical Journal Supplement Series, 99, 135

Abt, H. A. & Moyd, K. I. 1973, ApJ, 182, 809

Abt, H. A., Tan, H., & Zhou, H. 1997, ApJ, 487, 365

Acke, B., Min, M., Dominik, C., et al. 2012, A&A, 540, A125

Aller, L. H., Appenzeller, I., Baschek, B., et al., eds. 1982, Landolt-Börnstein: Numerical Data and Functional Relationships in Science and Technology - New Series, Group 6 Astronomy and Astrophysics, Vol. 2 Stars and Star Clusters, 54

Ansdell, M., Gaidos, E., Jacobs, T. L., et al. 2019, MNRAS, 483, 3579

Armitage, P. J. 2010, Astrophysics of Planet Formation

Armitage, P. J. 2011, ARA&A, 49, 195

Asensio-Torres, R., Janson, M., Hashimoto, J., et al. 2016, A&A, 593, A73

Aumann, H. H., Gillett, F. C., Beichman, C. A., et al. 1984, ApJ, 278, L23

Backman, D. E. & Paresce, F. 1993, in Protostars and Planets III, ed. E. H. Levy & J. I. Lunine, 1253–1304

Ballering, N. P., Rieke, G. H., Su, K. Y. L., & Gáspár, A. 2017, ApJ, 845, 120

Ballering, N. P., Rieke, G. H., Su, K. Y. L., & Montiel, E. 2013, ApJ, 775, 55

Baschek, B. & Slettebak, A. 1988, A&A, 207, 112

Bastian, N. & de Mink, S. E. 2009, MNRAS, 398, L11

Batalha, N. M., Rowe, J. F., Bryson, S. T., et al. 2013, ApJS, 204, 24

Bell, C. P. M., Mamajek, E. E., & Naylor, T. 2015a, MNRAS, 454, 593

Bell, E. A., Boehnke, P., Harrison, T. M., & Mao, W. L. 2015b, Proceedings of the National Academy of Science, 112, 14518

Bertin, P., Lallement, R., Ferlet, R., & Vidal-Madjar, A. 1993, A&A, 278, 549

Bessell, M. S. 1979, PASP, 91, 589

Beust, H., Lagrange, A.-M., Crawford, I. A., et al. 1998, A&A, 338, 1015

Beust, H., Lagrange, A.-M., Plazy, F., & Mouillet, D. 1996, A&A, 310, 181

Beust, H., Lagrange-Henri, A. M., Vidal-Madjar, A., & Ferlet, R. 1989, A&A, 223, 304

Beust, H. & Morbidelli, A. 1996, , 120, 358

Beust, H. & Morbidelli, A. 2000, , 143, 170

Beust, H., Vidal-Madjar, A., & Ferlet, R. 1991, A&A, 247, 505

Beust, H., Vidal-Madjar, A., Ferlet, R., & Lagrange-Henri, A. M. 1990, A&A, 236, 202

Bochanski, J. J., Faherty, J. K., Gagné, J., et al. 2018, AJ, 155, 149

Böhm, T., Holschneider, M., Lignières, F., et al. 2015, A&A, 577, A64

Bonsor, A., Raymond, S. N., Augereau, J.-C., & Ormel, C. W. 2014, MNRAS, 441, 2380

Borucki, W. J., Koch, D., Basri, G., et al. 2010, Science, 327, 977

Boyajian, T. S., LaCourse, D. M., Rappaport, S. A., et al. 2016, MNRAS, 457, 3988

Brandeker, A. 2011, ApJ, 729, 122

Brandeker, A., Liseau, R., Olofsson, G., & Fridlund, M. 2004, A&A, 413, 681

Breger, M. 1979, PASP, 91, 5

Bressan, A., Marigo, P., Girardi, L., et al. 2012, MNRAS, 427, 127

Britt, D. T., Consolmagno, G. J., & Merline, W. J. 2006, in 37th Annual Lunar and Planetary Science Conference, ed. S. Mackwell & E. Stansbery, Lunar and Planetary Science Conference, 2214

Brown, M. E. 2012, Annual Review of Earth and Planetary Sciences, 40, 467

Carry, B. 2012, , 73, 98

Castelli, F. & Kurucz, R. L. 2003, in IAU Symposium, Vol. 210, Modelling of Stellar Atmospheres, ed. N. Piskunov, W. W. Weiss, & D. F. Gray, A20

Cataldi, G., Brandeker, A., Olofsson, G., et al. 2014, A&A, 563, A66

Cataldi, G., Moór, A., Ohashi, N., et al. 2019, Research Notes of the American Astronomical Society, 3, 39

Chambers, K. C., Magnier, E. A., Metcalfe, N., et al. 2016, arXiv e-prints [[arXiv]1612.05560]

Chen, C. H. & Jura, M. 2003, ApJ, 582, 443

Chen, C. H., Mittal, T., Kuchner, M., et al. 2014, ApJS, 211, 25

Chen, C. H., Patten, B. M., Werner, M. W., et al. 2005, ApJ, 634, 1372

Cheng, K.-P., Grady, C. A., & Bruhweiler, F. C. 1991, ApJ, 366, L87

Cheng, K.-P. & Neff, J. E. 2003, AJ, 125, 868

Cheng, K.-P., Neff, J. E., Johnson, D. M., et al. 2017, AJ, 153, 39

Choquet, É., Milli, J., Wahhaj, Z., et al. 2017, ApJ, 834, L12

Cohen, M., Wheaton, W. A., & Megeath, S. T. 2003, AJ, 126, 1090

Cotten, T. H. & Song, I. 2016, ApJS, 225, 15

Currie, T., Guyon, O., Tamura, M., et al. 2017, ApJ, 836, L15

Currie, T., Lisse, C. M., Sicilia-Aguilar, A., Rieke, G. H., & Su, K. Y. L. 2011, ApJ, 734, 115

Cutri, R. M., Skrutskie, M. F., van Dyk, S., et al. 2003, VizieR Online Data Catalog, 2246

David, T. J. & Hillenbrand, L. A. 2015, ApJ, 804, 146

de Bruijne, J. H. J. & Eilers, A.-C. 2012, A&A, 546, A61

de León, J., Licandro, J., Serra-Ricart, M., et al. 2019, Research Notes of the American Astronomical Society, 3, 131

De Rosa, R. J., Patience, J., Wilson, P. A., et al. 2014, MNRAS, 437, 1216

de Zeeuw, P. T., Hoogerwerf, R., de Bruijne, J. H. J., Brown, A. G. A., & Blaauw, A. 1999, AJ, 117, 354

Defrère, D., Lebreton, J., Le Bouquin, J.-B., et al. 2012, A&A, 546, L9

Dent, W. R. F., Wyatt, M. C., Roberge, A., et al. 2014, Science, 343, 1490

Desidera, S., Covino, E., Messina, S., et al. 2015, A&A, 573, A126

Donaldson, J. K., Lebreton, J., Roberge, A., Augereau, J.-C., & Krivov, A. V. 2013, ApJ, 772, 17

Donaldson, J. K., Roberge, A., Chen, C. H., et al. 2012, ApJ, 753, 147

Draper, Z. H., Matthews, B. C., Kennedy, G. M., et al. 2016, MNRAS, 456, 459

Duchêne, G. 2015, Ap&SS, 355, 291

Duchêne, G., Arriaga, P., Wyatt, M., et al. 2014, ApJ, 784, 148

Eggleton, P. P. & Tokovinin, A. A. 2008, MNRAS, 389, 869

Eiroa, C., Marshall, J. P., Mora, A., et al. 2013, A&A, 555, A11

Eiroa, C., Rebollido, I., Montesinos, B., et al. 2016, A&A, 594, L1

Ekström, S., Georgy, C., Eggenberger, P., et al. 2012, A&A, 537, A146

Gaia Collaboration. 2018, VizieR Online Data Catalog, I/345

Ertel, S., Absil, O., Defrère, D., et al. 2014, A&A, 570, A128

Ertel, S., Defrère, D., Absil, O., et al. 2016, A&A, 595, A44

Faraggiana, R. & Bonifacio, P. 1999, A&A, 349, 521

Faramaz, V., Ertel, S., Booth, M., Cuadra, J., & Simmonds, C. 2017, MNRAS, 465, 2352

Feldt, M., Olofsson, J., Boccaletti, A., et al. 2017, A&A, 601, A7

Ferlet, R., Vidal-Madjar, A., & Hobbs, L. M. 1987, A&A, 185, 267

Fernández, R., Brandeker, A., & Wu, Y. 2006, ApJ, 643, 509

Fink, U. & Rubin, M. 2012, , 221, 721

Fitzsimmons, A., Hainaut, O., Meech, K., et al. 2019, arXiv e-prints, arXiv:1909.12144

Foreman-Mackey, D., Hogg, D. W., Lang, D., & Goodman, J. 2013, PASP, 125, 306

Frandsen, S. & Lindberg, B. 2000, in The Third MONS Workshop: Science Preparation and Target Selection, ed. T. Teixeira & T. Bedding, 163

Gänsicke, B. T., Aungwerojwit, A., Marsh, T. R., et al. 2016, ApJ, 818, L7

Gáspár, A., Rieke, G. H., & Balog, Z. 2013, ApJ, 768, 25

Geiler, F. & Krivov, A. V. 2017, MNRAS, 468, 959

Génova, R. & Beckman, J. E. 2003, ApJS, 145, 355

Gontcharov, G. A. 2012, Astronomy Letters, 38, 771

Grady, C. A., Brown, A., Welsh, B., et al. 2018, AJ, 155, 242

Grady, C. A., McCollum, B., Rawley, L. A., et al. 1996a, ApJ, 464, L183

Grady, C. A., Perez, M. R., Talavera, A., et al. 1996b, ApJ, 471, L49

Gray, R. O. & Corbally, J., C. 2009, Stellar Spectral Classification

Gray, R. O., Riggs, Q. S., Koen, C., et al. 2017, AJ, 154, 31

Greaves, J. S., Holland, W. S., Matthews, B. C., et al. 2016, MNRAS, 461, 3910

Gudennavar, S. B., Bubbly, S. G., Preethi, K., & Murthy, J. 2012, ApJS, 199, 8

Hales, A. S., Barlow, M. J., Crawford, I. A., & Casassus, S. 2017, MNRAS, 466, 3582

Harris, R. J., Andrews, S. M., Wilner, D. J., & Kraus, A. L. 2012, ApJ, 751, 115

Hauck, B. & Jaschek, C. 2000, A&A, 354, 157

Heinrichsen, I., Walker, H. J., Klaas, U., Sylvester, R. J., & Lemke, D. 1999, MNRAS, 304, 589

Hempel, M. & Schmitt, J. H. M. M. 2003, A&A, 408, 971

Hobbs, L. M. 1986, ApJ, 308, 854

Hobbs, L. M., Vidal-Madjar, A., Ferlet, R., Albert, C. E., & Gry, C. 1985, ApJ, 293, L29

Hobbs, L. M., Welty, D. E., Lagrange-Henri, A. M., Ferlet, R., & Vidal-Madjar, A. 1988, ApJ, 334, L41

Holland, W. S., Greaves, J. S., Zuckerman, B., et al. 1998, Nat, 392, 788

Holweger, H., Hempel, M., & Kamp, I. 1999, A&A, 350, 603

Holweger, H. & Rentzsch-Holm, I. 1995, A&A, 303, 819

Howarth, I. D., Murray, J., Mills, D., & Berry, D. S. 2004, Starlink User Note, 50

Howe, K. S. & Clarke, C. J. 2009, MNRAS, 392, 448

Hughes, A. M., Duchêne, G., & Matthews, B. C. 2018, ARA&A, 56, 541

Hughes, A. M., Wilner, D. J., Kamp, I., & Hogerheijde, M. R. 2008, ApJ, 681, 626

Hung, L.-W., Fitzgerald, M. P., Chen, C. H., et al. 2015, ApJ, 802, 138

Iglesias, D., Bayo, A., Olofsson, J., et al. 2018, MNRAS, 480, 488

Iglesias, D. P., Olofsson, J., Bayo, A., et al. 2019, arXiv e-prints, arXiv:1910.04747

Isobe, T., Feigelson, E. D., Akritas, M. G., & Babu, G. J. 1990, ApJ, 364, 104

Ivezić, Ž., Connolly, A., Vanderplas, J., & Gray, A. 2014, Statistics, Data Mining and Machine Learning in Astronomy (Princeton University Press)

Jaschek, C. & Andrillat, Y. 1998, A&AS, 130, 507

Jaschek, M., Jaschek, C., & Andrillat, Y. 1988, A&AS, 72, 505

Jaschek, M., Jaschek, C., & Andrillat, Y. 1991, A&A, 250, 127

Jura, M. 2015, AJ, 150, 166

Kalas, P. 2005, ApJ, 635, L169

Kalas, P., Graham, J. R., Fitzgerald, M. P., & Clampin, M. 2013, ApJ, 775, 56

Kasper, M., Apai, D., Wagner, K., & Robberto, M. 2015, ApJ, 812, L33

Kaufer, A., Stahl, O., Tubbesing, S., et al. 1999, The Messenger, 95, 8

Kausch, W., Noll, S., Smette, A., et al. 2015a, A&A, 576, A78

Kausch, W., Noll, S., Smette, A., et al. 2015b, A&A, 576, A78

Kennedy, G. M. & Wyatt, M. C. 2014, MNRAS, 444, 3164

Kerridge, J. F. 1985, , 49, 1707

Kiefer, F., Lecavelier des Etangs, A., Augereau, J.-C., et al. 2014a, A&A, 561, L10

Kiefer, F., Lecavelier des Etangs, A., Boissier, J., et al. 2014b, Nat, 514, 462

Kirchschlager, F., Wolf, S., Krivov, A. V., Mutschke, H., & Brunngräber, R. 2017, MNRAS, 467, 1614

Koen, C. 2003, MNRAS, 341, 1385

Kondo, Y. & Bruhweiler, F. C. 1985, ApJ, 291, L1

Kondo, Y. & Wamsteker, W., eds. 1987, Astrophysics and Space Science Library, Vol. 129, Exploring the universe with the IUE satellite

Kóspál, Á., Moór, A., Juhász, A., et al. 2013, ApJ, 776, 77

Kral, Q., Marino, S., Wyatt, M. C., Kama, M., & Matra, L. 2018, arXiv e-prints [[arXiv]1811.08439]

Kral, Q., Matrà, L., Wyatt, M. C., & Kennedy, G. M. 2017, MNRAS, 469, 521

Kral, Q., Wyatt, M., Carswell, R. F., et al. 2016, MNRAS, 461, 845

Kraus, A. L. & Ireland, M. J. 2012, ApJ, 745, 5

Kurucz, R. 1993, SYNTHE Spectrum Synthesis Programs and Line Data. Kurucz CD-ROM No. 18. Cambridge, Mass.: Smithsonian Astrophysical Observatory, 1993., 18

Lagrange, A.-M., Beust, H., Mouillet, D., et al. 1998, A&A, 330, 1091

Lagrange, A.-M., Bonnefoy, M., Chauvin, G., et al. 2010, Science, 329, 57

Lagrange, A. M., Desort, M., Galland, F., Udry, S., & Mayor, M. 2009, A&A, 495, 335

Lagrange, A. M., Ferlet, R., & Vidal-Madjar, A. 1987, A&A, 173, 289

Lagrange, A. M., Meunier, N., Rubini, P., et al. 2019, Nature Astronomy, 421

Lagrange-Henri, A. M., Beust, H., Ferlet, R., Hobbs, L. M., & Madjar, A. V. 1990a, A&A, 227, L13

Lagrange-Henri, A. M., Beust, H., Ferlet, R., Vidal-Madjar, A., & Hobbs, L. M. 1990b, A&A, 227, L13

Lagrange-Henri, A. M., Ferlet, R., Vidal-Madjar, A., et al. 1990c, A&AS, 85, 1089

Lagrange-Henri, A. M., Ferlet, R., Vidal-Madjar, A., et al. 1990d, A&AS, 85, 1089

Lagrange-Henri, A. M., Gosset, E., Beust, H., Ferlet, R., & Vidal-Madjar, A. 1992, A&A, 264, 637

Lagrange-Henri, A. M., Vidal-Madjar, A., & Ferlet, R. 1988, A&A, 190, 275

Le Bouquin, J.-B., Berger, J.-P., Lazareff, B., et al. 2011, A&A, 535, A67

Lebreton, J., Augereau, J.-C., Thi, W.-F., et al. 2012, A&A, 539, A17

Lecavelier Des Etangs, A., Deleuil, M., Vidal-Madjar, A., et al. 1997, A&A, 325, 228

Lecavelier Des Etangs, A., Vidal-Madjar, A., & Ferlet, R. 1999, A&A, 343, 916

Levison, H. F., Duncan, M. J., & Wetherill, G. W. 1994, Nat, 372, 441

Lieman-Sifry, J., Hughes, A. M., Carpenter, J. M., et al. 2016, ApJ, 828, 25

Lillo-Box, J., Barrado, D., Figueira, P., et al. 2018a, A&A, 609, A96

Lillo-Box, J., Leleu, A., Parviainen, H., et al. 2018b, A&A, 618, A42

Lindegren, L., Lammers, U., Bastian, U., et al. 2016, A&A, 595, A4

Lineweaver, C. H. & Norman, M. 2010, arXiv e-prints, arXiv:1004.1091

Lis, D. C., Bockelée-Morvan, D., Güsten, R., et al. 2019, A&A, 625, L5

Liseau, R. 2003, in ESA Special Publication, Vol. 539, Earths: DARWIN/TPF and the Search for Extrasolar Terrestrial Planets, ed. M. Fridlund, T. Henning, & H. Lacoste, 135–142

Lisse, C. M., Sitko, M. L., Russell, R. W., et al. 2017, ApJ, 840, L20

Lécuyer, C., Gillet, P., & Robert, F. 1998, Chemical Geology, 145, 249

Malamut, C., Redfield, S., Linsky, J. L., Wood, B. E., & Ayres, T. R. 2014, ApJ, 787, 75

Maldonado, J., Eiroa, C., Villaver, E., Montesinos, B., & Mora, A. 2012, A&A, 541, A40

Maldonado, J. & Villaver, E. 2017, A&A, 602, A38

Maldonado, J., Villaver, E., & Eiroa, C. 2018, A&A, 612, A93

Mamajek, E. E. 2012, ApJ, 754, L20

Mamajek, E. E. & Bell, C. P. M. 2014, MNRAS, 445, 2169

Manser, C. J., Gänsicke, B. T., Eggl, S., et al. 2019, Science, 364, 66

Marboeuf, U., Bonsor, A., & Augereau, J.-C. 2016, , 133, 47

Marino, S., Bonsor, A., Wyatt, M. C., & Kral, Q. 2018, MNRAS, 479, 1651

Marino, S., Matrà, L., Stark, C., et al. 2016, MNRAS, 460, 2933

Marino, S., Wyatt, M. C., Panić, O., et al. 2017, MNRAS, 465, 2595

Marion, L., Absil, O., Ertel, S., et al. 2014, A&A, 570, A127

Matrà, L., Dent, W. R. F., Wyatt, M. C., et al. 2017, MNRAS, 464, 1415

Matrà, L., Öberg, K. I., Wilner, D. J., Olofsson, J., & Bayo, A. 2019, AJ, 157, 117

Matthews, B. C., Krivov, A. V., Wyatt, M. C., Bryden, G., & Eiroa, C. 2014, Protostars and Planets VI, 521

Mayor, M. & Queloz, D. 1995, Nat, 378, 355

Mede, K. & Brandt, T. D. 2017, AJ, 153, 135

Mékarnia, D., Chapellier, E., Guillot, T., et al. 2017, A&A, 608, L6

Melis, C., Zuckerman, B., Rhee, J. H., et al. 2013, ApJ, 778, 12

Mellon, S. N., Mamajek, E. E., Zwintz, K., et al. 2019, ApJ, 870, 36

Mittal, T., Chen, C. H., Jang-Condell, H., et al. 2015, ApJ, 798, 87

Montesinos, B., Eiroa, C., Krivov, A. V., et al. 2016, A&A, 593, A51

Montesinos, B., Eiroa, C., Lillo-Box, J., et al. 2019, A&A, 629, A19

Montesinos, B., Eiroa, C., Mora, A., & Merín, B. 2009, A&A, 495, 901

Montgomery, S. L. & Welsh, B. Y. 2012, PASP, 124, 1042

Montgomery, S. L. & Welsh, B. Y. 2017, MNRAS, 468, L55

Moons, M. & Morbidelli, A. 1995, , 114, 33

Moór, A., Ábrahám, P., Juhász, A., et al. 2011a, ApJ, 740, L7

Moór, A., Ábrahám, P., Juhász, A., et al. 2011b, ApJ, 740, L7

Moór, A., Curé, M., Kóspál, Á., et al. 2017, ApJ, 849, 123

Moór, A., Henning, T., Juhász, A., et al. 2015a, ApJ, 814, 42

Moór, A., Juhász, A., Kóspál, Á., et al. 2013, ApJ, 777, L25

Moór, A., Kóspál, Á., Ábrahám, P., et al. 2015b, MNRAS, 447, 577

Moór, A., Pascucci, I., Kóspál, Á., et al. 2011c, ApJS, 193, 4

Mora, A., Merín, B., Solano, E., et al. 2001, A&A, 378, 116

Morales, F. Y., Bryden, G., Werner, M. W., & Stapelfeldt, K. R. 2016, ApJ, 831, 97

Morbidelli, A. 2010, Comptes Rendus Physique, 11, 651

Morbidelli, A., Chambers, J., Lunine, J. I., et al. 2000, Meteoritics and Planetary Science, 35, 1309

Müller, A., Keppler, M., Henning, T., et al. 2018, A&A, 617, L2

Murphy, S. J., Corbally, C. J., Gray, R. O., et al. 2015a, , 32, e036

Murphy, S. J., Corbally, C. J., Gray, R. O., et al. 2015b, , 32, e036

Murphy, S. J. & Paunzen, E. 2017, MNRAS, 466, 546

Mustill, A. J., Villaver, E., Veras, D., Gänsicke, B. T., & Bonsor, A. 2018, MNRAS, 476, 3939

Naoz, S. 2016, ArXiv e-prints [[arXiv]1601.07175]

Nesvorný, D., Jenniskens, P., Levison, H. F., et al. 2010, ApJ, 713, 816

Neuhäuser, R., Ginski, C., Schmidt, T. O. B., & Mugrauer, M. 2011, MNRAS, 416, 1430

Nielsen, M. B., Gizon, L., Schunker, H., & Karoff, C. 2013, A&A, 557, L10

Nilsson, R., Brandeker, A., Olofsson, G., et al. 2012, A&A, 544, A134

Nuñez, P. D., Scott, N. J., Mennesson, B., et al. 2017, A&A, 608, A113

O'Brien, D. P., Izidoro, A., Jacobson, S. A., Raymond, S. N., & Rubie, D. C. 2018, Space Sci.Rev., 214, 47

Olofsson, G., Liseau, R., & Brandeker, A. 2001, ApJ, 563, L77

Opitom, C., Fitzsimmons, A., Jehin, E., et al. 2019, arXiv e-prints, arXiv:1910.09078

Panitz, C., Horneck, G., Rabbow, E., et al. 2015, International Journal of Astrobiology, 14, 105–114

Paunzen, E. 2004, in IAU Symposium, Vol. 224, The A-Star Puzzle, ed. J. Zverko, J. Ziznovsky, S. J. Adelman, & W. W. Weiss, 443–450

Pawellek, N., Krivov, A. V., Marshall, J. P., et al. 2014, ApJ, 792, 65

Pecaut, M. J. & Mamajek, E. E. 2013, ApJS, 208, 9

Pecaut, M. J. & Mamajek, E. E. 2016, MNRAS, 461, 794

Pecaut, M. J., Mamajek, E. E., & Bubar, E. J. 2012, ApJ, 746, 154

Pilbratt, G. L., Riedinger, J. R., Passvogel, T., et al. 2010, A&A, 518, L1

Plavchan, P., Werner, M. W., Chen, C. H., et al. 2009, ApJ, 698, 1068

Pöppel, W. G. L., Bajaja, E., Arnal, E. M., & Morras, R. 2010, A&A, 512, A83

Porter, J. M. & Rivinius, T. 2003, PASP, 115, 1153

Quirrenbach, A., Amado, P. J., Caballero, J. A., et al. 2016, in SPIE, Vol. 9908, Ground-based and Airborne Instrumentation for Astronomy VI, 990812

Rappaport, S., Vanderburg, A., Jacobs, T., et al. 2018, MNRAS, 474, 1453

Rappaport, S., Zhou, G., Vanderburg, A., et al. 2019, MNRAS, 485, 2681

Raskin, G., van Winckel, H., Hensberge, H., et al. 2011a, A&A, 526, A69

Raskin, G., van Winckel, H., Hensberge, H., et al. 2011b, A&A, 526, A69

Raymond, S. N., Armitage, P. J., & Veras, D. 2018a, ApJ, 856, L7

Raymond, S. N., Armitage, P. J., Veras, D., Quintana, E. V., & Barclay, T. 2018b, MNRAS, 476, 3031

Raymond, S. N. & Izidoro, A. 2017, , 297, 134

Rebollido, I., Eiroa, C., Montesinos, B., et al. 2018, A&A, 614, A3

Rebollido, I., Eiroa, C., Montesinos, B., et al. 2019, A&A, submitted

Redfield, S. 2007, ApJ, 656, L97

Redfield, S., Kessler-Silacci, J. E., & Cieza, L. A. 2007, ApJ, 661, 944

Redfield, S. & Linsky, J. L. 2000, ApJ, 534, 825

Redfield, S. & Linsky, J. L. 2002, ApJS, 139, 439

Redfield, S. & Linsky, J. L. 2008a, ApJ, 673, 283

Redfield, S. & Linsky, J. L. 2008b, ApJ, 673, 283

Ricker, G. R., Winn, J. N., Vanderspek, R., et al. 2015, Journal of Astronomical Telescopes, Instruments, and Systems, 1, 014003

Rieke, G. H., Gáspár, A., & Ballering, N. P. 2016, ApJ, 816, 50

Rieke, G. H., Su, K. Y. L., Stansberry, J. A., et al. 2005, ApJ, 620, 1010

Riviere-Marichalar, P., Barrado, D., Augereau, J.-C., et al. 2012, A&A, 546, L8

Riviere-Marichalar, P., Barrado, D., Montesinos, B., et al. 2014, A&A, 565, A68

Riviere-Marichalar, P., Pinte, C., Barrado, D., et al. 2013, A&A, 555, A67

Roberge, A., Feldman, P. D., Lagrange, A. M., et al. 2000, ApJ, 538, 904

Roberge, A., Feldman, P. D., Weinberger, A. J., Deleuil, M., & Bouret, J.-C. 2006, Nat, 441, 724

Roberge, A., Kamp, I., Montesinos, B., et al. 2013, ApJ, 771, 69

Roberge, A. & Weinberger, A. J. 2008, ApJ, 676, 509

Roberge, A., Welsh, B. Y., Kamp, I., Weinberger, A. J., & Grady, C. A. 2014, ApJ, 796, L11

Rodriguez, D. R. & Zuckerman, B. 2012, ApJ, 745, 147

Rodriguez, E., Lopez de Coca, P., Rolland, A., Garrido, R., & Costa, V. 1994, A&AS, 106, 21

Rogers, R. R. & Yau, M. K. 1989, A short course in cloud physics

Royer, F., Zorec, J., & Gómez, A. E. 2007, A&A, 463, 671

Schmitt, J. H. M. M., Schröder, K.-P., Rauw, G., et al. 2014, Astronomische Nachrichten, 335, 787

Schneider, G., Grady, C. A., Hines, D. C., et al. 2014, AJ, 148, 59

Schneider, G., Silverstone, M. D., & Hines, D. C. 2005, ApJ, 629, L117

Schüppler, C., Krivov, A. V., Löhne, T., et al. 2016, MNRAS, 461, 2146

Sezestre, É., Augereau, J.-C., & Thébault, P. 2019, arXiv e-prints [[arXiv]1903.06130]

Sibthorpe, B., Kennedy, G. M., Wyatt, M. C., et al. 2018, MNRAS, 475, 3046

Slettebak, A. 1975, ApJ, 197, 137

Slettebak, A. 1982, ApJS, 50, 55

Smette, A., Sana, H., Noll, S., et al. 2015a, A&A, 576, A77

Smette, A., Sana, H., Noll, S., et al. 2015b, A&A, 576, A77

Smith, B. A. & Terrile, R. J. 1984, Science, 226, 1421

Smith, R., Churcher, L. J., Wyatt, M. C., Moerchen, M. M., & Telesco, C. M. 2009, A&A, 493, 299

Smith, R., Wyatt, M. C., & Haniff, C. A. 2012, MNRAS, 422, 2560

Somerville, W. B. 1988, The Observatory, 108, 44

Steckloff, J. K., Keane, J., Knight, M. M., et al. 2015, in Lunar and Planetary Science Conference, 2723

Su, K. Y. L., Rieke, G. H., Stansberry, J. A., et al. 2006, ApJ, 653, 675

Tabeshian, M. & Wiegert, P. A. 2016, ApJ, 818, 159

Teachey, A., Kipping, D. M., & Schmitt, A. R. 2018, AJ, 155, 36

Thalmann, C., Janson, M., Buenzli, E., et al. 2013, ApJ, 763, L29

Thébault, P. & Beust, H. 2001, A&A, 376, 621

Thureau, N. D., Greaves, J. S., Matthews, B. C., et al. 2014, MNRAS, 445, 2558

Tokovinin, A. 2008, MNRAS, 389, 925

Torres, C. A. O., Quast, G. R., Melo, C. H. F., & Sterzik, M. F. 2008, Young Nearby Loose Associations, ed. B. Reipurth, Vol. 5, 757

Ulmer-Moll, S., Santos, N. C., Figueira, P., Brinchmann, J., & Faria, J. P. 2019, A&A, 630, A135

van Dishoeck, E. F. & Black, J. H. 1988, ApJ, 334, 771

van Leeuwen, F. 2007, A&A, 474, 653

Vican, L., Schneider, A., Bryden, G., et al. 2016, ApJ, 833, 263

Vidal-Madjar, A., Kiefer, F., Lecavelier des Etangs, A., et al. 2017, A&A, 607, A25

Vidal-Madjar, A., Lagrange-Henri, A.-M., Feldman, P. D., et al. 1994, A&A, 290, 245

Vidal-Madjar, A., Lecavelier des Etangs, A., & Ferlet, R. 1998, , 46, 629

Villaver, E. & Livio, M. 2007, ApJ, 661, 1192

Wang, S. & Chen, X. 2019, arXiv e-prints [[arXiv]1904.04575]

Weidenschilling, S. J. 1977, Ap&SS, 51, 153

Welsh, B. Y., Craig, N., Crawford, I. A., & Price, R. J. 1998, A&A, 338, 674

Welsh, B. Y., Lallement, R., Vergely, J.-L., & Raimond, S. 2010, A&A, 510, A54

Welsh, B. Y. & Montgomery, S. 2013, PASP, 125, 759

Welsh, B. Y. & Montgomery, S. L. 2015, Advances in Astronomy, 2015, 980323

Welsh, B. Y. & Montgomery, S. L. 2018, MNRAS, 474, 1515

Welsh, B. Y. & Montgomery, S. L. 2019, Research Notes of the American Astronomical Society, 3, 25

Welty, D. E., Hobbs, L. M., & Kulkarni, V. P. 1994, ApJ, 436, 152

Welty, D. E., Morton, D. C., & Hobbs, L. M. 1996, ApJS, 106, 533

Wenger, M., Ochsenbein, F., Egret, D., et al. 2000a, A&AS, 143, 9

Wenger, M., Ochsenbein, F., Egret, D., et al. 2000b, A&AS, 143, 9

Werner, M. W., Roellig, T. L., Low, F. J., et al. 2004, ApJS, 154, 1

Wood, H. J. & Hollis, J. M. 1971, A&A, 12, 468

Wootten, A. & Thompson, A. R. 2009, IEEE Proceedings, 97, 1463

Worthey, G. & Lee, H.-c. 2011, ApJS, 193, 1

Wright, C. O., Egan, M. P., Kraemer, K. E., & Price, S. D. 2003, AJ, 125, 359

Wyatt, M. C. 2008, ARA&A, 46, 339

Wyatt, M. C., Panić, O., Kennedy, G. M., & Matrà, L. 2015, Ap&SS, 357, 103

Zechmeister, M. & Kürster, M. 2009, A&A, 496, 577

Zieba, S., Zwintz, K., Kenworthy, M. A., & Kennedy, G. M. 2019, arXiv e-prints [[arXiv]1903.11071]

Zorec, J., Rieutord, M., Espinosa Lara, F., et al. 2017, A&A, 606, A32

Zorec, J. & Royer, F. 2012, A&A, 537, A120

Zuckerman, B. 2019, ApJ, 870, 27

Zuckerman, B., Forveille, T., & Kastner, J. H. 1995, Nat, 373, 494

Zuckerman, B. & Song, I. 2012, ApJ, 758, 77

Agradecementos

Que curtos parecen catro anos, cando chega unha ó final. E que cheos de sucesos fortuítos, que cambian a vida para ben ou para mal. Neste punto, parece mentira que quen non está saíra da miña vida, e que quen chegou vaia quedar xa para sempre.

Voulle dar primeiro as gracias a Benja, pola ciencia, marabillosa e precisa, a que acumula e a que comparte, por todo o que me aprendeu, incluído o necesario das pequenas cousas, da relevancia do minucioso, e o gratificante do traballo duro e ben feito. Pero tamén polo persoal, claro. Polas conversas de política e cultura, polos viaxes no *Benjabus*, antes e durante a tese, por facer que ás veces sexa difícil decir se é mellor persoa ou profesional. Sobre todo, por entender o duros que foron para min estes anos. Calquera que atope a Benja no camiño, que o aproveite, que non creo que de moitas persoas se poida aprender tanto, e tan ben.

A Eva, que é todo un exemplo, unha gran científica, unha gran muller, unha desas persoas que é imposible non admirar. Ogallá parecerme algún día un pouco a ela. Sempre sen perder o sorriso, nen o xenio, as ganas de axudar, de participar en todo o que é fascinante. Porque sempre axudou en todo o que estivo na súa man, por construir co seu traballo esta experiencia magnífica, e con quen sei que me queda moito por diante, por traballar, por compartir. Incluídos algúns gusanitos.

Aos dous por darme esta oportunidade, que marca o inicio da miña carreira científica, e que xa non se olvida.

A Carlos, o meu outro director, que non sae na portada, pero si en todo o demais. Que non sempre nos entendemos, pero polo menos sempre intentamos comprendernos. A ver para cando ese libro, con todas esas historias que me contaches en Calar Alto, no Roque dos Muchachos, e nas horas de coche ou de avión. Que non se me olvide! Gracias por Casa Goyo, posiblemente a mellor superstición da historia. E polo que aprendín observando, polo sono tremendo que pasei, e por todas as horas que me fixeches traballar, que quedan aquí reflexadas. Ben puideches esperar un pouco máis para te xubilar, que aínda temos moito traballo por diante. E non, nada de galiñas, que seguen sen me dar as contas.

Ao edificio decrépito da Facultade de Ciencias. Dun xeito ou outro, hei botar en falta as ventás que non cerran, os buratos na parede, polos que entrou aquela invasión de abellas, a calefacción que non acende ata Novembro, faga o tempo que faga, e as luces que se funden. Ese edificio de infinitas escaleiras no que compartín almorzos, comidas e merendas, horas de traballo, charlas e discusións. Esta tese está feita *a pesares* dos compañeiros de despacho, que moi pronto se fixeron amigos. De Miguel, de Raúl, de Marina, de Sandra e de Asier (e agora tamén de Marta!). E de Dani e de Wei, que

non compartiamos despacho, pero si partidos de pádel (se se lles pode chamar así). Cada un ao seu xeito, todos me fixeron malgastar tempo. Bueno, malgastar. Depende a quen lle preguntes. Tamén a Gwen, que nos arranxa ceas, para vermonos un pouco máis aínda. E a Alex e Antonio.

Ao personal da cafetería, a Pili e a Miguel, a Ubaldo, a Javi e a Ana. A Ángeles. A toda esa xente que fai o día a día.

Ás miñas rapazas da UAM débolles un parágrafo especial. A Marina, que me da paz as menos das veces, pero sempre cando máis falla facía (vídeos de canciños por medio). A Doris, que non sei de onde saca enerxía, e que comparte comigo o de apuntarnos a tódalas festas. A Isa, que canto se bota de menos que esteas sempre ahí, co despacho cheo de pratos da cafetería, a correr sempre dun lado para outro, para poder facer de todo. E a Ania, que lle debo unha viaxe a Polonia. E a Malu, que lle debo unha a Brasil. Que ben me coidades, que ben me queredes.

Ás miñas constantes, a Sara e a Medea, que compartimos todo dende sempre, e para sempre. Que sempre me fan sentir orgullosa. Que non sempre están para cando hai festa, pero sempre están cando teñen que estar. A Romina e a David, que compatiron os anos de universidade, e moitos antes diso, e moitos despois. Que tamén sempre están ahí, ata para tocar os coll*ns cando escribo os agradecementos da tese. Os meus *Volumeneers*, as miñas ratas fashion.

A Suso[1], o mellor amigo que levei da carreira. Quén o diría, co teimudo que é. A Juan, que tampouco non se queda atrás. A Lucas, que me deches un mozo, e que a ver se volves dunha vez. A Yago e a Montse, que comparten concertos, cenas, e series. A Manuel, co que me fixen unha idea do que era a investigación.

A Ana. E tamén a Minia. Proba de que no país hai astrofísica.

A Cielobarbanza, a miña paixón feita afección.

Ao meu anaquiño de Galicia en Madrid, Xirandela. Sobre todo a Iria, Iago, Alex, Rebe e María. Pero non me olvido dos demáis, que fan festa que da gusto. Gracias por compartir a morriña, os viaxes e as foliadas, e por introducirme nas tradicións, e facerme ver que son nosas. E supoño que por todo o que queda por diante.

A Fer e a Alicia, que compartiron tantos días, paseos, comidas e cervexas. E agora a Estrellita, que ten ben a quen se parecer. E a Alba, por tódalas visitas, e as historias *asquerositas* que nos conta.

A Christine Chen, por me acoller uns meses en Baltimore, e por seguir trabllando comigo. E tamén a Aki Roberge e Carol Grady, que gracias a elas podo dicir que estiven na NASA. A Justin e Reika, os mellores caseiros. E a Teresa e Pepe, que sempre me reciben con brazos abertos.

Aos meus compañeiros de ESAC. A Alejandro, que marchou tan lonxe, pero aínda así facemos por nos ver tódolos anos. Á miña Alicia, que me acordo moito dela, e que a ver se ven a Boiro. A Cesar, que nunca ten tempo para unha caña. A Álvaro, a Nacho. A Pablo, que sempre mira por min. A Héctor, que está esperando a que lle invite a unha empanada, ou a unha ración de polbo. A Bruno e a Hervé, que me axudaron e apoiaron. Aínda o fan. Ás rapazas do fútbol, que non todo vai ser ciencia.

[1]Forza Depor!

Aos amigos que deixei en Canarias, e que están esparcidos polo mundo. A Masca, que non lle gusta que lle chame así, pero sabe que non o fago por mal. E a Clara, que moito a boto en falta. A Roi, por me aguantar durante o traballo de fin de maestría, e acordarse moito de min. A Ana e David, e á súa familia.

Á miña familia. A toda. Os Montoya, que diría meu pai. Ás mulleres da casa, miñas tías (as políticas tamén!), miñas abuelas, que sempre confiaron en que había de chegar ata aquí, que son exemplo do traballo, e tamén do cariño. En especial a Carmiña, que me cambiou os cueiros, aínda que non saiba cantar nanas. A meus tíos, que me facían escoller favorito de pequena, e favorito sodes todos. A meus abuelos, que habían estar ben orgullosos. E a meus primos, Fer, Dani, Samuel e Roi. E a miñas primas Luz, Sonia, Clara, María, Olga, Lucía e Zoe. E sobre todo a meu irmán, que por sorte, é a miña contraparte, o ben do mal que fago eu. E ao que non lle perdono que sempre me deixe sen churruscos. E a Charlie, probiño, non o vou deixar fóra.

A miña nai, que deu todo por nós. A meu pai, que nos aprendeu valores. Aos dous, que nos fixeron quenes somos.

A ti, Javi. Por todo o bo e todo o malo que compartimos, tódolos bicos e as apertas, tódalas veces que me espertas de noite, toda a paciencia que tes sempre comigo, e tódalas veces que me fas rir.

E a tódala xente que non aparece nestas páxinas, que se cruzou no meu camiño, e que me fixo chegar até aquí. Gracias.

Carlos, ¿qué?